Title
Non-linear Phenomena of Wing Flutter and the Effect of Laminar-Turbulent Transition

Author
Marti, Ferran

Publication Date
2017

Peer reviewed|Thesis/dissertation

UNIVERSITY OF CALIFORNIA,
IRVINE

Non-linear Phenomena of Wing Flutter and the Effect of Laminar-Turbulent Transition

DISSERTATION

submitted in partial satisfaction of the requirements
for the degree of

DOCTOR OF PHILOSOPHY

in Mechanical and Aerospace Engineering

by

Ferran Marti

Dissertation Committee:
Professor Feng Liu, Chair
Professor Derek Dunn-Rankin
Professor Roger Rangel

2017

TABLE OF CONTENTS

LIST OF FIGURES

LIST OF TABLES

LIST OF SYMBOLS

a	Distance of elastic axis behind midchord, percent semichord
b	Airfoil semichord
c	Airfoil chord
C_l	Lift coefficient, upward positive
C_m	Moment coefficient, nose-up positive
E	Energy
H	Boundary layer shape factor
h	Heaving displacement, downward positive
H_k	Kinematic boundary layer shape factor
I_α	Moment of inertia about the elastic axis, $I_\alpha = I_{cg} + m\,b^2\,x_\alpha^2$, $I_\alpha = m\,b^2, r_{cg}^2$
K	Constant of elasticity
L	Lift, upward positive
M	Moment, nose-up positive
m	Mass
M_∞	Free-stream Mach number
n	Amplification factor for e^N transition
N_{crit}	Critical amplification factor. $x = x_{tr}$ when $n = N_{crit}$
p	Pressure
q	Heat conduction flux
r	Radius of gyration, percent semichord
R^*	Residual
Re	Reynolds number

S	Surface
S_α	Static unbalance, $S_\alpha = m\,b\,x_\alpha$
t	Time
t^*	Pseudo time
u	Velocity component in x-direction
U_e	Velocity at the edge of the boundary layer
U_∞	Free-stream velocity
v	Velocity component in y-direction
V_F	Speed index, $V_F = U_\infty/(b\omega_\alpha\sqrt{\mu})$
x_α	Distance of center of gravity behind elastic axis, percent semichord
x_{cg}	Distance of center of gravity behind midchord, percent semichord
x_{tr}	Transition position
$\vec{F}_c$	Convective fluxes
$\vec{F}_v$	Viscous fluxes
n	Vector normal to cell face
W	Vector of conservative variables
cg	Center of gravity
ea	Elastic axis
g	Grid
r	Relative
α	Pitching displacement, nose-up positive
δ	Boundary layer thickness
δ^*	Boundary layer displacement thickness
Δt	Real time step
η_i	Generalized coordinate of mode i
γ	Heat capacity ratio
γ_{tr}	Intermittency due to transition

κ	Reduced frequency
μ	Airfoil mass ratio $\mu = m/(\pi\rho_\infty b^2)$
ν	Kinematic viscosity
Ω	Volume
ω_1, ω_2	Coupled natural frequency of modes 1 and 2 (eigenfrequencies)
ω_α	Uncoupled natural frequency of pitch
ω_h	Uncoupled natural frequency of heave
ϕ_i	Mode shape of the ith mode
ρ	Density
τ	Shear stress
θ	Boundary layer momentum thickness
$\tilde{\mu}$	Modified eddy viscosity
ξ_i	Modal damping of the ith mode

ACKNOWLEDGMENTS

I would like to first thank my adviser Professor Feng Liu for his mentorship, guidance and care through these years. His teachings have been invaluable and will serve me for the rest of my career. I can recall countless occasions where he would easily solve problems in our weekly meetings that had me stuck for many hours of thinking. As his graduate student he made me feel understood and I deeply appreciate all his efforts during my research with him in Beijing.

I would also like to thank Professors Derek Dunn-Rankin and Roger Rangel for agreeing to be part of this dissertation committee, and for their insightful comments to improve the quality of this document. This committee is special to me since Professor Dunn-Rankin was my Master of Science adviser and I greatly benefited from his mentorship during my time as his graduate student. Professor Rangel is the director of the Balsells Fellowships which gave me the opportunity of moving to the United States for my graduate studies.

Probably the first stone in this long journey was set many years ago when Mr. Peter Balsells decided to create the Balsells Fellowships and bring Catalan students to UC Irvine. I am deeply grateful to him, to the university and to the Catalan government for working together towards the creation of these fellowships that have brought many students to the U.S. and have given us an opportunity to enhance our education.

Ms. Louise Yeager deserves many thanks as she has help me through the years with much of the paperwork and administrative bureaucracy in the university.

I owe gratitude to Professor Aparna Chandramowlishwaran for letting me be part of a joint research team between her lab and ours to work on High Performance Computing (HPC) with Fluid Dynamic applications. I am also thankful to her graduate students, particularly Bahareh Mostafazadeh who has taught me many HPC concepts and with whom I have shared many working hours.

My appreciation to my classmates and labmates in the department for their friendship and for brainstorming through which I have improved my learning and quality of my research. I especially remember insightful conversations with Rayomand Gundevia, Kevin Laungluck-navalai, Shervin Taghavi and Lei Zhan.

I am deeply grateful to Joseph Farran and Mahidhar Tatineni who have helped with parallel computing issues in the corresponding supercomputers that they lead. This work used the Extreme Science and Engineering Discovery Environment (XSEDE), which is supported by National Science Foundation grant number ACI-1053575.

Finally I would like to thank my parents, my family in Spain, my family in the U.S. and my friends from both countries for making these years a remarkable experience sharing many meals, trips and experiences together. My deepest gratitude is to my wife and best friend Cynthia, who has been by my side through this journey. Her one of a kind personality has sparked a smile on me when I have needed it the most.

CURRICULUM VITAE

Ferran Marti

EDUCATION

Ph.D. in Mechanical and Aerospace Engineering — **Feb. 2017**
University of California, Irvine — *Irvine, California*
Dissertation: Free Laminar-Turbulent Transition in Aeroelastic Simulations
Advisor: Feng Liu

M.S. in Mechanical and Aerospace Engineering — **Dec. 2012**
University of California, Irvine — *Irvine, California*
Thesis: Droplet Evaporation in an Active Turbulence Grid Wind Tunnel
Advisor: Derek Dunn-Rankin

Aeronautical Engineering — **Sept. 2010**
Universitat Politecnica de Catalunya — *Terrassa, Spain*

EXPERIENCE

Collaborating Researcher with HPC Factory Lab. — **Apr. 2015–Present**
University of California, Irvine — *Irvine, California*

Engineer — **Jun. 2016–Present**
Creative Aero Engineering Solutions — *Buena Park, California*

Journal Reviewer — **Dec. 2016–Present**
ASME Journal of Fluids Engineering

Graduate Research and Teaching Assistant — **Jan. 2011–Dec. 2016**
University of California, Irvine — *Irvine, California*

Exchange Student — **Jun. 2013–Sept. 2013**
Peking University — *Beijing, China*

Research and Development Intern — **Oct. 2009–Mar. 2010**
Hewlett-Packard — *Sant Cugat, Spain*

PUBLICATIONS

F. Marti and F. Liu, *A Quasi-Steady Method to Simulate Free-Transition Over Unsteady Airfoils* **Jun. 2017**
Accepted for AIAA Aviation Forum. Denver, CO.

B. Mostafazadeh, F. Marti, F. Liu, and A. Chandramowlishwaran, *Parallel Algorithms for Unsteady Navier-Stokes Flow on Heterogeneous Architectures* **Jun. 2017**
Accepted for AIAA Aviation Forum. Denver, CO.

F. Marti and F. Liu, *Flutter Study of NACA 64A010 Airfoil Using URANS and e^N Transition Models Coupled with an Integral Boundary Layer Code* **Jan. 2017**
AIAA Scitech Forum. Dallas, TX.

F. Marti and F. Liu, *Multiple Equilibrium Points of Airfoil Flutter in Viscous Flow* **Jan. 2017**
AIAA Scitech Forum. Dallas, TX.

B. Mostafazadeh, F. Marti, F. Liu, and A. Chandramowlishwaran, *Laminar Unsteady Navier-Stokes Flow on Multicore Architectures* **Nov. 2016**
SuperComputing 2016. Salt Lake City, UT

F. Marti, O. Martinez, D. Mazo, J. Garman and D. Dunn-Rankin, *Evaporation of a droplet larger than the Kolmogorov length scale immersed in a relative mean flow* **Oct. 2016**
International Journal of Multiphase Flow

B. Mostafazadeh, F. Marti, F. Liu, and A. Chandramowlishwaran, *Parallel Algorithms for Unsteady Navier-Stokes Flow on GPU Architectures* **Apr. 2016**
GPU Technology Conference. San Jose, CA

F. Marti, J. Garman, K. Kakavand and K. Samaan, *Observations of Periodic Oscillatory Behavior in Flow Rates of Laboratory Syringe Pumps and Proposed Remedies* **Oct. 2011**
Western States Section Technical Meeting. The Combustion Institute. Riverside, CA.

ABSTRACT OF THE DISSERTATION

Non-linear Phenomena of Wing Flutter and the Effect of Laminar-Turbulent Transition

By

Ferran Marti

Doctor of Philosophy in Mechanical and Aerospace Engineering

University of California, Irvine, 2017

Professor Feng Liu, Chair

A Navier-Stokes Computational Fluid Dynamics (CFD) code is coupled with a Computational Structural Dynamics (CSD) code to study the flutter boundary of the NACA64A010 airfoil using Isogai's structural model in transonic conditions. This model simulates aeroelastic conditions on a sweptback wing. A well-known feature, only present in the inviscid flutter boundary of this airfoil, is the existence of multiple flutter points for a fixed freestream Mach number. The fully-turbulent flutter boundary has not been studied by many researchers using a Reynolds-Averaged Navier-Stokes approach. In the present study, the fully-turbulent flutter boundary reveals the existence of multiple equilibrium positions for a narrow range of flight conditions. The system moves away from the initial equilibrium position, finding a new set of equilibrium points and oscillating around it. This new set of equilibrium points reveals as stable or unstable for different structural properties of the wing.

We then proceed to study the effect of turbulent transition on flutter boundary. A laminar-to-turbulent transition model is implemented in the CFD code and validated. The effect of using a free-transition CFD code vs. a fully-turbulent approach is evaluated on three airfoils with different characteristics for subsonic and transonic conditions. While free-transition does not affect the pressure distribution at subsonic conditions, the transonic simulations reveal a change in the shock-wave position when laminar-turbulent effects are included. The

effect of transition on the flutter boundary of the NACA64A010 airfoil at transonic conditions is then investigated. A comparison between the free-transition, inviscid and fully-turbulent flutter boundaries reveals similarities between the inviscid and free-transition elastic responses. Those similarities are due to the shift in the fully-turbulent shock-wave position, when accounting for free-transition effects, moving closer to the inviscid shock location.

Chapter 1

Introduction

The use of computational methods to solve engineering problems has improved the engineering design tools and allowed scientists to gain understanding in the physical phenomena of fluid flow.

Performing science or engineering with only experimental methods is an expensive and time consuming task. Wind tunnels are used to simulate flow conditions of real flight using scaled models of the real size wing or full aircraft configurations. By matching non-dimensional conditions of real flight, the non-dimensional data can be translated to dimensional data at flight conditions for non-scaled real size aircrafts. One of the main difficulties is matching all non-dimensional numbers. Specially, in transonic or supersonic conditions, the Mach number needs to be matched, along with the Reynolds number and the specific heat ratio (if heat transfer effects must be considered). This generally leads to the use of cryogenic wind tunnels [44], where temperature is dropped below freezing point using special gasses as driven flow, and pressurized conditions are used to control all non-dimensional parameters. Such runs are very expensive due to the amount of energy needed to run the cryogenic part, but also the flow part of the tunnel. If normally multiple design configurations are tested,

the cost will keep on increasing. Computational Fluid Dynamics aims to reduce the cost while producing results, ideally, as good as the experimental conditions provide. In practice, if the smallest turbulent scales are to be captured in a numerical simulation of high Reynolds number (engineering applications tend to take place at high Reynolds number conditions), the numerical grid size and time step would be so small that the electric cost in running such supercomputers would exceed the cost of performing the previously mentioned experimental tests. In order to be able to use numerical methods that provide a reliable solution with a small cost, multiple approximations have been created which proved very successful when used within their own assumptions.

Initially in the sixties, panel methods were the only tool available for solving subsonic flow [33] by solving the incompressible potential equation along with corrections for compressibility effects. In the seventies, Murman and Cole [59] were the pioneers in solving the transonic small perturbation equation which allowed for a more accurate solution of transonic flows. It was not until 1981 when Jameson, Schmidt and Turkel [41], using the well-known JST scheme, solved the Euler equations in transonic conditions. Following their work, the addition of viscous fluxes along with algebraic turbulence models [16] [6] enabled the computations of steady turbulent flow. Further improvements in turbulence models to account for the transport of turbulent quantities improved the results obtained at the moment [74] [57]. The introduction of dual-time stepping by Jameson [39] finally allowed for efficient computation of unsteady flows. Further improvements in numerical methods [37] along with improvements in computing hardware [61] allowed for the computation of more complicated unsteady physics in full aircraft configurations.

After being able to obtain accurate results of steady and unsteady flowfield solutions, more ambitious approaches like aeroelasticity or optimization methods [38] aimed at improving the design tools providing more accurate results and creating more efficient flying crafts.

The objective of the present work is to solve the structural and fluid flow equations in a cou-

pled mode to obtain an aeroelastic solution of a loaded wing section. A further contribution of this dissertation is to account for free laminar-turbulent transition and assess whether its effect is significant compared to the common use of fully turbulent conditions.

1.1 Aeroelasticity

Aeroelasticity is the combination of aerodynamics and elasticity. Computational aeroelasticity combines Computational Fluid Dynamics (CFD) to obtain the force distribution on aerodynamic bodies using the previously mentioned methods, with Computational Structure Dynamics (CSD) to obtain structural deformation under a given loading.

This Fluid-Structure Interaction (FSI) problem is not only studied on aircrafts, but also on buildings, bridges, cars and even birds or insects. From an engineering point of view, the structure needs to be able to support any aerodynamic loading either static or dynamic. And from a scientific point of view, the study of an insect flapping wing can reveal many interesting features of the wing shape and even some of those could end up in human-made flying crafts.

Two approaches are generally used. If the deformations are small, such that a change in bending or torsion will not have a significant effect on the aerodynamic loading, an uncoupled approach might be used. After a given forced motion, the aerodynamic loading is applied to the structural solver to analyze the structural motion, and compare it with the initial forced motion assigned. This approach provides a cheap method to study if a given oscillation will tend to grow or decay, and therefore if those flight conditions are stable or unstable. If a more accurate approach is needed, a coupled method where the CFD and CSD equations are solved in time-accurate mode, provides a more expensive but better prediction of the stability or instability of a FSI problem. In a general three-dimensional code, Figure 1.1

exemplifies the transfer of information between the CFD and the CSD codes.

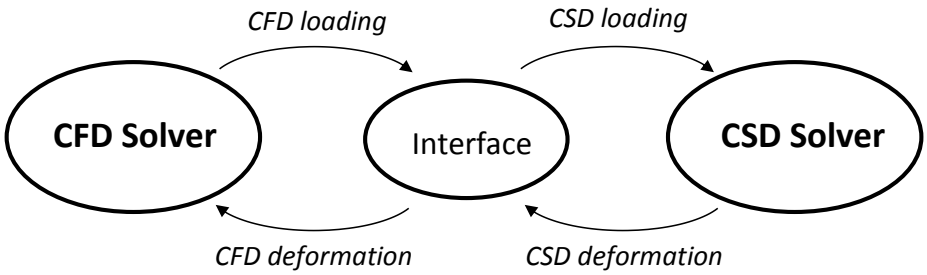

Figure 1.1: Transit of information between the Fluid and Structure solver in an aeroelastic analysis.

Once the flowfield is converged on the CFD code, the loading on the body must be transferred from the CFD mesh to the CSD mesh using an interface method between the two that conserves energy. The CSD code deforms the CSD grid, and such deformation must be transferred back using the same interface method into the CFD code. Given the new CFD deformed grid, a new loading will be computed and the process will iterate until both sets of equations are satisfied.

Given a rigid wing, the solution might be steady or unsteady. An example of unsteady flowfields in rigid bodies could be vortex shedding, or transonic buffet. While it is interesting to couple those physics with a flexible structure to understand how flexibility affects the final solution, stability studies are normally performed on structures where the flow solution is steady when the body is rigid. Coupling the CFD with the CSD code and generating an initial disturbance in what would otherwise be a steady solution, will bring the system back to stability or perhaps not. Figure 1.2(a) shows the heaving amplitude vs. time of a stable case, while Figure 1.2(b) shows an unstable example where the amplitude of the oscillations grow until reaching Limit Cycle Oscillations. Under a linear stability analysis, the dynamic system oscillations will grow or decay infinitely. When growing in an unstable case (known as flutter), non-linear aerodynamic and structural effects may become significant when the amplitude of the oscillations is large, and the effect is to stop the growth of the oscillations

entering in the range known as Limit Cycle Oscillations (LCO). In this dissertation only aerodynamic non-linear effects are studied.

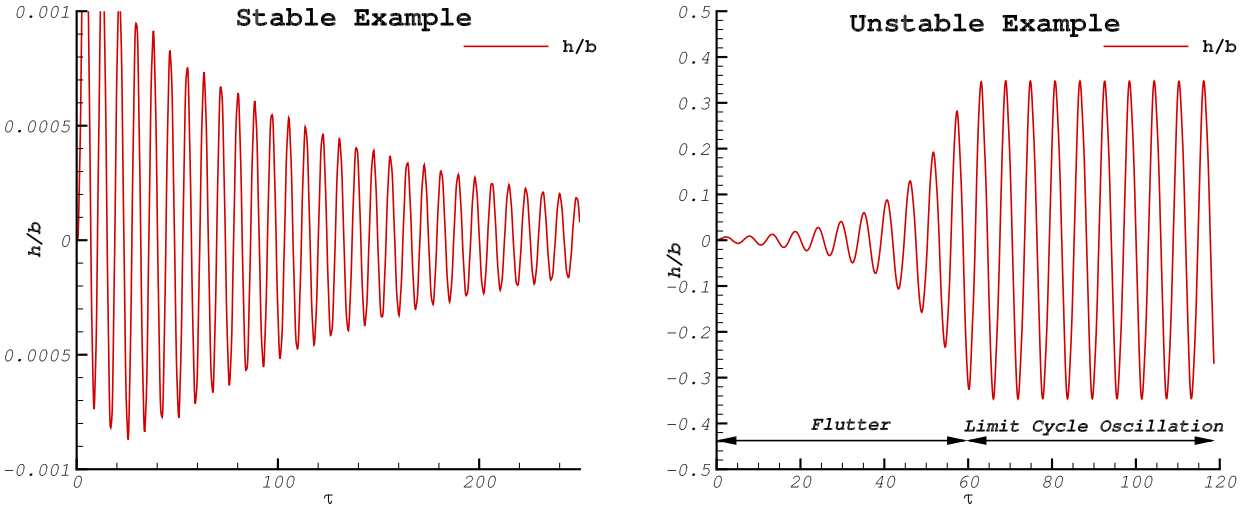

(a) (b)

Figure 1.2: Heaving response vs. time examples of a speed index value that is (a) stable, (b) unstable.

The speed index is a measure of the impact of the aerodynamic loading on the deformation of the wing. High values of speed index correspond to flexible wings with low inertia compared to the air mass.

$$V_F = \frac{U_\infty}{b\,\omega_\alpha\,\sqrt{\mu}} = \frac{1}{K_\alpha\,\sqrt{\mu}} \tag{1.1}$$

Low reduced natural frequency (K_α) means a soft structural response at a lower frequency value. Low values of mass ratio (μ) correspond to wings with a weight lighter than the air displaced by the wing.

Generally, a low speed index value results in a stable solution (Figure 1.2(a)), and a large V_F value results in an unstable response (Figure 1.2(b)). Between these two speed index values, there is a V_F which corresponds to the neutral stability case (Figure 1.3(a)). Given an initial perturbation, the system does not grow or decay in magnitude. Finding the speed

index values of neutral stability for a range of Mach numbers, produces what is known as the flutter boundary (Figure 1.3(b)).

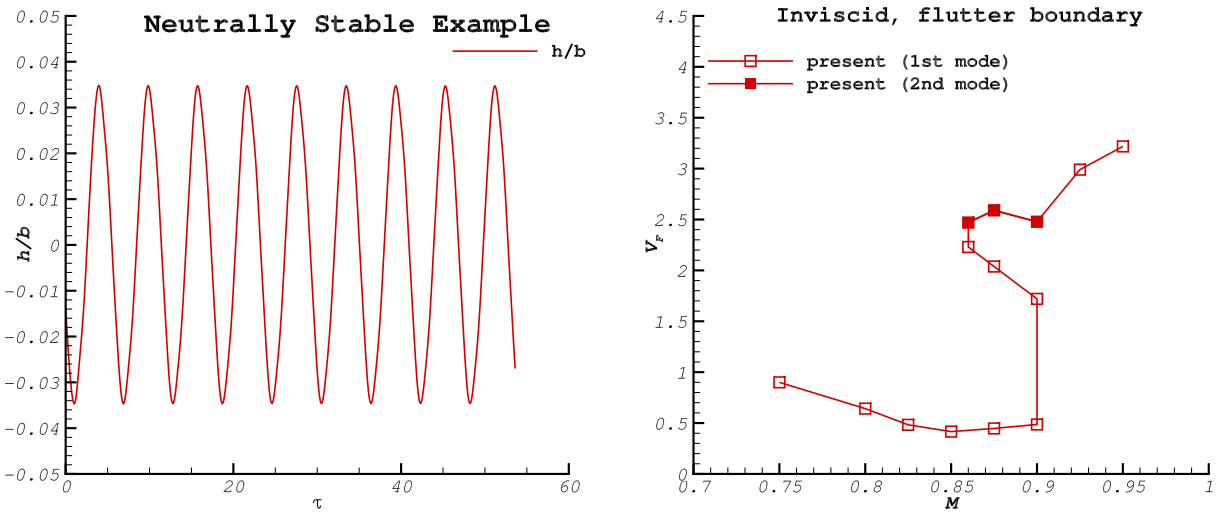

(a) (b)

Figure 1.3: (a) Example of a neutrally stable heaving response vs. time, (b) Flutter boundary example.

Figure 1.3(b), which will be detailed in Section 2.4, is the inviscid flutter boundary for the NACA64A010 airfoil. Any combination of $(Mach, V_F)$ to the left-top of the boundary will result in an unstable solution, and any combination at the right-bottom of the boundary will produce a stable response.

From a CSD perspective, the structural equations can be solved in direct or modal methods. The direct method normally uses Finite Elements (FE) to discretize the structural domain which contains a detailed geometry of the inner body structure, and this allows the use of non-linear structural equations which might be the only solution if large deformations exist. If the deformations are smooth, which is normally the case in wing aeroelasticity, a modal method is more convenient. Normally, using a FE code which contains the complete structural geometry, the modal shapes from the undeformed structured are obtained. Those modal shapes are then used in the FSI using the modal method as a vector space such that the specific weighted contribution of the first five to ten modes generates an accurate expansion

of the exact solution. The modal method is normally preferred due to the simplicity of not having to deal with a FE code and a fluids code at the same time. Sometimes, even the same surface grid could be used for FSI problems using the modal method, which facilitates the exchange of information between CFD and CSD codes. Although normally less than ten modes is enough to obtain an accurate solution, using all the modes (finite number, since there are a finite number of structural points) would reproduce the exact solution obtained by a linear FE analysis.

A simpler approach for two dimensional aeroelastic computations is to use the model defined by Isogai [36] which assumes the shape of the airfoil to remain unaltered, while allowing a pitching and heaving motion. This two-degree of freedom (DoF) model represent a mid-span section of a sweptback wing which is bending (two dimensional heaving DoF) and being torsioned (two dimensional pitching DoF). A sketch of the model is shown in Figure 1.4.

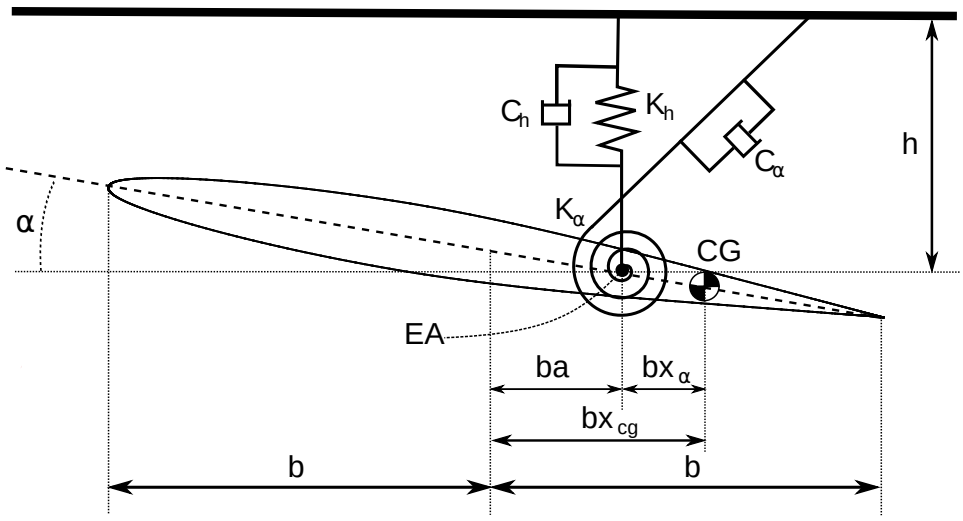

Figure 1.4: Isogai sketch of the two-degree of freedom aeroelastic model.

Although the sketch is generic, for the Isogai model $a = -2.0$ which places the elastic axis before the leading edge of the airfoil. This is justified since the model represents a midspan section of a sweptback wing. Since the wing is sweptback, when applying torsion, a midspan section would pitch with respect to a point ahead of the leading edge. Since there

are only two degrees of freedom in this model, only two modal shapes are possible. This creates a simple approach to using the modal method and obtain two dimensional aeroelastic results that represent the elastic response of a three dimensional wing. Isogai [36] was the first to report results based on a method using a linearized subsonic unsteady aerodynamic forces [1] . Edwards et al. [24] solved the low-frequency unsteady transonic small perturbation equation while Ehlers and Weatherill [25] solved the transonic small perturbation equation for a harmonically oscillating wing. These initial results provided excellent indications of the overall response of inviscid solutions, but further details were revealed with more recent solutions of the Euler equations. Liu et al. [51] , Alonso and Jameson [2] , Hall et al. [30] , and Bohbot et al. [10] represent some of the recent efforts to capture the flutter boundary solving the exact Euler equations. A transonic dip is obtained around $M_\infty = 0.85 - 0.9$. Multiple flutter points are obtained for a fixed Mach number within the $M_\infty = 0.85 - 0.9$ range. For a given Mach number, increasing the speed index sets the airfoil in unstable mode, a further increase results in a stable situation, and another increase reveals a second flutter point where the second mode becomes the dominant one.

Yang et al. [86] used an Euler code coupled with an integral boundary layer method while Prananta [62] solved the Thin-Layer Navier-Stokes equations. The solution of the Euler equations coupled with boundary layer methods revealed some differences in the flutter boundary of the Isogai model. Multiple flutter points are not obtained by those methods for the same Mach number any more, and while the transonic dip is still present, it appears smoother than in the inviscid situation.

The Reynolds-Averaged Navier-Stokes equations were solved by Bohbot et al. [10] , and by Chen et al. [18] revealing small differences with respect to boundary layer methods in the region $M_\infty = 0.85 - 0.9$. The flutter boundary in this region exhibits almost constant critical speed index values for the RANS equations, while boundary layer methods predicted an increase of the speed index with increasing Mach number. Chen et al. [18] revealed multiple

equilibrium points for $M_\infty = 0.875$ although those were not fully investigated. An initial equilibrium position of $h/b = 0$ and $\alpha = 0$ was found as unstable, but instead of producing pitching and heaving oscillations of growing amplitude around the given equilibrium point, the system would evolve into a new $\{h/b, \alpha\}$ equilibrium point and oscillate around it with growing or decaying oscillations.

The goal of the present work is to further examine the region where multiple equilibrium points exist for the fluid-structure interaction of the NACA 64A010 airfoil. Those multiple equilibrium points are not obtained in inviscid solutions, and there is little information reported for viscous cases aside from that reported by Chen et al. [18]. A Reynolds number of 10^7 is used in the present study.

Although this structural model has been used by many researchers to compute the flutter boundary for the inviscid equations, there are fewer results for viscous solutions, all of which assume fully turbulent flow. The second goal of this dissertation is to compute the flutter boundary of the NACA 64A010 airfoil for free transition conditions and analyze the differences from that predicted by using a fully turbulent flow.

1.2 Free transition

Laminar to turbulent transition is still a subject under study. While many turbulence models have been developed which produce good results for well behaved flows, not many options are available to account for transition prediction. A common practise for CFD users is to prescribe transition position based on experience or, based on the trip position used when comparing with experimental results. An even more general practice is to assume the flow to be completely turbulent and not account for any transition at all. While these practices are justified on the lack of a robust and validated transition model, it is still under debate

the effect that free transition might have in free flight conditions.

Johansen [42] shows almost no variation in C_p when no shock waves are present, and a reduction in drag coefficient. However for transonic flow, a delayed transition might affect the shock position which will significantly affect the distribution of C_p and the structural response of the wing.

Sturdza [78] shows a sharp increase of transition Reynolds number when the Mach number is increased. Boyle and Simon [13] show that an increase in freestream Mach number is related to a decrease in turbulent spot production rate which delays transition. On the other hand, a decrease in Reynolds number is known to delay transition.

Most popular approaches to transition prediction range from simple empirical correlations to e^N stability methods or two-equation transport models. Langry and Menter [46] propose a four-equation turbulence model where the traditional two-equation SST model [57] is solved along with an equation for the turbulence intermittency γ_{tr}, and an equation for the transition momentum thickness Reynolds number Re_θ. While the model is successfully used by Wang et al. [83] and Robitaille et al. [66] , solving four additional equations to the two-dimensional Navier-Stokes set of four equations is a significant increase in computing resources.

For two-dimensional problems, where cross flow instabilities and attachment-line transition are not present (since they have a three dimensional origin), if bypass transition does not occur then Tollmien-Schlichting waves are the main source of instability to trigger transition. Bypass transition is observed with wall roughness problems leading to an early transition position. A deeper discussion of the multiple transition mechanisms is detailed in Chapter 5.

An e^N method uses linear instability and accounts for the envelope of amplification factors of Tollmien-Schlichting waves, which is the approach adopted in the current work. Drela [23] describes the correlations used for an e^N model along with an integral boundary layer formulation to compute integral variables needed for the model. While the integral variables

could be directly obtained from their definition by integration in the boundary layer of a RANS code, a very fine grid is needed to obtain accurate integral parameters which increases significantly the computational cost especially in structured codes.

1.3 Summary of current work

Part I describes the multiple equilibrium points phenomenon existing in the flutter boundary of the NACA64A010 airfoil, when using the Isogai structural model, and fully turbulent flow. A description of the Computational Fluid Dynamics code is also included. The Isogai structural model is presented along with the numerical implementation for the Computational Structural Dynamics (CSD) code. The CSD code is validated with the inviscid flutter-boundary of the NACA64A010 airfoil.

Part II presents the implementation of a laminar-turbulent transition model, along with an Integral Boundary Layer code used to obtain accurate integral boundary layer variables needed for the model. After the model is validated in Section 5.3, three airfoils with different characteristics are simulated in subsonic and transonic conditions to understand the effect of free-transition vs. fully turbulent flow conditions.

Part III combines the two previous parts, to find the flutter boundary of the NACA64A010 airfoil in free-transition conditions.

Part I

Non-linear flutter: multiple equilibrium points

Chapter 2

Flutter prediction with the Isogai structural model

This chapter presents the detailed equations for the structural model defined by Isogai [36] along with the numerical methods used to solve them in Section 2.1. The model is used to find the flutter boundary using invisid flow, which also serves as a validation test of the model implementation, and the results are presented in Section 2.4. The Flow solver is introduced and validated in Sections 2.2 and 2.3 for fully turbulent conditions. Non-linear effects in fully-turbulent aeroelastic conditions using the Isogai wing generate multiple equilibrium points, which are described in Chapter 3.

2.1 Isogai two-dimensional structural model

The present Section introduces the structural dynamics equations, the discretization approach and the modal decomposition analysis used to solve them.

In a three-dimensional approach, the grid must be deformed and an interface between the

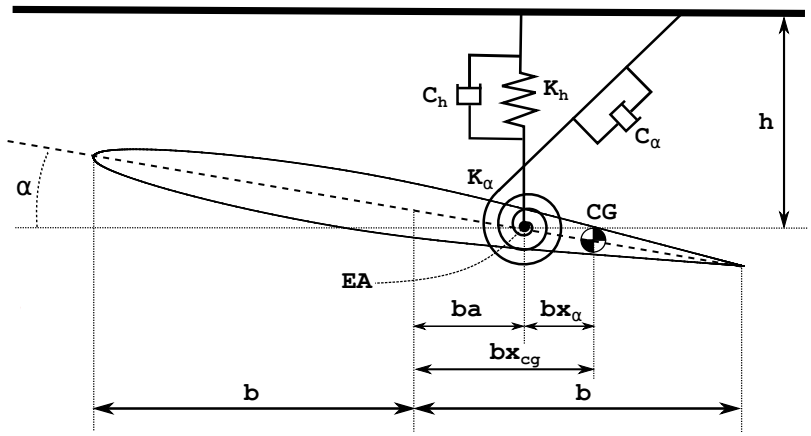

$a=-2.0$	$x_{cg}=-0.2$	$x_\alpha=1.8$
	$r^2_{cg}=0.24$	$r^2_\alpha=3.48$
	$\omega_h/\omega_\alpha=1$	$\mu=60$
$\omega_1/\omega_\alpha=0.713394$	$\Phi_1=(0.504446, 0.270411)$	
$\omega_2/\omega_\alpha=5.337706$	$\Phi_2=(3.77433, -2.02325)$	

Figure 2.1: NACA 64A010 structural model

aerodynamic loading and the structural deformation is needed. A detailed formulation of the three-dimensional aeroelastic formulation is included in appendix A. For a two-dimensional case, a structural grid is normally not needed and the entire grid is rotated around the elastic axis without the need for grid deformation. Grid deformation and transfer of loading and surface deformation between structural and aerodynamic grids are covered in appendix B for three-dimensional aeroelastic simulations.

For the present two-dimensional aeroelastic study, we use a two degrees-of-freedom model (pitch and heave) created by Isogai [36]. Alonso and Jameson [2] defined an efficient formulation for the structural implementation which is adopted in the present work. The same formulation was detailed in Liu et al. [51] .

For each real time step Δt, the flow equations are marched in parallel with the structural equations. The structural model of a two-dimensional airfoil represents a section of a three

dimensional swept wing. A sketch of the model is shown in Figure 2.1. Defining a vertical stiffness for heaving, and an angular one for pitching, a balance of force and moment leads to

$$m\,\ddot{h_{cg}} = -K_h h - L \tag{2.1}$$

$$I_{cg}\ddot{\alpha_{cg}} = -K_\alpha \alpha_{cg} + b\,x_\alpha K_h h + M_{cg} \tag{2.2}$$

The following relations are used: $\alpha_{cg} = \alpha$, and $h_{cg} = h + \alpha\, b\, x_\alpha$ for $|\alpha| << 1$. Taking the second derivative in time of h_{cg} and plugging it into Equation (2.1), one obtains

$$m\,\ddot{h} + S_\alpha \ddot{\alpha} + K_h h = -L \tag{2.3}$$

For small angles, and thin airfoils, $r_\alpha^2 = r_{cg}^2 + x_\alpha^2$ and $M_{cg} = M_{ea} + L\, b\, x_\alpha$. Using these relations combined into Equations (2.2) and (2.3), one obtains

$$S_\alpha + I_\alpha \ddot{\alpha} + K_\alpha \alpha = M_{ea} \tag{2.4}$$

Defining $\omega_\alpha^2 = K_\alpha / I_\alpha$, $\omega_h^2 = K_h/m$, a non-dimensionalization of Equations (2.3) and (2.4) is performed using a structural time τ where $d\tau = \omega_\alpha dt$, leading to

$$[M]\{\ddot{q}\} + [K]\{q\} = \{F\} \tag{2.5}$$

where

$$[M] = \begin{bmatrix} 1 & x_\alpha \\ x_\alpha & r_\alpha^2 \end{bmatrix}, \quad [K] = \begin{bmatrix} (\omega_\alpha/\omega_h)^2 & 0 \\ 0 & r_\alpha^2 \end{bmatrix}, \quad q = \begin{bmatrix} h/b \\ \alpha \end{bmatrix} \tag{2.6}$$

$$F = \frac{U_\infty^2 \rho_\infty}{\omega_\alpha^2 m} \begin{bmatrix} -C_l \\ 2C_m \end{bmatrix} = \frac{V_F^2}{\pi} \begin{bmatrix} -C_l \\ 2C_m \end{bmatrix} \tag{2.7}$$

A modal decomposition can be applied to Equation (2.5) using

$$\{q\} = [\phi]\{\eta\} = \sum_{i=1}^{2} \{\phi_i\}\eta_i \tag{2.8}$$

Since the two modes are independent, Equation (2.5) can be rewritten in modal form for a single mode as

$$\ddot{\eta}_i + \omega_i^2 \eta_i = Q_i \tag{2.9}$$

where the modes are scaled to produce

$$[\phi]^T[M][\phi] = [I], \quad [\phi]^T[K][\phi] = [\Lambda] = \begin{bmatrix} \omega_1^2 & 0 \\ 0 & \omega_2^2 \end{bmatrix}, \quad [\phi]^T\{F\} = \{Q\} \tag{2.10}$$

Although no structural damping is used for the present simulations, a general form of the previous formulation accounting for such damping would lead to

$$\ddot{\eta}_i + 2\xi_i\omega_i\dot{\eta}_i + \omega_i^2 \eta_i = Q_i \tag{2.11}$$

To solve Equation (2.11), one can transform it into a system of two first order equations defining

$$\{X_i\} = \begin{bmatrix} x_{1i} \\ x_{2i} \end{bmatrix} = \begin{bmatrix} x_{1i} \\ \dot{x}_{1i} \end{bmatrix} = \begin{bmatrix} \eta_i \\ \dot{\eta}_i \end{bmatrix} \tag{2.12}$$

and Equation (2.11) becomes

$$\{\dot{X}_i\} = [A_i]X_i + \{f_i\} \tag{2.13}$$

where

$$[A_i] = \begin{bmatrix} 0 & 1 \\ -\omega_i^2 & -2\omega_i\xi_i \end{bmatrix}, \quad [f_i] = \begin{bmatrix} 0 \\ Q_i \end{bmatrix} \tag{2.14}$$

Equation (2.13) can be decoupled by diagonalizing $[A_i]$ by finding the eigenvalues and eigenvectors of such matrix to obtain

$$\{\dot{Z}_i\} = [P_i^{-1}][A_i][P_i]Z_i + [P_i^{-1}]\{f_i\} \tag{2.15}$$

using $\{X_i\} = [P]\{Z_i\}$ where

$$[P_i] = \begin{bmatrix} (-\xi_i - \sqrt{\xi_i^2 - 1})/\omega_i & (-\xi_i + \sqrt{\xi_i^2 - 1})/\omega_i \\ 1 & 1 \end{bmatrix} \tag{2.16}$$

$$[P_i^{-1}] = \frac{-\omega_i}{2\sqrt{\xi_i^2 - 1}} \begin{bmatrix} 1 & -(-\xi_i + \sqrt{\xi_i^2 - 1})/\omega_i \\ -1 & (-\xi_i - \sqrt{\xi_i^2 - 1})/\omega_i \end{bmatrix} \tag{2.17}$$

The time derivative of Equation (2.15) is discretized with a second-order implicit scheme, and a pseudo-time is added to march to a converged solution using a five-stage Runge-Kutta scheme. For each mode, the following two decoupled equations need to be marched until the residual is converged

$$\frac{dz_{1,i}^{n+1}}{dt^*} + R_{1,i}^* = 0 \tag{2.18}$$

$$\frac{dz_{2,i}^{n+1}}{dt^*} + R_{2,i}^* = 0 \tag{2.19}$$

where the residual is

$$R_{1,i}^* = \Big(\frac{3}{2\Delta t} - \omega_i(-\xi_i + \sqrt{\xi_i^2 - 1}\Big) z_{1,i}^{n+1} - \frac{-\xi_i + \sqrt{\xi_i^2 - 1}}{2\sqrt{\xi_i^2 - 1}} Q_i^{n+1} - \frac{2}{\Delta t} z_{1,i}^n + \frac{1}{2\Delta t} z_{1,i}^{n-1} \tag{2.20}$$

$$R_{2,i}^* = \Big(\frac{3}{2\Delta t} - \omega_i(-\xi_i - \sqrt{\xi_i^2 - 1}\Big) z_{2,i}^{n+1} - \frac{\xi_i + \sqrt{\xi_i^2 - 1}}{2\sqrt{\xi_i^2 - 1}} Q_i^{n+1} - \frac{2}{\Delta t} z_{2,i}^n + \frac{1}{2\Delta t} z_{2,i}^{n-1} \tag{2.21}$$

All the parameters used in the previous equations to characterize the structural properties are determined in Isogai's work [36] . The eigenfrequencies and modal shapes are easily obtained with a short external script, and are added at the bottom of Figure 2.1. The grid is rigidly attached and rotated with the airfoil. Grid velocities are added to grid points due

to pitching and heaving.

2.2 Computational Fluid Dynamics (CFD) Approach

The methods used to obtain a flow solution for the present flutter computations are in the category of Computational Fluid Dynamics (CFD), and the in-house code used for this research is called Parallel Computation of AeroElasticity (ParCAE).

The history of modern CFD for aeronautics started around the 1970s when people solved the compressible potential flow equations. Some aircrafts were designed using those methods. In the early 80s, engineers were able to solve the Euler equations. Rapidly the CFD field accumulated a significant interest by the scientific community and along with supercomputer improvements led to solving the Navier-Stokes equations.

Because the turbulent length scales are too small in order to generate a computational grid that is able to solve high Reynolds number problems with even most modern supercomputers, turbulence models were developed to allow the use of coarser grids and save computational time. When using those, the Navier-Stokes equations are reformulated as the Reynolds-Average Navier-Stokes (RANS) equations (see Section 2.2.1). When using the RANS equations, faster solutions are obtained due to two main reasons: the reduction in the number of computations for each time step since fewer grid points are to be solved by the use of a coarser grid, and the reduction in the number of time steps since the small turbulent scales which have very small resident times are not solved and instead the averaged mean flow unsteadiness is responsible for determining the larger time step values.

However, some researchers prefer to not model the turbulent flow but directly solve the Navier-Stokes equations and capture all small length scales using Direct Numerical Simulation (DNS). This approach is so computationally intensive, that even with the use of large supercomputers only low Reynolds number problems have been solved nowadays.

Since turbulence modeling does not provide matching results with experimental data for all

cases, the scientific community is still actively involved in finding hybrid methods that with a small increase in computing time could reduce the inaccuracies of turbulence modelling. Methods that fall between RANS and DNS require larger computing times than the RANS cases but far below those required by DNS. On the other hand, they generate a more realistic flow solution since the modeling is restricted to the smallest flow length scales. Examples of such methods are Large Eddy Simulation (LES) or types of Detached Eddy Simulation (DES).

For the present study, flutter is generally well captured using a RANS formulation. Before non-linear effects are noticed when reaching Limit Cycle Oscillations, a linear stability analysis is still accurate to determine the stability or instability of a fluid-structure interaction problem. At those small oscillations, separation is almost non-existent and the need of an LES approach is therefore not justified. RANS modeling is generally well accepted for attached flows or even in flows with small separation regions. Using a RANS approach in a two-dimensional study simplifies the problem in many aspects: LES studies require a three-dimensional grid and are unsteady by definition, the RANS spatial and temporal resolution is much coarser, the accuracy of the numerical scheme can be set at second order when using RANS while generally higher order methods are employed in LES mode to avoid dissipating the smaller flow scales.

The following Sections contain some of the features of the CFD code used for the present research. There are multiple choices to make when creating a CFD code.

Three popular approaches are normally used for the spatial discretization of the flow equations: Finite Difference, Finite Volume and Finite Element Methods. While Finite Element Method (FEM) is commonly used for structural analysis, it is not as popular for solving the fluid flow equations even if it provides high accurate results. The main reason being the higher numerical effort required compared to other methods. Finite Differences (FD) are commonly used due to its simple implementation. However, the Cartesian grid required for

the computational space must be transformed into the curvilinear grid used for the physical space. Anderson [43] provides a basic introduction to the CFD field using FD. The Finite Volume Method (FVM) is the most popular along with FD. Blazek [9] provides an in-depth description of the FVM implementation for CFD applications. Its coding effort lies between FD and FEM. The main advantages of FVM over FD are the possibility of using unstructured grids, the fact that the computational domain and the physical one are the same, and the capacity of computing weak solutions. A weak solution is one where the solution might be non differentiable (shock waves). FD comes from a differential formulation of the Navier-Stokes equations which assumes the flow properties are differentiable and hence continuous. FVM is obtained from an integral formulation of the Navier-Stokes equations which allows the presence of discontinuities inside the control volume and is therefore more suitable for computing the correct shock wave position. Since we are interested in transonic flow, the spatial discretization choice for ParCAE is the Finite Volume Method.

A basic requirement for every CFD computation is a good quality grid. An ideal grid must be orthogonal to the wall, with a correct $y+$ value of less than two, and a grid stretching ratio less than 1.2. Generating a curvilinear quality grid in a complex geometry is a time consuming task. Therefore, many researchers choose a Cartesian grid approach instead of a body fitted one and avoid much of the griding difficulties.

- Cartesian grids (Fig. 2.2) – are more efficient in evaluating the cell fluxes from the Navier-Stokes equations and are easy to generate. On the other hand, the difficulties in the treatment of the boundary conditions around the testing geometry create a large disadvantage.

- Body-fitted grids (Fig. 2.3) – permit highly accurate solutions close to boundaries which is essential for shear layers or separated flows. However, there is a high complexity in generating body fitted grids with low skewness in the cells for complex geometries.

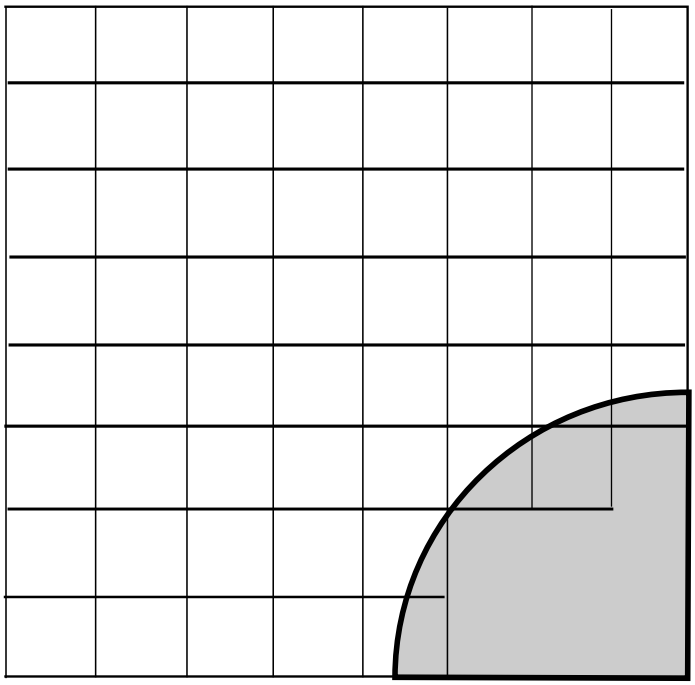

Figure 2.2: Cartesian grid around a quarter of a cylinder.

The choice for ParCAE has been the use of body-fitted grids due to their advantages over Cartesian grids. Within body-fitted grids, there is a choice between structured or unstructured grids (Fig. 2.4). This choice, not only affects the grid but the flow solver itself. For this reason, we also refer to structured and unstructured flow solvers.

- Structured grids – which affect the flow solver schemes making these more efficient and easy to implement than the corresponding unstructured ones. The grid cells are quadrilaterals in 2D and hexahedra in 3D grids. The grid points i, j, k are stored in the i, j, k position of an array which facilitates the access of their value and it is what makes the flow solver faster and simpler. On the other hand, generating structured grids for complex geometries is a complex and time consuming process.

- Unstructured grids – are a mix of quadrilaterals and triangles in 2D, and mainly hexahedra and tetrahedral in 3D. The facility of generating these grids for complex geometries, and the capability of local refinement makes them superior to structured

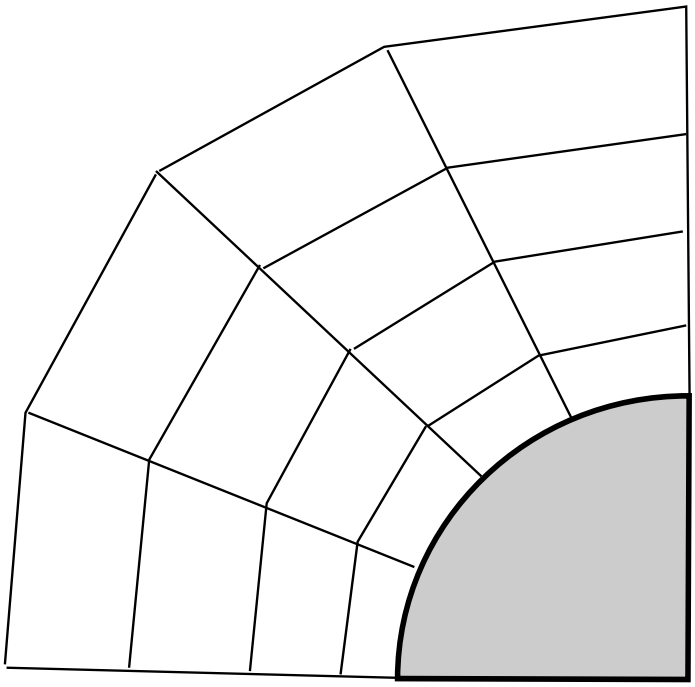

Figure 2.3: Body-fitted structured grid around a quarter of a cylinder.

grids. However, unstructured solvers have disadvantages over the structured ones. Since the grid points do not follow a particular order in their array, the efficiency in the schemes is lower than for the corresponding structured ones since an tabulated search for the neighboring cells is required for every flux computation of a single cell.

Both structured and unstructured methods are very popular nowadays. The disadvantages of generating structured grids can be partially overcome by the use of a multiblock approach (described in Section 2.2.5.3). For those reasons, ParCAE is a structured solver. More recent hybrid codes combine structured grids close to the wall due to their superior quality, and unstructured grids away from the wall to alleviate the number of grid points. A second type of codes use overlapping structured grids with the same intention as hybrid codes. Overlapping structured grids are able to cluster points where needed due to the use of local patches and alleviate the number of points in coarser regions. These are patches of structured grids which are computationally superior to unstructured grids, however the patches need a

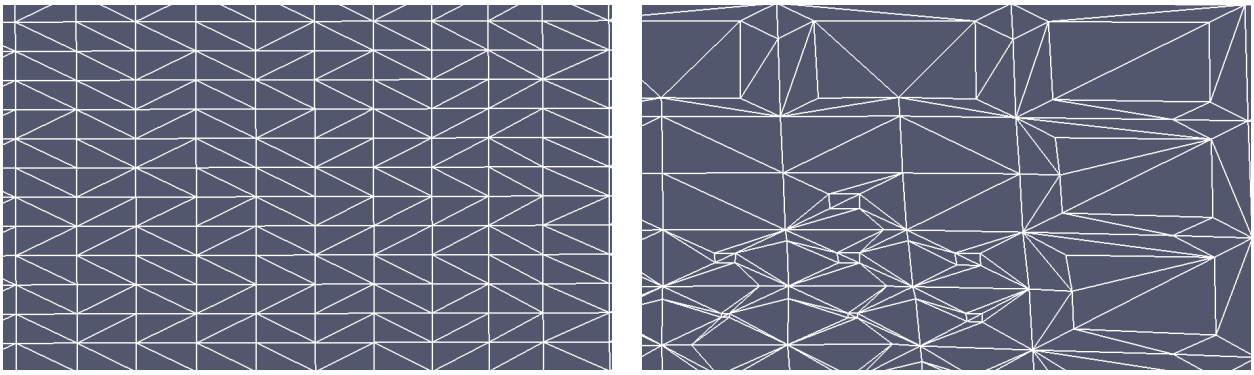

(a) (b)

Figure 2.4: Image of (a) structured and, (b) unstructured grids.

proper exchange of boundary conditions which creates a significant challenge for an accurate numerical implementation.

The next step when creating a Finite-Volume Method solver for structured grids is choosing between cell-centered (Figure 2.5(a)) or cell-vertex schemes (Figure 2.5(b)). Ref. [9] offers a detailed discussion in the subject. While in a cell-centered scheme the flow variables are defined at the center of the cells, in a cell-vertex approach they are defined at the grid points.

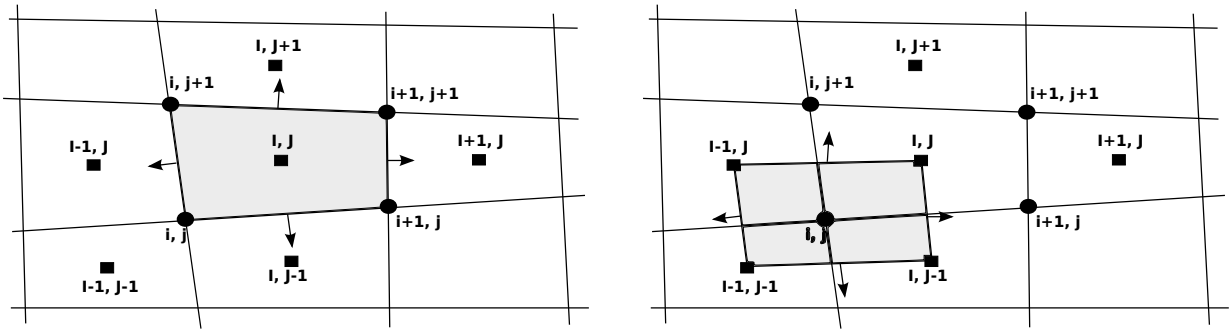

(a) (b)

Figure 2.5: Image of (a) Cell centered structured grid, (b) Cell vertex structured grid.

For non-distorted grids, both methods seem to provide the same accuracy. If the grid is not smooth, cell-vertex schemes tend to be superior. Cell-centered schemes have smaller discretization errors when computing the cells on the boundaries. The face of a cell-centered scheme matches with the solid wall boundary while for a cell-vertex scheme half of the cell

is located inside the wall boundary. Cell-centered schemes are also more convenient for unsteady flows since the mass matrix from the discretized Navier-Stokes equations can be lumped while a cell-vertex scheme requires a treatment of that matrix. This results in a simpler implementation of cell-centered schemes vs. cell-vertex schemes which has led to using a cell-centered approach in ParCAE.

Some books [43] [34] discuss the behavior of partial differential equations and their mathematical nature which is related with choosing the appropriate boundary conditions to obtain a well posed problem. The steady Navier-Stokes equations exhibit a mixed behavior of elliptic, hyperbolic and parabolic equations. The subsonic inviscid flow has an elliptic nature. The supersonic inviscid flow follows a hyperbolic behavior. And the parabolic nature is observed in the boundary layer equations where viscous effects are dominant. While hyperbolic and parabolic problems march quite well in space, elliptic problems require solving all grid points at once since the whole space is both the domain of dependence and the domain of influence at the same time. In 1966, Moretti and Abbett [58] presented a breakthrough in solving the supersonic blunt body problem. Solving the steady Navier-Stokes equations marching in space creates an ill-posed problem due to the mix nature of the equations. However, using a pseudo time and marching them in pseudo time to a steady state transforms the problem to a well-posed one. The Navier-Stokes equations are therefore an initial value problem. The pseudo time marching concept will be explored in Section 2.2.4.

When computing an unsteady problem, a temporal discretization must be used. Not only for an unsteady case, but for a steady case as well since a pseudo time marching is used to reach to a steady state condition. When designing a solver, one can choose between implicit or explicit temporal discretization. However, the optimum decision depends on the type of problem to be solved. An implicit scheme requires a major effort in the implementation and a larger computational time per time step. However, since the entire flow field is the domain of dependence of an implicit scheme, one can choose large time steps and the solution will

remain stable. In theory one should obtain an accurate solution of the flow field with just one infinite time step. In practice the non-linearity of the flow equations require some pseudo time steps to obtain a converged solution. An explicit scheme is easier to implement and each time step takes much less computational time than for an implicit case. However, the domain of dependence of each grid point determines the maximum local time step permissible to maintain a stable solution. For a pseudo time marching to steady state, both explicit an implicit discretizations seem reasonable. ParCAE uses an explicit approach. For a real time marching, the choice will depend on the highest frequency to be captured and the maximum allowed time step for an explicit scheme to remain stable. Aeroelastic phenomena tend to have long enough periods such that an implicit real time step becomes more appropriate. In an unsteady case where a physical high frequency must be captured and therefore an explicit scheme is more appropriate for the real time discretization, a pseudo time is not anymore used and the solution is directly marched in real time using very small real time steps which maintain temporal accuracy.

2.2.1 The Governing Flow Equations

2.2.1.1 Navier-Stokes equations

When writing the Navier-Stokes equations for an aeroelastic problem, a change in cell volume must be allowed in the formulation and a grid velocity should be defined to correctly compute the fluxes incoming into each cell. The Navier-Stokes equations in integral form suitable for aeroelastic computations are

$$\frac{\partial}{\partial t}\int_{\Omega}\vec{W}d\Omega + \oint_{\partial\Omega}(\vec{F_c}-\vec{F_v})\vec{n}dS = \int_{\Omega}\vec{Q}d\Omega \tag{2.22}$$

where the vector of state variables $\vec{W}$ is composed by the density ρ, the flow velocity $[u, v, w]^T$

and the total energy E.

$$\vec{W} = \begin{bmatrix} \rho \\ \rho u \\ \rho v \\ \rho w \\ \rho E \end{bmatrix} \tag{2.23}$$

From Equation 2.22, Ω represents the control volume enclosed by the surface $\partial\Omega$. $\vec{n}$ is the unit vector on the control volume surface, and the surface magnitude takes the value dS. The right hand side of Equation 2.22 is reserved for volumetric forces and heat source terms which will be set to 0 for ParCAE.

The convective fluxes

$$\vec{F_c} = \begin{bmatrix} \rho u_r & \rho v_r & \rho w_r \\ \rho u u_r + p & \rho u v_r & \rho u w_r \\ \rho v u_r & \rho v v_r + p & \rho v w_r \\ \rho w u_r & \rho w v_r & \rho w w_r + p \\ \rho E u_r + p u & \rho E v_r + p v & \rho E w_r + p w \end{bmatrix} \tag{2.24}$$

use relative velocities (represented by the subindex r in Equation 2.25) due to the moving grid. The variable p denotes pressure.

$$\begin{aligned} u_r &= u - u_g \\ v_r &= v - v_g \\ w_r &= w - w_g \end{aligned} \tag{2.25}$$

The subindex g stands for grid to refer to the grid velocity in Equation 2.25.

The viscous fluxes

$$\vec{F_v} = \begin{bmatrix} 0 & 0 & 0 \\ \tau_{xx} & \tau_{xy} & \tau_{xz} \\ \tau_{yx} & \tau_{yy} & \tau_{yz} \\ \tau_{zx} & \tau_{zy} & \tau_{zz} \\ \Theta_x & \Theta_y & \Theta_z \end{bmatrix} \tag{2.26}$$

contain viscosity and heat diffusion effects. For the viscous terms, some classic assumptions are used: isotropic fluid (same fluid properties in all directions, this does not mean isotropic turbulence), Newtonian fluid and Stokes hypothesis for bulk viscosity. For the heat diffusion terms, Fourier's law has been applied. Equation 2.27, 2.28 and 2.29 close the expression for the viscous fluxes.

$$\begin{aligned} \Theta_x &= u\tau_{xx} + v\tau_{xy} + w\tau_{xz} - q_x \\ \Theta_y &= u\tau_{yx} + v\tau_{yy} + w\tau_{yz} - q_y \\ \Theta_z &= u\tau_{zx} + v\tau_{zy} + w\tau_{zz} - q_z \end{aligned} \tag{2.27}$$

$$\begin{aligned} \tau_{xx} &= 2\mu\frac{\partial u}{\partial x} - \frac{2}{3}\mu\left(\frac{\partial u}{\partial x} + \frac{\partial v}{\partial y} + \frac{\partial w}{\partial z}\right), \qquad \tau_{xy} = \tau_{yx} = \mu\left(\frac{\partial u}{\partial y} + \frac{\partial u}{\partial y}\right) \\ \tau_{yy} &= 2\mu\frac{\partial v}{\partial y} - \frac{2}{3}\mu\left(\frac{\partial u}{\partial x} + \frac{\partial v}{\partial y} + \frac{\partial w}{\partial z}\right), \qquad \tau_{xz} = \tau_{zx} = \mu\left(\frac{\partial w}{\partial x} + \frac{\partial u}{\partial z}\right) \\ \tau_{zz} &= 2\mu\frac{\partial w}{\partial z} - \frac{2}{3}\mu\left(\frac{\partial u}{\partial x} + \frac{\partial v}{\partial y} + \frac{\partial w}{\partial z}\right), \qquad \tau_{yz} = \tau_{zy} = \mu\left(\frac{\partial v}{\partial z} + \frac{\partial w}{\partial y}\right) \end{aligned} \tag{2.28}$$

$$q_x = -\kappa\frac{\partial T}{\partial x}, \qquad q_y = -\kappa\frac{\partial T}{\partial y}, \qquad q_z = -\kappa\frac{\partial T}{\partial z} \tag{2.29}$$

Equation 2.28 represents the normal and shear stresses, and Equation 2.29 contains the heat

conduction terms where T denotes temperature. The dynamic viscosity μ is computed with Sutherland's [79] law assuming that it only depends on temperature. The same assumption is used for the thermal conductivity coefficient κ (Equation 2.30). When using a turbulence averaged formulation like in the case of the RANS equations, the mentioned μ and κ are referred as laminar dynamic viscosity and laminar thermal conductivity coefficient, respectively.

$$\kappa = c_p \frac{\mu}{Pr} \tag{2.30}$$

It is normally assumed that the Prandlt number Pr is constant in the entire field. c_p denotes the specific heat coefficient at constant pressure.

2.2.1.2 Perfect Gas

A perfect gas is an ideal gas where c_v (specific heat coefficient at constant volume) is constant. Assuming that there is local equilibrium, we can use an equation of state which for an ideal gas is

$$p = \rho R T \tag{2.31}$$

where R denotes the specific gas constant. Using the definitions

$$R = c_p - c_v, \qquad \gamma = \frac{c_p}{c_v} \tag{2.32}$$

and the energy relations

$$e = c_v T, \qquad E = e + \frac{1}{2}(u^2 + v^2 + w^2) \tag{2.33}$$

one can express the pressure p as a function of the vector of state variables $\vec{W}$ as

$$p = \rho(\gamma - 1)\left[E - \frac{1}{2}(u^2 + v^2 + w^2)\right] \tag{2.34}$$

where γ is the ratio of specific heats and e the internal energy. The temperature T can be computed from the equation of state for an ideal gas.

2.2.2 Turbulence modeling

In a laminar flow situation, the formulation shown above is complete. For a turbulent flow case, it is also complete if the grid is small enough to solve all turbulent length scales in the flowfield (This type of simulation is called Direct Numerical Simulation (DNS)). However, for engineering applications at high Reynolds numbers one cannot afford to solve such a large number of grid points. In those cases a coarser grid is used but the smallest length scales need to be modeled. Some precision is sacrificed in exchange for obtaining an approximate solution to a real engineering problem.

Depending on the amount of turbulent flow modeling, the computations can be categorized into Reynolds-Averaged Navier-Stokes type (RANS), Large-Eddy Simulation (LES) or Detached-Eddy Simulation (DES). In a RANS computation, all turbulent scales are modeled by the use of a turbulence model.

An LES [32] type of simulation is an interesting approach based on the observation that the smallest turbulent scales are more universal than the larger ones. For that reason, a filter is used so the small length scales are modeled and the larger eddies are computed. The grid required for such computation contains more grid points than in the RANS case but significantly less than for a Direct Numerical Simulation (DNS). Moreover, the subgrid-scale models used for the small length scales of the LES approach are simpler than the models used

for the RANS simulation due to the universal character of the small length scales. Therefore, LES requires a simpler implementation than the RANS and provides more accurate results at a higher computational cost.

Even if LES contains significantly fewer grid points than DNS, it still has a computational cost too high to perform engineering computations at high Reynolds numbers. For that reason, Spalart introduced another approached known as Detached Eddy Simulation (DES) [72] [73] aimed for high Reynolds-number separated flows. This hybrid between RANS and LES uses a RANS solver to compute the boundary layer and uses LES for the outer region to avoid modeling the large detached eddies.

Even though LES and DES provide interesting approaches to capturing turbulence more accurately, they require three-dimensional grids, small time steps, and higher order schemes. Due to the high computational cost associated with these reasons, and due to the well accepted solution of RANS codes for attached flows (the flow field is attached during the initial flutter cycles before reaching Limit Cycle Oscillations), a RANS formulation is employed in ParCAE.

A brief introduction to RANS and the Spalart-Allmaras turbulence model is included in the following sections.

2.2.2.1 Reynolds and Favre averaging

A well-known approach known as the Reynolds-Averaged Navier-Stokes equations (RANS) consists in a time averaging of flow variables. Given an instantaneous variable ϕ with mean value $\bar{\phi}$ and a fluctuating component ϕ' such that

$$\phi = \bar{\phi} + \phi' \tag{2.35}$$

the average of ϕ takes the form

$$\bar{\phi} = \frac{1}{T}\int_{t}^{t+T} \phi(\tau)d\tau \tag{2.36}$$

where T denotes the integrating time interval.

For cases where the density is not constant, it is better to use a density-weighted time averaging known as the Favre decomposition to facilitate the final expression of the averaged Navier-Stokes equations. Like with the RANS approach, the Favre decomposition uses

$$\phi = \tilde{\phi} + \phi'' \tag{2.37}$$

$$\tilde{\phi} = \frac{1}{\bar{\rho}(t)T}\int_{t}^{t+T} \rho(\tau)\phi(\tau)d\tau \tag{2.38}$$

to compute the averaged quantities. The optimum formulation employs a Reynolds averaging for pressure and density, and a Favre averaging for the rest of the variables.

By inserting the average and fluctuation parts of each variable into the Navier-Stokes equations, the same original formulation of the Navier-Stokes equations is recovered but for the averaged values and with two extra terms in the viscous fluxes. Those terms are the so-called

- Reynolds-stress tensor (Equation 2.39) – accounts for the transport of mean momentum due to turbulent fluctuations.

$$\bar{\bar{\tau}}_{ij}^{R} = -\bar{\rho}\widetilde{v_i''v_j''} \tag{2.39}$$

The terms v_i'' and v_j'' denote the i, j components of the Favre fluctuating part of the

velocity vector $[u, v, w]$.

- Turbulent heat-flux vector (Equation 2.40) – accounts for the heat transport due to turbulent fluctuations.

$$\vec{F}_D^T = -\bar{\rho}\widetilde{h''\vec{v}''} \tag{2.40}$$

where h denotes enthalpy.

The solution of the averaged Navier-Stokes equations requires the modeling of these two new terms. The models are divided into first- or second-order closures. Even if the second-order ones provide more flexibility, they are more complex and sometimes produce numerical problems. For those reasons first-order closures are more widely used.

In these first-order closure, the Boussinesq hypothesis [11] [12] is used where the Reynolds stress tensor is assumed to have the same form as the viscous stress tensor. The concept of turbulent eddy viscosity μ_T is introduced. The Reynolds stress tensor is dropped from the final averaged Navier-Stokes formulation, and the dynamic viscosity from the viscous stress tensor introduced in Section 2.2.1 is enhanced by

$$\mu = \mu_L + \mu_T. \tag{2.41}$$

The laminar dynamic viscosity μ_L depends on the temperature by Sutherland's formula and the turbulent eddy viscosity μ_T must be modeled. The turbulent heat-flux vector follows an analog formulation and is evaluated as

$$\vec{F}_D^T = -\kappa_T \nabla T \tag{2.42}$$

where κ_T denotes the turbulent thermal conductivity coefficient. As in the viscous case, the

turbulent heat-flux vector is dropped from the averaged Navier-Stokes equations, and the thermal conductivity coefficient is enhanced by

$$\kappa = \kappa_L + \kappa_T = c_p \left(\frac{\mu_L}{Pr_L} + \frac{\mu_T}{Pr_T} \right). \tag{2.43}$$

The turbulent Prandlt number is assumed constant for the entire flow field. Therefore, simulating a turbulent flow adds an extra unknown μ_T which is obtained from any of the following popular turbulence models, most of which are coded in ParCAE:

- Baldwin and Lomax [6]
- Spalart and Allmaras [74]
- $k - \varepsilon$ of Launder and Spalding [47]
- $k - \omega$ of Wilcox [84]
- $k - \omega$ Shear Stress Transport (SST) of Menter [57]

2.2.2.2 Spalart-Allmaras turbulence model

The SA turbulence model solves a transport equation for eddy viscosity and is the model used for all the turbulent computations in this research.

The original formulation of the SA model, written in a non-conservative form, is modified using the continuity equation into a conservative form to be consistent with the already discretized Navier-Stokes equations. The following transport equation is solved in addition to Equation (2.22) .

$$\frac{\partial \tilde{\mu}}{\partial t} + \frac{\partial (\tilde{\mu} u_{r,j})}{\partial x_j} = C_{b1}(1 - f_{t2})\tilde{S}\tilde{\mu} - \left[c_{w1} f_w - c_{b1} \frac{f_{t2}}{\kappa^2} \right] \left(\frac{\tilde{\nu}}{d} \right)^2 \rho + \frac{\rho}{\sigma} \left[\frac{\partial}{\partial x_j} \left((\nu + \tilde{\nu}) \frac{\partial \tilde{\nu}}{\partial x_j} \right) + c_{b2} \frac{\partial \tilde{\nu}}{\partial x_j} \frac{\partial \tilde{\nu}}{\partial x_j} \right]$$

(2.44)

The trip term is not included. Instead an intermittency function described in Chapter 5 is implemented to guarantee a smooth laminar-turbulent transition, to be used in free or forced transition. The notation used in Equation (2.44) is the original from [74] . The velocity $u_{r,j}$ in the convective term of equation (2.44) is a relative velocity as in Equation (2.25) due to the moving grid. The variable $\tilde{\mu} = \tilde{\nu}\rho$.

2.2.3 Spatial Discretization

The integral form of the Navier-Stokes equations Equation 2.22 is used in each cell assuming constant properties for the full interior of the cell. For cell I, J, K,

$$\frac{d(\vec{W}\Omega)_{I,J,K}}{dt} = -\sum_{m=1}^{N_F}[(\vec{F}_c - \vec{F}_v)_m \vec{n}_m \Delta S_m]_{I,J,K} \tag{2.45}$$

is the discretized version of the Navier-Stokes equation where N_F is the number of cell faces (six for a three-dimensional hexahedral grid, and four in two-dimensional quadrilateral grid). For aeroelastic simulations, the cell volume $\Omega_{I,J,K}$ must remain inside the time derivative to allow for grid deformations through the unsteady time evolution. In a code where the grid is not deformed, the cell volume can be moved out of the time derivative.

The Right Hand Side (RHS) of Equation 2.45 is usually known as the residual and is denoted by $-\vec{R}_{I,J,K}$.

The Left Hand Side (LHS) of Equation 2.45 will be developed in Section 2.2.4 while the RHS will be addressed in the present Section. The convective and viscous fluxes integrating the RHS generally receive a different treatment, due to their different physical nature.

2.2.3.1 Convective Fluxes: Central Differencing with Artificial Dissipation

The convective fluxes are the hardest to compute due to the different nature of the Partial Differential Equations describing subsonic or supersonic inviscid fluxes. This section is devoted to the analysis of the term

$$\sum_{m=1}^{N_F}[(\vec{F}_c)_m\vec{n}_m\Delta S_m]_{I,J,K} \tag{2.46}$$

from the RHS of Equation 2.45. Multiple methods have been developed through the years due to the numerical instabilities obtained when using second order or higher order schemes, while still obtaining accurate solutions. Classic approaches for compressible flow computations include

- central differencing [41]
- flux-vector splitting [75] [50]
- flux-difference splitting [67]

Due to numerical instabilities which prevent a flow solution from converging to a final state, the concepts of artificial dissipation [41], Total Variation Diminishing (TVD) [31] and flux limiters [49] are commonly used to stabilize the converging solution. Although a solution carries truncation error (due to the order of accuracy of the difference operator when representing the differential operator) and round off errors (due to the computer accuracy), those are not the only reason for which a scheme may diverge. More commonly, a scheme may become ill-posed, like in the case of a central scheme with supersonic flow, and produce a non-converging solution.

In practice, artificial dissipation is added to a central scheme to suppress numerical oscilla-

tions in the solution. The idea of upwind schemes like flux-vector splitting or flux-difference splitting arose with the idea of not using any artificial dissipation and obtaining a well posed scheme based on the mathematical characteristics of the flow. In practice, such methods still generate oscillations around shock waves, and some type of limitation must be imposed in order to achieve a converged solution. Those limiting methods are known as TVD and flux limiters.

For the present research, although upwinding methods were used, only the results obtained with central differencing are included in this dissertation. Further documentation in upwind methods can be found in [67] [75] [50].

The scheme used is well-known as the JST [41] (Jameson Schmidt Turkel) scheme.

As an example, taking $m = 1$ from Equation 2.46 being the face $I+1/2, J, K$, the convective flux on that face using the JST scheme takes the form

$$[\vec{F}_c \vec{n} \Delta S]_{I+1/2,J,K} \approx \vec{F}_c(\vec{W}_{I+1/2,J,K})(\vec{n}\Delta S)_{I+1/2,J,K} - \vec{D}_{I+1/2,J,K} \tag{2.47}$$

where $\vec{D}$ is the artificial dissipation, and

$$\vec{W}_{I+1/2,J,K} = \frac{1}{2}(W_{I,J,K} + W_{I+1,J,K}). \tag{2.48}$$

The dissipative term is a blend between second- and fourth-order differences where the second-order difference resembles the viscous dissipation. The main idea of the scheme is to use a pressure sensor to find the location of a shock wave and suppress the fourth-order dissipation term and activate the second order dissipation. When blending the central differencing scheme with the second-order dissipation, it effectively acts as a first-order scheme, which limits the numerical oscillations around shocks. Away from the shocks, the pressure

sensor deactivates the second-order dissipation, and activates the fourth-order dissipation which provides a minimum amount of artificial viscosity to avoid odd-even decoupling waves due to using a grid with consistent grid spacing. The JST scheme is therefore second-order accurate, and locally drops down to first-order around a shock to improve numerical stability.

The pressure switch introduced in JST [41] was improved by Swanson and Turkel [81]. Various authors have performed slight modification to the switch similar to the one from Swanson and Turkel. The pressure switch implemented in ParCAE for cell I, J, K, exemplified in the I direction is

$$\Gamma_I = \frac{|p_{I+1} - 2p_I + p_{I-1}|}{0.5[|p_I - p_{I-1}| + |p_{I+1} - p_I| + |p_{I+1} + 2p_I + p_{I-1}|]} \tag{2.49}$$

where the J, K indices have been dropped. Using this switch, the second and fourth order coefficients for the face $I + 1/2, J, K$ are

$$\begin{aligned} \epsilon^{(2)}_{I+1/2} &= min[\alpha_1, max(\Gamma_I, \Gamma_{I+1})] \\ \epsilon^{(4)}_{I+1/2} &= max[0, (\beta_1 - \beta_2\, \epsilon^{(2)}_{I+1/2})] \end{aligned} \tag{2.50}$$

where typical values for the constants are $\alpha_1 = 0.5$, $\beta_1 = 1/32$ and $\beta_2 = 2$. Finally, the artificial dissipation term for the cell face $I + 1/2$ is

$$\vec{D}_{I+1/2} = \hat{\Lambda}^S_{I+1/2}\, [\epsilon^{(2)}_{I+1/2}(\vec{W}_{I+1} - \vec{W}_I) - \epsilon^{(4)}_{I+1/2}(\vec{W}_{I+2} - 3\vec{W}_{I+1} + 3\vec{W}_I - \vec{W}_{I-1})] \tag{2.51}$$

where $\hat{\Lambda}^S_{I+1/2}$ is the sum of the spectral radii of the convective flux Jacobians for face $I+1/2$ in all I, J, K directions.

Further improvements to the basic JST scheme are the Matrix Dissipation Scheme [81] or the SLIP scheme [40]. The results shown in this dissertation have been obtained with the

classic JST scheme.

2.2.3.2 Viscous Fluxes

The discretization of the viscous fluxes from Equation 2.45 leads to

$$\sum_{m=1}^{N_F}[(\vec{F}_v)_m \vec{n}_m \Delta S_m]_{I,J,K}. \tag{2.52}$$

Following the steps for the convective fluxes, and creating an example for face $I-1/2$, the variables of state are obtained with Equation 2.48. The Navier-Stokes equations 2.26, 5.4 and 2.28, contain velocity and temperature gradients in the viscous fluxes expressions which need to be evaluated at the face cells. Following an integral formulation [80], Green's theorem is used and an auxiliary control volume centered on the real cell face is created (Figure 2.6).

As an example, computing $\partial u/\partial x$ on face $I-1/2$ using Green's method in an integral form leads to

$$\int_{\Omega_{aux}} \frac{\partial u}{\partial x} d\Omega = \oint_{\partial\Omega_{aux}} u\, n_x\, dS. \tag{2.53}$$

Discretizing the previous equation for the auxiliary control volume of Figure 2.6 becomes

$$\left(\frac{\partial u}{\partial x}\right)_{I-1/2} \approx \frac{1}{\Omega_{aux}} \sum_{m=1}^{N_F} (u\, n_{x_{aux}}\, S_{aux})_m \tag{2.54}$$

where N_F is the number of faces of the auxiliary control volume (six for a three-dimensional structured grid, and four for a two-dimensional quadrilateral grid), and Ω_{aux}, S_{aux} and $n_{x_{aux}}$ are the volume, surface and x component of the unit surface vector of the auxiliary control

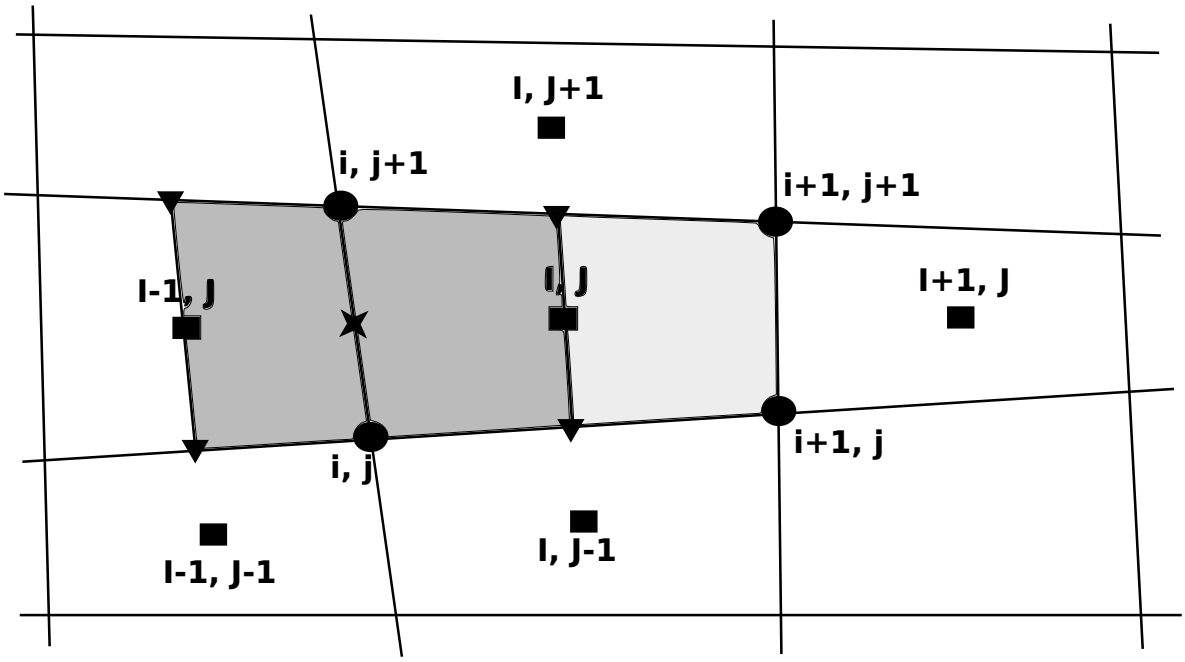

Figure 2.6: Auxiliary control volume for the evaluation of the gradients of velocity and temperature on face $I - 1/2$.

volume, respectively. u_m for the auxiliary control volume may be directly obtained from the cell centered values when available, or averaged otherwise.

2.2.4 Temporal Discretization

Since the time step needed to capture accurate aeroelastic wing movement is long when compared with the stability requirements that would come from using an explicit scheme for real time marching, a common strategy known as dual time-stepping developed by Jameson [39], and implemented in ParCAE, allows the use of large real time steps through an implicit temporal scheme.

Dual-time stepping is an implicit-explicit time marching scheme. A pseudo time is used for the explicit scheme to drive the solution to a converged state while the solution is not advancing in real time. When the solution is converged for the present time, an implicit

scheme is used to advance the solution in real time. To reach a converged solution in pseudo time with fewer iterations, local time stepping (Section 2.2.5.2) is needed.

2.2.4.1 Explicit pseudo-time marching

For a steady state solution, the discretization of Equation 2.45 should not contain the LHS. However, it is convenient to maintain the LHS of Equation 2.45 and rename the time t as a pseudo time t^*. The converged solution is obtained by marching Equation 2.55 in pseudo time to a pseudo steady state until the residual $\vec{R}_{I,J,K}$ approaches zero.

$$\frac{d(\vec{W}\Omega)_{I,J,K}}{dt^*} = -\vec{R}_{I,J,K} \tag{2.55}$$

The indices I, J, K are omitted in the following formulation, and the current pseudo time level for a given cell is denoted by n. Since the cell volume is not constant due to grid deformation, the term Ω remains inside the time derivative of the LHS of Equation 2.55. However, for the pseudo time marching the problem is static and no grid deformation is possible which allows us to reformulate Equation 2.55 as

$$\frac{d(\vec{W}^n)}{dt^*} = -\frac{1}{\Omega}\vec{R}^n. \tag{2.56}$$

The LHS of Equation 2.56 is discretized using a hybrid multi-stage Runge-Kutta scheme [55], [56] which enhances stability while requiring low storage.

Blazek [9] states that a classic multi-stage approach is more suitable for upwinding while the hybrid multi-stage scheme performs better for a central discretization. However, the hybrid multistage method can also be optimized for upwinding by choosing different coefficients. Due to the similarity in the formulation of both schemes, ParCAE uses a general formulation

that allows for the use of both methods by changing the input coefficients in the code. The following formulation describes the hybrid approach which has been used for all the numerical simulations presented in this dissertation.

The residual is first separated in a convective part $\vec{R}_c$ and a viscous part $\vec{R}_d$ which also contains the numerical dissipation terms.

$$\vec{R}^n = \vec{R}_c^n - \vec{R}_d^n. \tag{2.57}$$

The 5-stage hybrid scheme is formulated as

$$\begin{aligned}
\vec{W}^0 &= \vec{W}^n \\
\vec{W}^1 &= \vec{W}^0 - \alpha_1 \frac{\Delta t^*}{\Omega}[\vec{R}_c^0 - \vec{R}_d^{(0,\beta)}] \\
\vec{W}^2 &= \vec{W}^0 - \alpha_2 \frac{\Delta t^*}{\Omega}[\vec{R}_c^1 - \vec{R}_d^{(1,\beta)}] \\
\vec{W}^3 &= \vec{W}^0 - \alpha_3 \frac{\Delta t^*}{\Omega}[\vec{R}_c^2 - \vec{R}_d^{(2,\beta)}] \\
\vec{W}^4 &= \vec{W}^0 - \alpha_4 \frac{\Delta t^*}{\Omega}[\vec{R}_c^3 - \vec{R}_d^{(3,\beta)}] \\
\vec{W}^{n+1} &= \vec{W}^0 - \alpha_5 \frac{\Delta t^*}{\Omega}[\vec{R}_c^4 - \vec{R}_d^{(4,\beta)}]
\end{aligned} \tag{2.58}$$

where

$$\vec{R}_d^{(m-1,\beta)} = \beta_m \, \vec{R}_d^{m-1} + (1 - \beta_m) \, \vec{R}_d^{(m-2,\beta)} \tag{2.59}$$

and m is the stage position from one to five. The coefficients α_m and β_m extracted from [9] and used in ParCAE are specified in Table 2.1 for a central scheme, and a first and second order upwind schemes.

Since β_2 and β_4 are set to zero, the computation of $\vec{R}_d^1$ and $\vec{R}_d^3$ is skipped which makes the

	Central scheme		1st-order upwind		2nd-order upwind	
stage	α	β	α	β	α	β
1	0.2500	1.00	0.2742	1.00	0.2742	1.00
2	0.1667	0.00	0.2067	0.00	0.2067	0.00
3	0.3750	0.56	0.5020	0.56	0.5020	0.56
4	0.5000	0.00	0.5142	0.00	0.5142	0.00
5	1.0000	0.44	1.0000	0.44	1.0000	0.44

Table 2.1: Coefficients for a hybrid 5-multistage scheme.

	1st-order upwind	2nd-order upwind
stage	α	α
1	0.0533	0.0695
2	0.1263	0.1602
3	0.2375	0.2898
4	0.4414	0.5060
5	1.0000	1.0000

Table 2.2: Coefficients for a 5-multistage scheme.

hybrid scheme especially efficient due to the reduction in computational time.

To recover the original multistage scheme, all β_m coefficients must be set to 1. The appropriate α_m coefficients for a first- and second-order upwind multistage scheme with 5 stages are presented in Table 2.2 [9].

2.2.4.2 Dual time-stepping

The idea of dual time-stepping, first introduced by Jameson [39], is used for unsteady flows and is a hybrid implicit-explicit scheme. It uses an implicit scheme for the real time and an explicit scheme (Section 2.2.4.1) for the pseudo time.

The discretization of Equation 2.45 leads to

$$\frac{d(\vec{W}\Omega)_{I,J,K}}{dt} = -\vec{R}_{I,J,K} \tag{2.60}$$

where the LHS is discretized using an implicit second-order backward-difference scheme for the real time derivative

$$\frac{3(\vec{W}\,\Omega)^{(n+1)}_{I,J,K} - 4(\vec{W}\,\Omega)^{(n)}_{I,J,K} + (\vec{W}\,\Omega)^{(n-1)}_{I,J,K}}{2\,\Delta t} = -\vec{R}_{I,J,K}. \tag{2.61}$$

where Δt denotes the real time step, and n the real time stage. To solve Equation 2.61, Jameson includes the pseudo time concept as

$$\frac{3(\vec{W}\,\Omega)^{(n+1)}_{I,J,K} - 4(\vec{W}\,\Omega)^{(n)}_{I,J,K} + (\vec{W}\,\Omega)^{(n-1)}_{I,J,K}}{2\,\Delta t} + \vec{R}_{I,J,K} = \vec{R}^{*}_{I,J,K} \tag{2.62}$$

$$\frac{d(\vec{W}\Omega)_{I,J,K}}{dt^{*}} = \vec{R}^{*}_{I,J,K} \tag{2.63}$$

where * represents the pseudo variables. For each real time step Δt, Equation 2.61 is solved. When the RHS of Equation 2.62 becomes zero, the solution of Equation 2.62 is the same as the one in Equation 2.61. For each real time step, Equation 2.63 is marched in pseudo time to a pseudo steady state using the techniques described in Section 2.2.4.1.

2.2.5 Boundary Conditions and Acceleration Techniques

2.2.5.1 Boundary conditions

When the flow equations are discretized in space, the state variables at one cell depend on the variables of the adjacent cells. For this reason, the cells in contact with a boundary require a special treatment. This is accomplished by the use of ghost cells.

There are two layers of ghost cells around the exterior of every boundary. Figure 2.7 shows the reference from 0 to 3 used for the cells across a boundary.

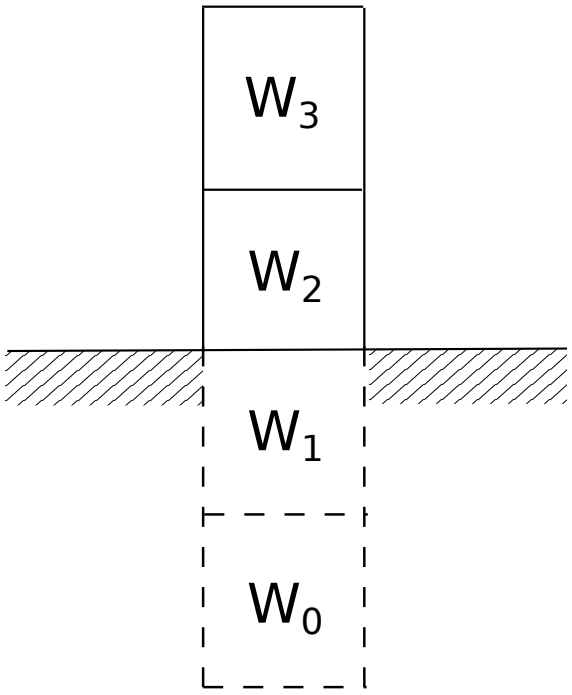

Figure 2.7: Ghost cells (W_0 and W_1) at a boundary.

Depending on the boundary conditions to be imposed, different relations will be used to assign values to the variables in the ghost cells region. The boundary conditions used to obtain the results in this dissertation are

- Adiabatic solid wall.
- Farfield.
- Symmetry plane.

Special treatment is required for the ghost cells at the corner between two connecting boundaries. A linear extrapolation is used in those cases.

2.2.5.2 Numerical Acceleration techniques

With the aim of reducing the computational time for a solution to converge, the following techniques are used.

- Local time stepping – applied in an explicit scheme where the time step is bounded by the grid spacing. Local time stepping applies the maximum allowed time step for each cell for steady state problems or in pseudo time for unsteady cases.
- Residual smoothing – used to give an implicit character to an explicit scheme allowing larger CFL numbers. It also helps to reduce high frequency errors.
- Multigrid – generally talking about V or W cycles, is one of the most efficient accelerators. From the original grid, coarser grids are generated. The solution from finer grids is transferred to the coarser grids and the flow equations are solved again for these coarser grids levels. Once the solution on the coarser grids is obtained, flow corrections are transferred back to the finer grids. The efficiency of the method is based on the damping of low frequency errors. Given a grid level, high frequency errors relative to that grid spacing are quickly damped out while the low frequency error components remain. Therefore, the solution from a fine grid is transferred to a coarser grid where the low frequency errors from the fine grid become the new high frequency errors in the coarse grid, and are easily eliminated. Another advantage of the multigrid method is that larger pseudo time steps can be used in the coarser grid levels, marching faster to a steady state in pseudo time.

2.2.5.3 Multiblock and parallelization

The structured grid is broken into multiple blocks which facilitates the meshing process around complicated geometries, but also allows for the parallelization of the code using data

parallelism. Ideally, breaking a grid into two symmetric blocks and using two processors instead of one would reduce the computing time in half. In a real system, the exchange of boundary information between processors, and non ideal distributions of the workload, among other less common factors, increases the overall required computing time.

Message Passing Interface (MPI) is used in ParCAE to run multiblock grids in supercomputers. The San Diego supercomputer Comet has been used to run most of the simulations in this dissertation.

2.3 Validation of CFD code using RAE2822 airfoil

The RAE 2822 airfoil is simulated at $M_\infty = 0.75$, $Re = 6.2 \times 10^6$ and corrected angle of attack $\alpha_{corrected} = 2.81°$ to validate the capability of ParCAE to accurately compute turbulent flows. The numerical results are compared with Case 10 of Reference [20] . Transition is imposed at 3% of the chord to match the experimental conditions. To guarantee a smooth transition, the local intermittency function [15] described in Equation 5.18 is used. Eddy viscosity is set to zero before $x_{tr}/c = 0.03$, and it is multiplied by γ_{tr} when $x > x_{tr}$.

The computational mesh is available from NASA Glenn Research Center [17] and has been used in multiple previous studies [52] . It is a single block, C-grid with 369×65 points as shown in Figure 2.8.

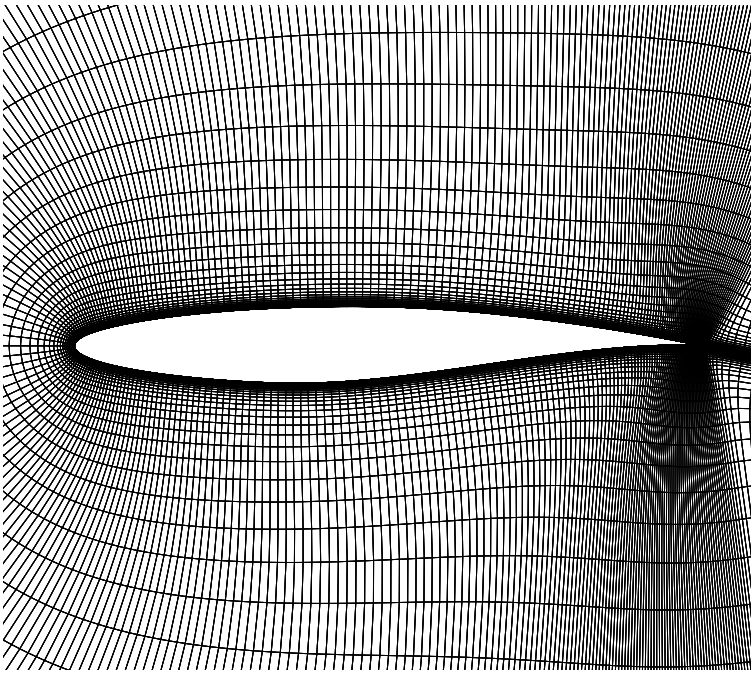

Figure 2.8: RAE 2822 airfoil C-grid close up view.

Figure 2.9 compares numerical with experimental results. On the first row of the figure, the pressure coefficient and skin friction are plotted. The pressure coefficient shows good agreement in shock position and captures the characteristic pressure bump at the leading

edge of the upper surface. The skin friction agrees reasonably well with the experimental data. Separation is observed after the shock wave followed by a flow reattachment. The effect of laminar-turbulent transition clearly impacts the skin friction around $x/c = 0.03$. Only for the RAE2822, the skin friction is referenced to the local boundary layer dynamic pressure, not the free stream dynamic pressure.

The second row of the same figure shows the displacement boundary layer thickness, and the momentum boundary layer thickness. Both are in very good agreement with the experimental data showing a sharp rise after the shock.

The third row of the figure compares velocity profiles within the boundary layer for two x/c positions. While there is good agreement for $x/c = 0.90$, the profile at $x/c = 0.75$ is in poor agreement with the experimental results. This is understandable since it is near the small separation bubble after the sock. A discrepancy is also observed close to the wall for $x/c = 0.90$. Similar disagreement with experimental data is found in other computations [52], [3], [35] .

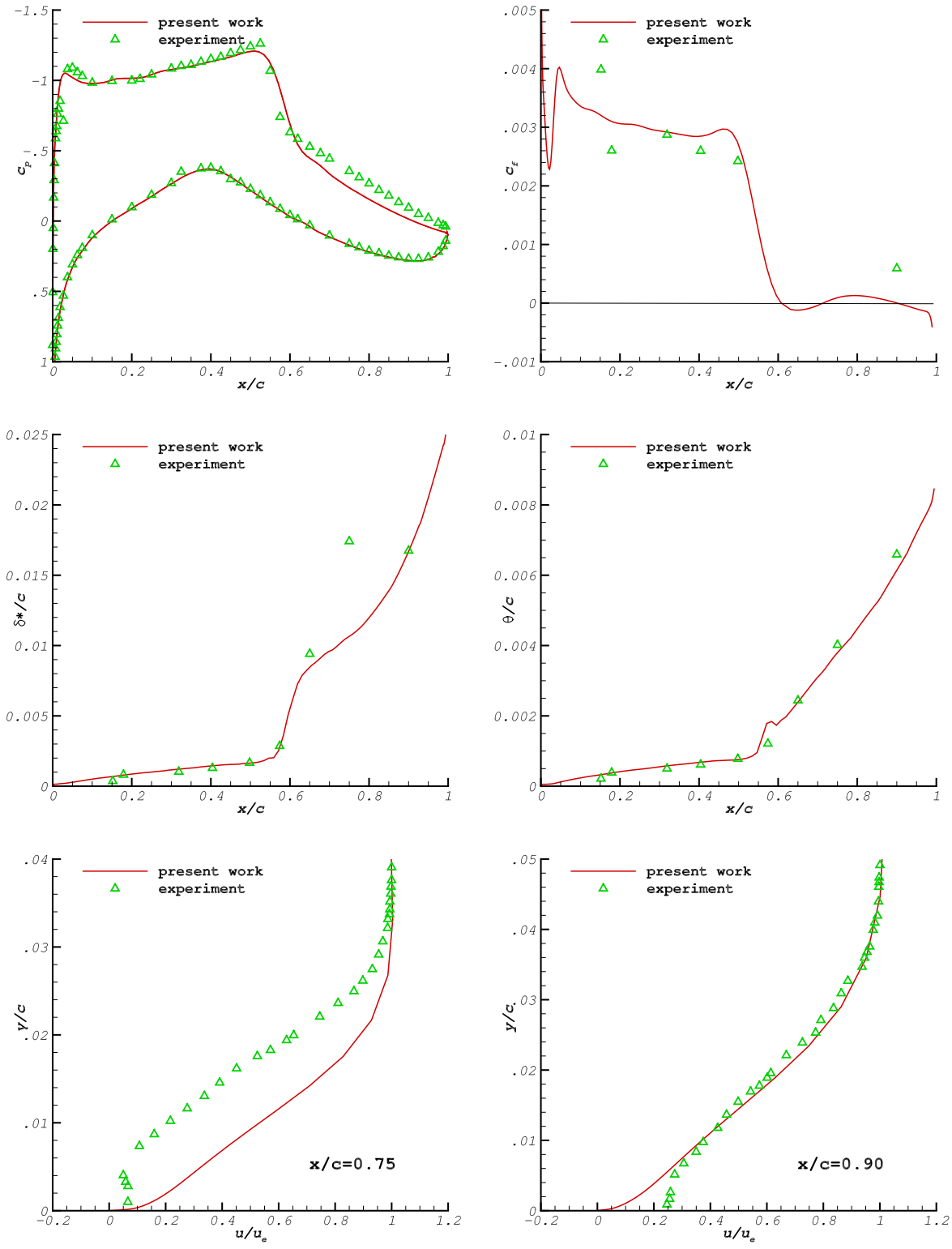

Figure 2.9: Comparison between RANS solutions and experiment data [20] for Case 10 of the RAE 2822 airfoil. $Re = 6.2 \times 10^6$, $M_\infty = 0.75$, $x_{tr}/c = 0.03$, $\alpha_{corrected} = 2.81$. Plots of pressure coefficient C_p, skin friction C_f, displacement thickness δ^*/c, momentum thickness θ/c, and boundary layer velocity profiles at $x/c = 0.75$ and $x/c = 0.9$.

2.4 NACA 64A010 Flutter boundary by the Euler Equations

The aeroelastic code is first tested for the Euler equations at zero angle of attack for the NACA64A010 airfoil since many previous publications [2], [30], [62] are easily available and there is general acceptance of the validity of those results. The good agreement with other researchers' results serves as validation for the aeroelastic implementetation of our research code. For a given Mach number, computations are performed to sweep through a range of speed index values to determine the flutter boundary. The speed index is defined as $V_F = 2\,U_\infty/(c\,\omega_\alpha\sqrt{\mu})$, where μ is the mass ratio between the structure density and the air density which represents inertial effects of the structure. Given a fixed mass ratio, the higher the speed index, the more flexible the structure is. A symmetric C-grid of 288×64 cells is used.

The meaning of the flutter boundary, and how to determine it, has been presented in the Introduction 1.1. Ideally, given a fixed free-stream Mach number, the boundary is found by changing the speed index value until finding a neutrally stable response. A more practical approach is used with the goal of determining the boundary more accurately and efficiently. A least-squares fitting of a curve crossing the peaks of the heaving response in time is obtained, in order to determine the growth or decay rate in an exponential form. Figure 2.10 shows a positive growth rate after the exponential fit is applied.

This method is based on the definition of linear stability where

$$\frac{h}{b} = \frac{h_0}{b}\,e^{((a+i\,\omega)\,t)}, \quad \left|\frac{h}{b}\right| = \frac{h_0}{b}\,e^{(a\,t)} \tag{2.64}$$

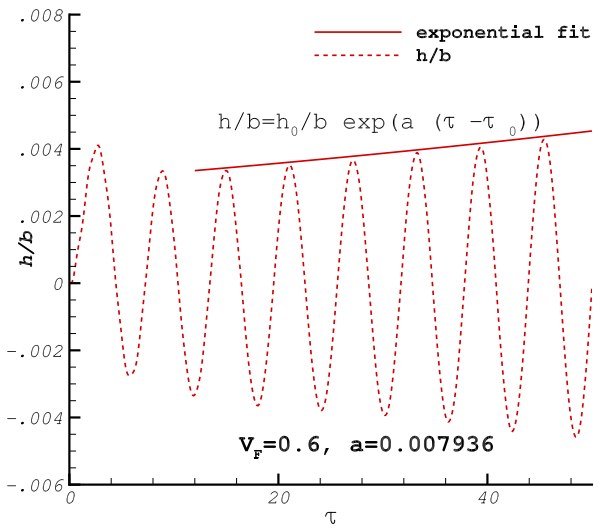

Figure 2.10: Exponential fit to determine the growth rate of the structural response for the Euler equations at $M_\infty = 0.825$ and $V_F = 0.6$. $h_0/b = 0.00335$, $\tau_0 = 11.788$, and the least squares fit of $h/h_0 = 0.9988\, exp(0.007936\,(\tau - \tau_0))$.

The constant a is the growth rate, while ω is part of the imaginary term forming the oscillatory behavior. A search for the peaks is performed after manually imposing a pair $(\tau_0, h_0/b)$. The first cycles must be ignored since they might be in transient state due to the imposed initial condition.

A least-squares fit through the absolute value of the heaving peaks is shown in Figure 2.10. After obtaining the growth rate for a pair of speed indexes (one above and one below the flutter boundary value), a linear interpolation is used between them to find the speed index of neutral stability ($a = 0$).

The flutter boundary results for $M_\infty = 0.75 - 0.95$ are presented in Figure 2.11 and compared with the inviscid flutter boundary from other authors [30], [10], [62] showing good agreement. The transonic dip is obtained, and the stable pocket around $V_F = 2.3$ for $M = 0.85 - 0.9$ is also captured. This pocket is only reported for inviscid simulations.

The pocket corresponds to having multiple flutter boundary points for a given Mach number. By increasing the speed index at $M_\infty = 0.875$ the system evolves from stable to unstable

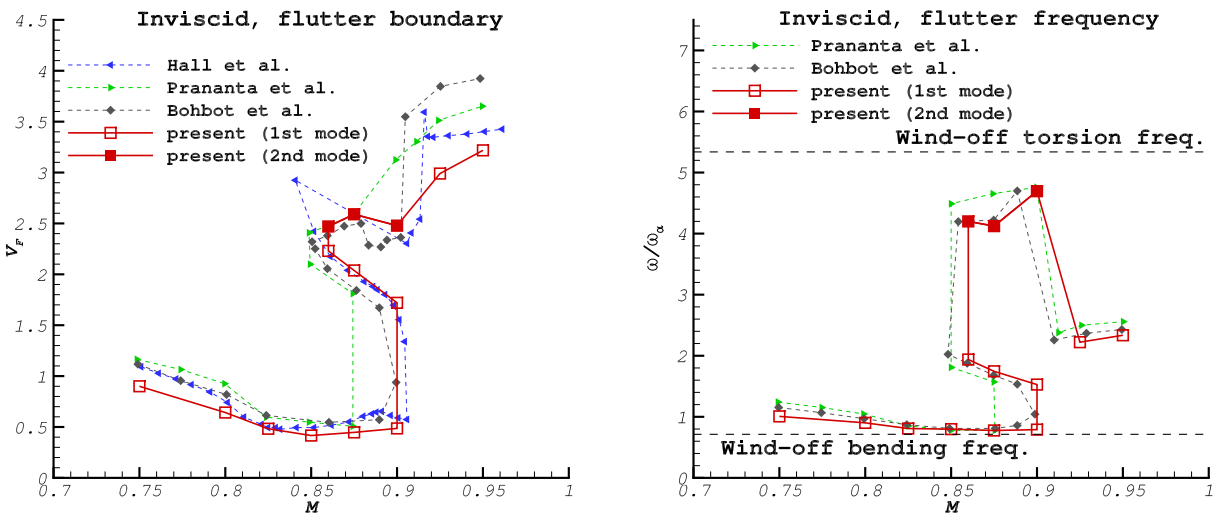

(a) (b)

Figure 2.11: Flutter boundary (left) and non-dimensional frequency at the flutter boundary (right) for inviscid solution. Comparison with numerical simulations from other authors [62], [30], [10] .

at $V_F = 0.447$, to stable at $V_F = 2.038$, and to unstable again for $V_F = 2.59$, leaving all points on the left side of the curve from Figure 2.11a as unstable, and the ones on the right side as stable. Figure 2.11b shows the frequency response at the flutter boundary. The results agree well with numerical simulations from other authors. The Mach region showing multiple flutter points, reveals the second unstable flutter point is caused by the instability of the second mode, and responds at a much higher frequency than instabilities caused by the first mode.

Figure 2.12 shows an unstable response at $M_\infty = 0.825$ and $V_F = 0.5$. It is a condition near the neutrally stable point $V_F = 0.483$ and the growth rate is therefore small. The simulation is truncated after 32 periods. Due to the small growth, the drag coefficient appears constant and the second mode seems inactive. Figure 2.13 corresponds to the same Mach number but at $V_F = 0.9$. Due to the higher growth rate in the instabilities, the drag coefficient oscillates and the oscillation amplitude grows monotonically until the system reaches Limit Cycle Oscillations. The second mode shows minimal oscillation compared to the first mode.

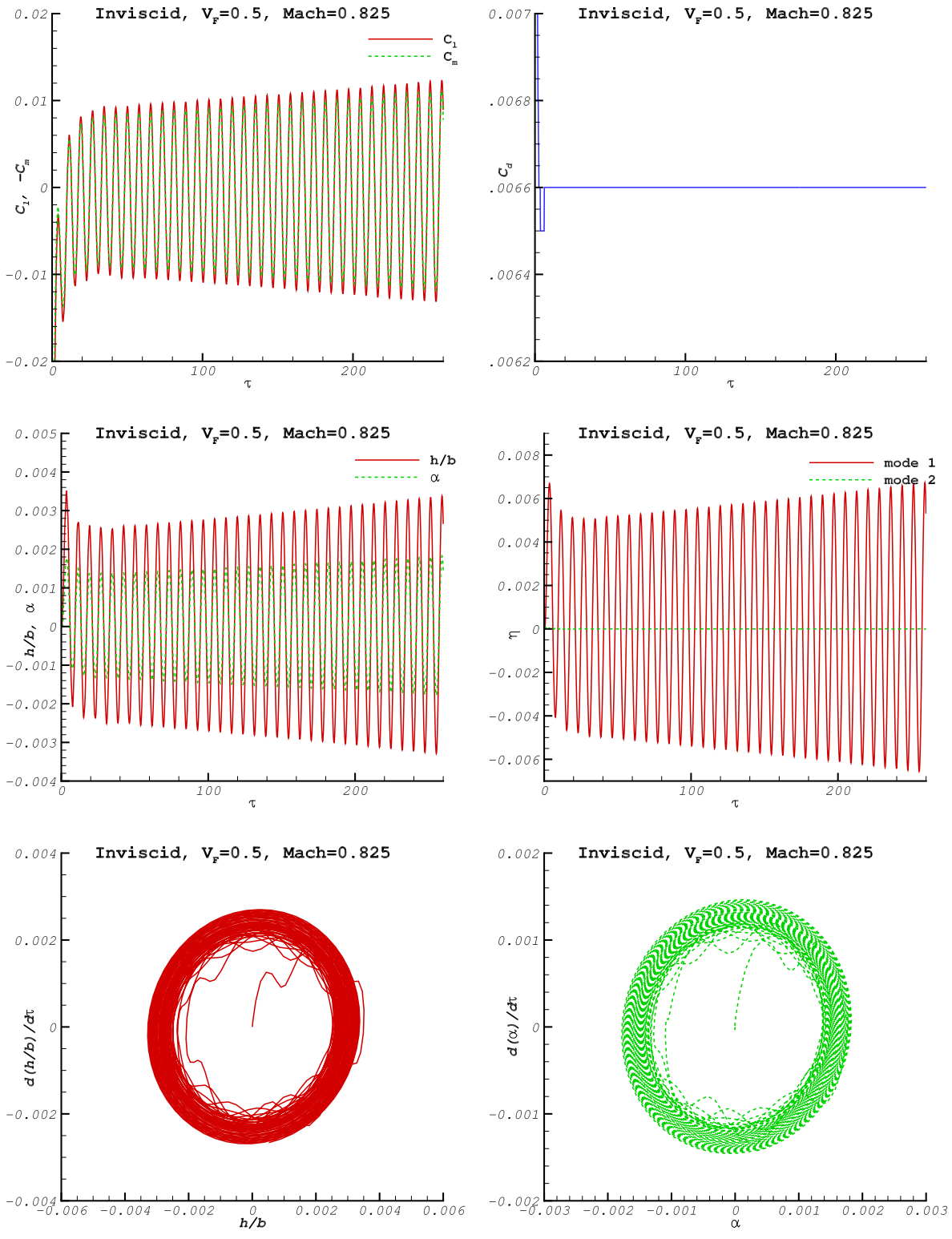

Figure 2.12: Euler results for flutter of NACA 64A010 at $M_\infty = 0.825$, $V_F = 0.5$.

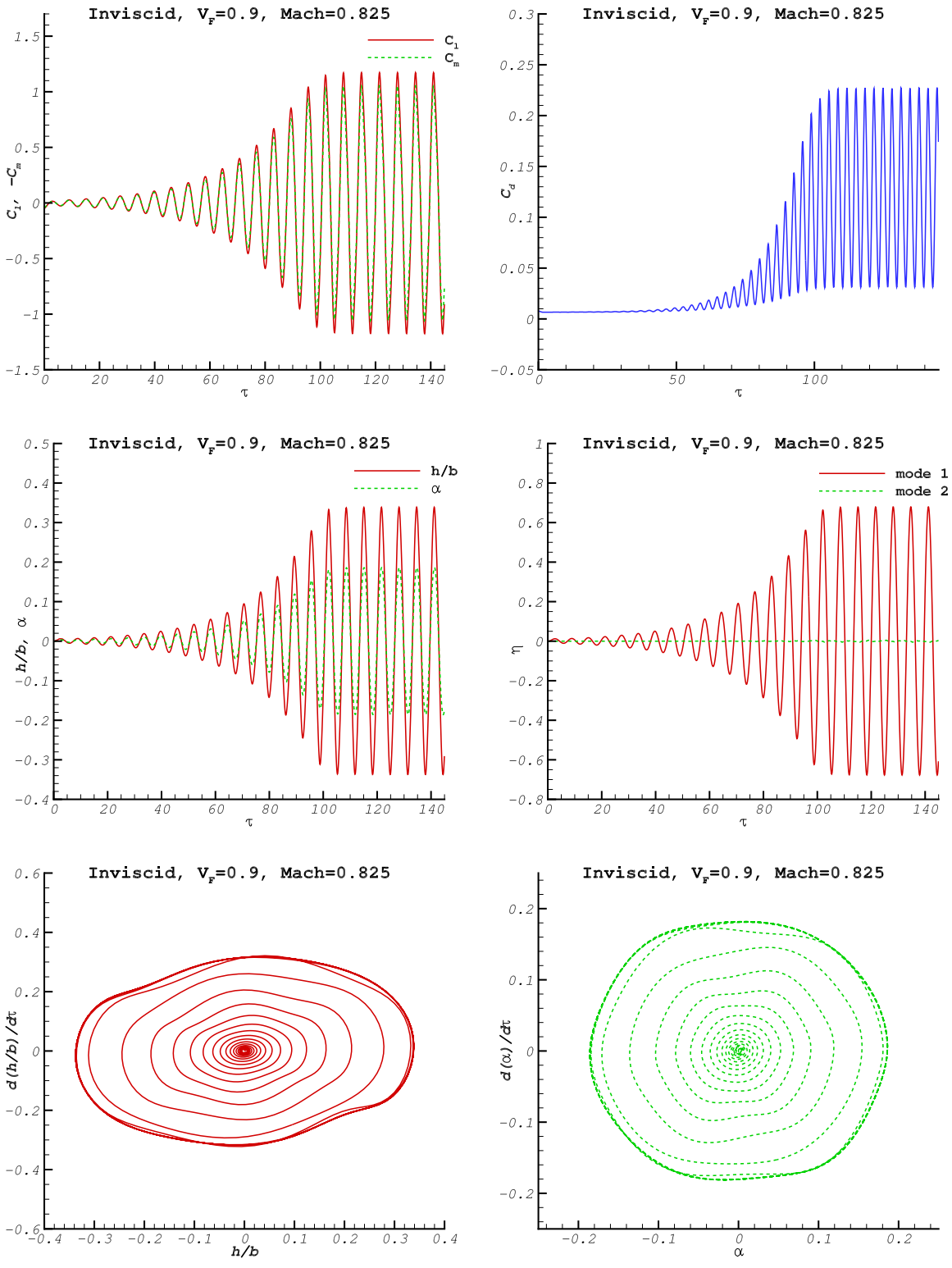

Figure 2.13: Euler results for flutter of NACA 64A010 at $M_\infty = 0.825$, $V_F = 0.9$.

To study the multiple flutter boundary point condition, $M_\infty = 0.875$ is examined. Figures 2.14 - 2.18 show results for $V_F = 0.5, 1.9, 2.1, 2.5, 2.6, 2.7$ where only $V_F = 2.1, 2.5$ are stable, and the rest are unstable. The unstable cases are marched until LCO (defined in Section 1.1). Figure 2.14 shows results of C_l and C_m, while C_d is not shown since its contribution to the dynamic system is of lower order. Heaving and pitching are shown in Figure 2.15, revealing the heaving amplitude always to be larger than the pitching. While both degrees of freedom are in phase for $V_F = 0.5$, a phase shift appears while increasing V_F reaching a complete out of phase of π for $V_F \geq 2.5$. Figure 2.16 shows the first mode to be the dominant one, before reaching the second flutter point at $V_F = 2.59$. For $V_F = 2.6, 2.7$ the second mode appears as the dominant, generating a structural response at a much higher frequency. These results agree with those in Figure 2.11b. Figures 2.17 and 2.18 show the phase plots in heaving and pitching for the given V_F values.

The initial conditions are generated by a forced pitch motion of one degree during three periods at the natural frequency of the system. The results in the figures only show the evolution after the initial three forced periods. Some transition effects are shown on the first two periods of the elastic response until it adapts from the initial condition to each specific free response. Variations in the magnitude of the forced pitch for the initial condition did not affect the final state of stability of the dynamic system.

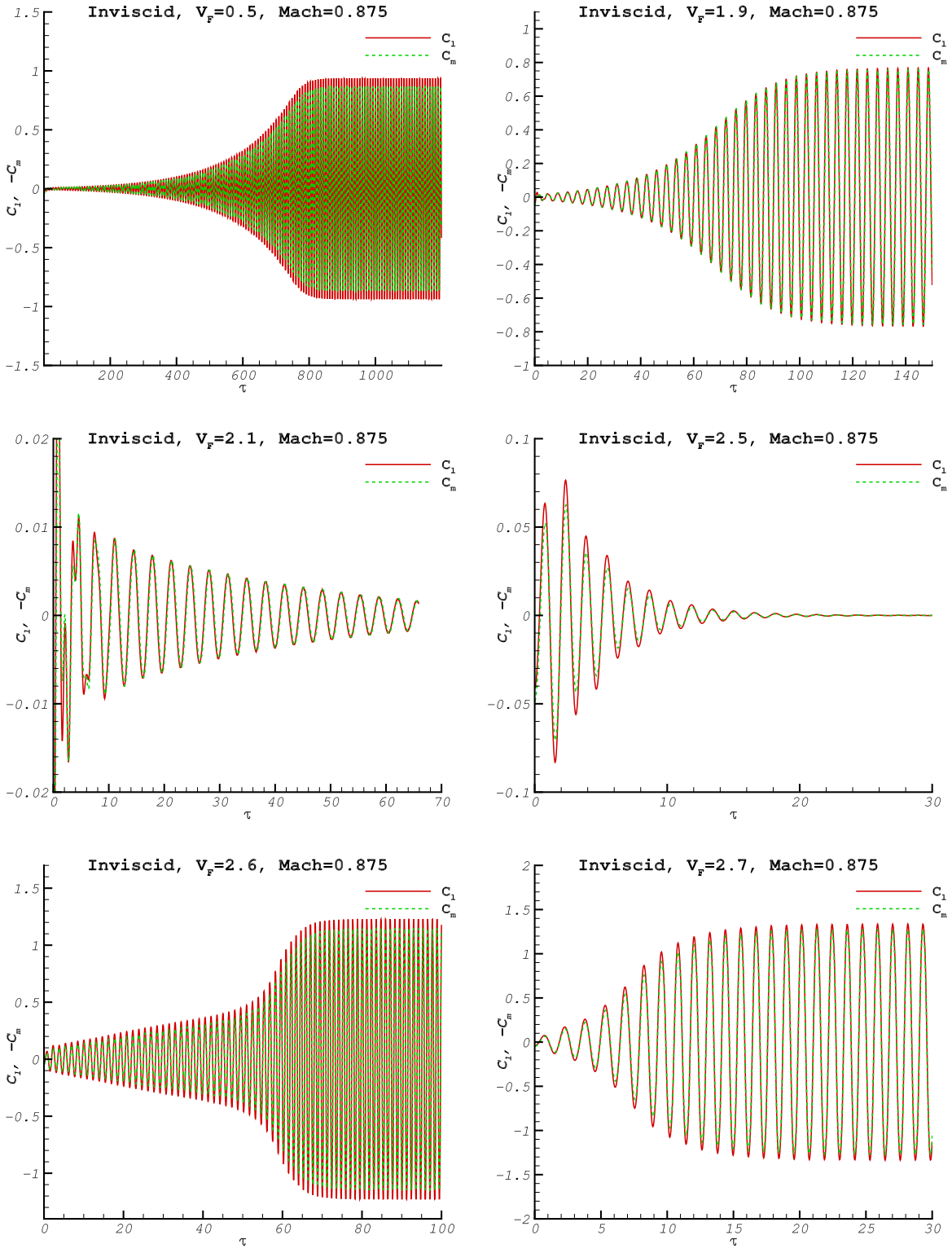

Figure 2.14: Lift and moment coefficients for Euler results of NACA 64A010 flutter at $M_\infty = 0.875$, $V_F = 0.5 - 2.7$.

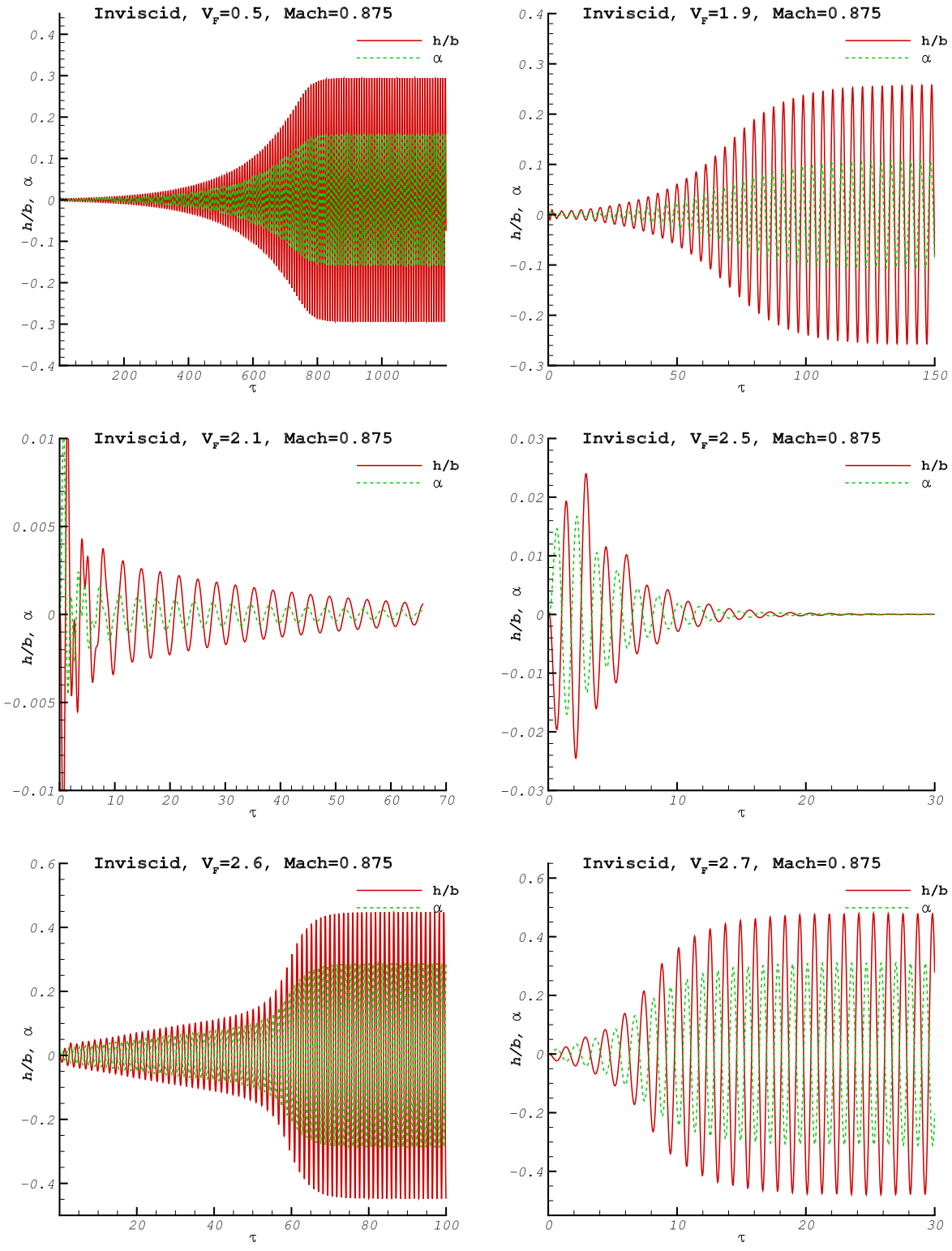

Figure 2.15: Heaving and pitching for Euler results of NACA 64A010 flutter at $M_\infty = 0.875$, $V_F = 0.5 - 2.7$.

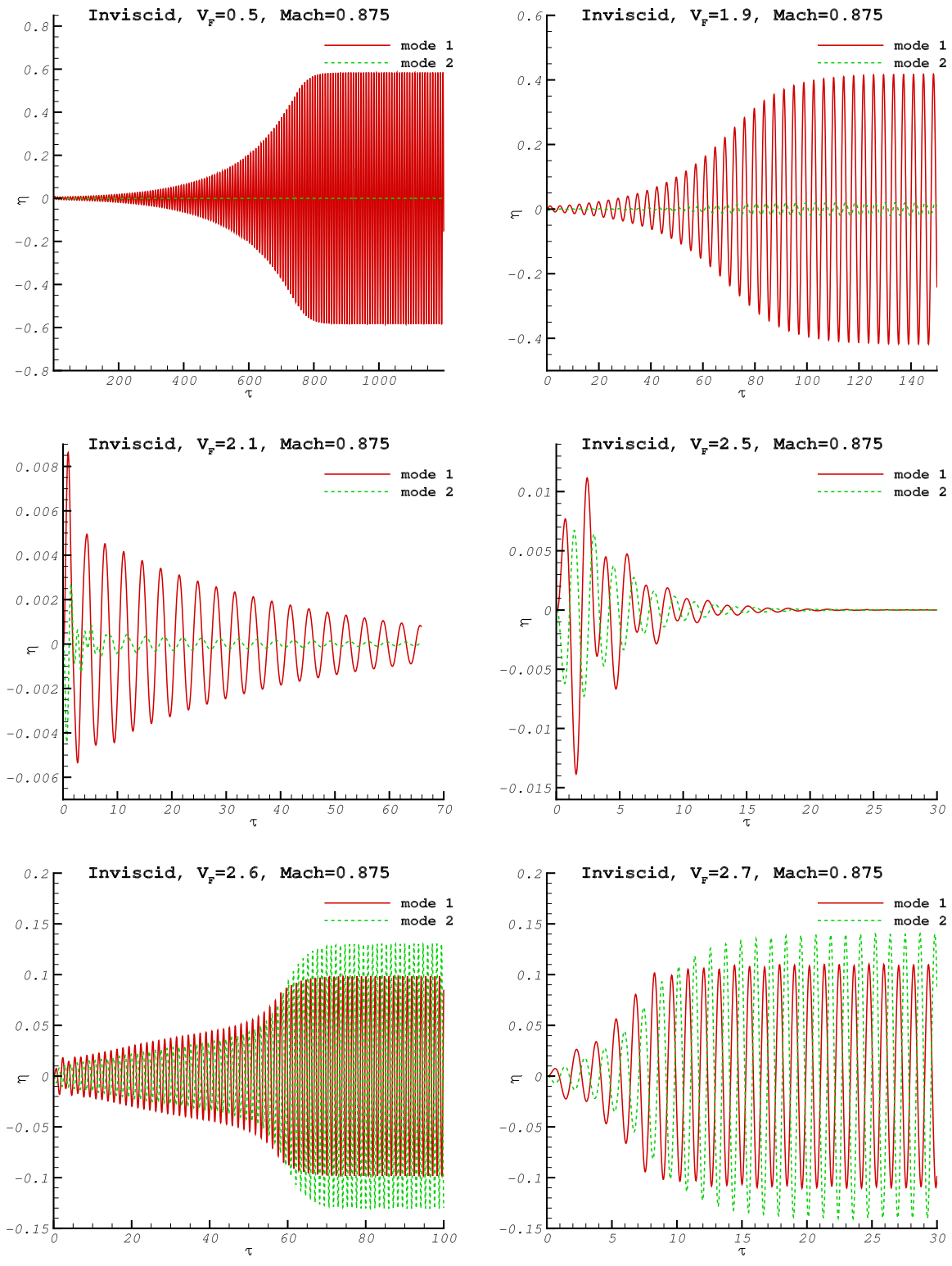

Figure 2.16: Generalized coordinates for Euler results of NACA 64A010 flutter at $M_\infty = 0.875$, $V_F = 0.5 - 2.7$.

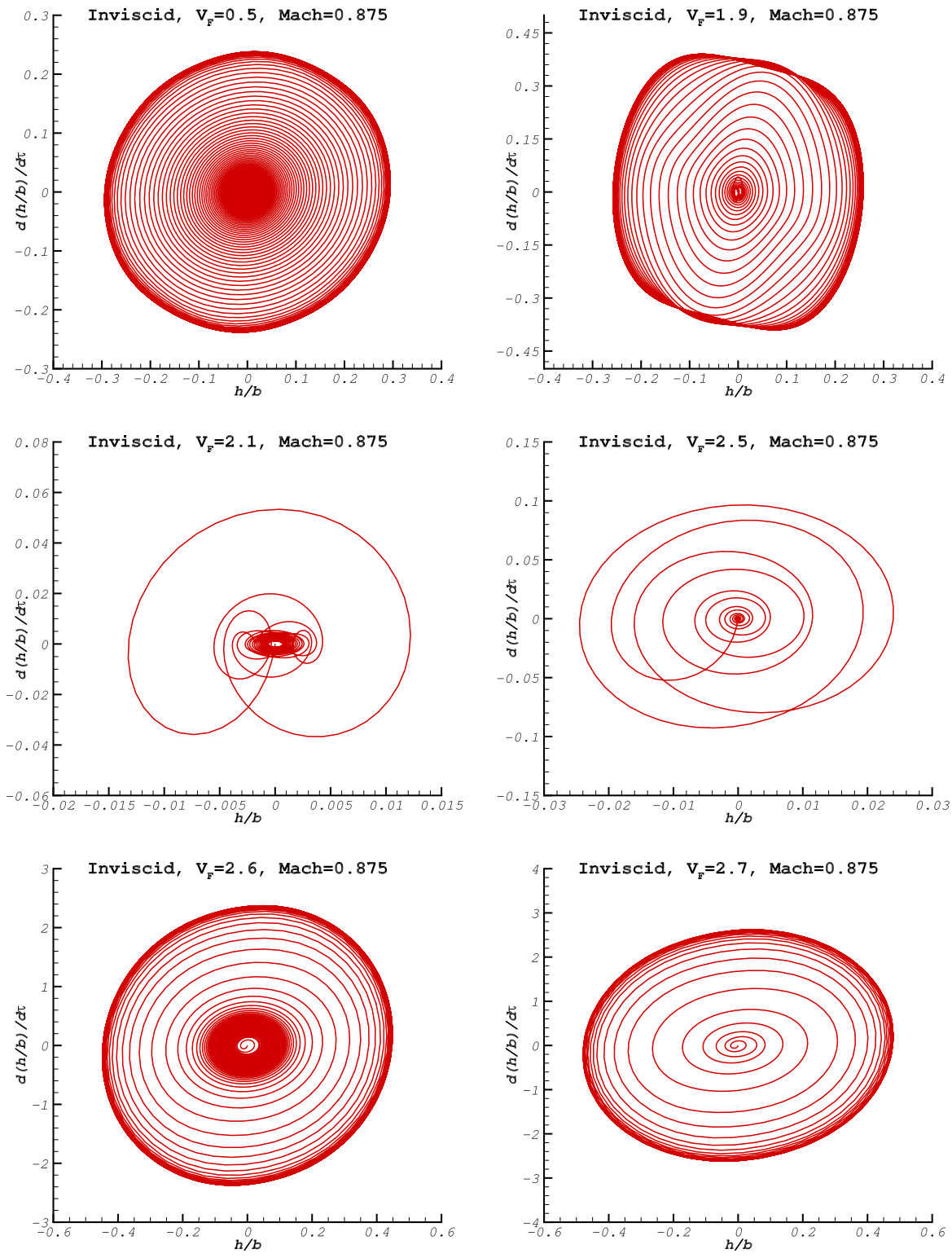

Figure 2.17: Heaving phase for Euler results of NACA 64A010 flutter at $M_\infty = 0.875$, $V_F = 0.5 - 2.7$.

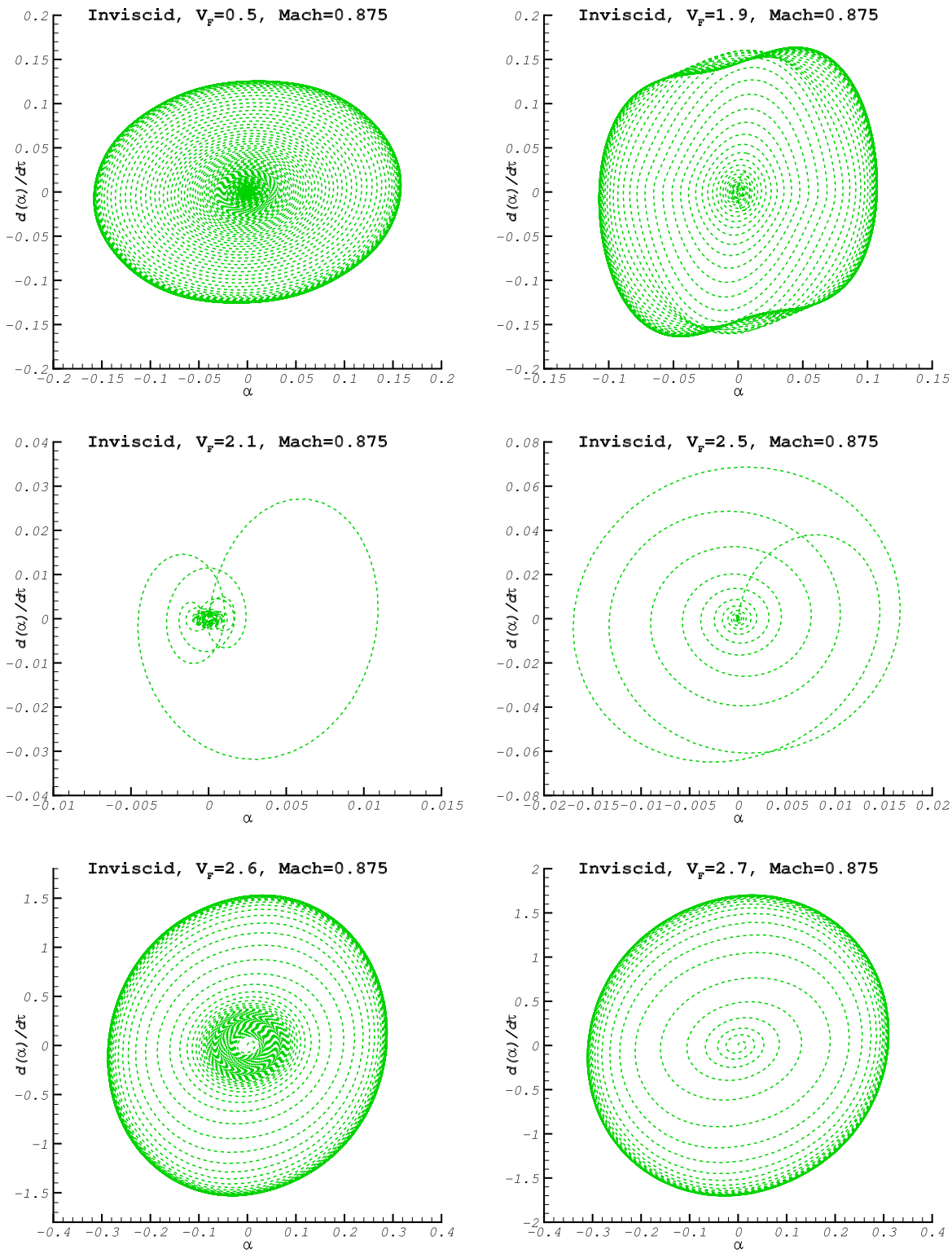

Figure 2.18: Pitching phase for Euler results of NACA 64A010 flutter at $M_\infty = 0.875$, $V_F = 0.5 - 2.7$.

Chapter 3

Non-linear behavior of the NACA64A010 airfoil using Isogai's model for fully turbulent flow

In the previous Chapters, the Computational Fluid Dynamics and the Computational Structural Dynamics codes have been described, along with validations for steady-state fully-turbulent flow and for inviscid aeroelasticity. The present Chapter explores the flutter boundary of the NACA64A010 airfoil using Isogai's model for fully-turbulent flow (Section 3.1). Due to the non-linearity of the CFD code, multiple equilibrium points are revealed in Section 3.2.

3.1 Flutter boundary for fully turbulent conditions

The elastic response of the NACA 64A010 is studied for the URANS equations using Spalart-Allmaras turbulence model at $Re = 10^7$. Three symmetric grid levels are generated to obtain

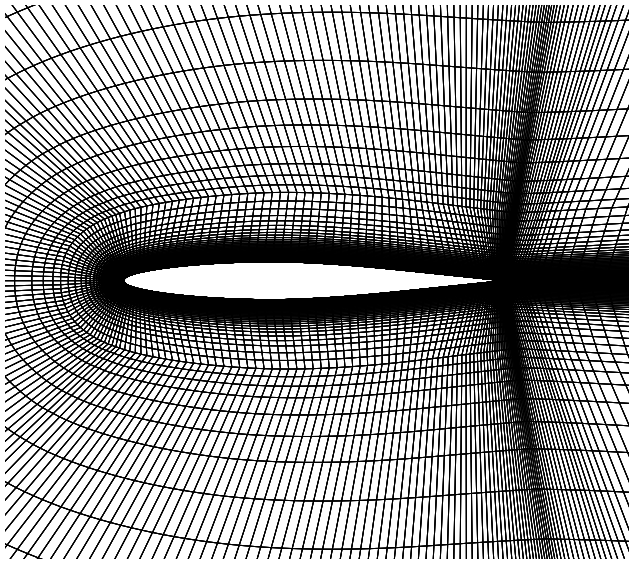

Figure 3.1: Coarse grid level of NACA 64A010 for RANS simulation with 312×72 cells.

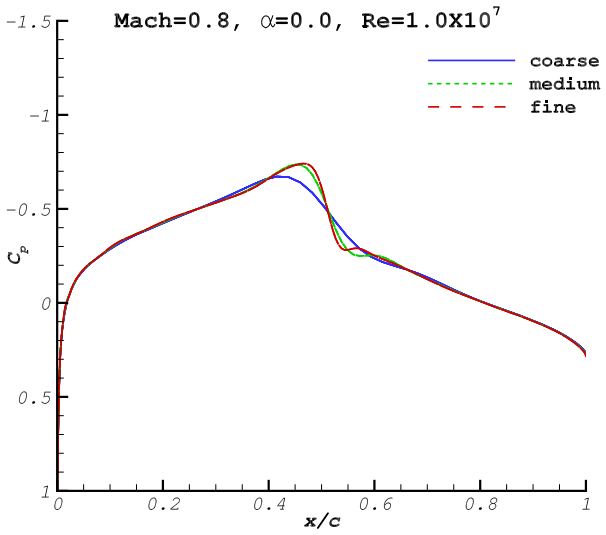

Figure 3.2: Grid independence study for RANS simulation.

grid independent results by coarsening the finer grid in every direction for each level. The coarser grid of 312×72 cells is shown in Figure 8.1. Figure 3.2 shows the pressure distribution for $M_\infty = 0.8$ for each grid level. While the 3 grids produce the same results away from the shock, the coarse grid is too diffusive to capture a sharp shock wave. The medium and fine grids produce comparable results at the shock location, therefore the medium grid of 624×144 cells is chosen for the flutter studies.

The dynamic response in a turbulent flow differs from that obtained with the Euler equations. For $M_\infty = 0.825$, Figures 2.12 and 2.13 show two unstable solutions for $V_F = 0.5, 0.9$. The same conditions tested for fully turbulent flow, shown in Figures 3.3 and 3.4, reveal $V_F = 0.5$ as stable.

Figures 3.5a and 3.6a show the flutter boundary results for $M_\infty = 0.75 - 0.95$. In Figure 3.5a results by other researchers are also included. While the agreement in the Euler boundary was excellent until $M_\infty = 0.9$, the turbulent results show more dispersion. However, the main trend agrees well with the results from Bohbot et al. [10] (used SA model). They

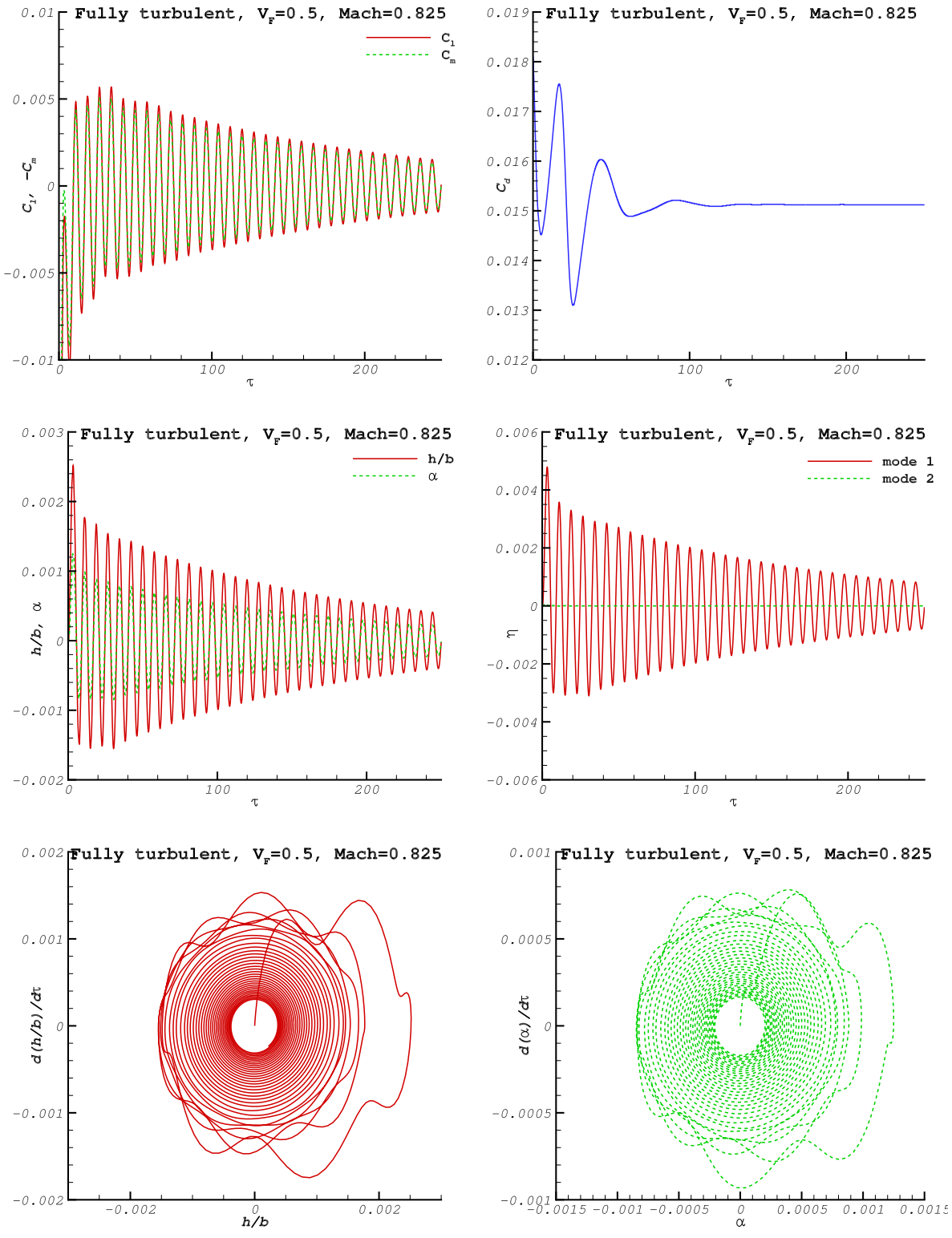

Figure 3.3: RANS results for flutter of NACA 64A010 at $M_\infty = 0.825$, $V_F = 0.5$.

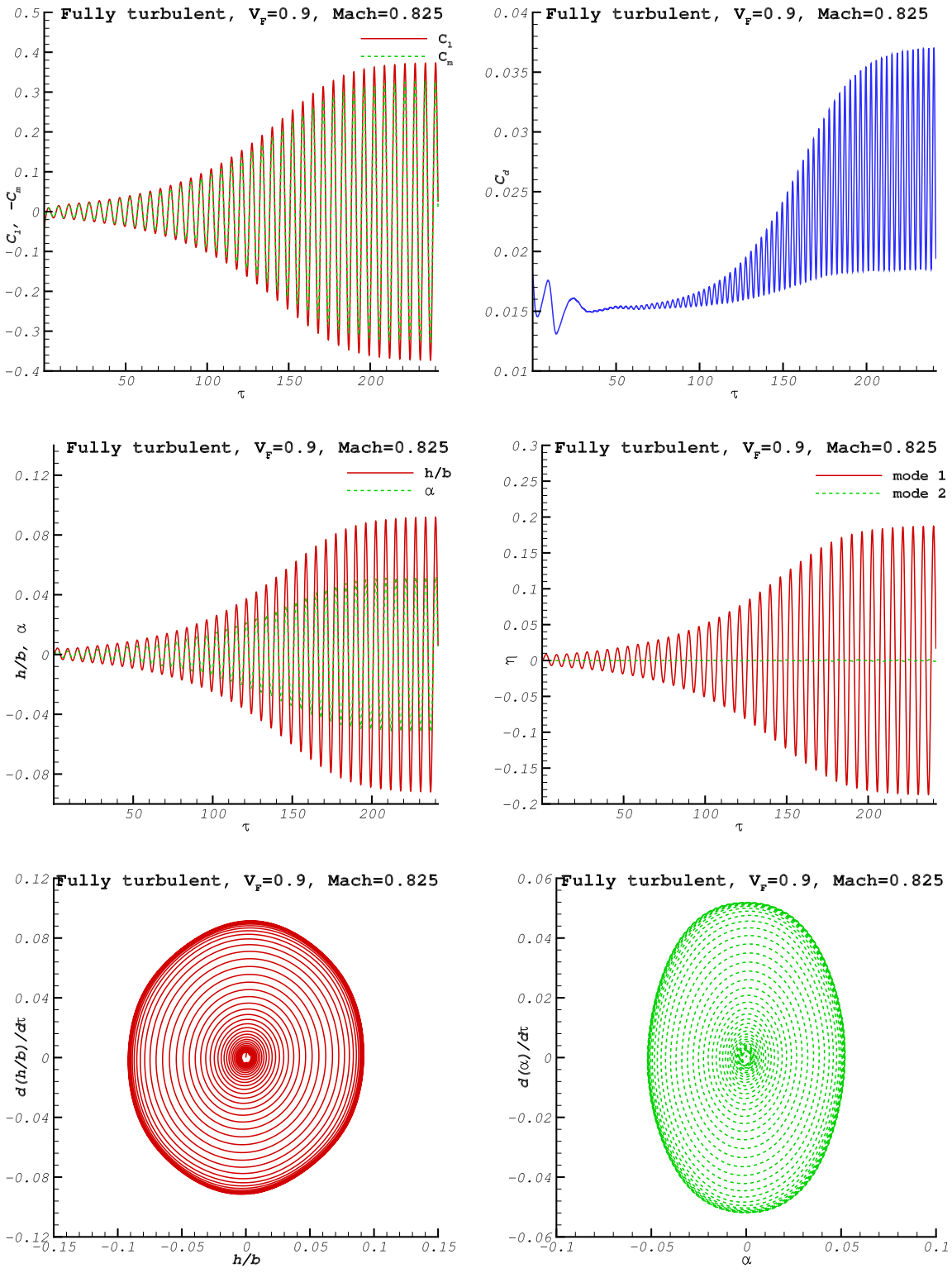

Figure 3.4: RANS results for flutter of NACA 64A010 at $M_\infty = 0.825$, $V_F = 0.9$.

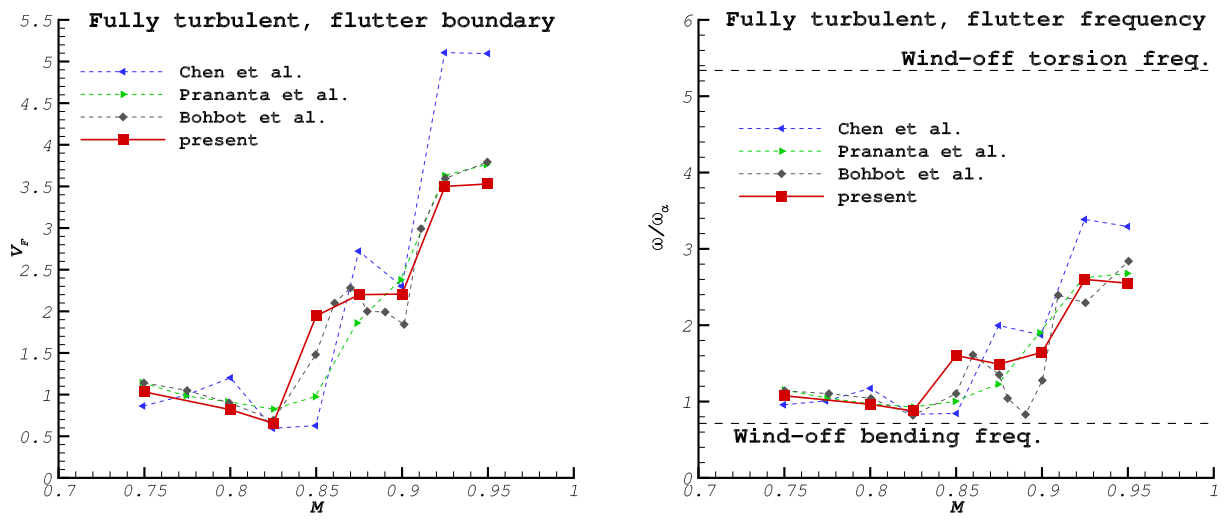

(a) (b)

Figure 3.5: Flutter boundary (left) and non-dimensional frequency at the flutter boundary (right) for fully turbulent RANS solution. Comparison with other numerical simulations.

show a good agreement for low and high Mach numbers when compared with Prananta et al. [62] (Thin-Layer Navier-Stokes), and a fair agreement with Chen et al. [18] (SA model). Figure 3.6a includes the closed region where multiple equilibrium points exist.

The effect of the speed index in unstable conditions is studied. Two Mach numbers away from the multiple equilibrium points region are chosen ($M_\infty = 0.825, 0.95$). Figure 3.7a shows the amplitude in heaving and pitching when LCO is reached for multiple speed index values above the flutter boundary of each corresponding Mach number. While the heaving amplitude for $M_\infty = 0.95$ is higher than for $M_\infty = 0.825$, the pitching amplitude shows comparable values. The trend however appears different. The ratio in heaving/pitching amplitudes for $M_\infty = 0.825$ is almost constant, while it increases with V_F for $M_\infty = 0.95$. Figure 3.7b shows the non-dimensional time to reach LCO, which is similar for both Mach numbers when accounting for the difference between the flutter boundary and the plotted V_F value. For $M_\infty = 0.825$, the flutter boundary is at $V_F = 0.656$, while for $M_\infty = 0.95$ it is at $V_F = 3.53$. Therefore, the time to reach LCO depends on the difference between the simulated speed index and the flutter boundary V_F, but it appears to have a small Mach

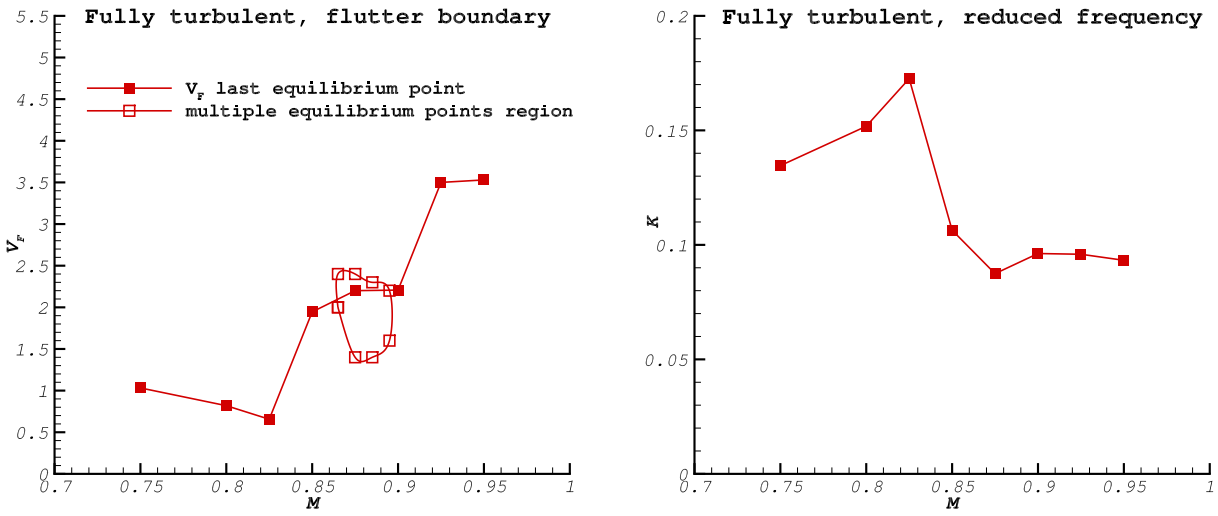

(a) (b)

Figure 3.6: Flutter boundary showing region of multiple equilibrium points for fully turbulent RANS solution (left). Reduced frequency at the flutter boundary for for fully turbulent RANS solution (right). The flutter boundary on the left image indicates the region of stability for the first equilibrium point, if only a single equilibrium points exists, or for the second and last equilibrium point, in case multiple equilibrium points exist.

dependence.

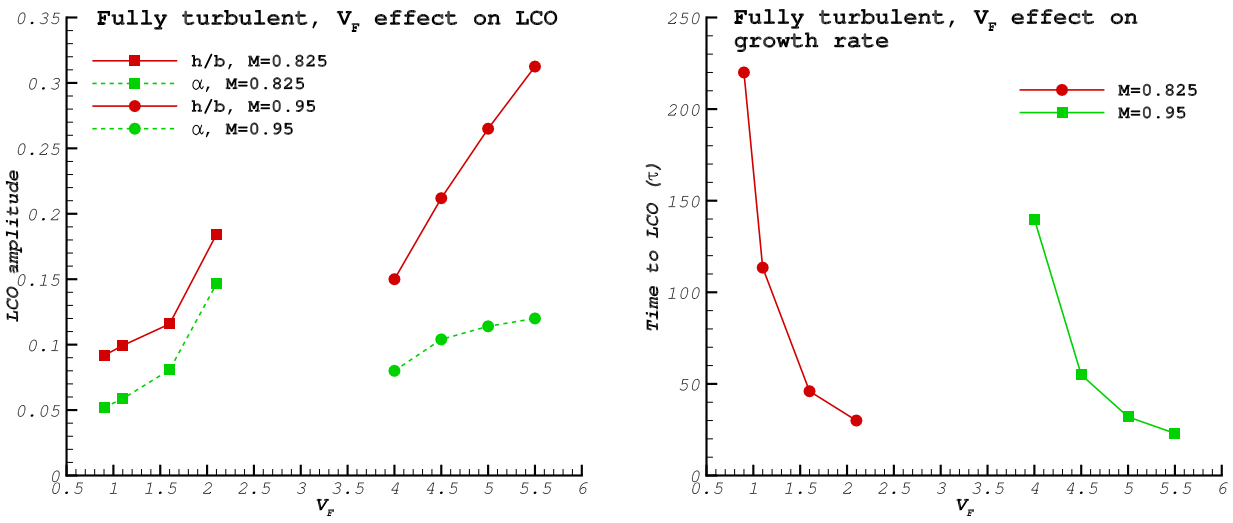

(a) (b)

Figure 3.7: Effect of V_F on Limit Cycle Oscillations. Amplitude of heaving and pitching (left), and non-dimensional time to reach LCO (right) for $M_\infty = 0.825$, and $M_\infty = 0.95$.

3.2 Multiple equilibrium points caused by non-linear effects

Chen et al. [18] discovered multiple equilibrium points for $M_\infty = 0.875$. Under further inspection, Figure 3.6a revealed a pocket where multiple equilibrium points exist. The solid squares in Figure 3.6a indicate a neutrally stable condition around the initial equilibrium point, if only a single equilibrium point exists, or around the second and last equilibrium point, in case multiple equilibrium points exist. The open squares indicate a closed region where the dynamic system oscillating around the initial equilibrium point $h/b = 0$ and $\alpha = 0$ is unstable, but evolves into a new equilibrium point which reveals as stable (if below the solid squares line) or unstable (otherwise). For the Mach ranges where a single equilibrium point is found, the flutter boundary is easy to define. However, under a linear stability analysis which determines the stability of a dynamic system around a given point, the lower boundary for multiple equilibrium points would become the new flutter boundary.

In order to clarify the meaning of Figure 3.6a, Figure 3.8 is created where each color represents a different region. The light green region is the traditional region of stability where the initial symmetric equilibrium point is stable. The pink region, defines the traditional unstable region where the system oscillates around the initial, symmetric equilibrium point, albeit its amplitude grows. The dark green region, limits cases where the original symmetric equilibrium point is unstable and the system finds a new asymmetric equilibrium point which becomes stable. The last dark purple region, determines the original symmetric equilibrium point to be unstable, finding a new asymmetric equilibrium point. The system then oscillates around this new asymmetric equilibrium point with oscillations growing in magnitude until reaching LCO.

Like in the inviscid situation, 3 periods of forced pitch motion at one degree of amplitude are

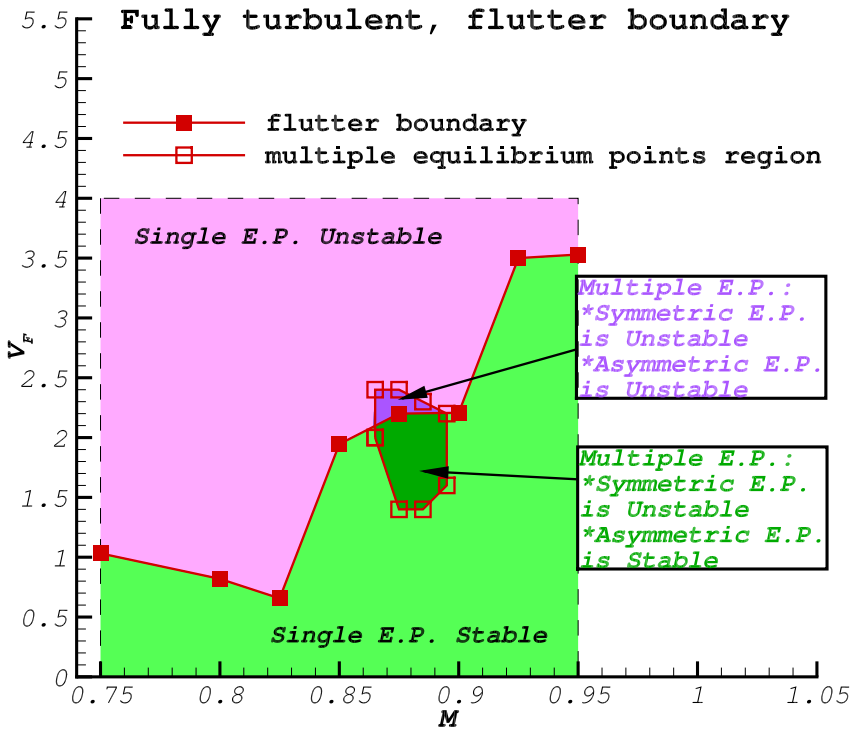

Figure 3.8: Flutter boundary using colors to describe the different regions where single or multiple equilibrium points exist.

applied to generate the initial condition for the elastic system. For the low and high transonic range, away from the region of multiple equilibrium points, variations in the amplitude of the forced pitch motion to generate the initial conditions have no effect in the final state of stability of the elastic system. This is not the case for $M_\infty = 0.865 - 0.895$ where bifurcations appear, and multiple equilibrium points are found. The direction of the pitch motion used to obtain the initial condition determines the sign of the asymmetry in the final equilibrium point.

Comparing Figure 3.5 with 2.11, clear differences in the dynamic response between turbulent and inviscid flow are observed. The characteristic S-shape of the inviscid flutter boundary is not obtained in the turbulent simulation. In the turbulent case, the frequency response at flutter conditions is always driven by the first mode which eliminates the high frequency response observed in the inviscid simulations. Figure 3.6b reveals low values of reduced frequency (κ) for turbulent conditions. κ can be obtained combining V_F and ω/ω_α using

$$\kappa = \frac{1}{V_F\sqrt{\mu}}\frac{\omega}{\omega_\alpha} \tag{3.1}$$

The case of $M_\infty = 0.875$ is chosen as an example of the multiple equilibrium points phenomenon. Figures 3.9 - 3.13 show the dynamic response of the system for $V_F = 0.7, 1.9,$ $2.1, 2.3, 2.5, 2.7$. While bifurcation appears at $V_F = 1.4$, it is stable. The range $1.4 \leq V_F \leq 2.2$ generates stable solutions converging to equilibrium points different from the original $\{h/b = 0,\ \alpha = 0\}$. $V_F \geq 2.2$ sets the boundary where oscillations grow until reaching LCO around asymmetric equilibrium points, and $V_F \geq 2.4$ is the higher limit for the existence of multiple equilibrium points.

While the lift and moment coefficients seem to always be in phase (Figure 3.9), a non-zero

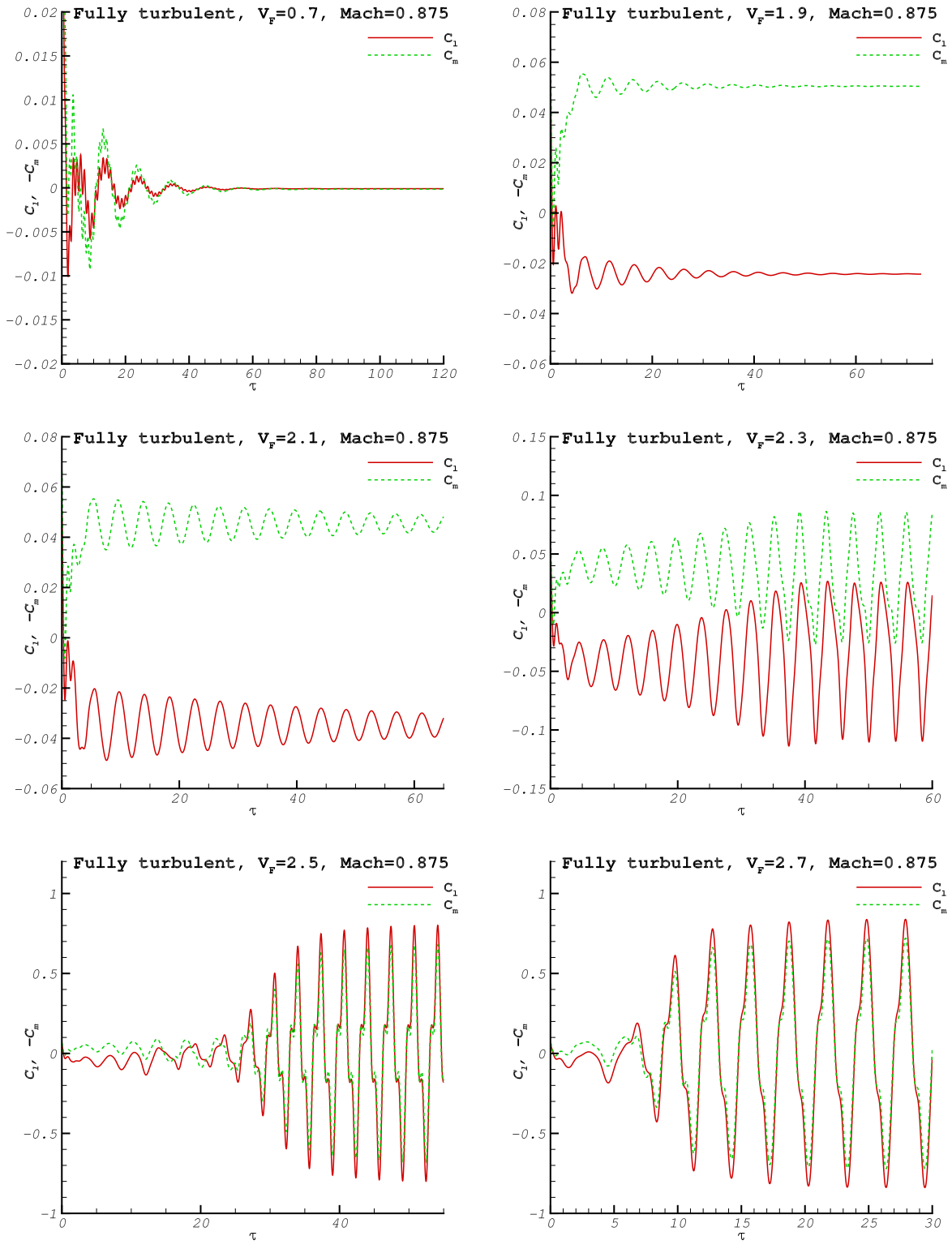

Figure 3.9: Lift and moment coefficient for RANS results of NACA 64A010 flutter at $M_\infty = 0.875$, $V_F = 0.7 - 2.7$.

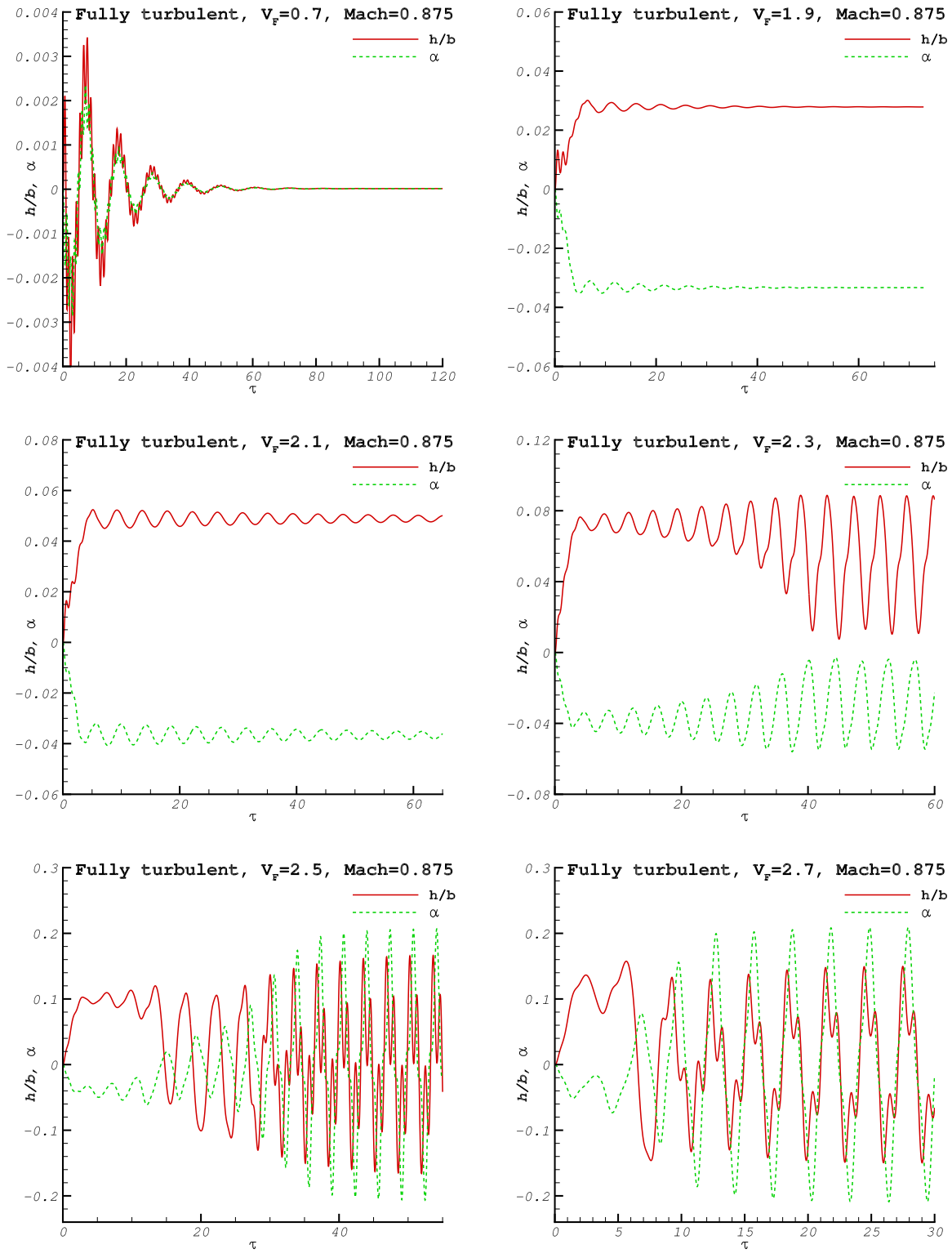

Figure 3.10: Heaving and pitching for RANS results of NACA 64A010 flutter at $M_\infty = 0.875$, $V_F = 0.7 - 2.7$.

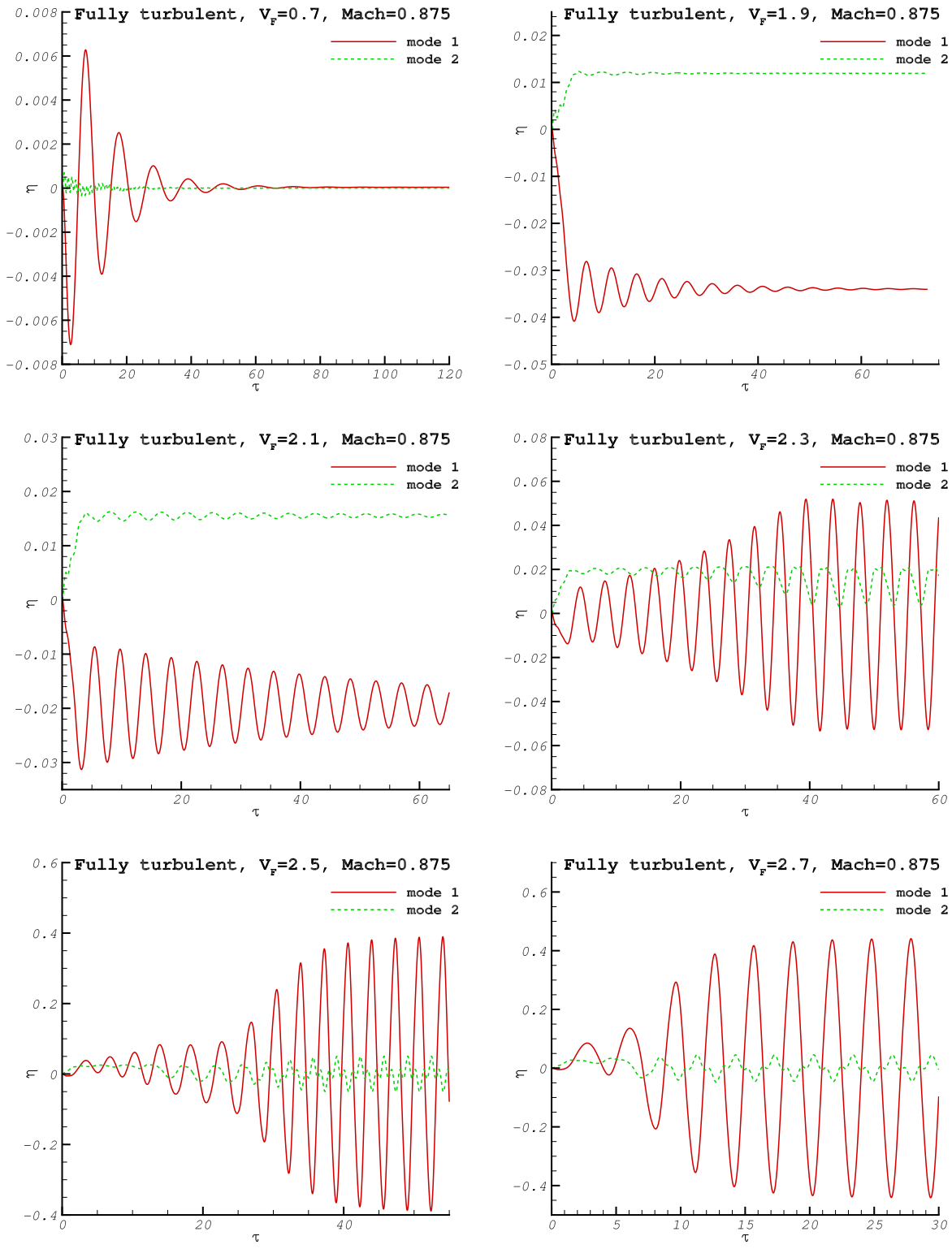

Figure 3.11: Generalized coordinates for RANS results of NACA 64A010 flutter at $M_\infty = 0.875$, $V_F = 0.7 - 2.7$.

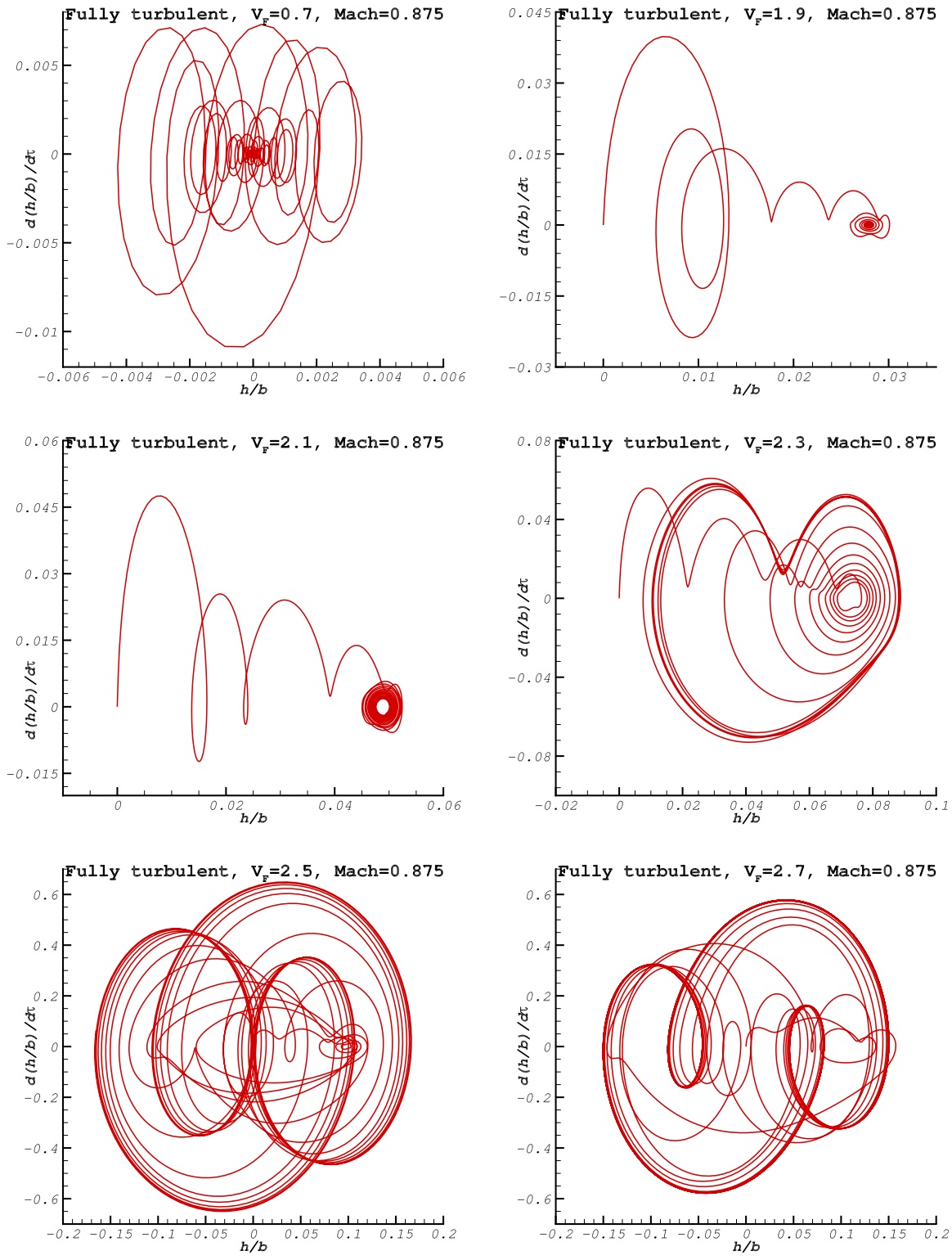

Figure 3.12: Heaving phase for RANS results of NACA 64A010 flutter at $M_\infty = 0.875$, $V_F = 0.7 - 2.7$.

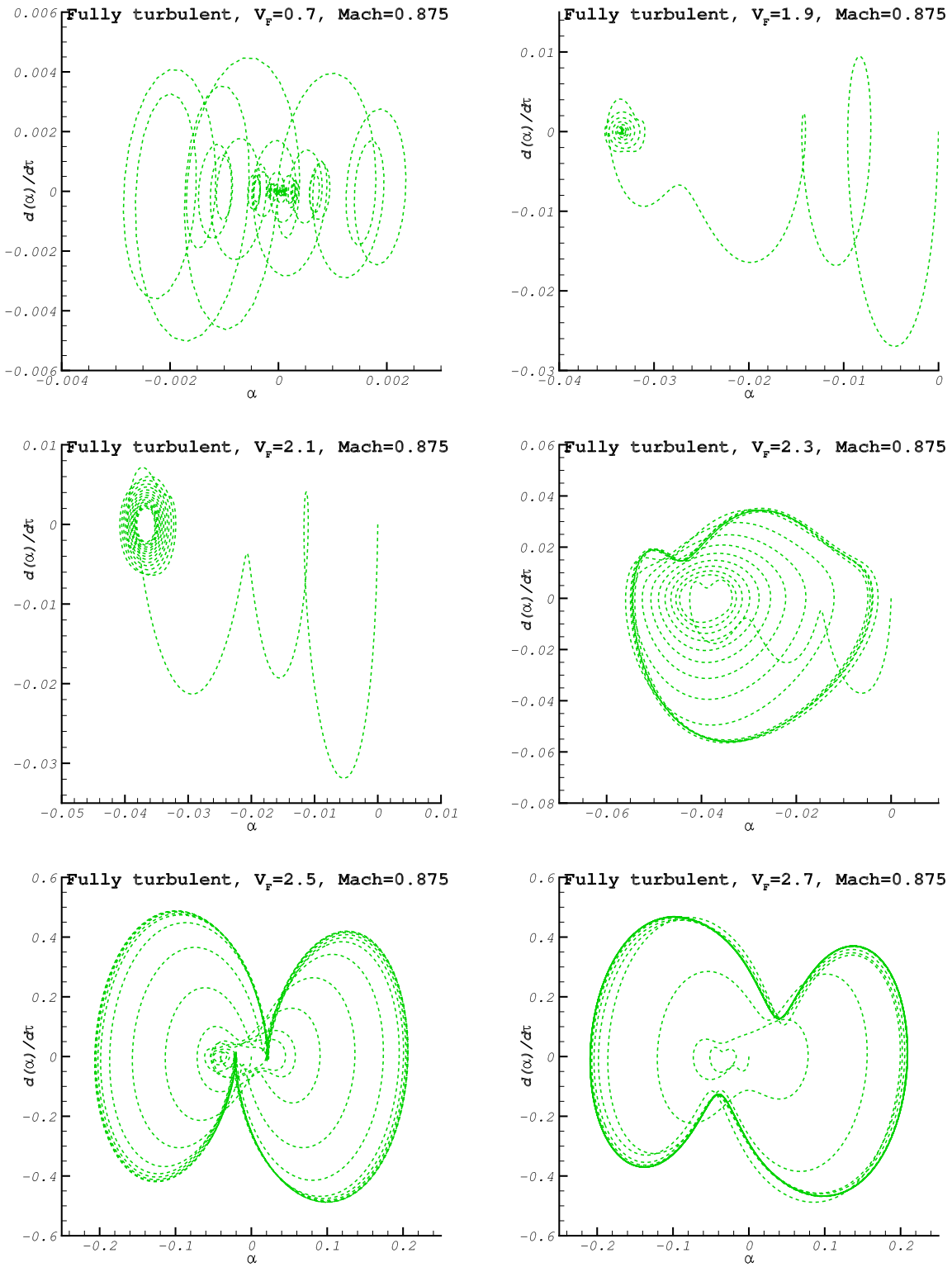

Figure 3.13: Pitching phase for RANS results of NACA 64A010 flutter at $M_\infty = 0.875$, $V_F = 0.7 - 2.7$.

mean value is observed for the cases showing multiple equilibrium points. For those cases, the mean value of C_l and C_m have the same sign.

For $V_F = 2.3$, the heaving and pitching responses in Figure 3.10 show a constant shifting in the equilibrium point during the system response until LCO is reached. That shift is clearly observed in the phase plots, where the motion changes from smooth round oscillations into a deformed phase when LCO is reached. That kink, specially noticed in the heaving phase plots, is due to a small perturbation when increasing the heaving position, shown in Figure 3.10.

The cases of $V_F = 2.5, 2.7$ start oscillating around a non-zero equilibrium point (Figure 3.10), but quickly move back to the original zero equilibrium position. A significant kink in heaving is found for $V_F = 2.5, 2.7$, while a small perturbation present in pitching is almost not observed. Those are clearly revealed in the phase plots. The kinks are less significant for the higher speed index case of 2.7 which suggests the kinks might vanish if the speed index is further increased. Those kinks, are caused by a multiple frequency response of the second mode (Figure 3.11).

While the second mode is always less dominant than the first mode, it is also the reason for creating multiple equilibrium points at $V_F = 2.3$, as shown in Figure 3.11. This conclusion cannot be extracted for lower V_F values, where both modes oscillate around non-zero positions.

The phase plots in Figures 3.12 and 3.13 show the dynamic system moving away from the the original $\{h/b = 0,\, \alpha = 0\}$ equilibrium point for $V_F = 1.9, 2.1, 2.3$.

Figure 3.14 shows pressure and Mach contours for the final state of $V_F = 1.9$. The final position of $\{h/b = 0.02786, \alpha = -1.9107°\}$ produces a negative lift of $C_l = -0.02432$, and a nose-down moment of $C_m = 0.05042$. The small lift, even at almost two degrees of angle of attack, is caused by the large separation of the flow at the foot of the shock wave, as

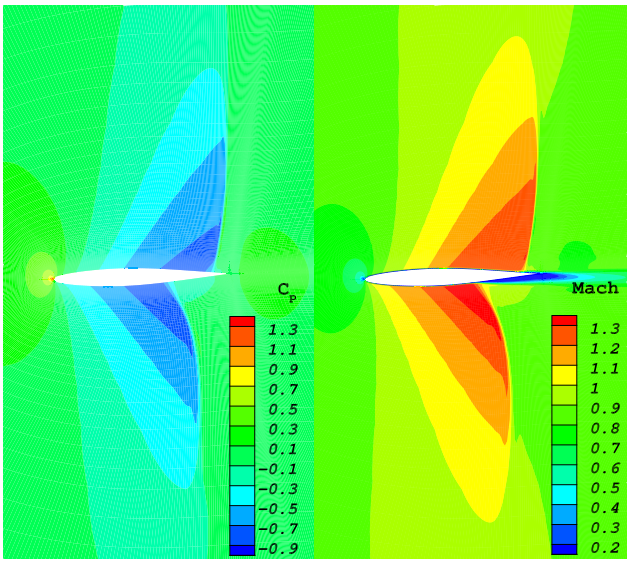

Figure 3.14: C_p (left) and $Mach$ (right) contours for fully turbulent simulation at $M_\infty = 0.875$ and $V_F = 1.9$ after elastic oscillations have vanished.

observed in the Mach contours figure. Figure 3.15 shows the streamlines along with a Mach contour color map of the final state of the elastic system for $V_F = 0.7$ and 1.9. While the solution is symmetric for $V_F = 0.7$, the asymmetric solution for $V_F = 1.9$ is caused by a large separation bubble after the shock position which effectively modifies the zero-camber of the airfoil into a ficticius cambered airfoil with specific lift and moment characteristics to balance the sturctural loading of the wing.

For the unsteady speed index case of $V_F = 2.5$, the large pitching amplitude of 12° obtained at LCO generates a fully detached flow after the shock. Figure 3.16 shows the streamlines and Mach contours for the highest angle of attack stage during an LCO period. An oblique shock wave emmanating from the foot of the separation region is merging with a normal shock at the trailing edge of the airfoil which originates a lambda shock pattern.

Some simulations are performed at $Re = 10^6$ around the multiple equilibrium point region to study if the phenomenon is also revealed at lower Reynolds numbers. While the flutter boundary for $Re = 10^6$ is not mapped, the existence of multiple equilibrium points is also found. Figure 3.17 shows oscillations around a non-zero equilibrium point, dominated by

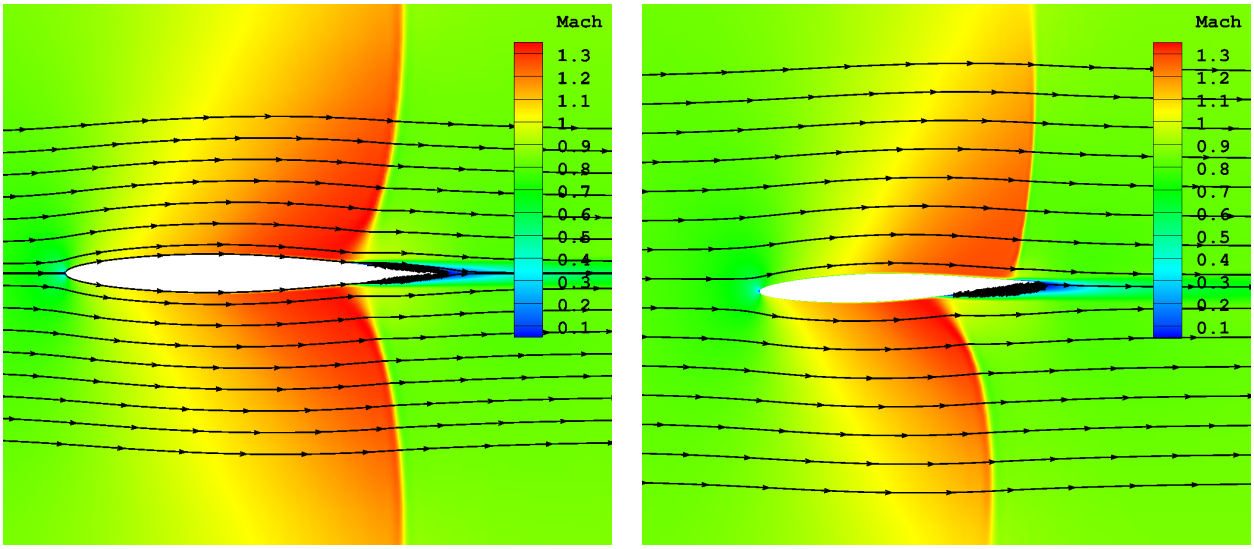

(a) (b)

Figure 3.15: Streamlines and Mach contour for the final steady state of the elastic solution at $M_\infty = 0.875$ and $V_F = 0.7$ (left), $V_F = 1.9$ (right).

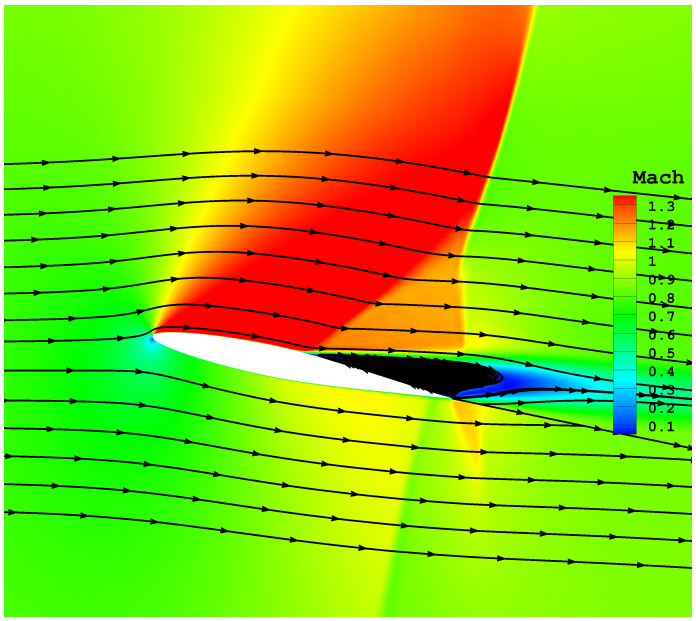

Figure 3.16: Streamlines and Mach contour for the $\alpha = 12°$ state of the LCO solution at $M_\infty = 0.875$ and $V_F = 2.5$.

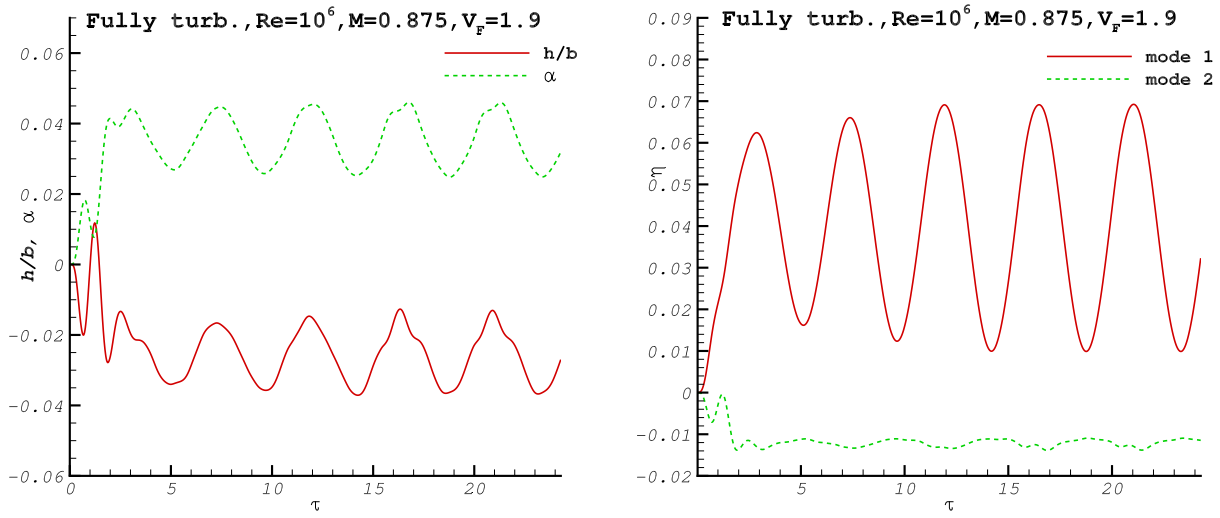

(a) (b)

Figure 3.17: Effect of Reynolds number on the existence of multiple equilibrium points. Heaving and pitching (a), and modal coordinates (b) for $Re = 10^6$, $M_\infty = 0.875$, $V_F = 1.9$.

the first mode.

Chapter 4

Conclusions Part I

The phenomenon of multiple-equilibrium-points in fully-turbulent flow for transonic flutter has been explored using the NACA64A010 airfoil and Isogai's structural model. The initial equilibrium point $\alpha_1 = 0, h_1/b = 0$ is unstable, and a new equilibrium point $\alpha_2, h_2/b$ is created. The heaving and pitching coordinates move into the new equilibrium point, oscillating around it. For some speed index values, the new equilibrium point is found stable, and for other V_F values the oscillations grow in magnitude until reaching LCO centered on the new equilibrium point. The region of multiple equilibrium points is centered on $M_\infty = 0.875$ creating a closed pocket in a V_F vs. M_∞ plot. Although the full range of M_∞ is explored for $Re = 10^7$, only a few M_∞ are simulated for $Re = 10^6$ to show that this phenomenon also exists for a range of Reynolds numbers.

At the beginning of the current Part, the Computational Fluid Dynamics code is presented and validated. The Computational Structural Dynamics code is also described and is used to compute the inviscid flutter-boundary for the NACA64A010 airfoil using the Isogai structural model. The inviscid flutter-boundary does not reveal the multiple-equilibrium-points phenomenon. However it reveals the existence of multiple flutter points for a fixed M_∞.

Increasing V_F, the dynamic response switches from stable to unstable at the first flutter-point, from unstable to stable at a higher V_F value, and from stable to unstable again at the second flutter-point. While the instability of the dynamic system at the first flutter-point is caused by the first mode, the second flutter-point is dominated by the instability of the second mode, and reacts at a much higher frequency than the frequency response of the first flutter-point.

Part II

Free laminar-turbulent transition prediction

Chapter 5

Free transition prediction model

The theory behind laminar-turbulent transition is still a topic of research nowadays. Although there is a common agreement on the multiple paths leading to transition, the mechanisms are so complicated that laminar-turbulent transition is still not only difficult to understand but more so to predict.

Some well known transition mechanisms found in airplane wings are Tollmien-Schlichting waves, crossflow instabilities, bypass transition and attachment line instabilities.

The two-dimensional small perturbations generated as laminar flow instabilities traveling in the streamwise direction are referred to as Tollmien-Schlichting waves. The growth of TS waves develops in three-dimensional perturbations, leading to the formation of turbulent spots and finally when those spots merge, leading to a fully turbulent flow.

Attachment line transition takes place in sweptback wings when perturbations from the wing-body junction or others generated in upper swept region travel through the leading edge triggering transition. Our simulations do not account for attachment line transition since they are two-dimensional. Attachment line transition increases with the swept angle,

and with the thickness of the leading edge radius. Therefore, our results are still valid for wings with low swept back angle.

Crossflow instabilities are only present in three-dimensional wings, and therefore not included in the present two-dimensional study. This type of instabilities is more common than attachment line transition for traditional wings, and should be included when studying three-dimensional transition prediction. Crossflow instabilities are perturbations travelling in the spanwise direction of a wing. The initial two-dimensional Tollmien-Schilchting waves start to show spanwise differences which triggers a three-dimensional wave mechanism increasing in energy until non-linear effects start coalescing those waves into three-dimensional vortical structures. Crossflow instabilities are not dominant unless the wing has a considerable swept angle. Therefore, our two-dimensional simulations are still valid for low-swept back wings where TS waves are the main instability factor.

Bypass transition is a non-linear transition mechanism by which the linear growth of TS waves is bypassed and a sudden transition occurs. Bypass transition is normally caused by surface roughness or tripping bands which produce a sudden perturbation triggering laminar-turbulent transition. This type of transition mechanism is hard to predict, and it is not accounted for in our simulations, which assume a smooth surface free of irregularities.

Due to the infinitesimal initial nature of TS waves, it is appropriate to use a linearized version of the Navier-Stokes equations to study the stability of the boundary layer. The Orr-Sommerfeld equation is a complicated derivation obtained from linearly perturbing the Navier-Stokes equations. It is traditionally used to determine the stability of a viscous flow given a velocity profile as input, by doing an eigenvalue analysis. Using velocity profiles for different wedge geometries from the Falkner-Skan solutions as inputs to the Orr-Sommerfeld equation, a data base of stability is generated for multiple realistic boundary layer profiles. Drela [23] uses this data base to create a free transition model based on the linear growth of unstable Tollmien-Schlichting waves, as the main mechanism to generate laminar-turbulence

transition. Traditionally, it was found transition to take place when the most unstable TS wave had amplified by a factor of $e^9 \approx 8100$ which lead to the creation of the so-called e^N method or e^9 method.

The chosen method to predict free transition is the e^N model which requires integral boundary layer variables as inputs: boundary layer momentum thickness θ, and boundary layer shape factor $H = \delta^*/\theta$. An integral boundary layer code is added to ParCAE to produce high quality results of the needed integral variables without the need of using an extremely fine grid in the boundary layer region.

5.1 Integral boundary layer method

Integral boundary layer codes use information at the edge of the boundary layer to solve a set of parabolic equations marching in the flow direction, to determine the evolution of integral quantities. Therefore, the flow quantities at the edge of the boundary layer must be known a priori. The main variable is the velocity at the edge of the boundary layer. Obtaining it is not a trivial process. When both, the boundary layer thickness and edge velocity are unknown the classic definition of the boundary layer thickness being that at which the flow velocity is 99% of the edge velocity is of no use in a numerical computation.

Some authors successfully solved this problem by using laminar and turbulent boundary layer thickness correlations [76], [77] . A different approach [48], [60] to finding the edge velocity, which is adopted in this research, makes use of Bernoulli equation for compressible flows along with ideal gas and isentropic relations to obtain

$$U_e(i) = \sqrt{U_\infty^2 - \frac{2\gamma}{\gamma - 1}\frac{p_\infty}{\rho_\infty}\left[\frac{p_e(i)}{\rho_\infty}^{\frac{\gamma-1}{\gamma}} - 1\right]} \tag{5.1}$$

Using the boundary layer approximation of zero pressure gradient normal to the wall, one can replace p_e by p_w in the previous equation. This results in a simple equation which only requires wall values in order to find the edge velocity.

The previous methods are valid for steady conditions only. While much effort has been invested to adapt these methods to unsteady simulations, nothing has proved as successful as still using Equation (5.1) for small Strouhal numbers where the error is therefore small. For the present flutter study, the reduced frequency at LCO is $k = 0.1 - 0.2$ and the heaving amplitude is $h_0/c = 0.1 - 0.2$ which correspond to $St = k(h_o/c)/\pi \sim 10^{-2}$.

Furthermore, the previous relation must be used before a shock wave occurred so the isentropic condition is not violated. This condition is satisfied since laminar-turbulent transition always takes place before or at the shock position (given the flow conditions simulated in this dissertation). If transition did not occur prior to the shock, the strong adverse pressure gradient of the shock quickly triggers boundary layer transition.

To compute the integral boundary layer parameters (δ^* and θ) needed for the transition model, Nebel et al. [60] use a high quality grid to obtain an accurate velocity profile at the laminar boundary layer region. The integral parameters are directly obtained from the RANS computations using their definition. The displacement thickness is

$$\delta^*(i) = \int_0^\delta \left(1 - \frac{\rho(i,j)U(i,j)}{\rho_e(i)U_e(i)}\right) d\eta \tag{5.2}$$

and the momentum thickness

$$\theta(i) = \int_0^\delta \frac{\rho(i,j)U(i,j)}{\rho_e(i)U_e(i)} \left(1 - \frac{U(i,j)}{U_e(i)}\right) d\eta \tag{5.3}$$

The shape factor is a ratio of the previous, $H = \delta^*/\theta$.

Instead of using a high density grid in the wall region, Drela [22] uses a compressible integral boundary layer formulation which ensures high quality results of the integral variables assuming one has a correct boundary layer edge velocity. The latter approach is adopted in our current work solving two coupled ordinary differential equations

$$\frac{d\theta}{d\xi} + (2 + H - M_e^2)\frac{\theta}{U_e}\frac{dU_e}{d\xi} = \frac{C_f}{2} \tag{5.4}$$

$$\theta\frac{dH^*}{d\xi} + [2H^{**} + H^*(1 - H)]\frac{\theta}{U_e}\frac{dU_e}{d\xi} = 2C_D - H^*\frac{C_f}{2} \tag{5.5}$$

where ξ is the local coordinate parallel to the wall. To close the integral boundary layer equations, the following correlations detailed in Reference 23 are needed

$$H^* = H^*(H_k, M_e, Re_\theta) \quad H^{**} = H^{**}(H_k, M_e) \tag{5.6}$$

$$C_f = C_f(H_k, M_e, Re_\theta) \quad C_D = C_D(H_k, M_e, Re_\theta) \tag{5.7}$$

Equations (5.4) and (5.5) are solved with a Newton-Raphson method, similar to the one proposed by Johansen [42] although modified for the compressible version of the integral boundary layer equations. Rewriting Equations 5.4 and 5.5 as

$$f_1 = \frac{d\theta}{d\xi} + (2 + H - M_e^2)\frac{\theta}{U_e}\frac{dU_e}{d\xi} - \frac{C_f}{2} \tag{5.8}$$

$$f_2 = \theta\frac{dH^*}{d\xi} + [2H^{**} + H^*(1 - H)]\frac{\theta}{U_e}\frac{dU_e}{d\xi} - 2C_D + H^*\frac{C_f}{2} \tag{5.9}$$

the solution is obtained by an iterative process when both $f_1 = 0$ and $f_2 = 0$. The Newton-Raphson method computes the corrections in θ_i and H_i as (where station $(i-1)$ is known, and (i) increases in the streamwise direction)

$$\begin{bmatrix} \frac{df_1}{d\theta_i} & \frac{df_1}{dH_i} \\ \frac{df_2}{d\theta_i} & \frac{df_2}{dH_i} \end{bmatrix} \times \begin{bmatrix} \delta\theta_i \\ \delta H_i \end{bmatrix} = - \begin{bmatrix} f_1 \\ f_2 \end{bmatrix} \tag{5.10}$$

where δ are corrections, which are under-relaxed to enhance numerical convergence.

Johansen [42] presents a direct and an inverse solution procedure, using the inverse solution when separation occurs before transition, and using the direct solution around a stagnation point. The direct method solves the IBL equations as they are indicated. The inverse method uses the skin friction from the RANS code instead of using the skin friction correlation provided in the IBL code (Equation 5.7).

A first approach of using the direct method for the entire laminar range is coded. The second coded approach follows the steps of Johansen, using the direct method until the flow approaches separation, at which point the inverse method is used. The two approaches produce almost identical transition prediction results. While both methods are tested in the validation section of the present work, only the fully direct method is used for flutter computations. In the direct approach, if separation takes place, transition is imposed where the flow separated. While laminar separation can occur, for high Reynolds number flows the distance between the laminar separation point and the transition point is very small. Therefore the error associated with the direct method is small and using the direct method is the fastest approach to convergence. If instead, the inverse method is chosen, since it uses the skin friction from the RANS code instead of using the skin friction correlation defined in Equation 5.7, a better matching between the CFD and the Integral Boundary Layer code is obtained at a higher cost due to the numerical oscillations while converging. The CFD

edge velocity, which is used in the skin friction correlation, converges much faster than the RANS skin friction value, which justifies the cheaper cost in using the direct approach over the inverse method.

5.2 Transition models

Drela's e^N model [23] is implemented along with Sturdza's model [78] showing very similar results. Sturdza's model is designed for supersonic flows even though it was used by Lee and Jameson [48] for transonic two-dimensional and three-dimensional wings with excellent performance. The results shown in the present work make use of Sturdza's model which introduces a temperature ratio T_w/T_e into the original Drela model to account for compressibility effects of boundary layers.

The location of the initial instability takes place when

$$log_{10}\left(\frac{Re_{\theta_0}}{K_0}\right) \geq \left(\frac{1.415}{H_k - 1} - 0.489\right) tanh\left(\frac{20}{H_k - 1} - 12.9\right) + \frac{3.295}{H_k - 1} + 0.44 \tag{5.11}$$

$$K_0 = \frac{2}{\pi} tan^{-1}\left(10\frac{T_w}{T_e} - 10\right) + 1 \tag{5.12}$$

Before the previous condition is satisfied, any instability created in the real flow (not the RANS solution) are damped out. Therefore the N-factor is zero before the location of θ_0 and H_0. After this point, a set of Tollmien-Schilchting waves are created which grow in the streamwise direction with different amplification factors for each wave frequency. The following N-factor correlation model tracks the growth of the most unstable Tollmien-Schlichting wave, computing the linear amplification rate. Traditionally the amplification determining

transition was 8100, giving name to the e^9 method although smaller N_{crit} values proved more accurate for the present simulated conditions. The N_{crit} value has been correlated with free stream turbulence intensity and values ranging from $N_{crit} = 4-12$ have been used in multiple research articles depending on the free stream turbulence conditions.

The slope of the N-factor envelope is

$$\frac{dN}{Re_\theta} = \frac{0.01}{K_b}\big(2.4H_kK_a - 3.7 + 2.5K_c tanh[1.5(H_k - 3.1)] + 0.125 + K_d - K_m\big) \tag{5.13}$$

$$K_a = 1 + 0.2(H_k - 2.5918)\left(1 - \frac{T_e}{T_w}\right) \tag{5.14}$$

$$K_b = 4.7\left(\frac{T_w}{T_e} - 1\right) + 1\,, \qquad K_c = \frac{T_w}{T_e}\,, \qquad K_d = 1.2\left(\frac{T_w}{T_e} - 1\right)^{3/2} \tag{5.15}$$

After Equation 5.11 is satisfied, N starts growing by integrating Equation 5.13 until $N = N_{crit}$ where transition takes place.

The transition position information must be transferred from the Integral Boundary Layer code to the CFD code in a smooth manner and accounting for a real transition length. An intermittency function γ_{tr} created by Cebecci [15] is implemented. Eddy viscosity is set to zero before x_{tr}, and it is multiplied by γ_{tr} when $x > x_{tr}$. The intermittency function has a value of zero when $x = x_{tr}$, and grows until the end of the transition length reaching a value of one. The intermittency is a measure of the turbulent content. The flow is intermittently turbulent, with regions of laminar flow.

$$\gamma_{tr} = 1 - exp\bigg[-G(x - x_{tr})\int_{x_{tr}}^{x}\frac{dx}{U_e}\bigg] \tag{5.16}$$

where

$$G = \frac{3U_e^3 Re_{x_{tr}}^{-1.34}}{C^2\nu^2}\,, \qquad C^2 = 213(logRe_{x_{tr}} - 4.7323) \tag{5.17}$$

Cebecci [15] presents a correlation between the Reynolds number based on the transition length (γ_{tr} ranging from 0 to 1) $Re_{\Delta x}$, and the Reynolds number based on the transition position $Re_{x_{tr}}$

$$Re_{\Delta x} = C\, Re_{x_{tr}}^{2/3} \tag{5.18}$$

which indicates that the transition length increases when delaying the transition position.

$x_{tr,UP}$			$x_{tr,DOWN}$		
RANS	XFOIL	exp	RANS	XFOIL	exp
0.368	0.37	0.35	0.60	0.63	0.6

Table 5.1: NLF(1)-0416 transition positions with $N_{crit} = 7$

5.3 Validation of free transition model

The transition model is validated in the present Section using some classic benchmarks for steady conditions (Section 5.3.1) comparing our simulations with experimental data, and with the well-known code XFOIL [22]. XFOIL is an extremely fast code, used in subsonic conditions, that accounts for laminar-turbulent transition.

In Section 5.3.2, the transition model is used in a forced pitching motion with the NACA0012 airfoil, where free-transition results produce a better matching with the experimental data than fully turbulent conditions do.

5.3.1 Free transition steady code validation with NLF(1)-0416 and NACA0012

A transition prediction comparison with experimental data [70] and the code XFOIL for the NLF(1)-0416 airfoil is summarized in Table 5.1. Three grid levels are tested to obtain grid-independent results where each coarse level is obtained by reducing in half the number of cells in each direction. The coarse grid is presented in Figure 5.1 and the pressure coefficient contours are shown in Figure 5.2 for the test condition $Re = 4{\times}10^6$, $M_\infty = 0.3$ and $\alpha = 2.03°$. The results shown using the inverse method in Table 5.1 are obtained for the fine grid level of 944×256 cells and $N_{crit} = 7$. Using larger values of N_{crit} resulted in delayed transition positions compared to the experimental data.

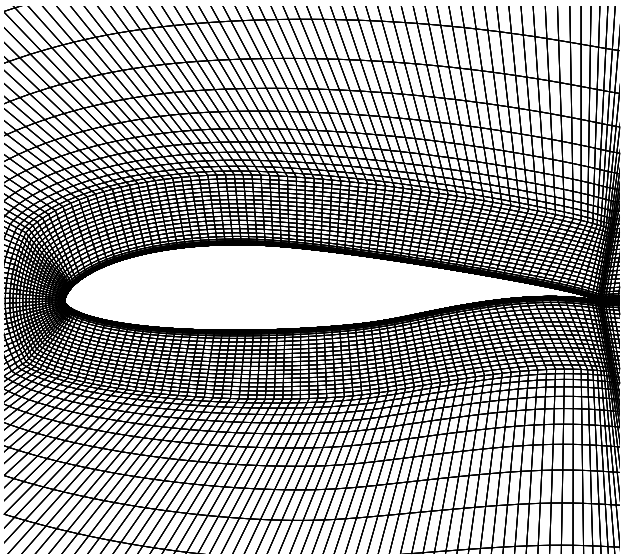

Figure 5.1: Coarse grid for the NLF(1)-0416 airfoil. Grid size of 236 × 64.

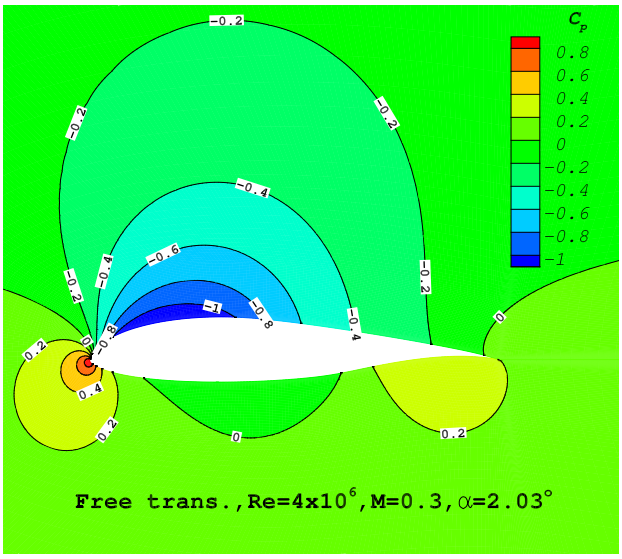

Figure 5.2: Coarse flow field solution of pressure distribution for NLF(1)-0416 airfoil at test conditions.

Figure 5.3 illustrates the effect of the intermittency function described in Equation (5.18) to guarantee a smooth change of eddy viscosity when transition takes place at the top surface of the NLF(1)-0416 airfoil. Before transition, eddy viscosity is set to zero. After the transition point, the intermittency function gradually increments the value of eddy viscosity until it is fully activated when intermittency becomes one. Figure 5.3 shows high values of eddy viscosity inside the turbulent boundary layer region, and zero (or small) values at the wall and outside the boundary layer region.

Figure 5.4 compares pressure distribution, skin friction, shape factor and momentum thickness against the code XFOIL. A very good agreement is observed in all plots. The pressure distribution shows a kink at the top and bottom transition positions due to the sudden growth in the boundary layer thickness. The shape factor peak is slightly ahead of the one obtained with XFOIL. This is due to the difference in the predicted transition position, which can be corrected by slightly increasing N_{crit}, and due to the higher diffusion present in the RANS code where a parabolic boundary layer method is not employed.

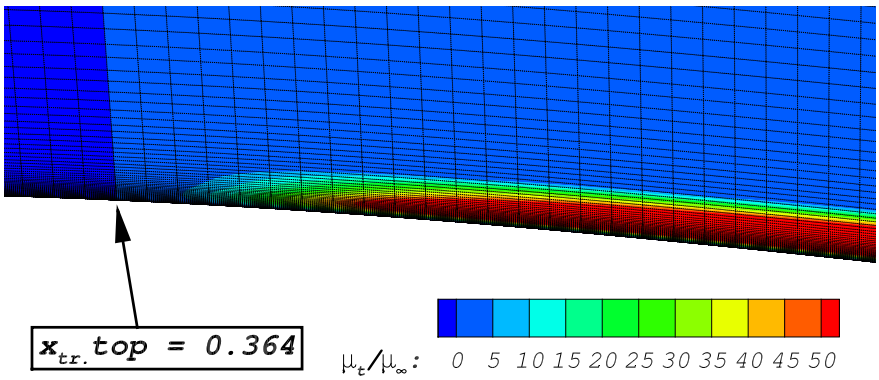

Figure 5.3: Eddy viscosity after transition smoothly increasing due to the intermittency function.

	$x_{tr,UP}$			$x_{tr,DOWN}$		
α	RANS	XFOIL	exp	RANS	XFOIL	exp
0	0.516	0.515	0.44	0.516	0.515	0.44
2	0.328	0.321	0.25	0.703	0.705	0.62
4	0.153	0.145	0.11	0.865	0.873	0.72
6	0.034	0.055	0.048	0.930	0.970	0.81
8	0.019	0.027	0.022	0.965	0.996	0.90

Table 5.2: NACA 0012 transition positions with $N_{crit} = 9$

The present code is also tested against experimental results [29] and the code XFOIL for the NACA 0012 airfoil at multiple angles of attack and using the direct method. The NACA0012 results shown in the present Section will be further explored in Section 6.1. This Section shows the effect of changing N_{crit} and the validity of using the direct method for transition prediction.

Table 5.2 shows the comparison in transition position prediction when $N_{crit} = 9$ is used in our implementation and in XFOIL. Both predictions are delayed when compared to the experimental results. The simulations are rerun with $N_{crit} = 7$ showing a much better agreement with the experimental results (Table 5.3). The experimental conditions of $Re = 2.88 \times 10^6$ and $M_\infty = 0.16$ are simulated. Grids with multiple resolutions are tested generating similar transition positions. The transition prediction results shown in the tables are for the fine C-grid level of 928×240 cells.

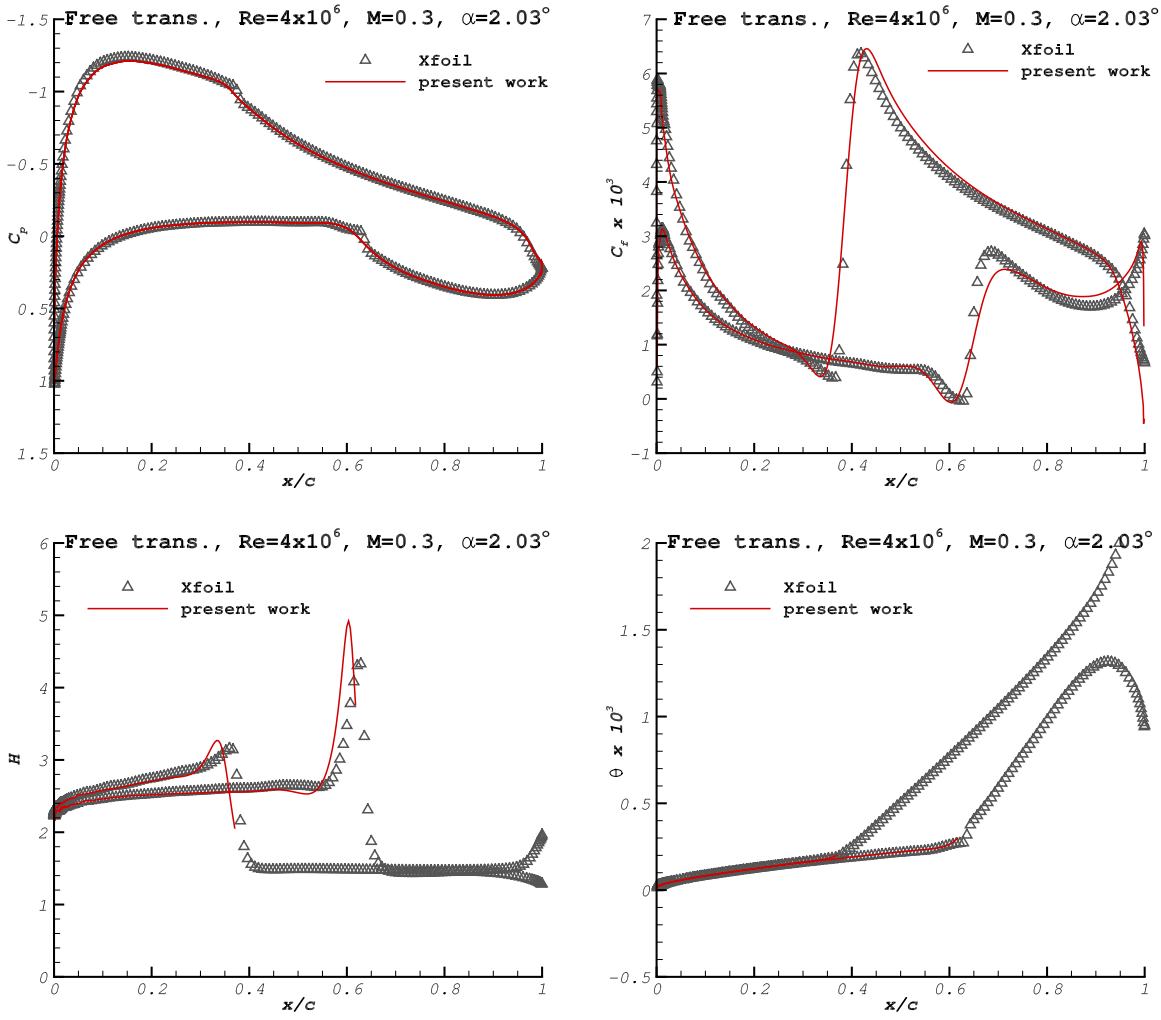

Figure 5.4: Free transition simulation of NLF(1)-0416 airfoil at $Re = 4 \times 10^6$, $M_\infty = 0.3$ and $\alpha = 2.03°$. Results of pressure distribution (a), skin friction (b), shape factor (c) and momentum thickness (d). Comparison with numerical results from XFOIL.

	$x_{tr,UP}$			$x_{tr,DOWN}$		
α	RANS	XFOIL	exp	RANS	XFOIL	exp
0	0.454	0.453	0.44	0.454	0.453	0.44
2	0.274	0.270	0.25	0.63	0.634	0.62
4	0.122	0.117	0.11	0.806	0.811	0.72
6	0.031	0.047	0.048	0.920	0.941	0.81
8	0.015	0.025	0.022	0.958	0.993	0.90

Table 5.3: NACA 0012 transition positions with $N_{crit} = 7$

The pressure distribution, skin friction, shape factor and momentum thickness of the present solution at $\alpha = 2.0°$ are compared with those by XFOIL, showing a very good agreement. The comparison in Figure 5.5 reveals again the pressure kink in the pressure distribution at the transition position, although for this case it is smoother than for the NLF(1)-0416 airfoil. A small difference is observed at the transition position in the shape factor results. That rise of shape factor is related to the small dip in skin friction close to the transition position.

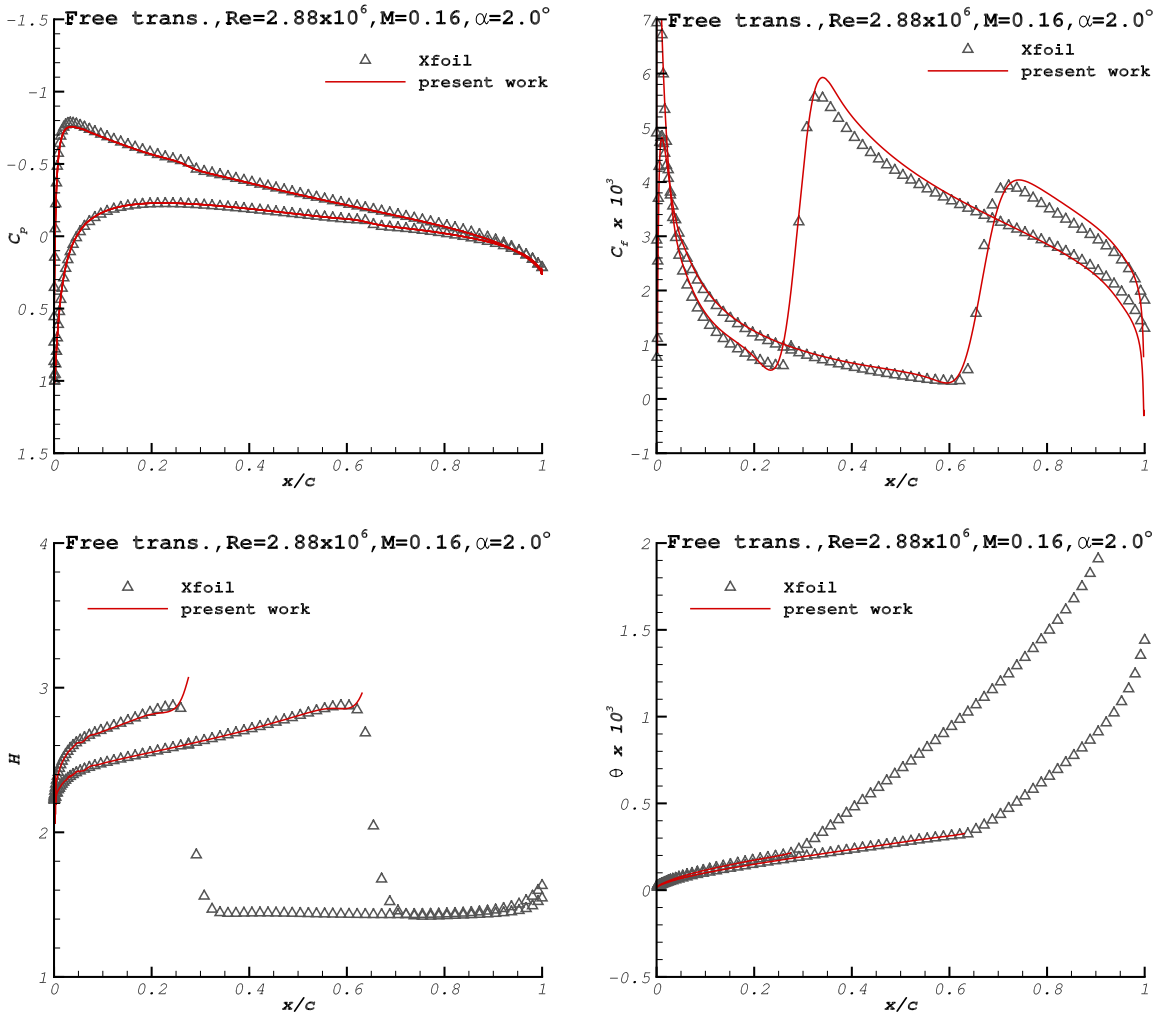

Figure 5.5: Free transition simulation of NACA 0012 airfoil at $Re = 2.88 \times 10^6$, $M_\infty = 0.16$ and $\alpha = 2.0°$. Results of pressure distribution (a), skin friction (b), shape factor (c) and momentum thickness (d). Comparison with numerical results from XFOIL.

5.3.2 Free transition unsteady code validation with NACA 0012 forced pitching

Although the transition position was not measured in the experiment [45] , a trip point was not used to force transition either. The results in this section show an improvement in lift and moment coefficients when accounting for free transition instead of using a fully turbulent approach.

A forced pitching motion for the NACA 0012 airfoil around the quarter chord point is imposed

$$\alpha(t) = \alpha_m + \alpha_0 \, sin(\omega \, t) \tag{5.19}$$

or using the reduced frequency, the previous equation becomes

$$\alpha(t) = \alpha_m + \alpha_0 \, sin\Big(\frac{2 \, U_\infty \, \kappa \, t}{c}\Big) \tag{5.20}$$

Case 5 of Reference 45 is simulated with $M_\infty = 0.755$, $Re = 5.5 \times 10^6$, $\alpha_m = 0.016°$, $\alpha_0 = 2.51°$, $\kappa = 0.0814$. The initial condition for the unsteady run was a converged steady state with $\alpha = \alpha_m$. After two or three periods, the solution achieved periodicity. However, five periods were simulated with 100 time steps per period.

A comparison of inviscid, fully turbulent and free transition results against the experimental data is shown in Figure 5.6. The Euler mesh has 192×56 cells while the RANS grids have 464×120 with an estimated $y+ = 0.16$ at the wall. Similar lift results are obtained for all the simulations. However, disagreement in moment coefficient reveals differences in the pressure distribution throughout the oscillating motion. The bottom images of Figure 5.6

show the pressure distribution at 1/4 and 1/2 of the period. The shock wave position of the free transition case agrees better with the inviscid solution, while the fully turbulent shock is ahead. This justifies the improvement in moment coefficient when changing from fully turbulent to free transition conditions. The inviscid moment coefficient, however, still produces the best match with the experimental results. Since neither transition position, nor free-stream turbulence intensity were measured in the experimental setup, it is difficult to estimate a value for N_{crit} to use in the transition model. A value of $N_{crit} = 7$ was used to be consistent with the results from Section 5.3.1. However, changing the value of N_{crit} would affect the transition position, which would change the shock position. An improvement in the matching between experimental and free-transition simulations could be obtained by exploring multiple values of N_{crit}. The present Euler results are similar to those obtained in Reference [27] and [64] and the fully turbulent solution is similar to Reference 63. The kink in moment coefficient close to $\alpha = -2^{\circ}, 2^{\circ}$ is captured in all the numerical simulations, being smoother in the fully turbulent case.

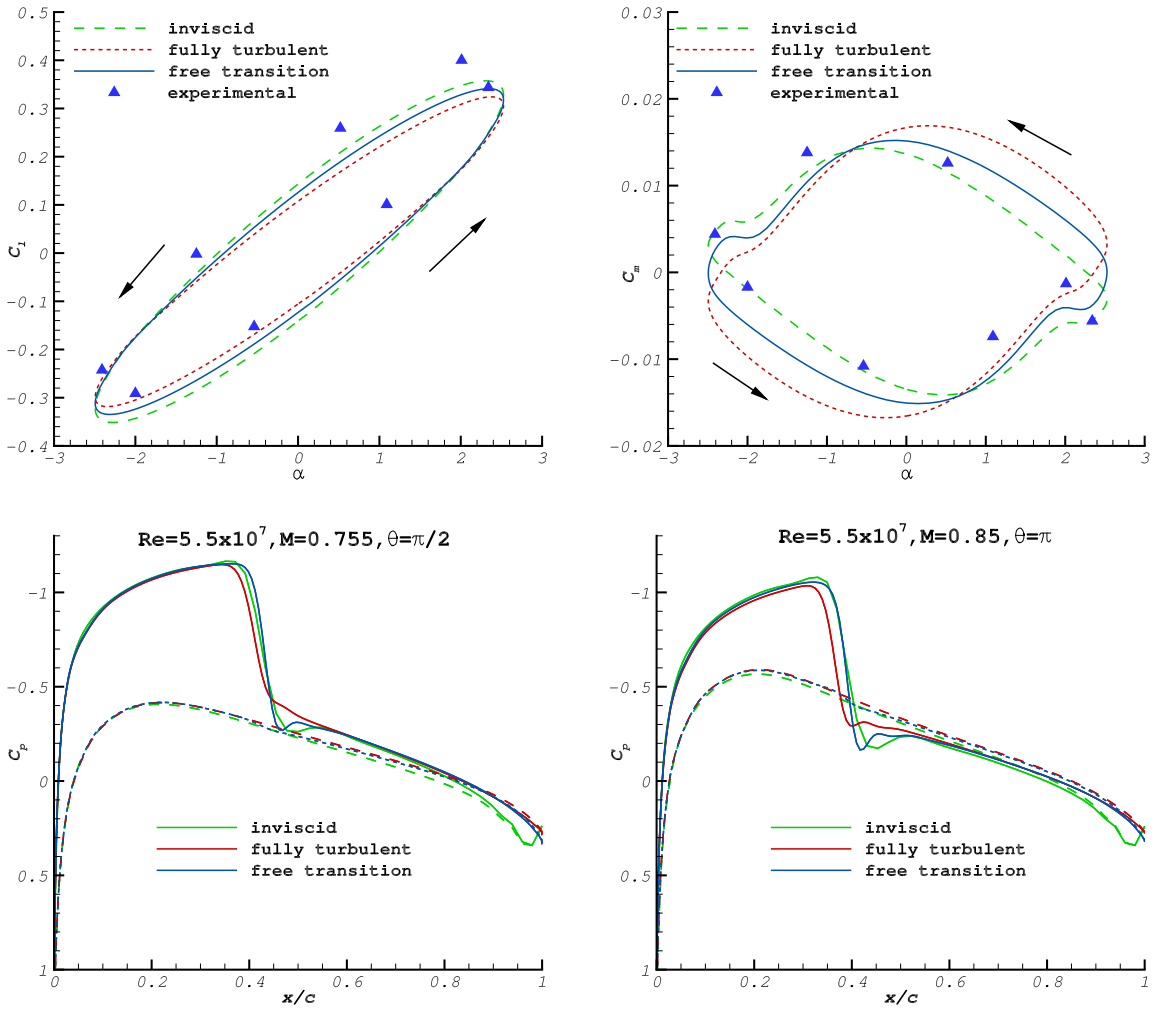

Figure 5.6: Pitching of NACA 0012 airfoil at $Re = 5.5 \times 10^7$ and $M_\infty = 0.755$ around $x/c = 0.25$, 0.016° of angle of attack, amplitude of 2.51°, and reduced frequency $k = 0.0814$. Comparison of inviscid, fully turbulent, free transition and experimental results of lift (a) and moment (b) coefficients; pressure distribution at $T/4$ (c) and at $T/2$ (d).

Chapter 6

Free transition effect on subsonic and transonic conditions

ParCAE has been validated for fully turbulent and free transition conditions. The $N_{crit} = 7$ value has proved to provide the best matching with the available experimental results. Although some solutions for the NACA0012 airfoil at subsonic conditions where shown in the previous validation Chapter (Section 5.3.1), those were limited to studying the effect of N_{crit} value, and to show the correct solution is obtained when using the fully direct method for transition prediction, described in Section 5.1. The present Chapter performs a full comparison of free transition, fully turbulent and inviscid results for subsonic and transonic conditions of three airfoils with different aerodynamic characteristics to understand the effects of laminar-turbulent transition. Some free-transition experimental results are available for each of the simulated airfoils, and those are also included as a validation benchmark.

6.1 NACA0012

Figure 6.1 shows the coarse level grid used for the NACA0012 simulations. The complete C-grid as well as a zoom in on the airfoil are displayed.

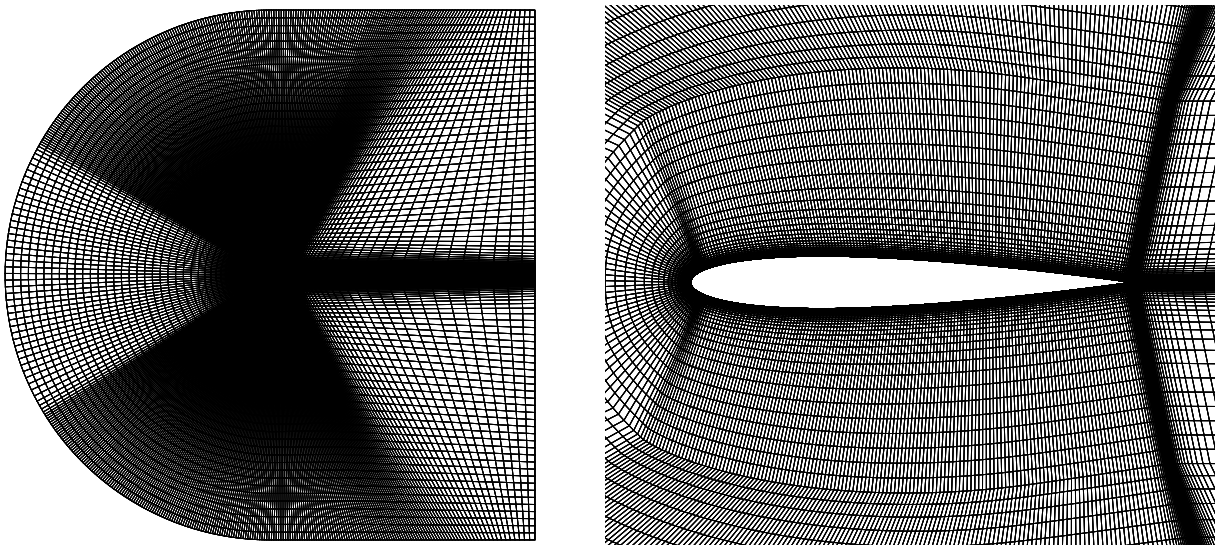

(a) (b)

Figure 6.1: Coarse mesh (464 X 120) for airfoil NACA0012. (a) Complete C-mesh topology, (b) zoomin of airfoil mesh.

6.1.1 Free-stream conditions: $Re = 2.88 \times 10^6$, $M_\infty = 0.16$. Effect of transition on subsonic conditions of a subsonic airfoil, and validation for $\alpha = 0.0^\circ, 2.0^\circ, 4.0^\circ$.

A grid independence study to validate the implementation of transition prediction reveals good agreement in the pressure distribution along the wall for fine, medium, and coarse grids. Figure 6.2 shows a small kink at transition positions of $x_{tr}top = 0.36$ and $x_{tr}bottom = 0.54$ due to the sudden growth of the boundary layer when transitioning from laminar to a turbulent state. A zoom in on the pressure at the leading edge reveals a minor deviation

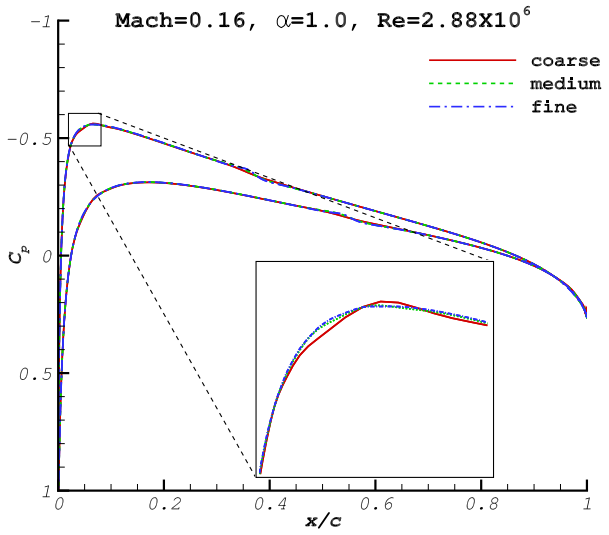

Figure 6.2: Grid independence study of NACA0012 for free transition conditions.

for the coarse grid level. The transition prediction for the three grids is shown in Table 6.1 showing a good agreement and a converging trend as the grid is refined.

	Fine	Medium	Coarse
$x_{tr}top$	0.365	0.364	0.359
$x_{tr}bottom$	0.541	0.542	0.537

Table 6.1: Transition position prediction for NACA0012 at $M_\infty = 0.16$, $Re = 2.88 \times 10^6$, $\alpha = 1.0°$ for three grid levels.

For the following computations, the medium grid level is used although the error by using the coarse grid would be small as revealed in the grid independence study section.

Transition prediction for the NACA0012 is validated against experimental results [29] for subsonic conditions at multiple angles of attack. Figures 6.3(a),(b) show transition position for the top surface and lift coefficient, respectively. The numerical predictions are compared with the experimental results revealing good agreement in transition although the experiment shows an earlier transition at high negative angle of attack values. The difference in transition position could be improved if decreasing the value of N_{crit}. Figure 6.3(b) shows very good agreement in lift vs. angle of attack between free transition, fully turbulent and experimental

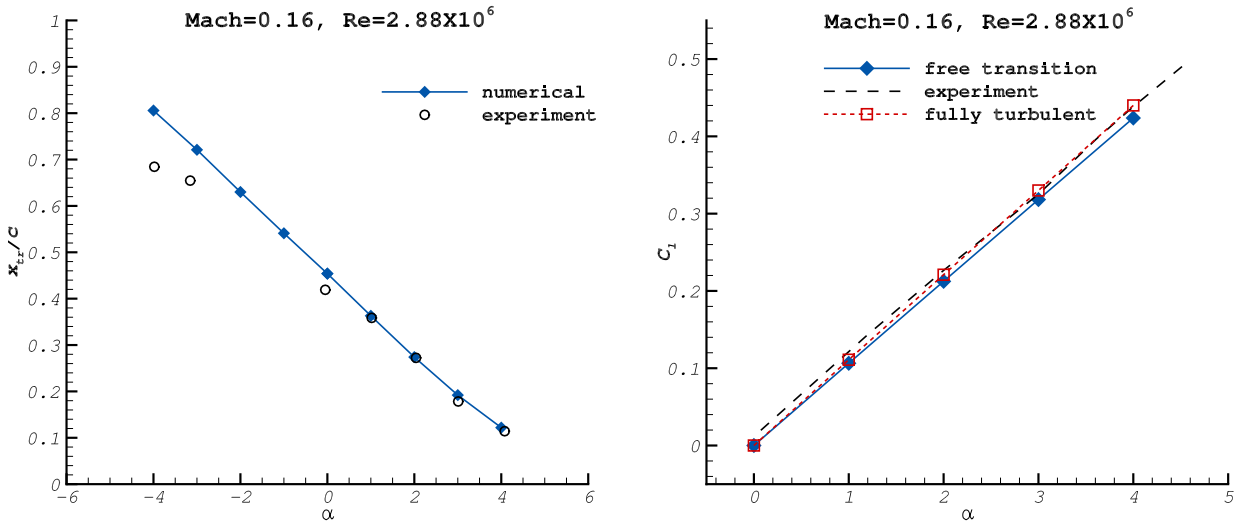

(a) Transition position comparison for multiple angles of attack.

(b) Lift coefficient comparison of computational free transition, computational fully turbulent, and experimental free transition results.

Figure 6.3: Validation of transition prediction for NACA0012 airfoil. (a) Transition position. (b) Lift coefficient.

conditions. For all the simulated airfoils, a very good agreement between free transition and fully turbulent lift is found for subsonic conditions only.

The polar curve is shown in Figure 6.4(a). Since the experimental transition position is slightly earlier than our simulation, the experimental drag is also slightly larger since a smaller portion of the wing is affected by laminar flow. Figure 6.4(b) shows the friction drag and pressure drag components for fully turbulent and free transition conditions. The friction drag is not affected by the change in angle of attack. When increasing the angle of attack, the transition position on the top surface moves forward, but transition on the bottom surface is delayed. This could overall contribute to a similar laminar wet area which justifies the invariance of friction drag for variations in angle of attack. The pressure drag however, shows a small increase with increasing lift.

Figures 6.5 and 6.6 show wall pressure and skin friction for fully turbulent and free transition conditions for $\alpha = 0.0°, 1.0°, 2.0°, 3.0°, 4.0°$. The experimental top surface pressure is also

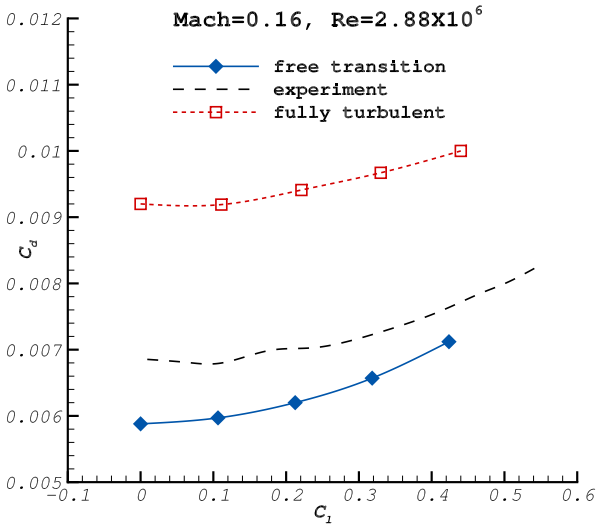

(a) Drag coefficient comparison of computational free transition, computational fully turbulent, and experimental free transition results.

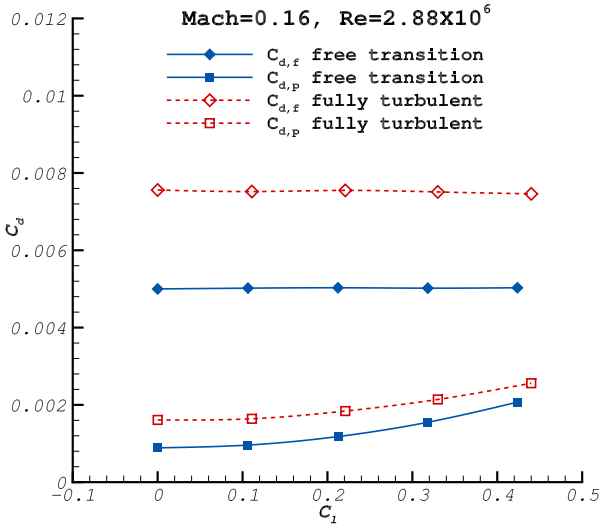

(b) Friction and pressure drag coefficient for free transition and fully turbulent simulations.

Figure 6.4: Validation of transition prediction for NACA0012 airfoil. (a) Drag coefficient. (b) Friction and pressure drag.

plotted for $\alpha = 0.0°, 2.0°, 4.0°$. A very good agreement is found for the wall pressure distribution for free transition, fully turbulent, and experimental conditions. Free transition is not affecting the wall pressure for subsonic free stream conditions. This explains the similar lift coefficient results obtained for both flow conditions in Figure 6.3(a). The free transition skin friction shows significant differences with respect to the fully turbulent friction value. Those differences result in a variation in drag, as confirmed in previous Figures. The free stream skin friction shows a sharp growth when transition takes place since the turbulent wall shear is higher than the laminar wall shear.

The transition position is linearly correlated with the lift coefficient, and displayed in Figure 6.6(b).

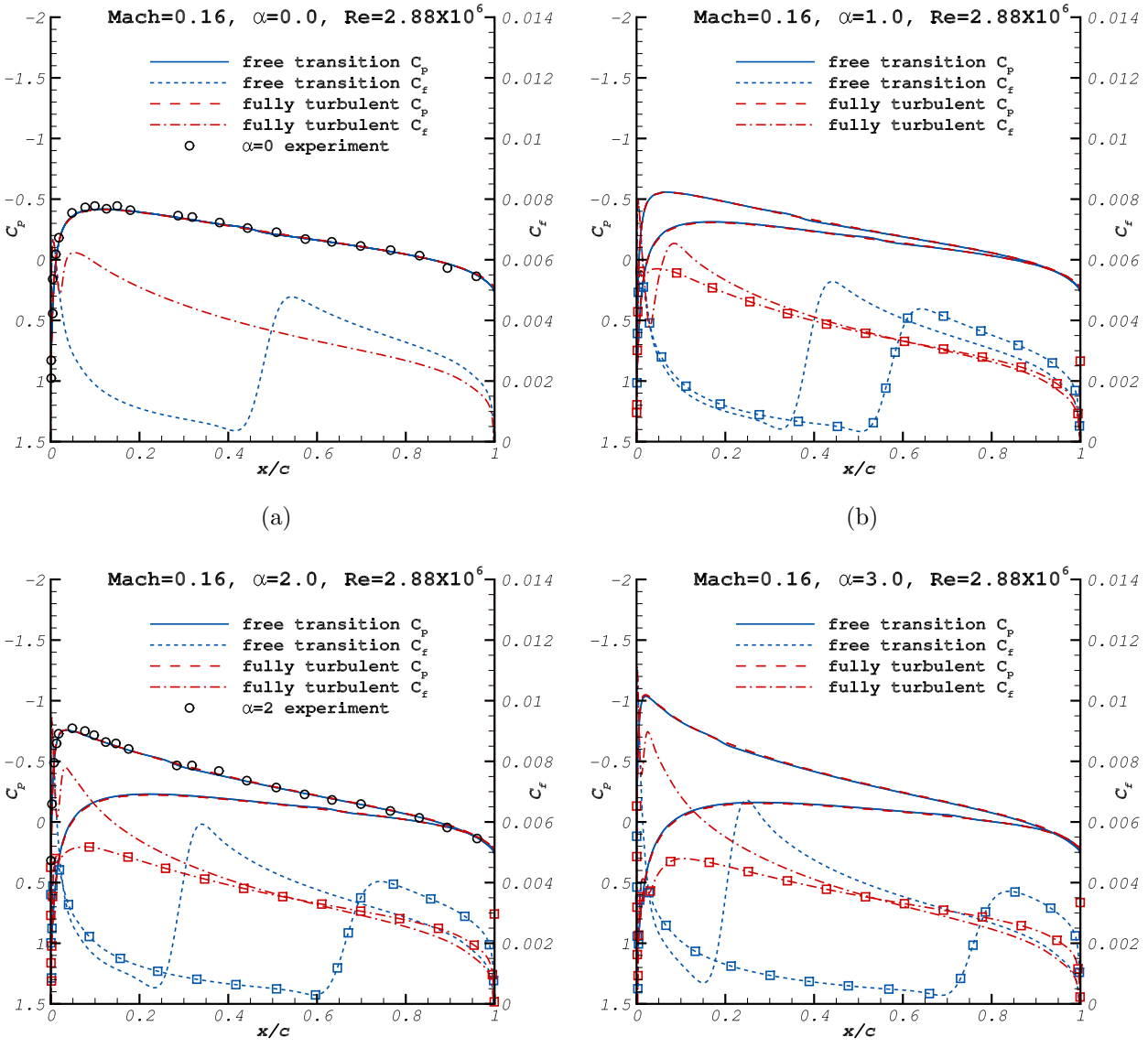

(a) (b)

(c) (d)

Figure 6.5: Pressure coefficient and skin friction comparison for free transition and fully turbulent simulations in the subsonic range of NACA0012 airfoil. Pressure coefficient of experimental results at $\alpha = 0.0°, 2.0°$ are included. The lower surface skin friction is highlighted with square symbols.

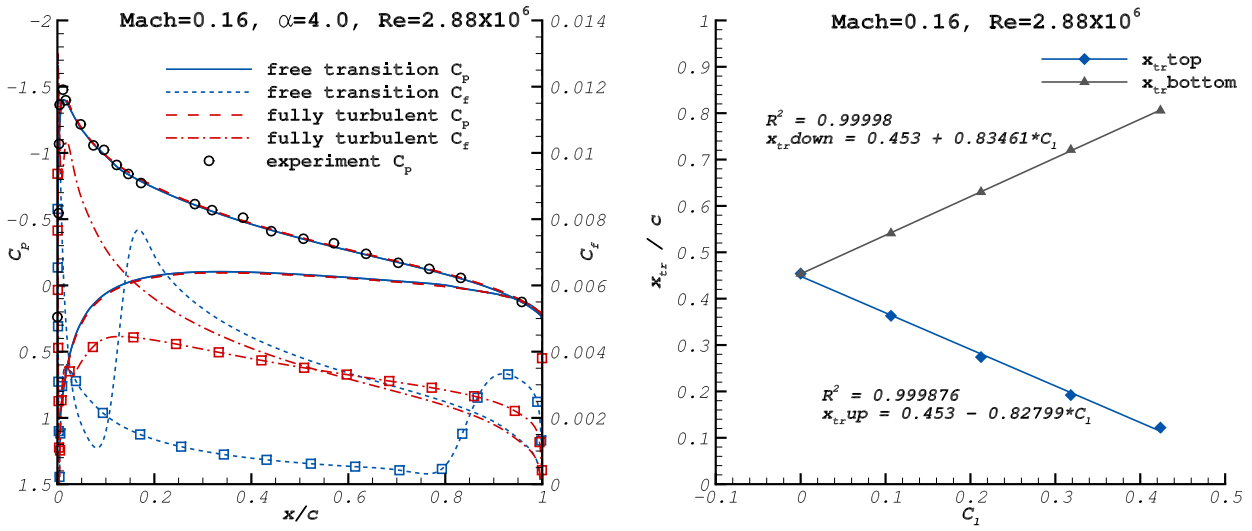

(a) (b)

Figure 6.6: (a) Pressure coefficient comparison for numerical free transition, numerical fully turbulent and experimental free transition conditions in the subsonic range of NACA0012 airfoil. Skin friction comparison of numerical simulations is included with square symbols for the lower airfoil surface. (b) Summary of transition prediction position dependance on lift coefficient for subsonic NACA0012 airfoil.

6.1.2 Free-stream conditions: $Re = 5.5 \times 10^6$, $M_\infty = 0.755$. Effect of transition on transonic conditions of a subsonic airfoil.

Figure 6.7 shows wall pressure and skin friction for free transition and fully turbulent conditions at $\alpha = 0.0°, 1.0°, 2.0°, 3.0°$ and transonic conditions. A stronger shock wave appears on the top surface when increasing the angle of attack. The free transition shock is consistently delayed with respect to the fully turbulent shock position. The skin friction reveals completely different trends for fully turbulent and free transition flow. Larger separation regions are obtained with free transition conditions since the flow is more prone to separation due to the smaller wall shear found in laminar boundary layers. When the flow separates due to encountering a shock, it reattaches for all tested angles of attack. The transition position on the top surface takes place close to the shock position due to the favorable pressure gradient helping maintain a laminar flow.

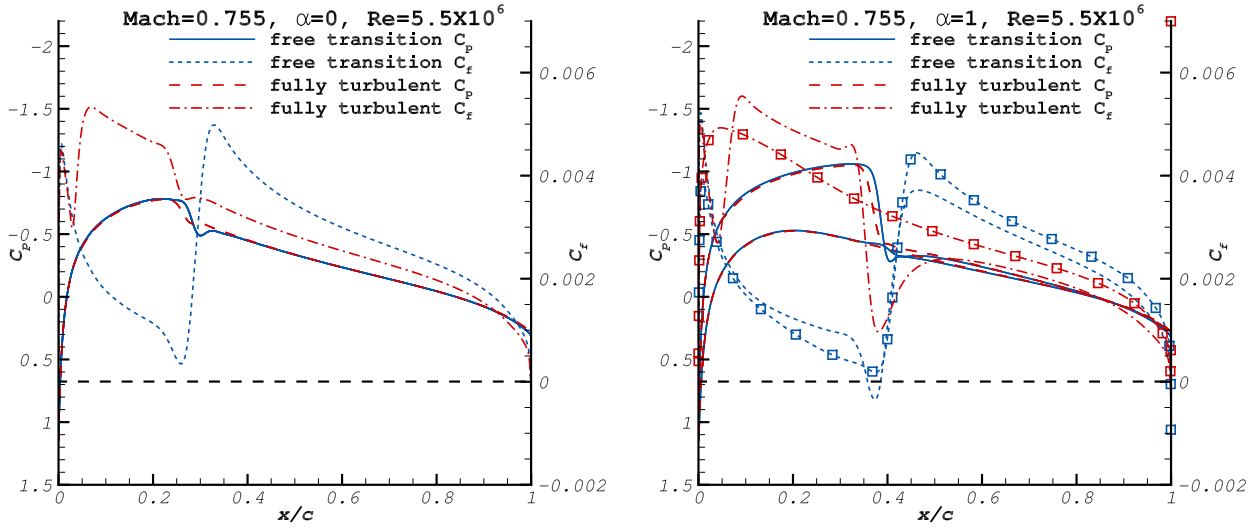

(a)

(b)

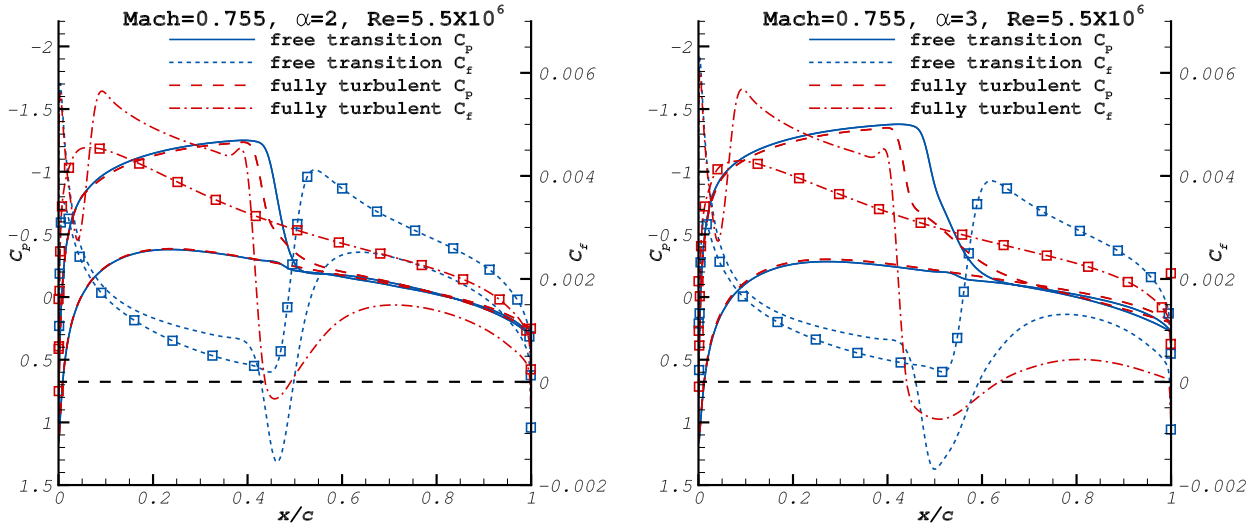

(c)

(d)

Figure 6.7: Pressure coefficient and skin friction comparison for free transition and fully turbulent simulations in the transonic range of NACA0012 airfoil. The lower surface skin friction is highlighted with square symbols.

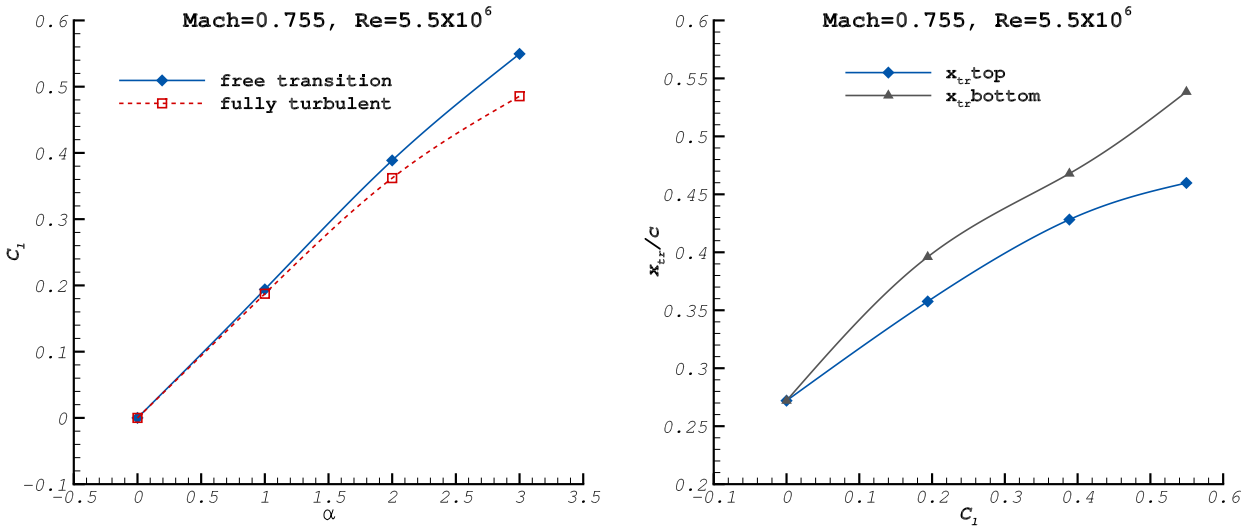

(a) (b)

Figure 6.8: Summary of (a) free transition and fully turbulent comparison of lift coefficient dependence on angle of attack, (b) transition position, for NACA0012 airfoil at transonic conditions.

Figure 6.8(a) shows a deviation of the free transition and the turbulent lift when increasing the angle of attack. This is due to the differences in the top shock wave position shown in Figure 6.7. Figure 6.8(b) shows the transition position moving back as the angle of attack is increased. The bottom transition behaves as it normally does for subsonic conditions. On the top surface however, transition also moves back since the top surface has supersonic flow and the pressure gradient is favorable until the shock wave is found.

Figures 6.9(a) and (b) show the drag variation with lift for free transition and fully turbulent conditions. Although the friction drag is higher than the pressure drag for $\alpha = 0.0°, 1.0°$ since the shock is weak, the pressure drag shows a sharp rise for $\alpha = 3.0°, 4.0°$ when the strength of the shock increases. The friction drag decreases with lift since transition on top and bottom surfaces is delayed when increasing the angle of attack, increasing the laminar shear portion of the wing.

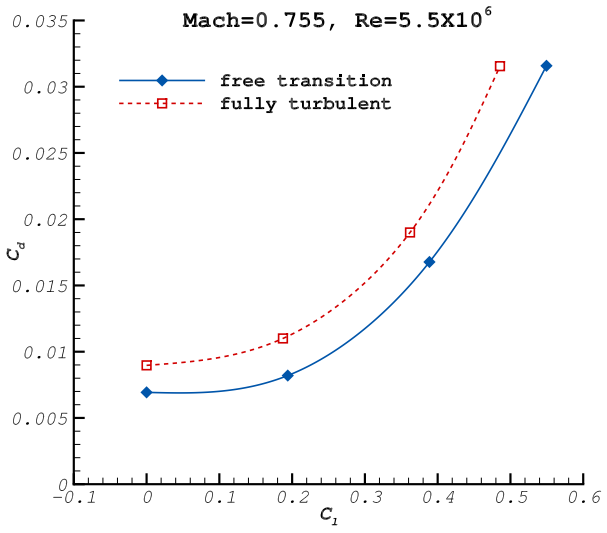

(a)

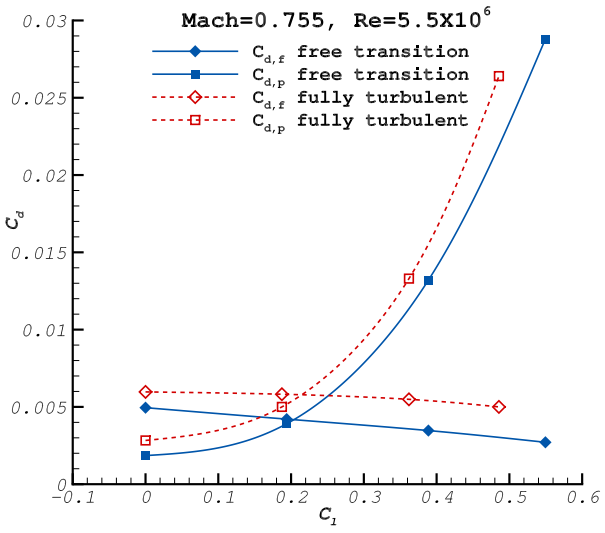

(b) Friction and pressure drag.

Figure 6.9: Polar curves for free transition and fully turbulent results of NACA0012 in transonic conditions.

6.2 NACA64A012

Figure 6.10 shows the coarse level grid used for the NACA64A012 simulations. The complete C-grid as well as a zoom in on the airfoil are displayed.

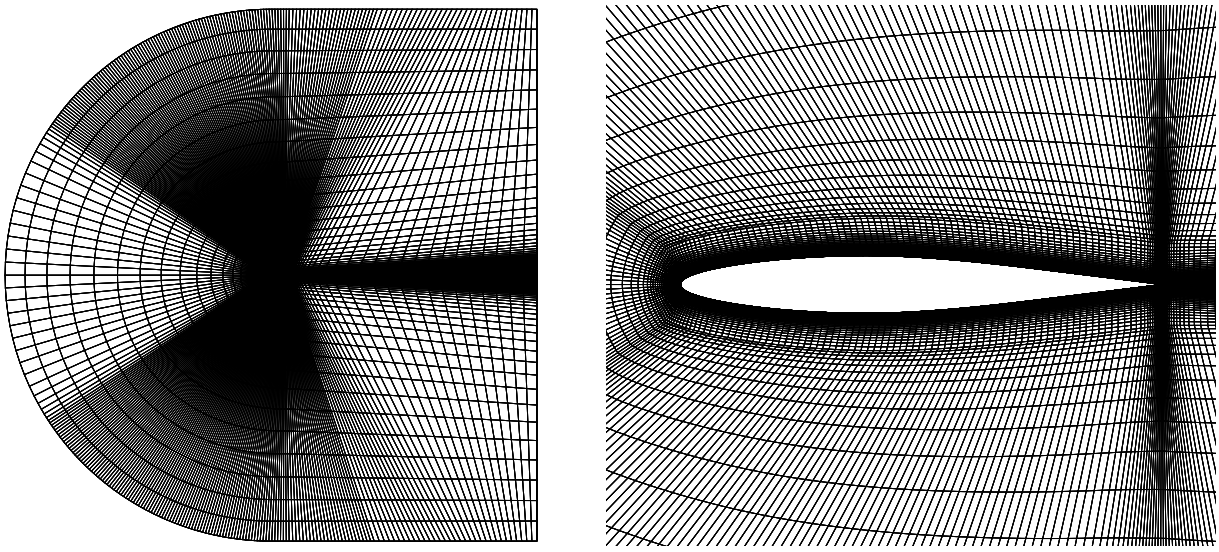

(a) (b)

Figure 6.10: Coarse mesh for airfoil NACA64A012 (336 X 88). (a) Complete C-mesh topology, (b) zoomin of airfoil mesh.

6.2.1 Validation at free-stream conditions: $Re = 1.16 \times 10^6$, $M_\infty = 0.4$, $\alpha = -2.0^\circ, 0.0^\circ, 2.0^\circ$

Figure 6.11 shows two images from [4] of experimental transition results. Figure 6.11(a) indicates the transition position on the top surface as a measure of relative light intensity change using luminescent experimental methods. The minimum value before a a sudden rise in relative intensity change, determines the experimental transition position for $Re = 1.16 \times 10^6$, $M_\infty = 0.4$, and $\alpha = -2.0^\circ, 0.0^\circ, 2.0^\circ$. Approximately, values of $x/c = 0.5, 0.55, 0.6$ are observed for corresponding $\alpha = -2.0^\circ, 0.0^\circ, 2.0^\circ$ positions. Comparing those with our numerical simulations shown in Figure 6.12, a very good agreement is obtained. The transition

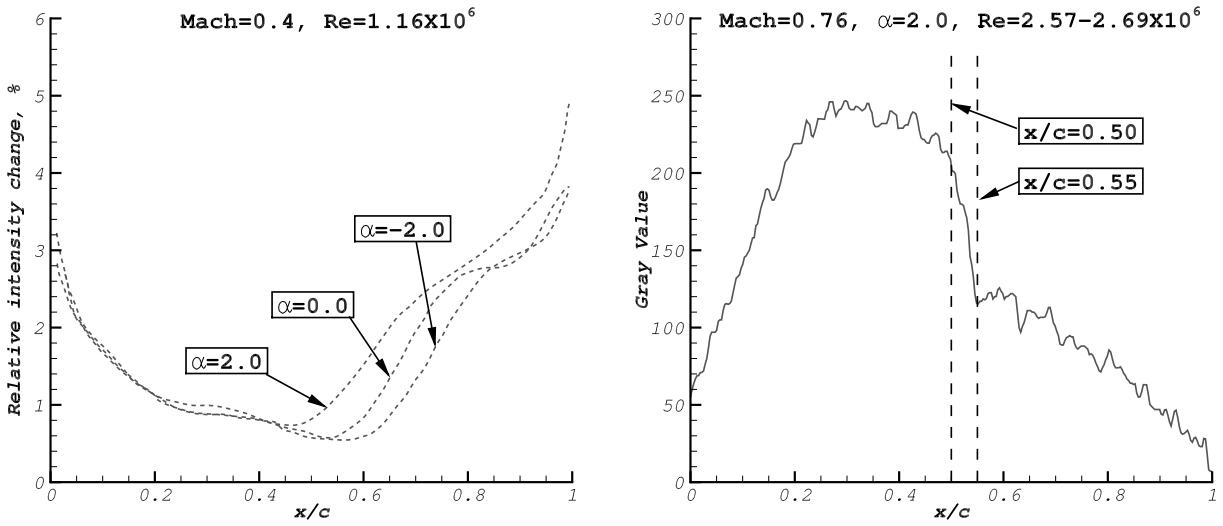

(a) (b)

Figure 6.11: Experimental results on free transition with NACA64A012 from [4] (edited). Airfoil coated with Ru (VH127) paint and excited with a light source to capture luminescent images. (a) Chordwise luminescent profiles at $Mach = 0.4$, $Re = 1.16 \times 10^6$. Transition onset takes place when the intensity jumps (approximately at $x/c = 0.5, 0.55, 0.6$ for corresponding $\alpha = 2.0°, 0.0°, -2.0°$ for the top airfoil surface). (b) Post-processed Figure 15a from [4] showing the pixel intensity in a gray value scale. The sudden change in color at $x/c = 0.5 - 0.55$ determines transition. The original Figure from [4] shows a photo of the top surface of the airfoil with laminar regions in white and turbulent regions in dark. Multiple turbulent wedges due to imperfections near the leading edge of the original photo, create an early transition on localized regions. A clean region without wedges is chosen to post-process the original photo using the software ImageJ and create Figure (b). $Mach = 0.76$, $Re = 2.57 - 2.69 \times 10^6$ $\alpha = 2.0°$.

prediction on the top surface takes place at $x/c = 0.495, 0.549, 0.606$ for corresponding angle of attack position of $\alpha = -2.0°, 0.0°, 2.0°$. Figure 6.12(a) shows wall pressure on the top surface, while Figure 6.12(b) shows the corresponding skin friction distribution which achieves minimum values at transition, followed by a sudden rise when a turbulent boundary layer begins.

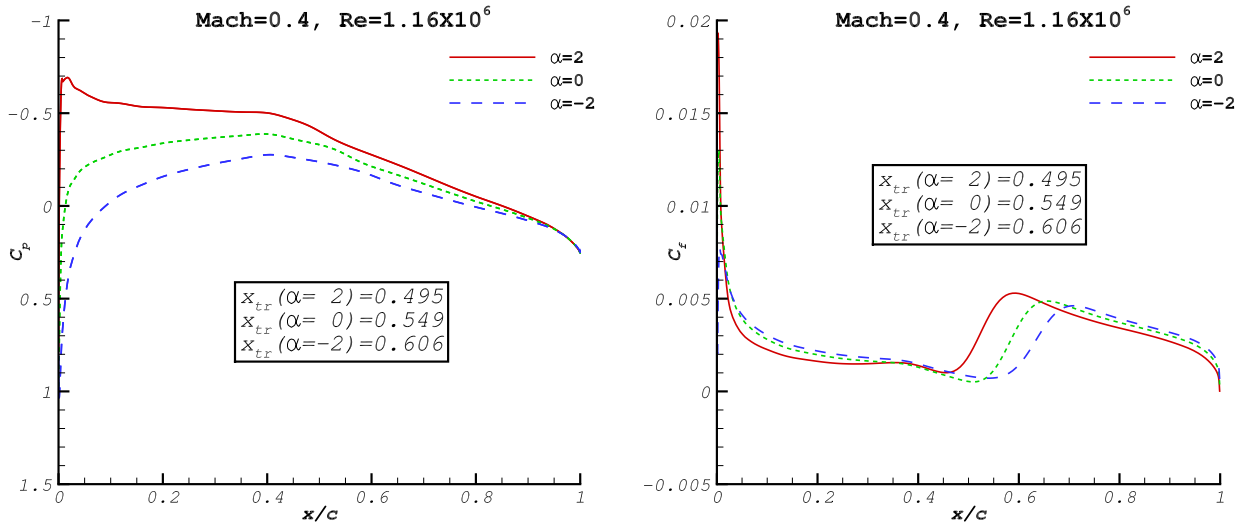

(a) (b)

Figure 6.12: Free transition simulations for various angles of attack for NACA64A012 at $Mach = 0.4$, $Re = 1.16 \times 10^6$ to validate transition prediction of Figure 6.11(a). (a) computed pressure distribution, (b) computed skin friction.

6.2.2 Free-stream conditions: $Re = 2.6 \times 10^6$, $M_\infty = 0.2$. Effect of transition on subsonic conditions of a classic airfoil.

The NACA64A012 airfoil is tested at multiple angles of attack for subsonic conditions revealing differences compared to the subsonic free transition results of the NACA0012 case. Figures 6.13 and 6.14(a) show wall pressure and skin friction for $\alpha = 0.0°, 1.0°, 2.0°, 3.0°, 4.0°$ in free transition and fully turbulent conditions. Increasing the angle of attack, brings the pressure peak closer to the leading edge, which increases the adverse pressure gradient region promoting an early transition as shown in Figure 6.14(b). The pressure distribution at the bottom surface is not significantly affected by the change in angle of attack, and the pressure kink due to the change in airfoil thickness remains at a similar position creating a small dependence of bottom transition position on variations in the angle of attack. The fully turbulent wall pressure perfectly overlaps the free transition pressure, like for the subsonic NACA0012 case. Therefore, free transition is not affecting the pressure distribution

which is the main contributor to the lift coefficient. Figure 6.15(a) shows the variation of lift with angle of attack, where an almost linear trend is obtained, and no differences between free transition lift and fully turbulent lift can be appreciated. On the other hand, although the free transition drag is smaller than the turbulent drag, an interesting trend in the free transition polar curve is shown in Figure 6.15(b). The sharp rise in drag for the higher lift cases is caused by the corresponding top surface early transition shown in Figure 6.14(b). Such early transition on the top surface acts as almost a fully turbulent case, and the free transition drag polar moves closer to the fully turbulent polar curve. The contributions to drag due to pressure and wall friction are shown in Figure 6.16. While most of the drag is caused by friction, when the friction drag increases due to the top transition moving closer to the leading edge, so does the corresponding pressure drag which slightly overpasses the fully turbulent pressure drag component. This overlap is caused by small differences in the pressure peak at the leading edge between free transition and fully turbulent conditions.

6.2.3 Free-stream conditions: $Re = 2.6 \times 10^6$, $M_\infty = 0.76$. Effect of transition on transonic conditions of a classic airfoil, and validation for $\alpha = 2.0°$.

The NACA64A012 airfoil is simulated at transonic conditions for $\alpha = 0.0°, 1.0°, 2.0°, 3.0°$. Figure 6.17 shows wall pressure and skin friction for free transition and fully turbulent conditions. A consistent delay of the top surface free transition shock wave position is observed compared to the fully turbulent shock. This is in agreement with the free transition transonic results shown for the NACA0012 airfoil. By increasing the angle of attack, the shock wave at the bottom surface disappears. A small kink in free transition C_p is still present at the bottom surface due to transition thickening the boundary layer. This kink is specially noticeable for $\alpha = 3.0°$. Like in the NACA0012 case, the difference in wall pressure

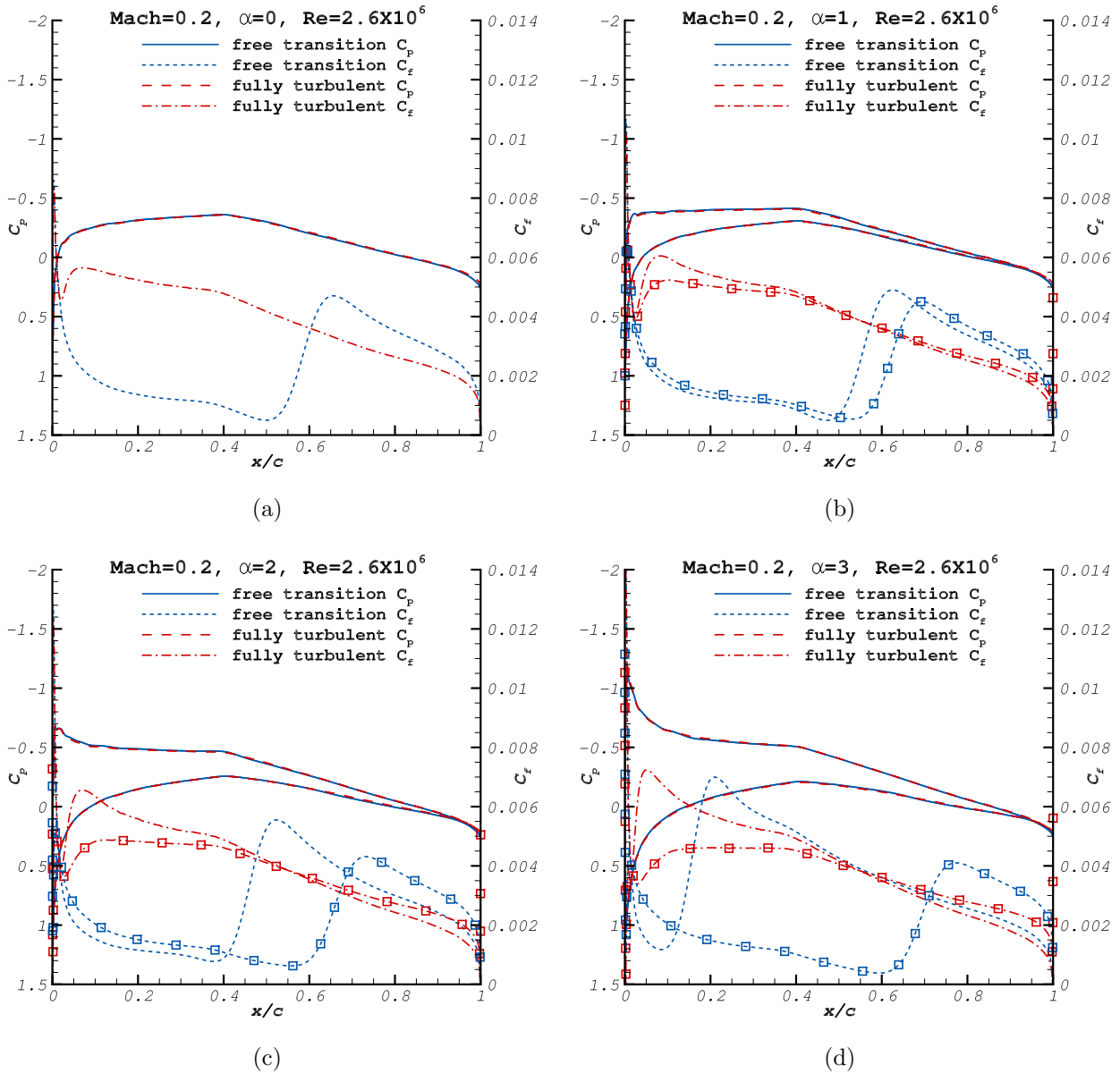

Figure 6.13: Subsonic simulation of angle of attack effect in free transition flow for NACA64A012 airfoil. Pressure distribution comparison with fully turbulent simulations. Skin friction comparison of free transition and fully turbulent conditions with lower surface highlighted with square symbols.

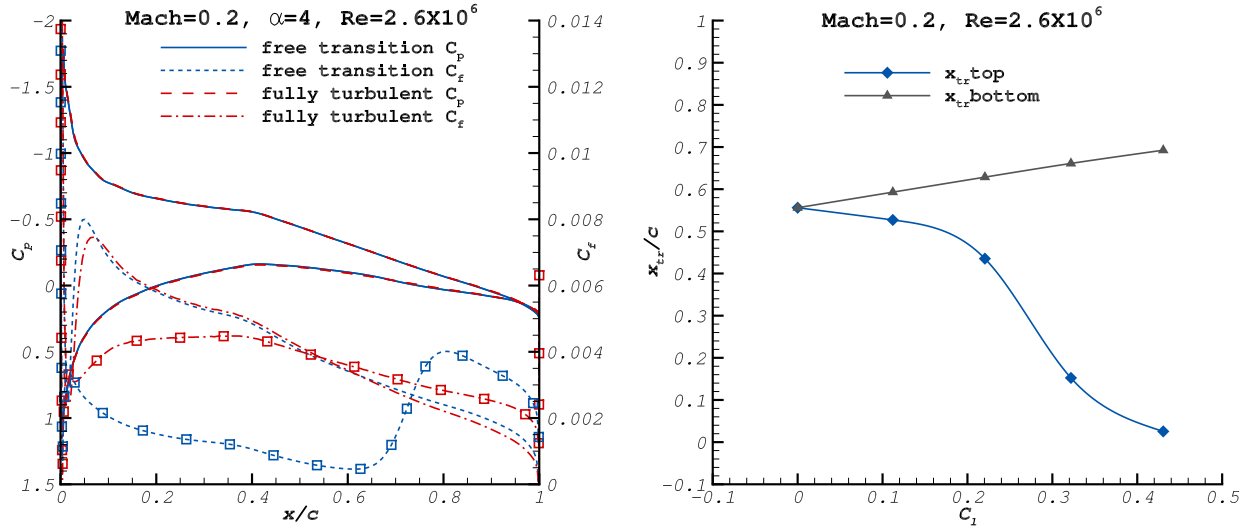

(a) (b)

Figure 6.14: a) Subsonic simulation of angle of attack effect in free transition flow for NACA64A012 airfoil. (a) Pressure distribution and skin friction comparison of free transition and fully turbulent simulations. The skin friction on the lower airfoil surface is indicated with square symbols. (b) Transition position as a function of lift coefficient.

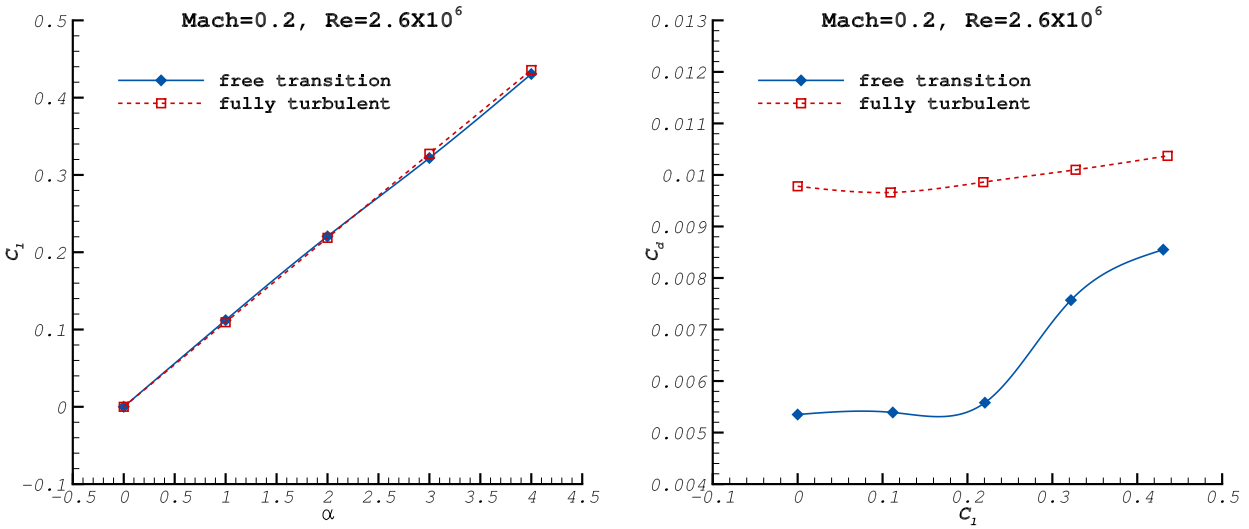

(a) (b)

Figure 6.15: Free transition and fully turbulent comparison for subsonic NACA64A012 airfoil of (a) lift coefficient dependence on angle of attack, (b) polar curve.

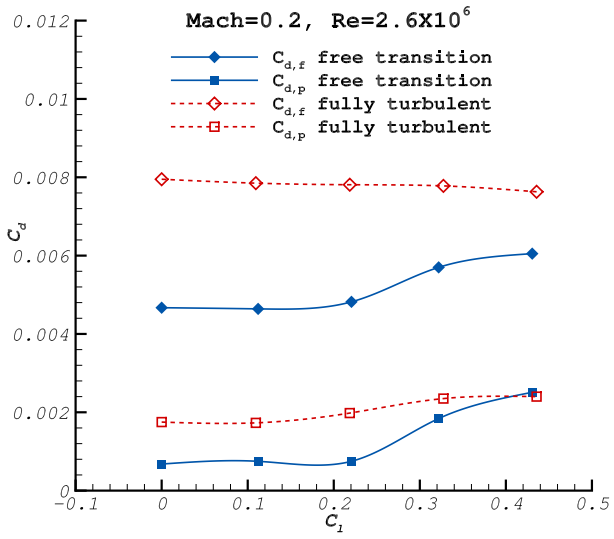

Figure 6.16: Friction and pressure drag coefficient of free transition and fully turbulent conditions for subsonic NACA64A012 airfoil.

between the two flow conditions generate differences in lift coefficient vs. angle of attack, as seen in Figure 6.18(a). The skin friction reveals flow separation at the shock position, followed by a boundary layer reattachment. Stronger separation regions are obtained for free transition conditions. Figure 6.18(b) shows the transition position on the top surface is extended until the shock position due to the favorable pressure gradient displayed. On the bottom surface, the pressure peak moves forward when increasing the angle of attack, and the adverse pressure gradient decreases at the same time. Therefore for $\alpha = 1.0°$, the beginning of a strong adverse pressure gradient has moved forward, which bring transition closer to the leading edge. For the higher angle of attack cases of $\alpha = 2.0°, 3.0°$, the beginning of adverse pressure gradient keeps moving forward but the adverse gradient is smoother which effectively delays transition. Figure 6.19 shows the drag increasing with lift, while the free transition drag is lower than the fully turbulent drag. For small values of the angle of attack, the friction drag is higher than the pressure drag. As the shock gets stronger when increasing angle of attack, the pressure drag overpasses the friction drag and is the main contributor to the total drag component.

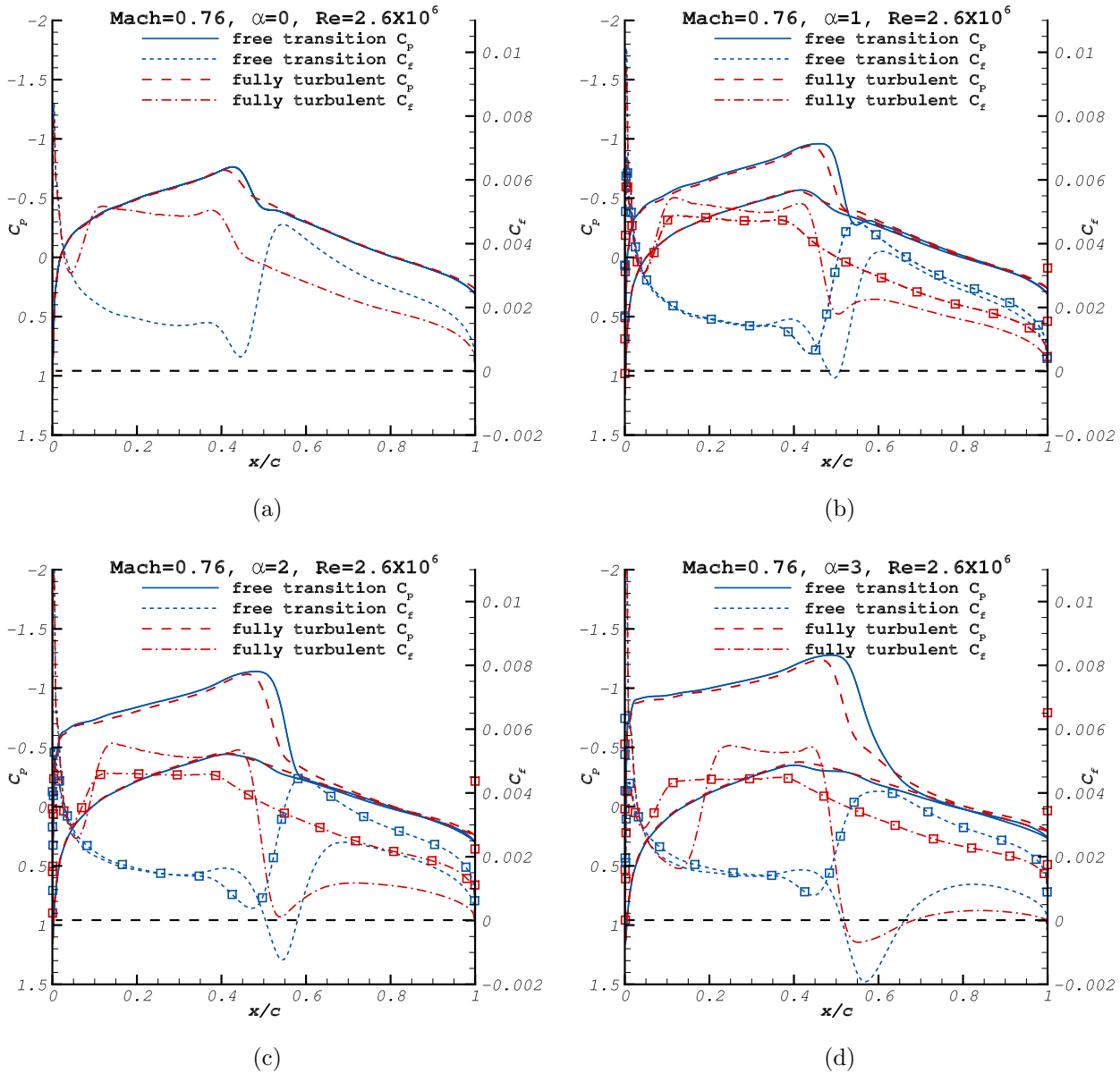

Figure 6.17: Transonic simulation of angle of attack effect in free transition flow for NACA64A012 airfoil. Pressure distribution and skin friction comparison with fully turbulent simulations. Airfoil lower surface skin friction displayed with square symbols. (c) validation of experimental results of Figure 6.11(b)

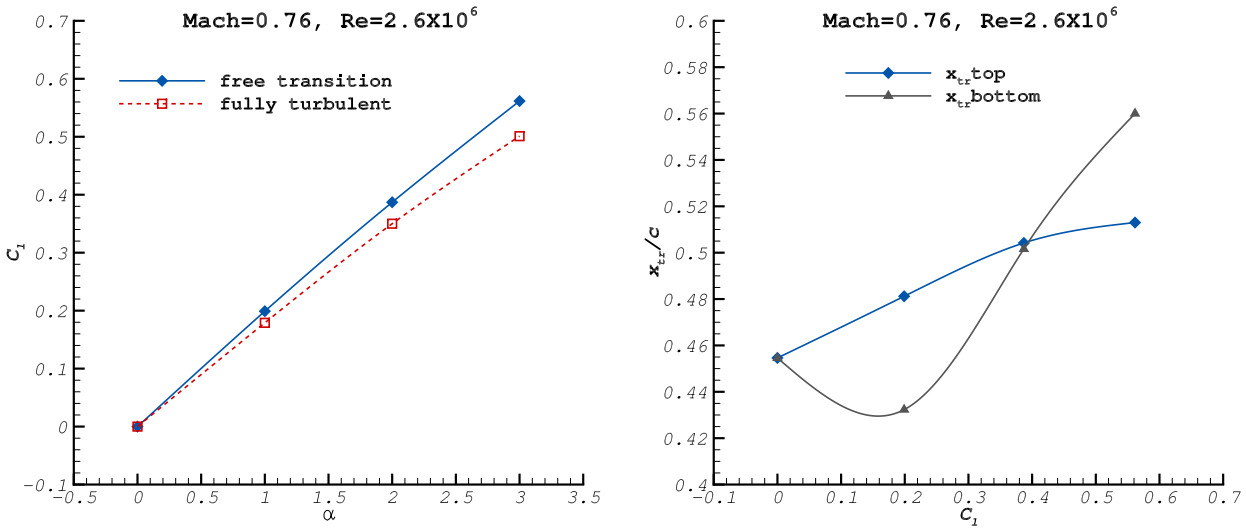

(a) (b)

Figure 6.18: Transonic NACA64A012 airfoil results of (a) free transition and fully turbulent comparison of lift coefficient dependence on angle of attack, (b) transition position.

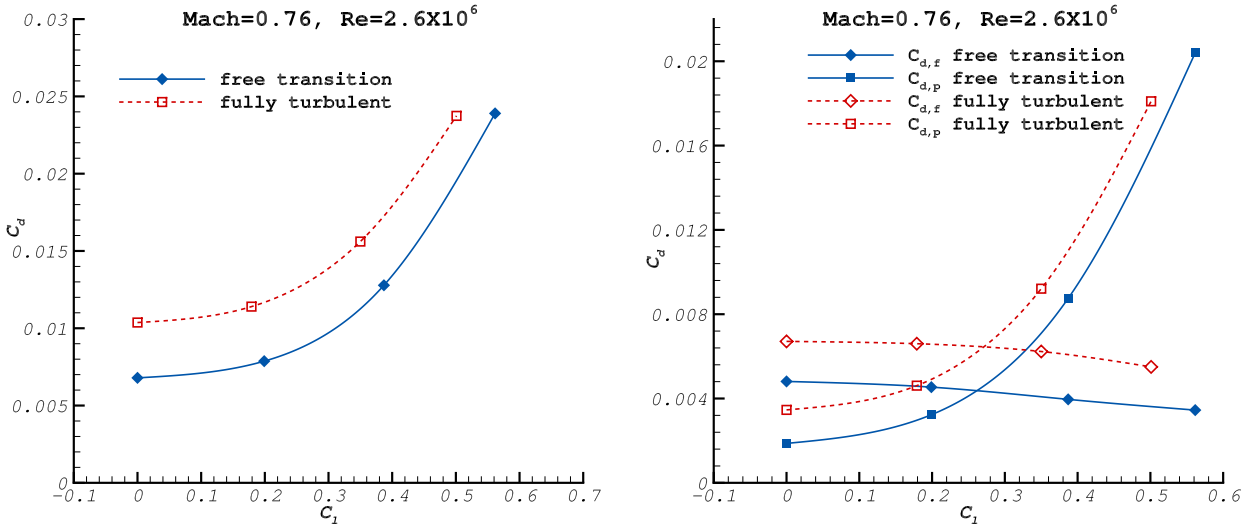

(a) (b)

Figure 6.19: Polar curve for transonic NACA64A012 airfoil at free transition and fully turbulent conditions. (b) Friction and pressure drag.

6.3 NLR7301

Figure 6.20 shows the coarse level grid used for the NLR7301 simulations. The complete C-grid as well as a zoom in on the airfoil are displayed.

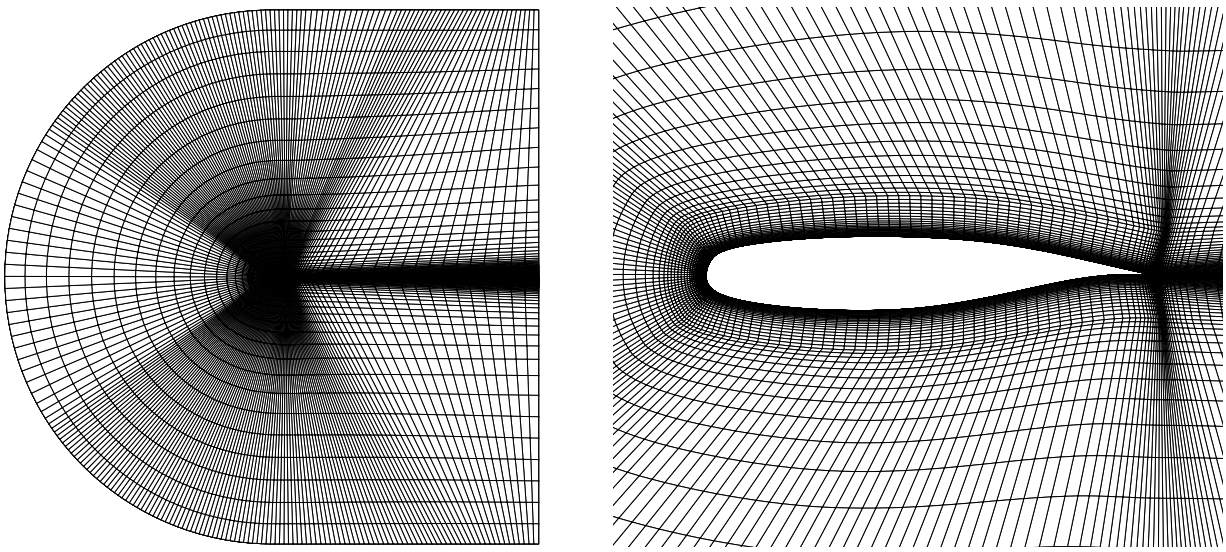

(a) (b)

Figure 6.20: Coarse mesh (256 X 80) for airfoil NLR-7301. (a) Complete C-mesh topology, (b) zoomin of airfoil mesh.

6.3.1 Validation at free-stream conditions: $Re = \{1.12 - 2.3\} \times 10^6$, $M_\infty = 0.3 - 0.8$, $\alpha = 0.2^\circ - 0.4^\circ$

The supercritical NLR7301 airfoil is validated for multiple Mach number conditions following the experimental results [26]. The test conditions for each Mach number are summarized in Table 6.2 showing small variations in Reynolds number and angle of attack.

The top and bottom transition position prediction is compared against the experimental data, and displayed in Figure 6.21(a). A very good agreement is found, showing a very small variation of transition at the bottom surface, and a significant shift in the top surface

Mach	Reynolds	α
0.3	1,200,000	0.4
0.5	1,700,000	0.4
0.6	1,900,000	0.38
0.7	2,100,000	0.39
0.724	2,200,000	0.38
0.747	2,200,000	0.2
0.774	2,200,000	0.25
0.8	2,300,000	0.4

Table 6.2: Corrected conditions used for transition prediction for NLR-7301 airfoil.

for the high Mach number cases. The lift, drag and moment coefficients for free transition, fully turbulent and experimental data are compared and displayed in Figures 6.21(b), 6.22(a) and 6.23. The free transition and experimental lift are in good agreement. Although small lift differences appear for $M_\infty = 0.8$, the main trend is correctly captured. The lift coefficient is almost constant until it peaks at $M_\infty = 0.747$ and sharply decreases for higher Mach numbers. The fully turbulent lift shows similar characteristics with different values showing and offset at lower values than the corresponding free transition lift components. The rise in drag for the high Mach number cases, can be understood with Figure 6.22(b) where the friction drag, and the pressure drag are included. The steep drag shown in Figure 6.22(a) is therefore caused by a sharp increase in pressure drag due to the stronger shock created at higher free stream Mach values. Although the simulated free transition drag does not decrease for $M_\infty = 0.747$, the experimental drag shows a small value for that particular Mach number. This could be explained from Figure 6.22(b). As the free stream Mach number increases, the top transition position suddenly moves back increasing the laminar portion of the airfoil which reduces the skin friction drag. At the same time, the shock get stronger increasing the pressure drag. A balance exists for the experimental case, where the drop in skin friction drag is more significant than the increase in pressure drag, which effectively reduces the total drag component, as shown in Figure 6.22(a). The moment coefficient shown in Figure 6.23 also reveals a good comparison between our free transition

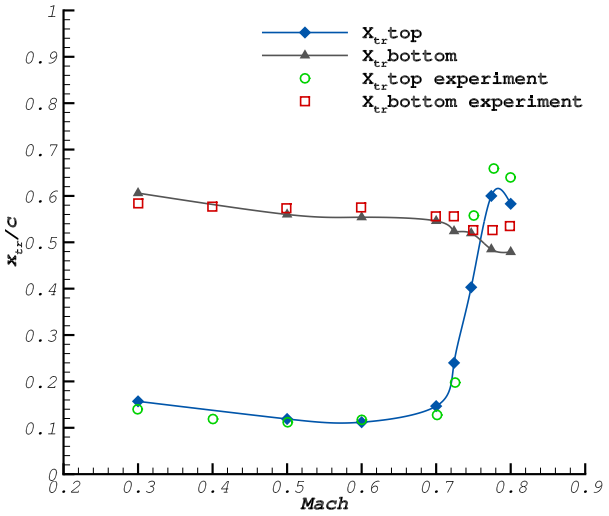

(a) Transition position validation for multiple Mach number cases listed on Table 6.2 for NLR-7301 airfoil.

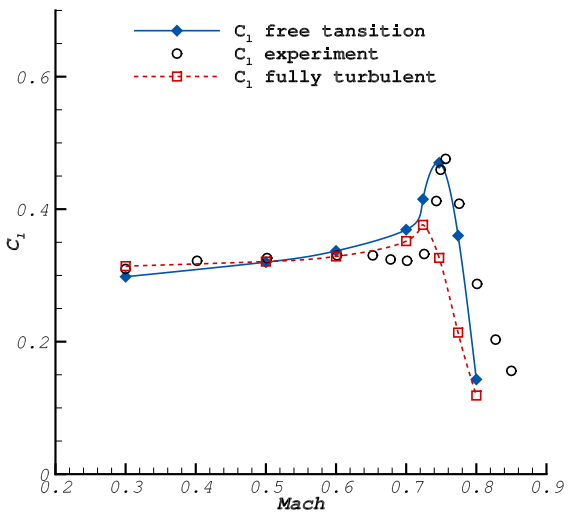

(b) Lift coefficient comparison of computational free transition, with experimental free transition results for test conditions in Table 6.2. Fully turbulent simulations are also included.

Figure 6.21: Validation of transition prediction for NLR-7301 airfoil. (a) Transition position. (b) Lift coefficient.

prediction and the experimental results, with a small deviation for $M_\infty = 0.8$.

Figures 6.24 and 6.25 show a comparison of numerical pressure distribution for free transition and fully turbulent conditions. While almost no differences are observed for subsonic conditions, as the Mach number is increased the free transition shock wave is delayed with respect to the fully turbulent shock. Major differences in pressure distribution are obtained for $M_\infty = 0.747$ even before reaching the shock wave.

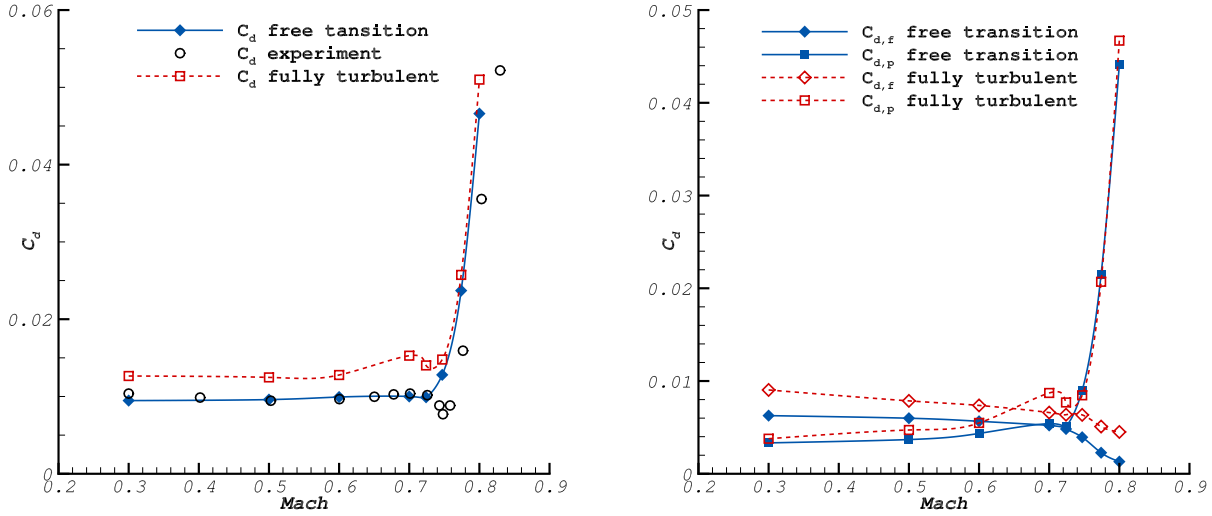

(a) Drag coefficient comparison.

(b) Friction and pressure drag.

Figure 6.22: Drag comparison of numerical free transition, numerical fully turbulent and experimental free transition conditions for free stream values from Table 6.2.

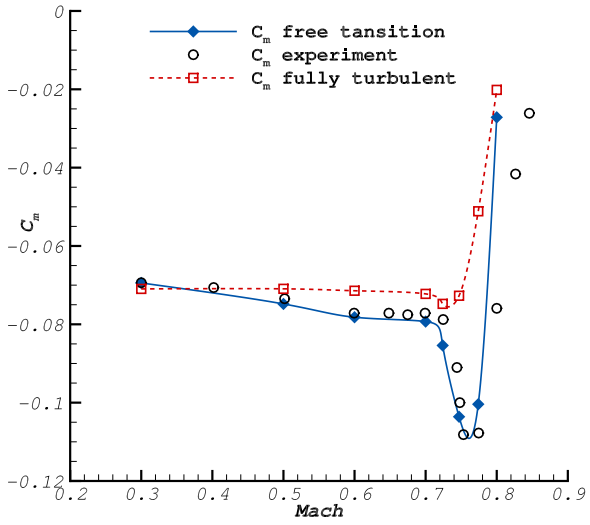

Figure 6.23: Moment coefficient comparison of computational free transition, computational fully turbulent, and experimental free transition conditions for free stream values from Table 6.2.

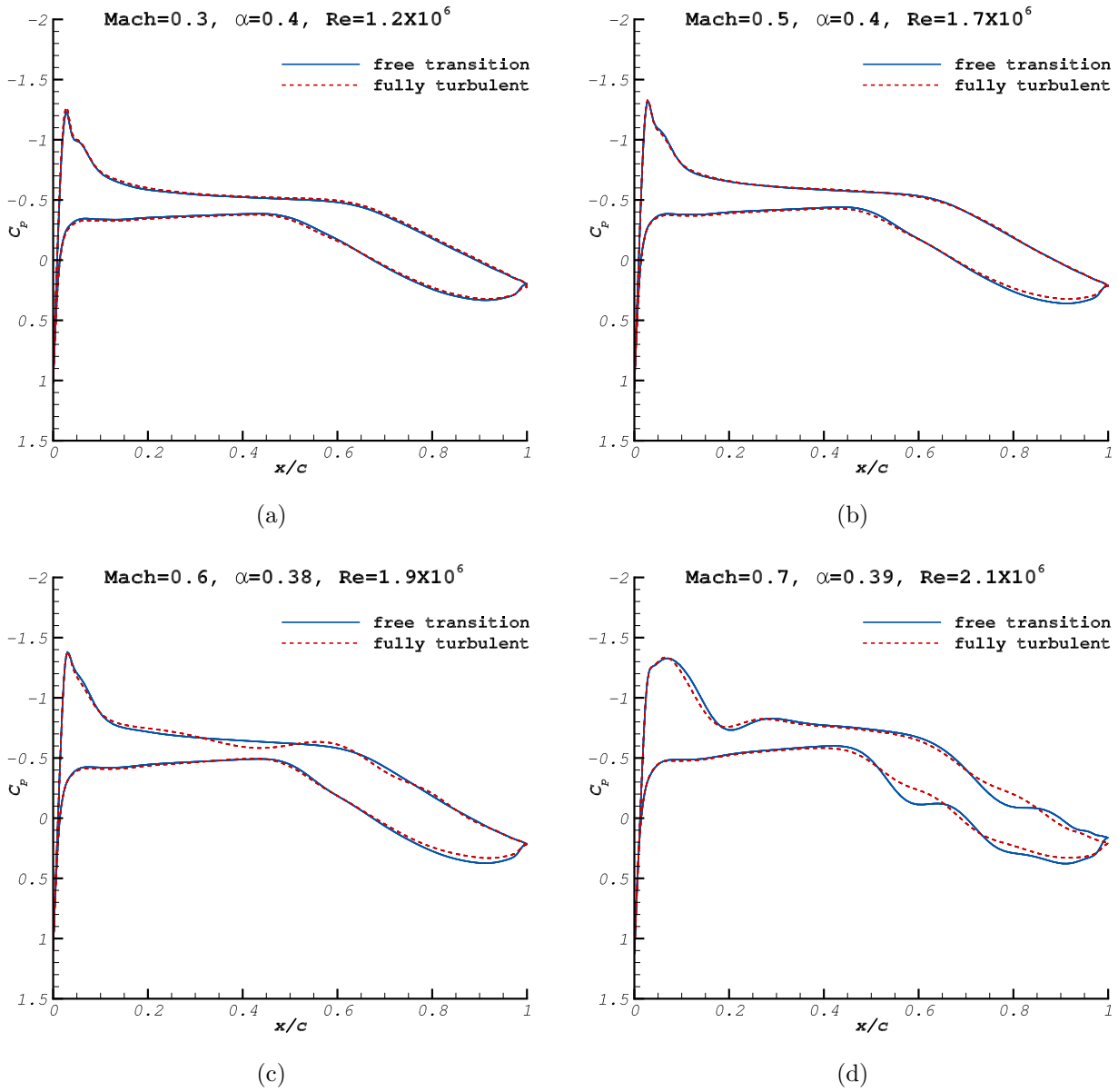

Figure 6.24: Pressure coefficient comparison for free transition and fully turbulent simulations in the subsonic range of NLR-7301 airfoil.

Figures 6.26 and 6.27 show a comparison of free transition pressure distribution for numerical and experimental conditions, and numerical values of skin friction distribution. A very good agreement is obtained for subsonic pressure distributions between numerical and experimental values. However, as the free-stream Mach number increases, slight pressure differences are revealed which are the reason for discrepancies in the previous figures for lift and moment coefficients. The numerical skin friction reveals separation on both surfaces for $M_\infty = 0.774 - 0.8$. While only the bottom surface boundary layer is able to reattach for $M_\infty = 0.774$, both surfaces maintain a detached boundary layer after separation for the highest $M_\infty = 0.8$ case.

6.3.2 Free-stream conditions: $Re = 2.2 \times 10^6$, $M_\infty = 0.2$. Effect of transition on subsonic conditions of a supercritical airfoil.

The NLR7301 airfoil is tested for free transition, and subsonic conditions at angles of attack $\alpha = -2.0^\circ, -1.0^\circ, 0.0^\circ, 1.0^\circ, 2.0^\circ, 3.0^\circ$. Figure 6.28 shows wall pressure and skin friction for the top and bottom surfaces for each of the tested conditions. Increasing the angle of attack increases the pressure suction on the top surface, and it decreases for the bottom surface. Although wall pressure is not shown for fully turbulent conditions, the differences between free transition and fully-turbulent pressure are very small, which explains the similarity in fully turbulent and free-transition lift coefficient vs. angle of attack shown in Figure 6.29(a). The skin friction distributions are highly correlated with the transition position shown in Figure 6.29(b). The top surface transition position quickly moves forward for $\alpha = -2.0^\circ, -1.0^\circ, 0.0^\circ$ and remains at a very similar position close to the leading edge pressure peak for the higher angle of attack cases. This is also observed in the forward shifting of the skin friction rise when the flow transitions from laminar to turbulent state. The bottom surface transition is almost constant except for $\alpha = -2.0^\circ$. This is also seen in the skin friction plot where the rise in wall shear takes place earlier than in the other angle

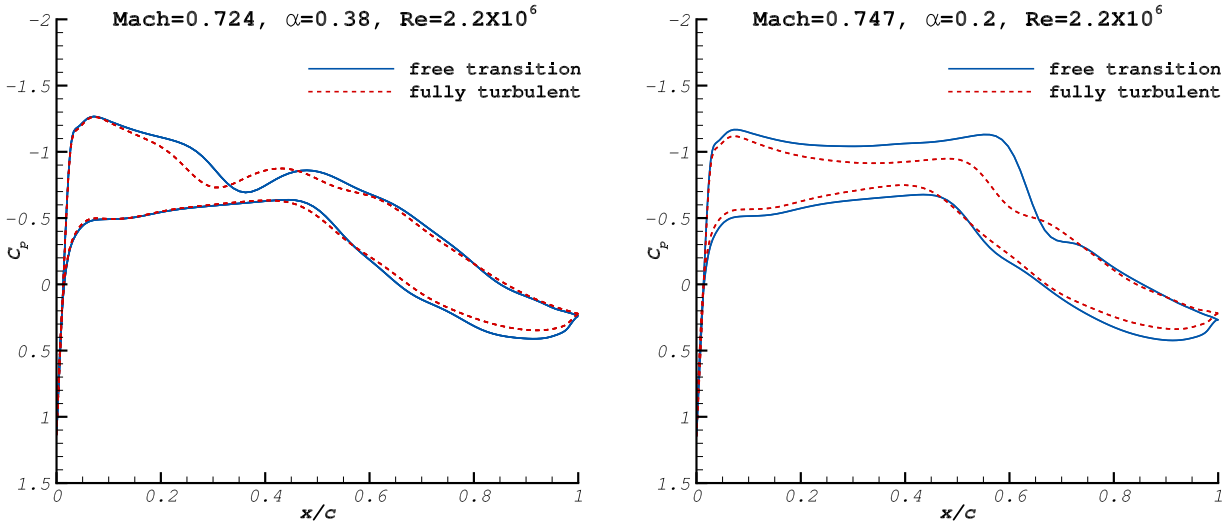

(a)

(b)

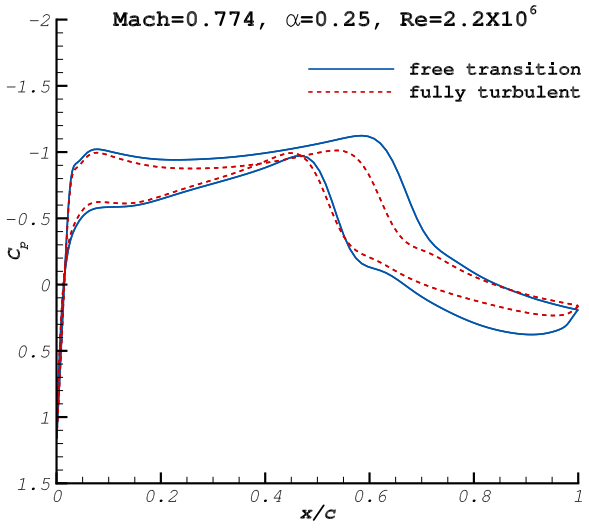

(c)

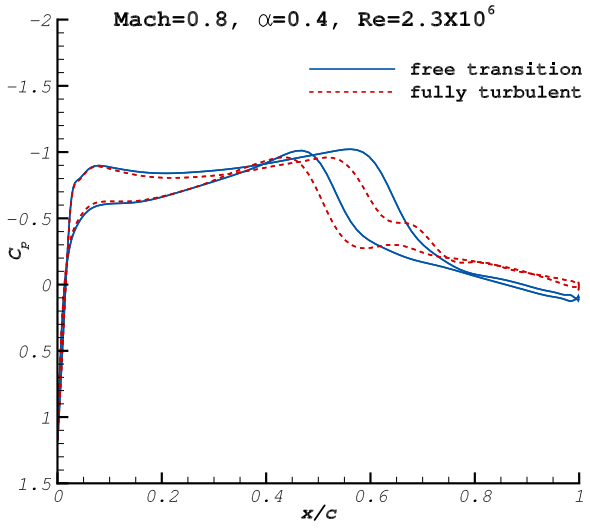

(d)

Figure 6.25: Pressure coefficient comparison for free transition and fully turbulent simulations in the transonic range of NLR-7301 airfoil.

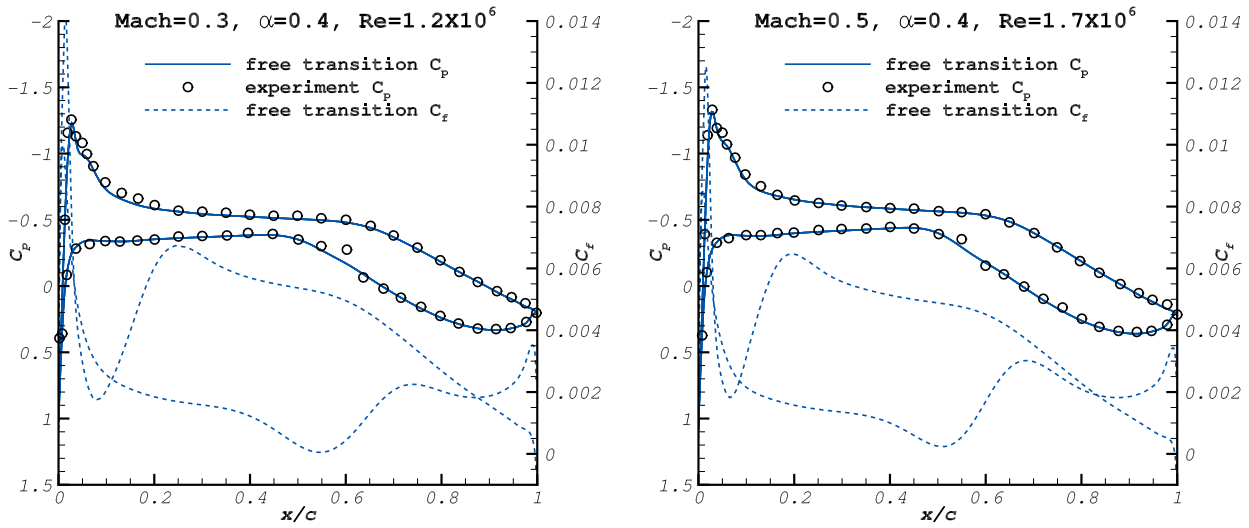

(a)

(b)

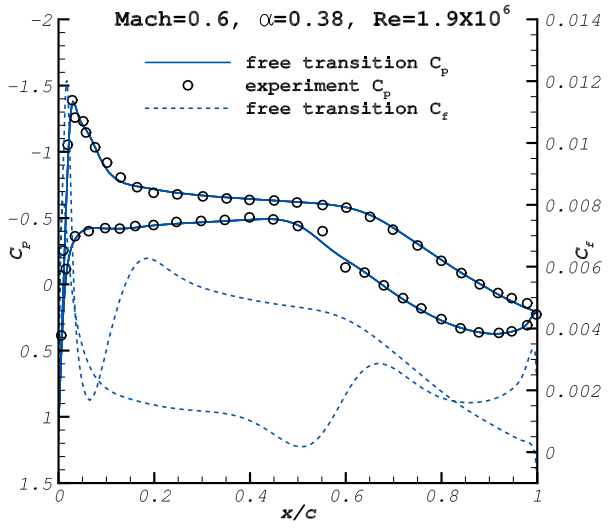

(c)

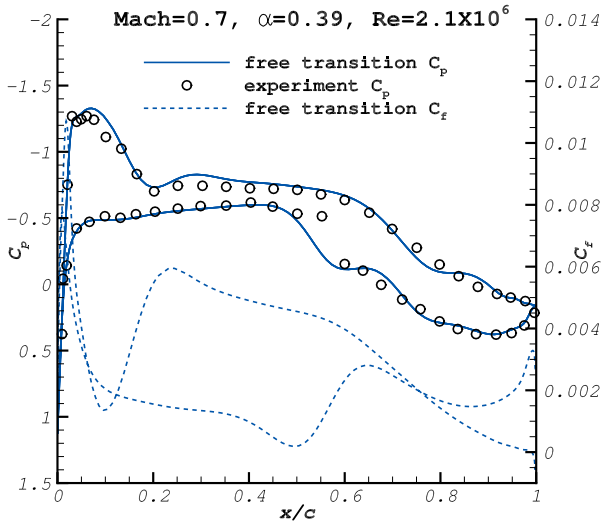

(d)

Figure 6.26: Pressure coefficient comparison with experimental data, and skin friction coefficient for the subsonic range of NLR-7301 airfoil. Forward skin friction deep corresponds to upper surface.

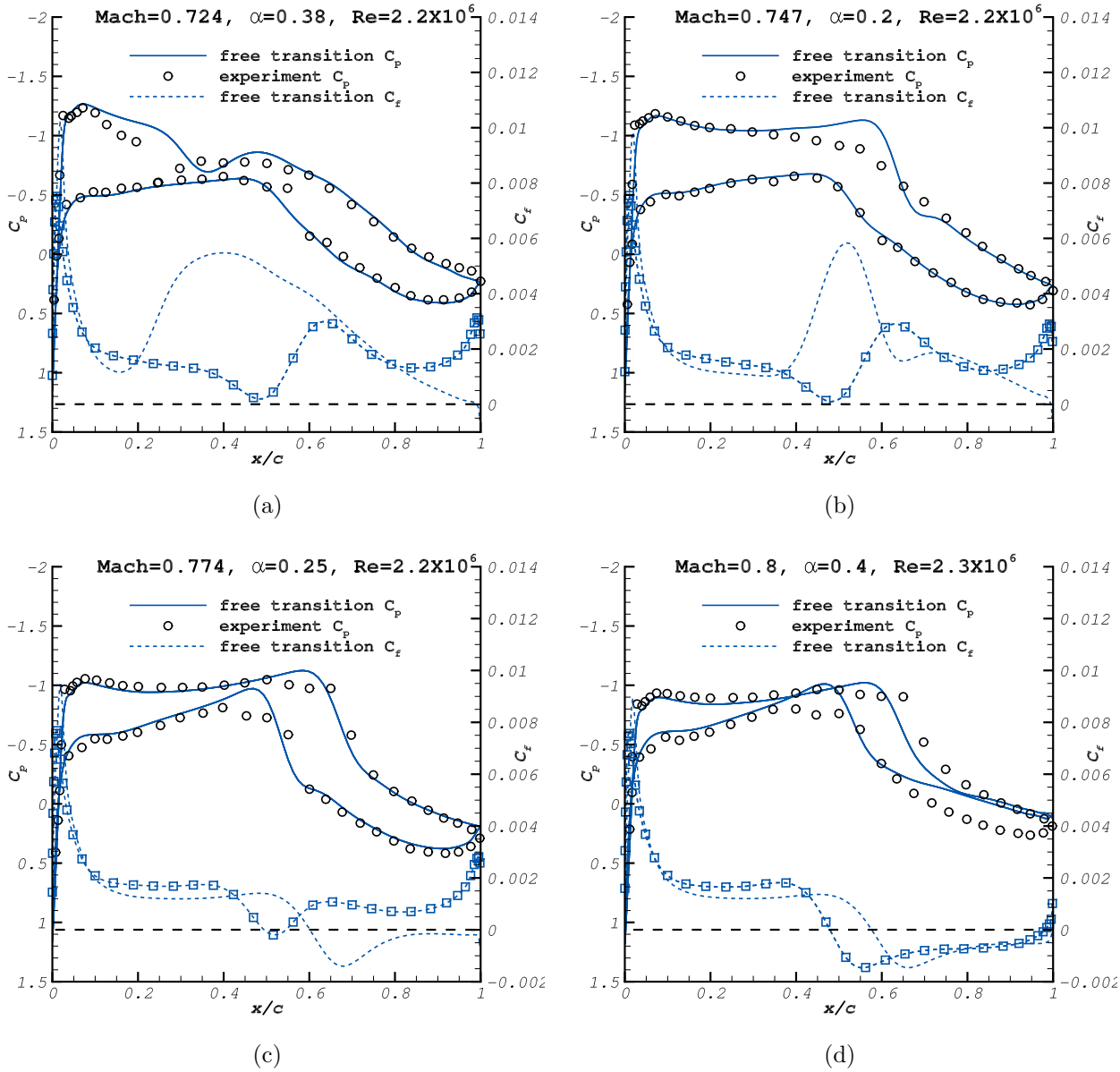

Figure 6.27: Pressure coefficient comparison with experimental data, and skin friction coefficient for the transonic range of NLR-7301 airfoil. Lower surface skin friction is represented with square symbols.

of attack cases. Figure 6.30 shows drag coefficient vs. angle of attack for free transition and fully turbulent conditions. While the polar curve for fully turbulent conditions reveals a normal trend showing the lowest drag for $\alpha = 0.0°$, the free transition polar is monotonically increasing. Since the top surface transition is delayed for the negative angles of attack, a large laminar portion of the wing contributes to a small skin friction drag. The skin friction drag dominates over the pressure drag for subsonic conditions as seen in Figure 6.30(b).

6.3.3 Free-stream conditions: $Re = 2.2 \times 10^6$, $M_\infty = 0.774$. Effect of transition on transonic conditions of a supercritical airfoil.

The NLR7301 airfoil is tested for free transition, and transonic conditions at angles of attack $\alpha = -2.0°, -1.0°, 0.0°, 1.0°, 2.0°, 3.0°$. Figure 6.31 shows the top and bottom wall pressure and skin friction distributions. While the top surface shock wave moves forward when increasing the angle of attack, the bottom surface shock moves slightly back maintaining an almost constant position for the higher angle of attack cases. Figure 6.32(a) shows the lift coefficient vs. angle of attack for free transition and fully turbulent conditions. A significant difference is observed. Although the pressure distribution is not shown for fully turbulent conditions, the free transition shock is delayed with respect to the turbulent shock which justifies the differences obtained in lift. Figure 6.32(b) shows the predicted transition positions. Transition is extended almost until the shock position, taking place due to the laminar separation shown in the skin friction plots of Figure 6.31. The top surface boundary layer is separated for all angles of attack when encountering the shock, but only reattaches for the negative angle of attack cases. The bottom surface only separates for $\alpha = -2.0°, -1.0°, 0.0°$ and remains detached for $\alpha = -2.0°$. Figure 6.33(a) shows the polar curves for free transition and fully turbulent conditions. The major contribution to the total drag is due to pressure drag as shown in Figure 6.33(b), while the friction drag remains at an almost constant value. Negative angles of attack generate higher drag due to the bottom

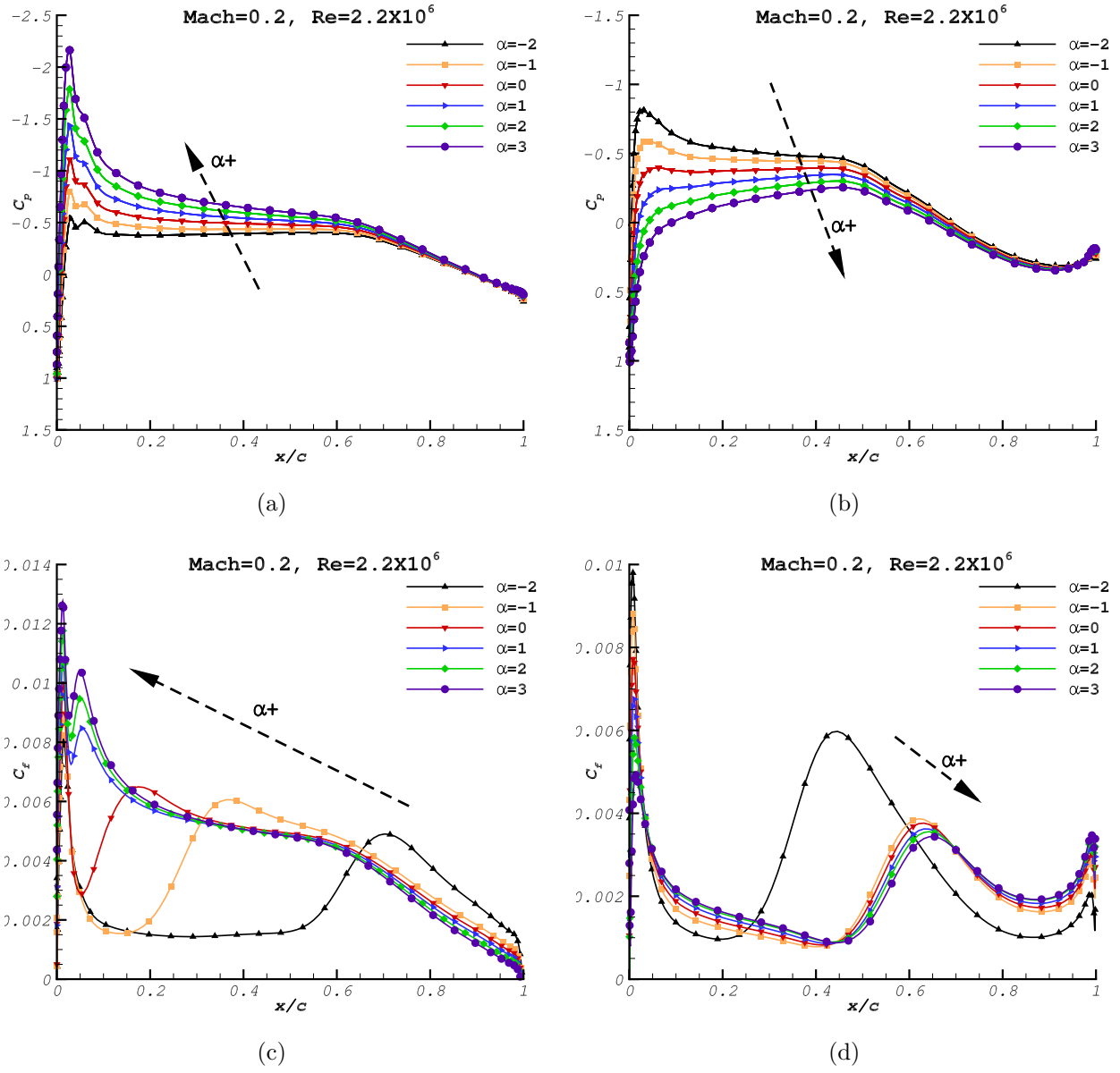

Figure 6.28: Effect of angle of attack for $Mach = 0.2$ and $Re = 2,200,000$ in NLR-7301 airfoil. (a) Pressure coefficient for upper surface and (b) lower surface. (c) Skin friction for upper surface and (d) lower surface.

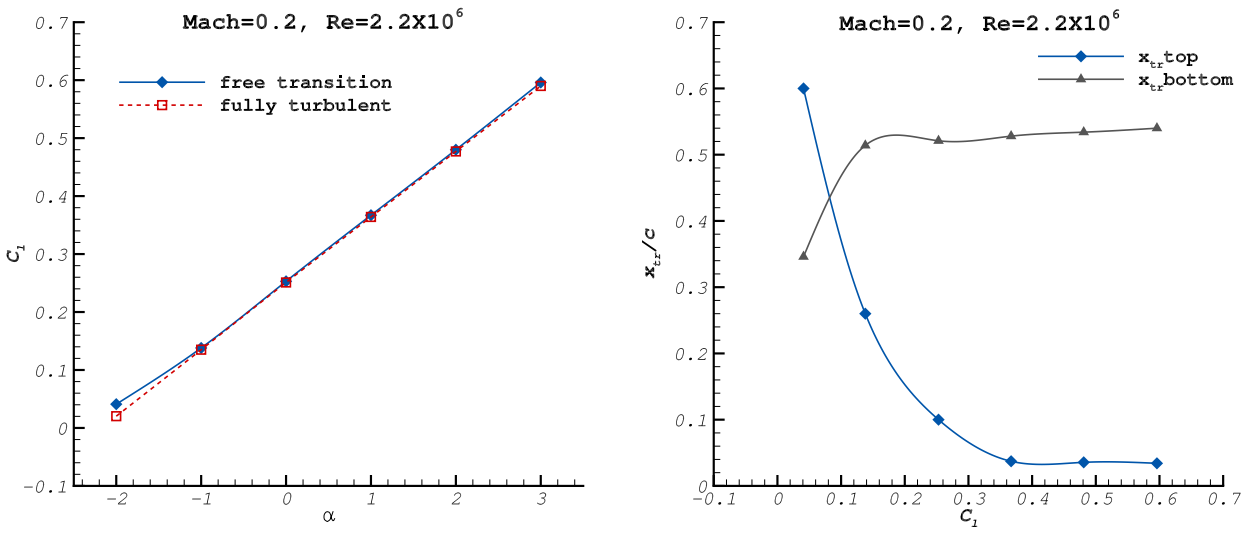

(a) (b)

Figure 6.29: (a) Free transition and fully turbulent comparison for subsonic conditions of NLR-7301 airfoil of lift coefficient dependence on angle of attack. (b) transition position dependency on lift coefficient.

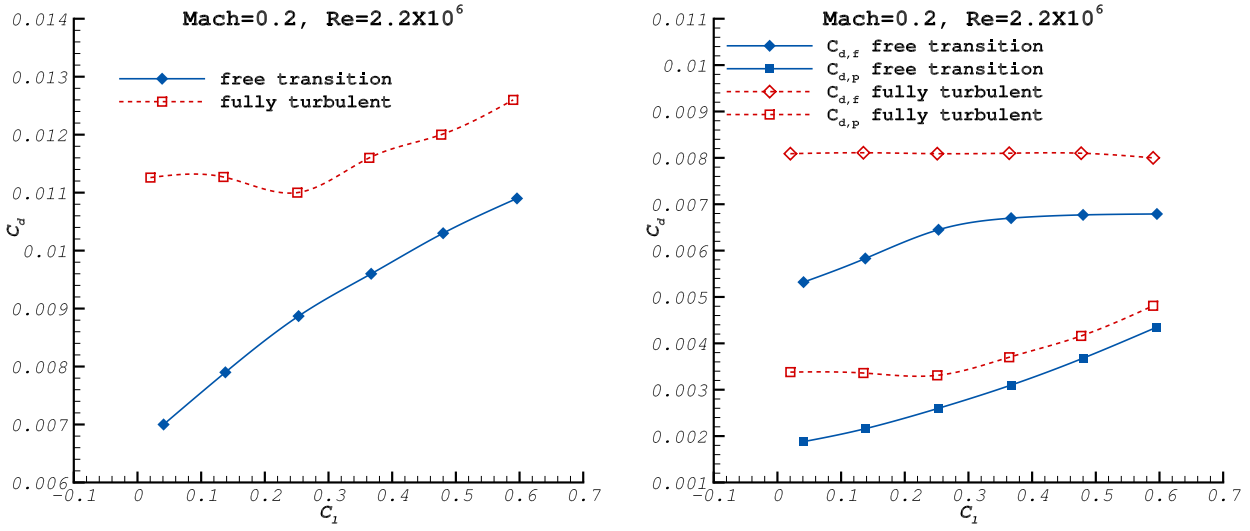

(a) (b)

Figure 6.30: Free transition and fully turbulent comparison for subsonic conditions of NLR-7301 airfoil of (a) polar curve, and (b) friction and pressure drag coefficients.

surface shock being stronger than in the zero angle of attack situation.

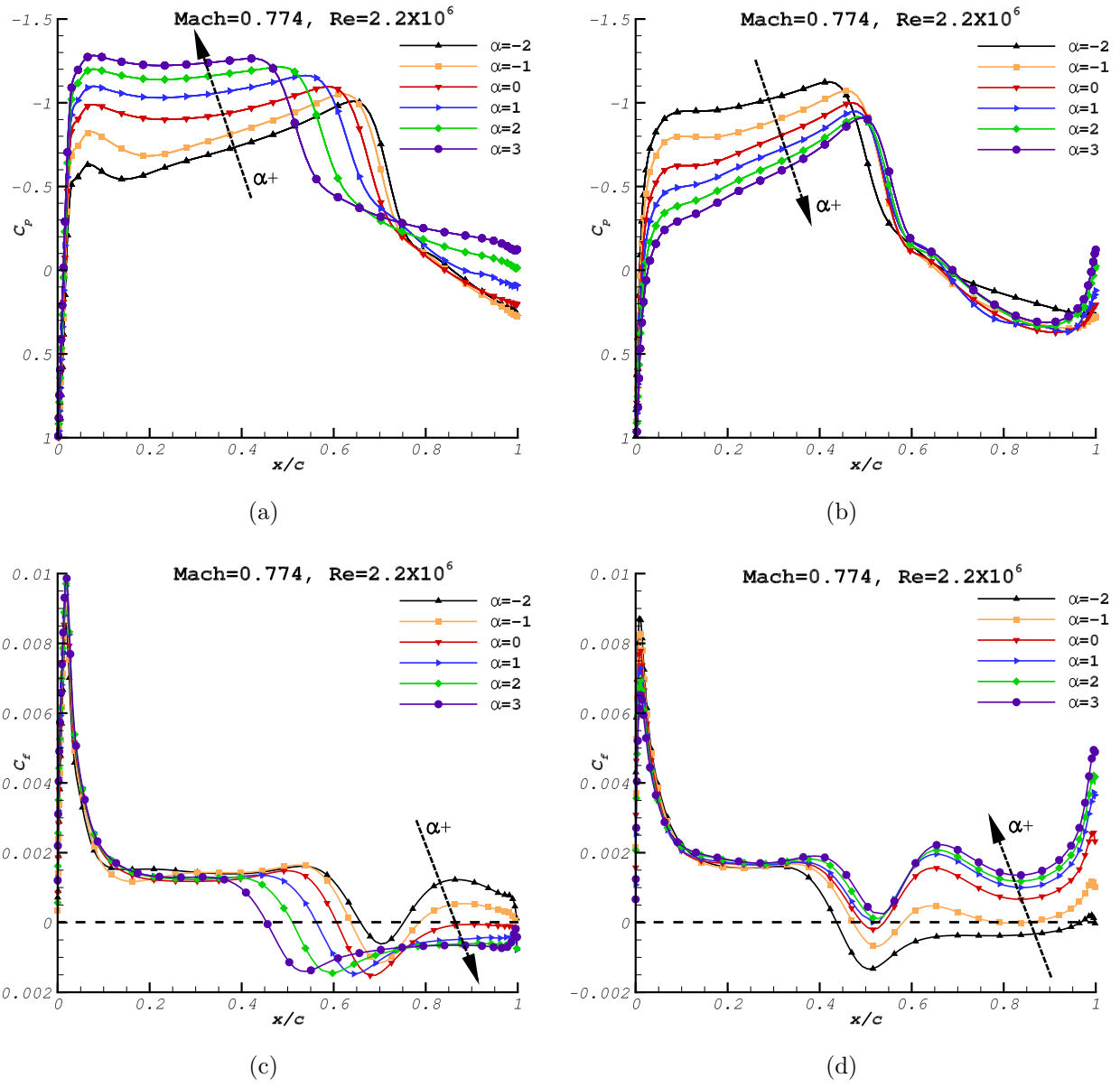

Figure 6.31: Effect of angle of attack for $Mach = 0.774$ and $Re = 2,200,000$ in NLR-7301 airfoil. (a) Pressure coefficient for upper surface and (b) lower surface. (c) Skin friction for upper surface and (d) lower surface.

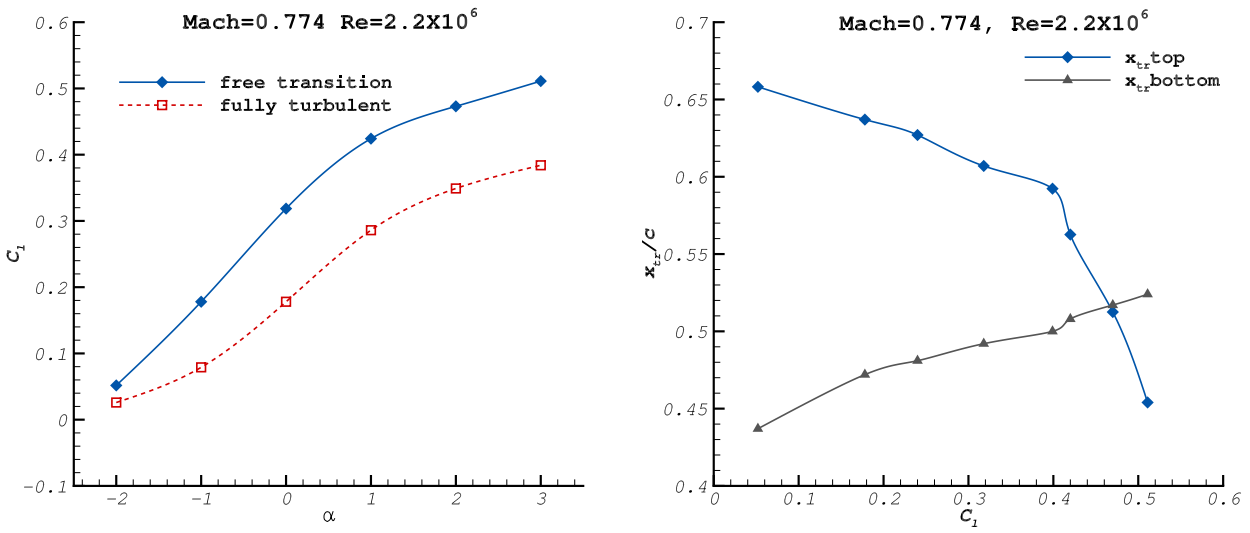

(a) (b)

Figure 6.32: (a) Free transition and fully turbulent comparison for transonic conditions of NLR-7301 airfoil of lift coefficient dependence on angle of attack. (b) transition position dependency on lift coefficient.

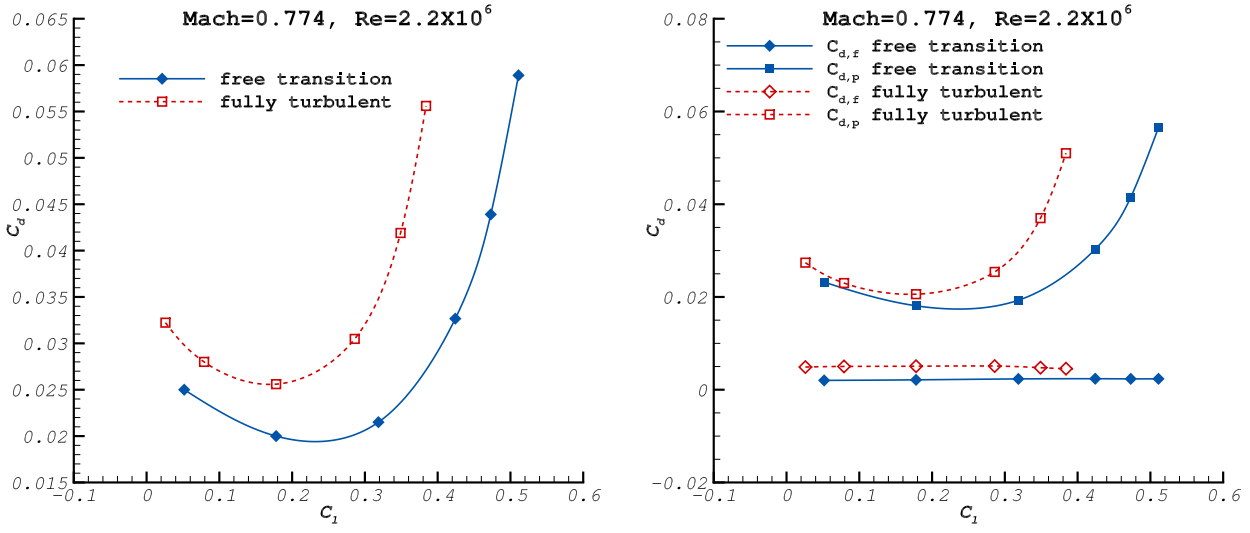

(a) (b)

Figure 6.33: Free transition and fully turbulent comparison for subsonic conditions of NLR-7301 airfoil of (a) polar curve, and (b) friction and pressure drag coefficients.

Chapter 7

Conclusions Part II

A laminar-turbulent transition model is implemented into our CFD code. The transition model is of the e^N type, where Tollmien-Schlichting waves are responsible for laminar-turbulent transition. The model needs integral boundary layer parameters as inputs. Instead of using a highly refined grid close to the wall region to obtain accurate integral boundary-layer values, an Integral Boundary Layer code is incorporated into our CFD code, only to generate the inputs needed for the transition model.

The transition position prediction is fed into the CFD code using an intermittency function to gradually increase the magnitude of the eddy viscosity.

The transition model is validated against free-transition experimental results for the NLF(1)-0416 and the NACA0012 airfoils. A forced pitching motion on the NACA0012 reveals a better solution using free-transition than fully turbulent conditions.

The airfoils NACA0012, NACA64A012 and NLR7301 are validated for the available free-transition experimental results. A sweep of angle of attack is performed for subsonic and transonic conditions for the three airfoils. The subsonic pressure distribution and lift co-

efficient are not affected by using free-transition conditions, and the fully turbulent values almost overlap the free-transition solution. The free-transition drag is lower than the fully turbulent drag. The largest contribution to drag at subsonic conditions is from friction. Differences between free-transition and fully turbulent results are observed for transonic conditions. The effect of free-transition is to bring the shock wave closer to the inviscid shock position. The laminar boundary layer is thinner than the corresponding turbulent boundary layer. Therefore, the flow moving around the free-transition airfoil encounters an effective airfoil (airfoil geometry modified by displacement thickness) between the inviscid case (pure geometry), and the fully-turbulent case (geometry modified by a larger displacement thickness). Although the major contribution to drag at transonic conditions was from pressure, due to the shock drag, the free-transition drag was generally lower than the fully turbulent drag.

It has been found, for transonic conditions, a significant difference in pressure distribution and lift coefficient between fully-turbulent and free-transition conditions. Lift is the dominant force in heaving of an elastic wing, while the contour of pressure distribution is what changes the moment coefficient, which affects pitching.

Part III

Isogai-wing-model flutter in free-transition flow

Chapter 8

NACA 64A010 Flutter by the Navier-Stokes equations with free transition

The last Part of this dissertation combines the work from the previous two Parts to obtain the transonic flutter boundary with free laminar-turbulent transition for the NACA64A010 airfoil using the Isogai structural model. The results in this Part are previously presented in [53].

Section 8.1 performs a grid independence study on free-transition prediction at transonic conditions. The effect of free-transition on the steady state NACA64A010 airfoil is studied in Section 8.2. The results of forcing a pitching and heaving motion are shown in Section 8.3. Section 8.4 presents the flutter boundary at free-transition conditions and Sections 8.2 and 8.3 are referenced to justify the aeroelastic response.

8.1 Free transition grid independence study of NACA 64A010

The elastic response of the NACA 64A010 airfoil in free transition conditions is analyzed for $Re = 10^7$ at zero angle of attack. A set of fine, medium and coarse grids is designed with corresponding $y+$ of 0.66, 1.33 and 2.7 at the wall. The coarse grid is shown in Figure 8.1 with 312×72 cells. Each grid level has twice the number of cells in each direction as their next coarser grid level. Figure 8.2 shows the pressure distribution of the grid independence study performed for free transition conditions at $M_\infty = 0.80$, $\alpha = 0.0°$ and $N_{crit} = 7$. The transition position results are summarized in Table 8.1 showing a convergence in the result as the grid intensity increases.

x_{tr}/c		
coarse	medium	fine
0.478	0.496	0.507

Table 8.1: NACA 64A010 transition positions with $Ncrit = 7$

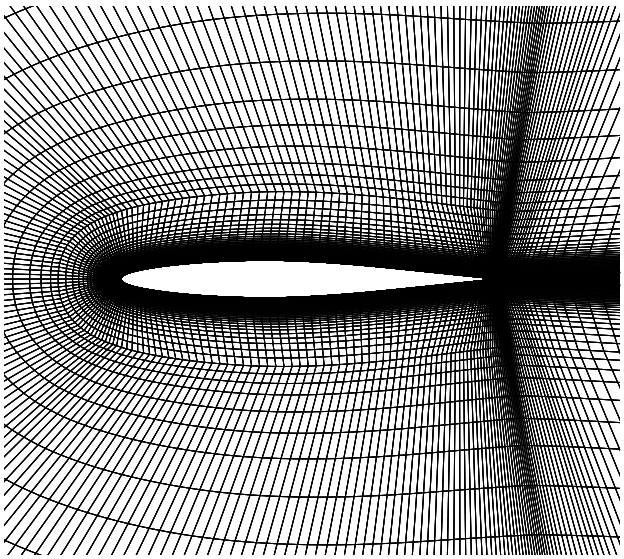

Figure 8.1: Coarse grid level of NACA 64A010 with 312×72 cells.

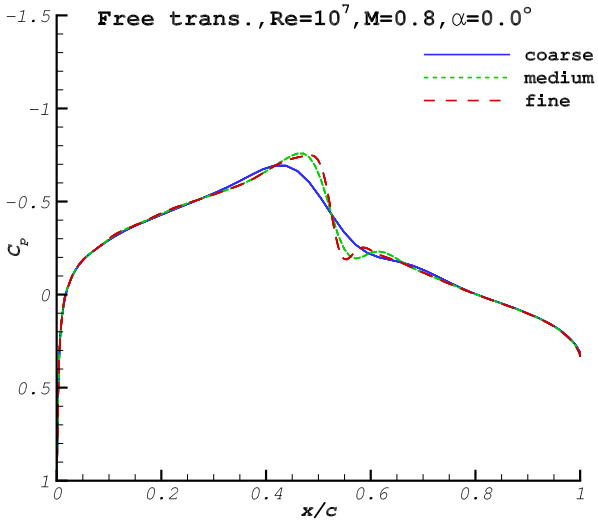

Figure 8.2: Grid independence study for free transition conditions.

The medium grid of 624×144 cells is chosen for the flutter studies. All the following viscous

results are obtained with such grid.

8.2 Effect of free transition in steady NACA 64A010 for $\alpha = 0.0°, 0.5°, 1.0°,\ 2.0°, 3.0°$

A comparison of free transition, fully turbulent and inviscid conditions in Figure 8.3 reveals significant differences in lift and moment coefficient when increasing the angle of attack. C_l and C_m are the loading in the structural model used in Equation (2.7) for flutter prediction. The drag, however, is lower for free transition conditions than in the fully turbulent case, as expected. The transition position moves forward for higher angle of attack, which seems to bring the free transition lift and moment curves closer to the fully turbulent ones.

The transition position is delayed due to the favorable pressure gradient shown in Figure 8.4 until the flow separates before the foot of the shock wave. Figure 8.4a shows the same shock position for the inviscid and free transition conditions. When the angle of attack increases to $\alpha = 1°$, there is a disagreement in the position of the shock for each flow condition. The pressure distribution is almost identical for the three conditions until the shock wave appears, where the shock for the free transition conditions is between the inviscid shock and the fully turbulent shock.

8.3 Effect of free transition in pitching and heaving of NACA 64A010

A forced motion is imposed to understand the differences in lift and moment for inviscid, fully turbulent and free transition conditions before the airfoil is set free for flutter analysis.

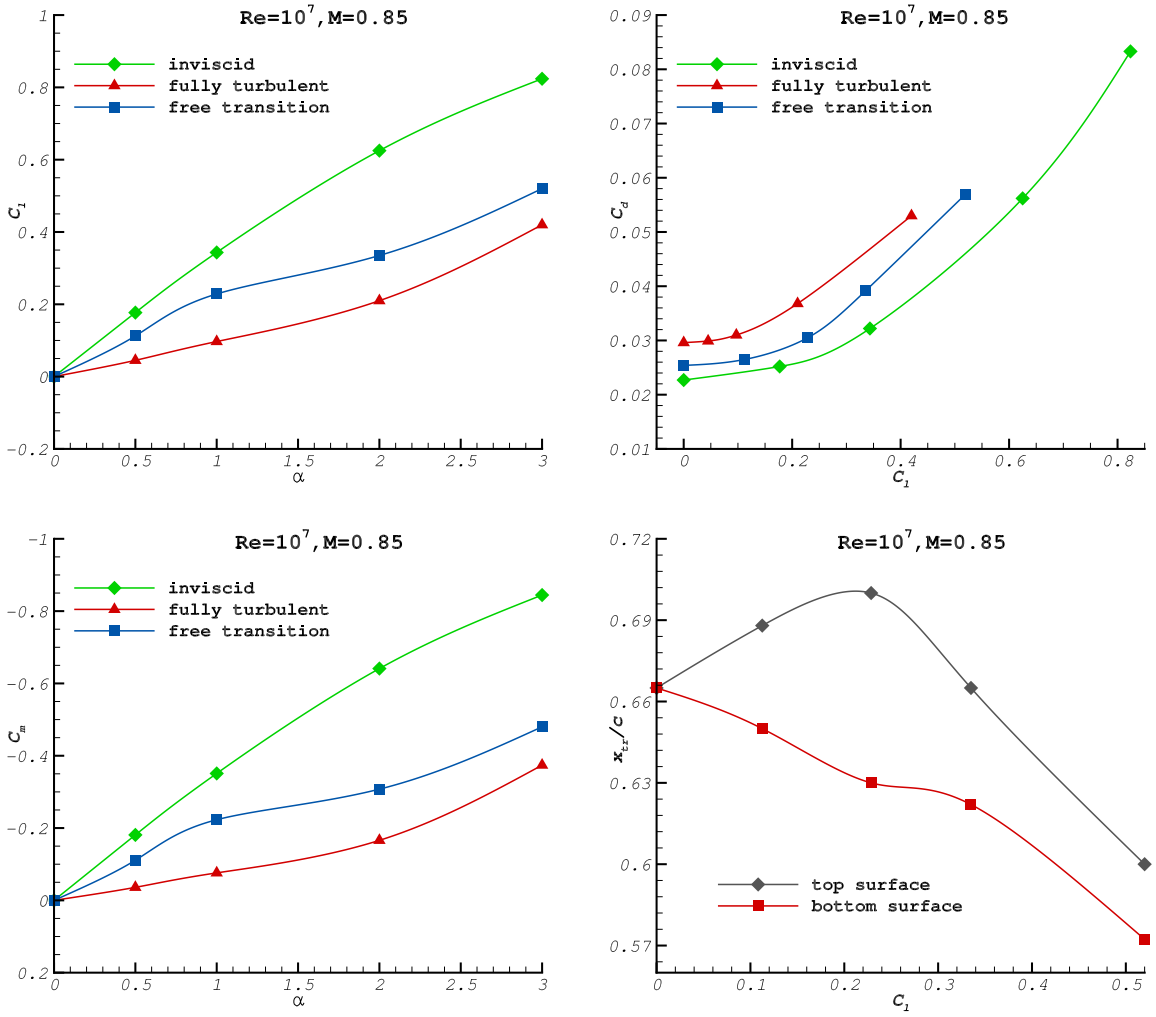

Figure 8.3: Comparison of inviscid, fully turbulent and free transition results of lift (a), drag (b) and moment (c) coefficients. C_m defined positive nose-up, around elastic axis $x/c = -0.5$. Free transition transition position prediction for top and bottom surface (d). NACA 64A010 airfoil at $Re = 10^7$ and $M_\infty = 0.85$.

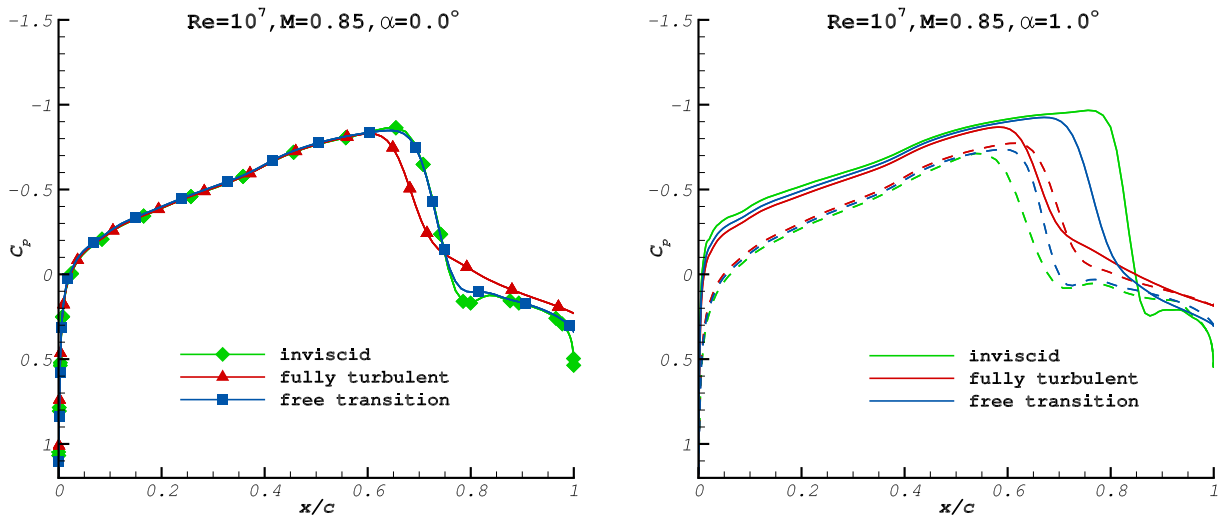

(a) (b)

Figure 8.4: Pressure distribution comparison of NACA 64A010 airfoil for inviscid, fully turbulent and free transition conditions at $Re = 10^7$, $M_\infty = 0.85$ and angle of attack $\alpha = 0.0°$(a) and $\alpha = 1.0°$(b).

The initial condition used for flutter studies is a flow field after a pitching motion with a 1° amplitude. When the elastic system is unstable, the oscillations start increasing in magnitude and when the amplitude is 2° they are generally set to a consistent growth not affected by the initial condition transient. An amplitude of 2° is therefore chosen for pitching studies. Two Mach numbers are picked and multiple reduced frequencies are tested. Figure 8.5 is a summary of lift and moment coefficients, along with a pressure distribution plot at 1/4 of the period.

The first two rows for $M_\infty = 0.85$ simulate reduced frequencies that cover the entire flutter range obtained at $M_\infty = 0.85$ found in the coming sections. The low $\kappa = 0.05$ case is close to a quasi-steady situation, and the differences could be related to the results presented for steady state in Section 8.2. The inclination in the lift and moment plots, and the looping direction of the arrows, identify major differences in the fully turbulent case, while the free transition results are closer to the inviscid simulation. The shock wave position shown at the top surface is also ahead for the fully turbulent condition. The higher $\kappa = 0.3$ case still

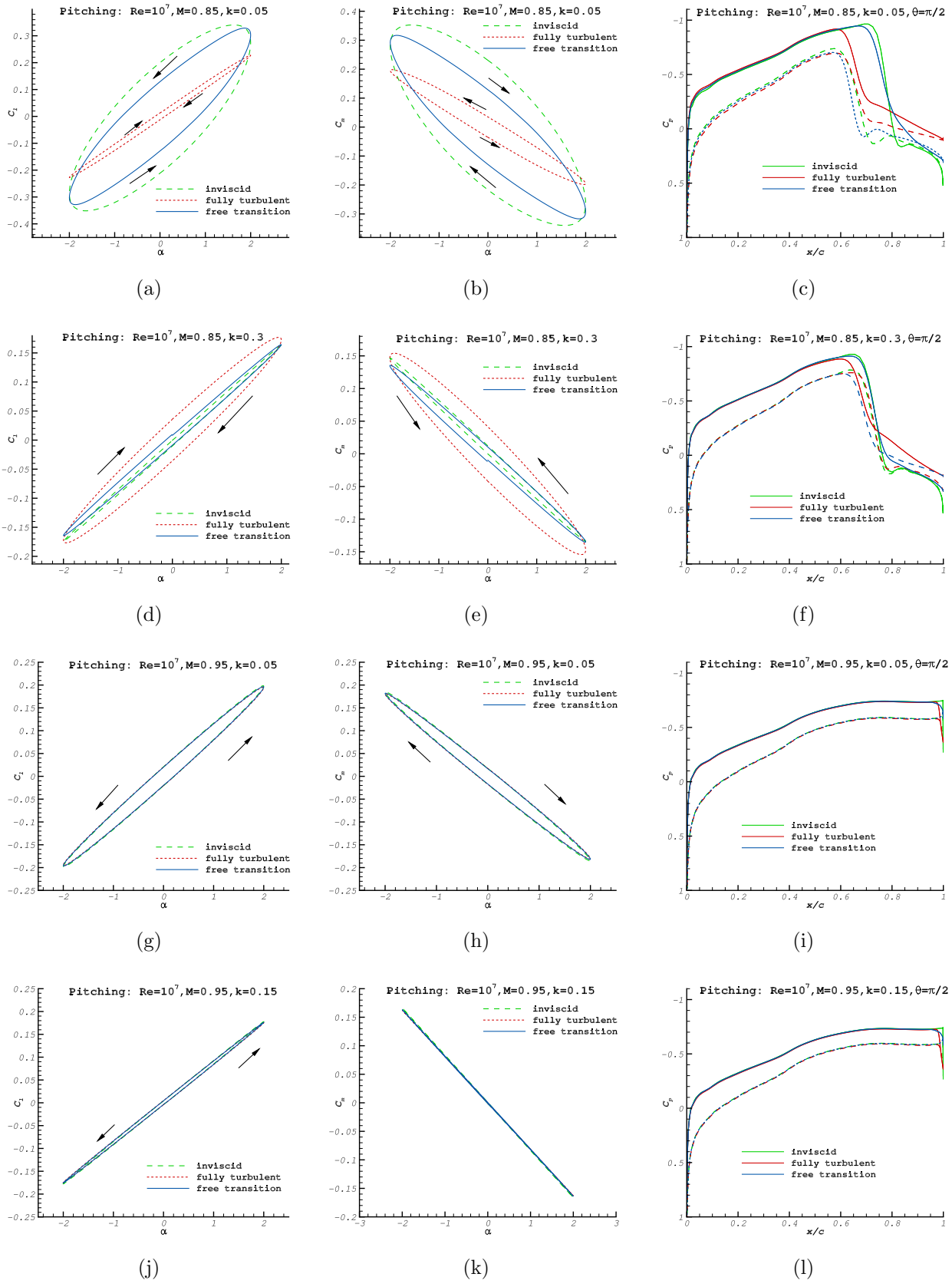

Figure 8.5: Pitching of NACA 64A010 airfoil at $Re = 10^7$ and $M_\infty = 0.85, 0.95$ around $x/c = -0.5$, $AoA = 0.0°$, amplitude of 2°, and reduced frequency $\kappa = 0.05, 0.15, 0.3$.

reveals some differences between the three flow conditions, but not as significant as for the lower $\kappa = 0.05$.

The two bottom rows of Figure 8.5 show the pitching results obtained for $M_\infty = 0.95$ and in this case, the range of reduced frequencies to be covered due to the flutter results found in the coming section is $\kappa = 0.05 - 0.15$. At such a high Mach number, the shock wave is pushed to the trailing edge, and the three flow conditions show identical results.

Figure 8.6 shows heaving results at the same conditions tested for pitching but with a typical amplitude obtained at LCO of $h/c = 0.06$ or $h/b = 0.12$. The conclusions from this figure are the same as that obtained for a pitched motion condition. The high Mach number cases produce an identical response regardless being inviscid, fully turbulent or in free transition. The $M_\infty = 0.85$ case shows differences in lift and moment, being those more significant for the low reduced frequency case.

It is therefore shown that pitching and heaving generate similar conclusions, and that the flow field for $M_\infty = 0.95$ is identical regardless of the flow condition used. However, the forced pitching and heaving for $M_\infty = 0.85$ produce different flow fields for each flow condition, showing similarities between the inviscid and the free-transition flow solutions.

8.4 NACA64A010 Flutter for free transition conditions

A range of Mach number from $0.75 - 0.95$ is simulated for different speed index values (V_F) to obtain the flutter boundary shown in Figure 8.7. Results of inviscid and fully turbulent conditions from Part I (also reported in Marti and Liu [54]) are included for comparison purposes. The free transition results agree very well with the inviscid simulations for the range $M_\infty = 0.75 - 0.85$ and $M_\infty = 0.925 - 0.95$. Such good agreement is due to the delay in the shock wave position for free transition conditions which is located close to the inviscid

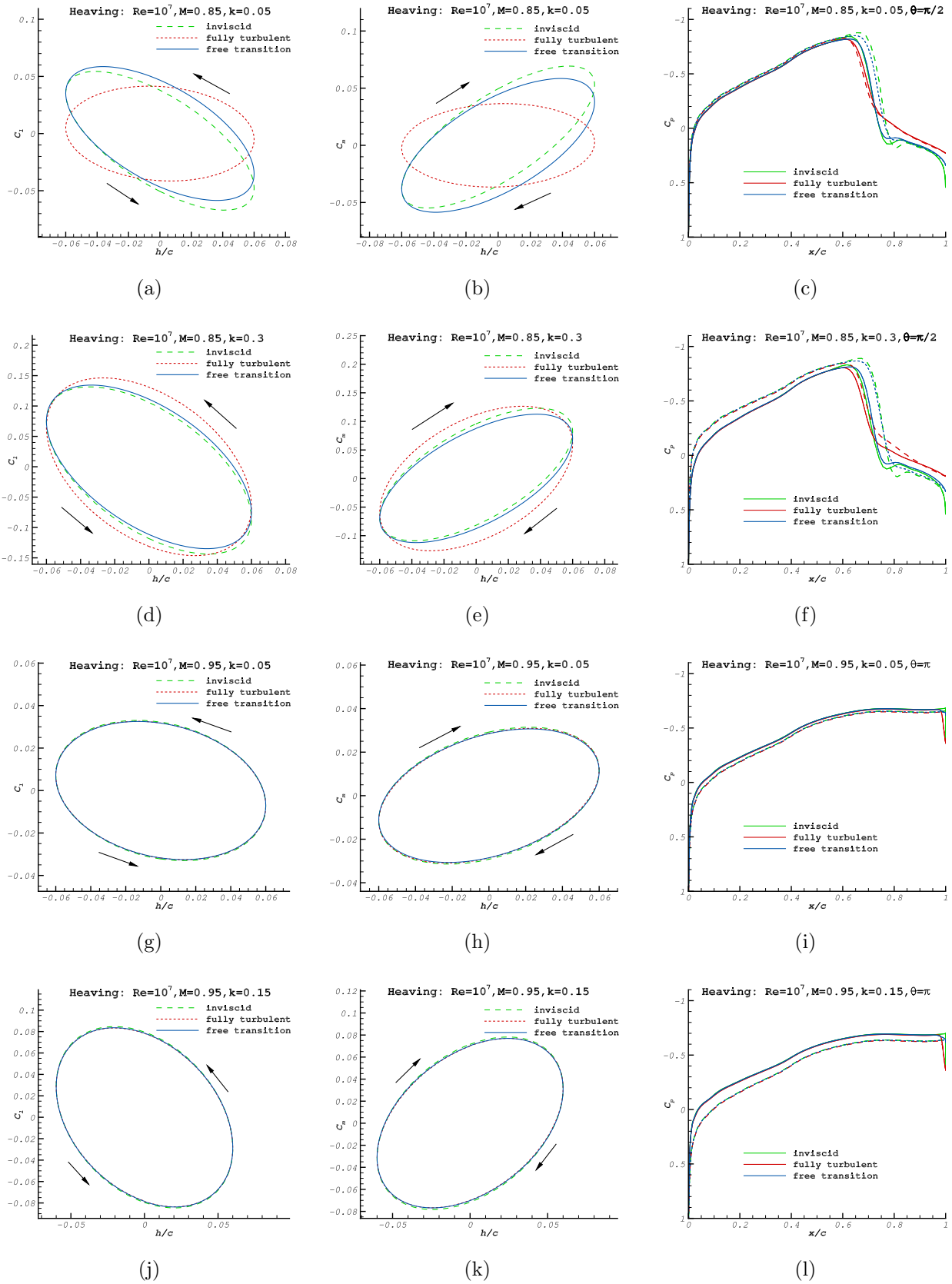

Figure 8.6: Heaving of NACA 64A010 airfoil at $Re = 10^7$ and $M_\infty = 0.85, 0.95$ around $y/c = 0.0$, $AoA = 0.0°$, amplitude of $y/c = 0.06$, and reduced frequency $\kappa = 0.05, 0.15, 0.3$.

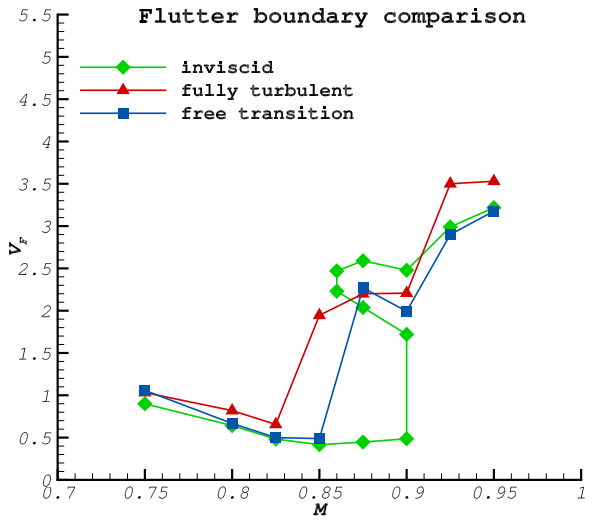

Figure 8.7: Flutter boundary comparison for inviscid, fully turbulent and free transition conditions.

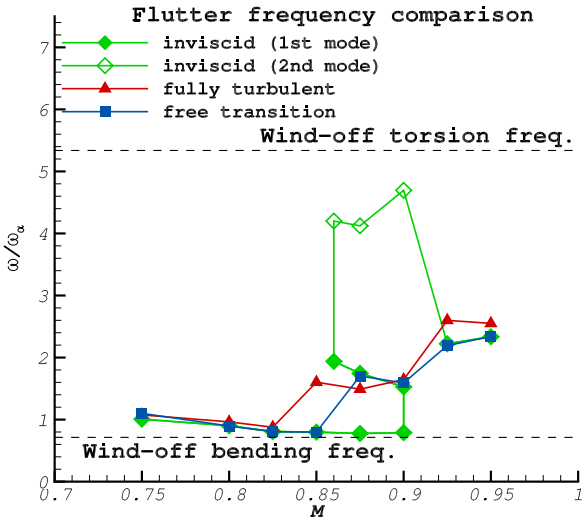

Figure 8.8: Comparison of non-dimensional frequency at the flutter boundary for inviscid, fully turbulent and free transition conditions.

shock position.

For the mid-range $M_\infty = 0.85 - 0.9$ different physics appear for each flow case. In Part I, we perform a detailed analysis in comparing the differences between inviscid and fully turbulent conditions. While the inviscid simulations reveal multiple flutter points for a given Mach number, the fully turbulent results show multiple equilibrium points for a given $\{M_\infty, V_F\}$ couple. Neither of these two scenarios is found in the free transition case.

The frequency response at flutter conditions is shown in Figure 8.8. The frequency is non-dimensionalized by the structural frequency. The results show a similar behavior as those in the previous figure. Free transition and inviscid results agree for the low and high Mach number range, while the three diverge in the mid-range Mach. The inviscid case shows a high frequency response for the mid-range Mach due to the dominance of the second mode.

Figure 8.9 combines the two previous images to obtain a reduced frequency plot where the

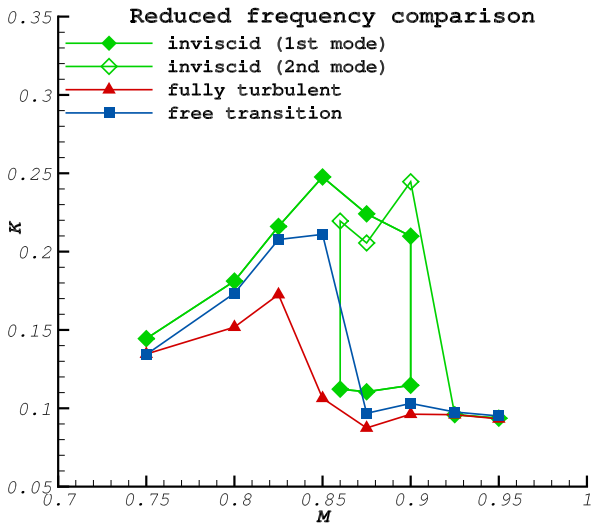

Figure 8.9: Comparison of reduced frequency at the flutter boundary for inviscid, fully turbulent and free transition conditions.

frequency at the flutter boundary is non-dimensionalized by the flow conditions using

$$\kappa = \frac{1}{V_F\sqrt{\mu}}\frac{\omega}{\omega_\alpha} = \frac{b\,\omega}{U_\infty} \tag{8.1}$$

For the cases of $M_\infty = 0.925 - 0.95$, the three flow conditions show the same frequency response. In the previous section, it was determined that for $M_\infty = 0.95$ the heaving and pitching response were identical for the three flow cases generating the same flow field. Therefore, differences in the flutter boundary are only due to the dynamic system itself. On the other hand, for the heaving and pitching case of $M_\infty = 0.85$, the change in shock wave position creates a different mean flow field as seen in the previous section. Difference between inviscid, fully turbulent and free transition flutter boundary at $M_\infty = 0.85$ are therefore due to the different mean flow fields present already in the forced pitching and heaving motions previously described.

For $M_\infty = 0.75$, the fully turbulent results agree very well with the free transition results since a shock wave does not exist. Therefore, the effect of free transition is in the shear

distribution, but the pressure distribution remains the same.

Figures 8.10, 8.11 and 8.12 show an example of the history response for $M_\infty = 0.875$ and $V_F = 2.1, 2.3, 2.5$ where the flutter boundary is at $V_F = 2.27$. Figure 8.10 shows heaving and pitching, along with generalized coordinates for each mode. The first mode is always the dominant one. The solution for $V_F = 2.3$ is not marched until LCO due to the slow growth rate being very close to the neutrally stable situation. The $V_F = 2.5$ case is run until LCO showing a kink in heaving which was also present in the fully turbulent simulations in Part I. Figure 8.11 shows lift and moment coefficients along with transition position. A centered oscillatory behavior is shown for $V_F = 2.1, 2.3$ in transition, while there is a shift in the center of the transition range for higher magnitude oscillations at LCO, as seen for $V_F = 2.5$. The kinks shown in heaving for $V_F = 2.5$, affect the transition history at LCO, not producing a clean sinusoidal shape. Figure 8.12 reveals a kink in pitching for $V_F = 2.5$ which was difficult to visualize in the previous figures. The phase plots for $V_F = 2.5$ are almost identical to those reported for fully turbulent conditions [54] .

The effect of the speed index for V_F values higher than the flutter boundary is presented in Figure 8.13 for $M_\infty = 0.8, 0.85, 0.875$. From lower to higher Mach, the corresponding flutter boundary is at $V_F = 0.667, 0.488, 2.27$. The two lower Mach cases show a heaving amplitude higher than the pitching amplitude, which is a normal response. For the $M_\infty = 0.875$ case however, the kink shown in Figure 8.10 is responsible for producing a lower heaving amplitude compared to the pitching one. The second image of Figure 8.13 reveals a similar trend in the increase of the frequency response with the speed index. The third image, shows a sharp decrease in the elapsed time to reach LCO with increasing V_F. The last image of Figure 8.13 shows the range of motion of transition position. Generally, heaving and pitching are in phase, and the peaks in transition position from Figure 8.11 correspond with heaving and pitching peaks from Figure 8.10. At a peak, the heaving velocity is zero, and most of the effect of transition position will be due to the high pitching angle. Therefore, the

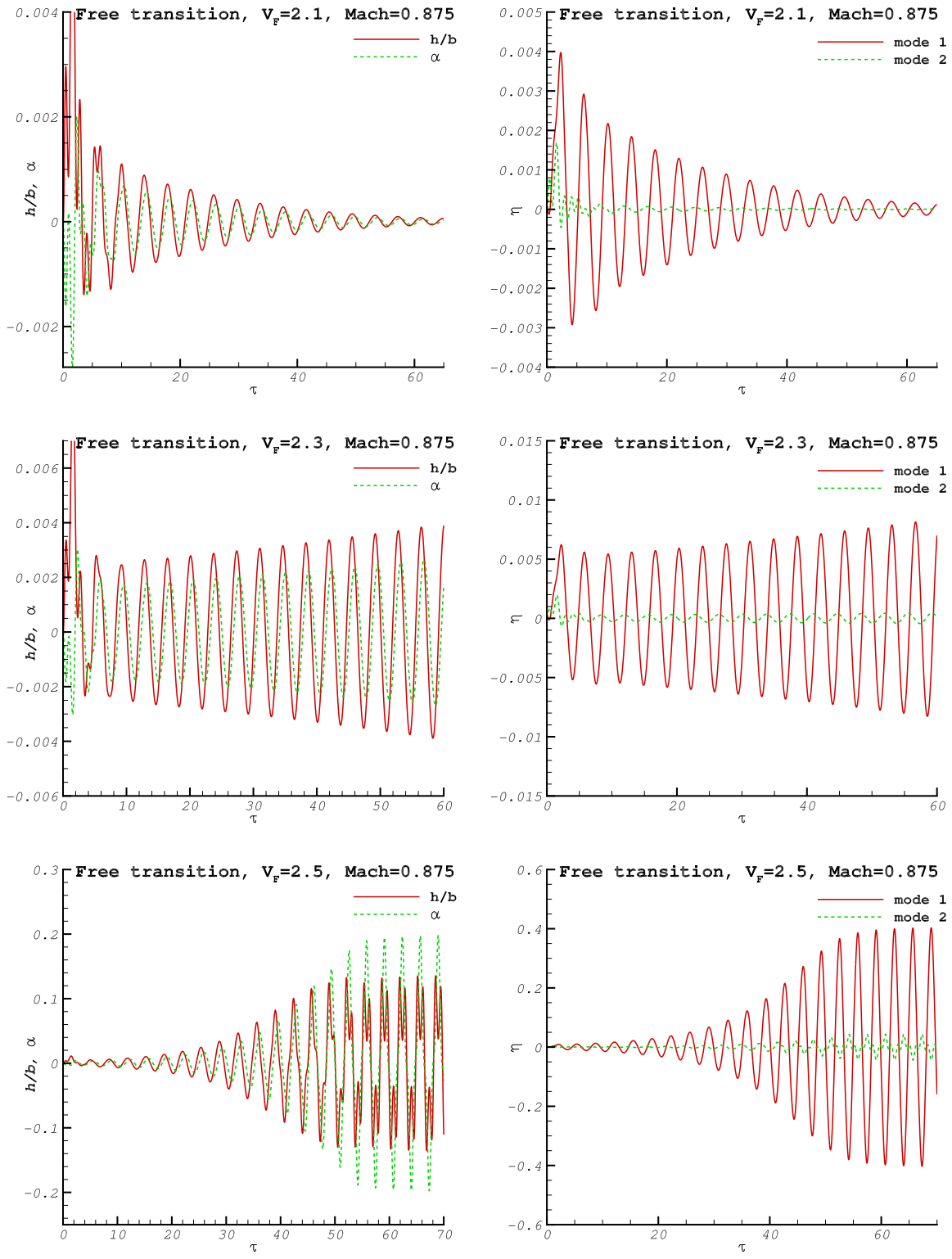

Figure 8.10: Heaving and pitching (left) and modal coordinates (right) for free transition results of NACA 64A010 flutter at $M_\infty = 0.875$, $V_F = 2.1, 2.3, 2.5$.

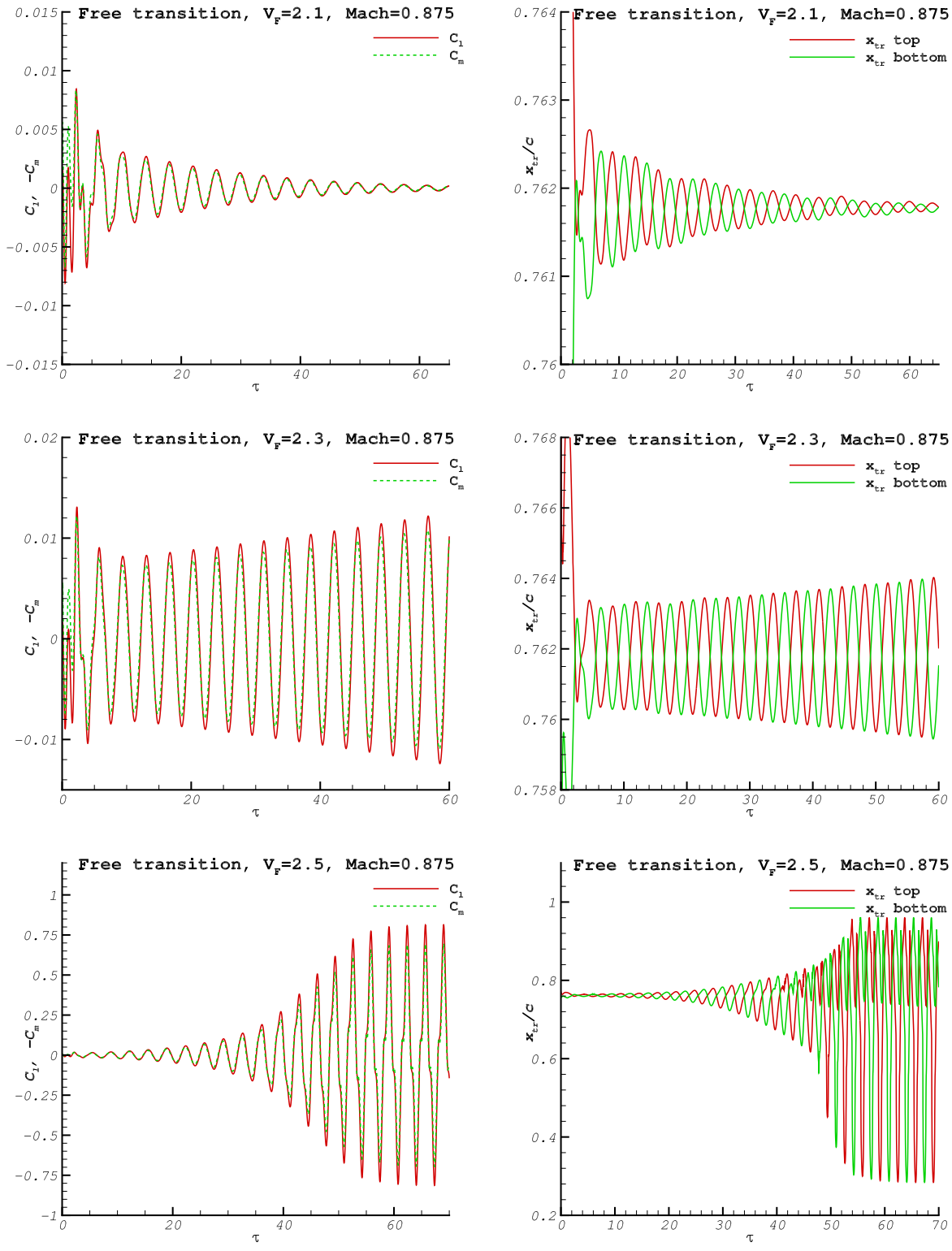

Figure 8.11: Lift and moment coefficients (left) and transition position (right) for free transition results of NACA 64A010 flutter at $M_\infty = 0.875$, $V_F = 2.1, 2.3, 2.5$.

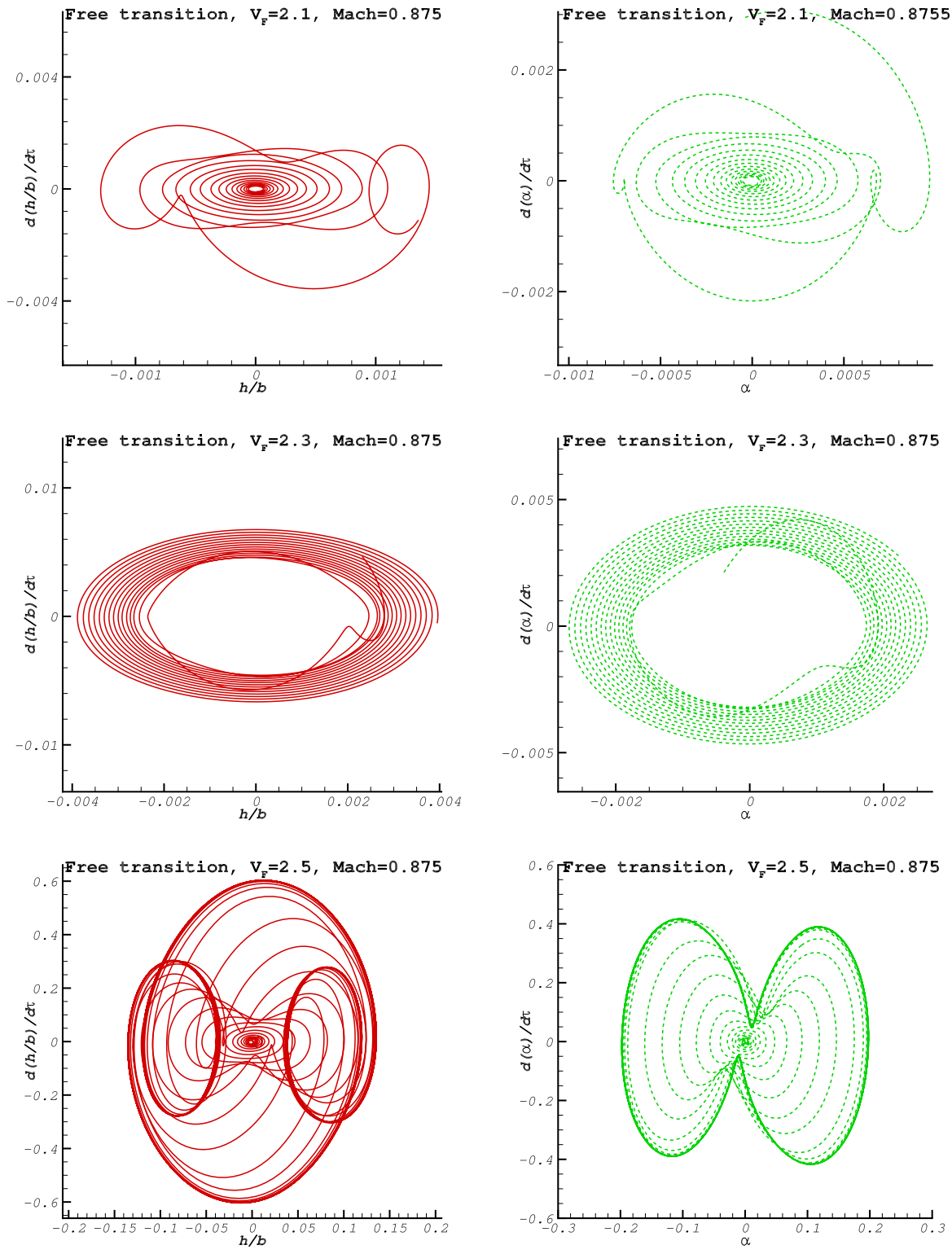

Figure 8.12: Heaving (left) and pitching (right) phase for free transition results of NACA 64A010 flutter at $M_\infty = 0.875$, $V_F = 2.1, 2.3, 2.5$.

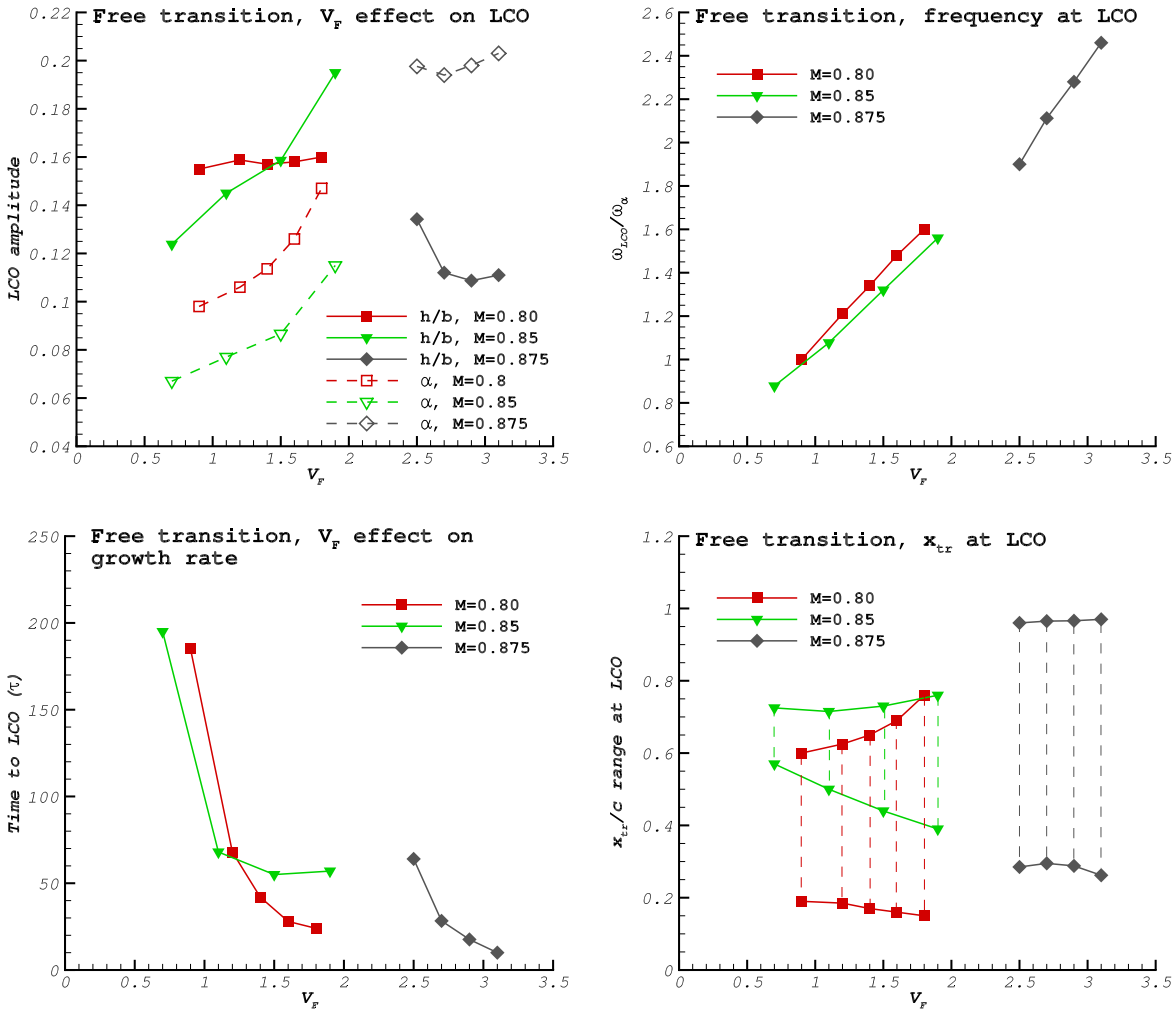

Figure 8.13: Limit Cycle Oscillation results for $M_\infty = 0.80, 0.85, 0.875$ for multiple speed index values above the corresponding flutter boundary.

range of transition position seems to be dominated by the magnitude of the pitching motion. The first image of Figure 8.13 shows a higher pitching amplitude for $M_\infty = 0.875$, followed by $M_\infty = 0.8$ and $M_\infty = 0.85$. This agrees with the last image of Figure 8.13 where the higher range for transition position corresponds to $M_\infty = 0.875$, followed by $M_\infty = 0.8$ and $M_\infty = 0.85$.

Chapter 9

Conclusions Part III

The effect of laminar-turbulent transition is studied in a fluid-structure interaction of the NACA 64A010 airfoil for Reynolds number 10 million and Mach number range of 0.75-0.95. The shock wave in free transition is delayed compared to the fully-turbulent case. This brings the free-transition shock close to the position obtained for inviscid simulations.

Three freestream Mach ranges are differentiated in the flutter boundary.

The lower range of $M_\infty = 0.75 - 0.85$, and the higher range of $M_\infty = 0.925 - 0.95$ reveal a free-transition boundary almost identical to the inviscid flutter-boundary, but different from the fully-turbulent case. Forced pitching and heaving at those Mach numbers reveal the flowfield to be very similar for free-transition and inviscid conditions. The forced-motion flowfield for the high Mach range is almost identical for the three flow conditions. For the low Mach range, the forced-motion flowfield for free-transition agrees with the inviscid case but strongly disagrees with the fully-turbulent flowfield.

Therefore, since the forced-motion fully-turbulent flowfield differs from the other two flow conditions in the low-Mach range, when the system is set free in elastic mode, the fully-

turbulent flutter-response will also differ.

For the high-Mach range, where the forced-motion flowfield is the same for the three flow conditions, the difference in the fully-turbulent flutter boundary is caused by the new dynamic system. When adding the two degrees-of-freedom from the structural equations to the many degrees-of-freedom from the CFD grid, the new dynamic system affects the fully-turbulent elastic response only.

The mid-range $M_\infty = 0.875 - 0.9$ shows different flutter responses for inviscid, free-transition and fully-turbulent conditions. The inviscid solution predicts multiple flutter points, the fully-turbulent case reveals multiple equilibrium points, and the free-transition simulation shows a smooth boundary without any of the two phenomena.

Differences in the three flutter boundaries are strongly affected by non-linear effects. In the low-Mach range, the shock is weak and non-linear effects are not strong which creates a boundary with a similar trend for the three flow conditions. In the high-Mach range, the shock is pushed until the trailing edge. Therefore non-linear effects are not dominant since the shock position is not changing and the flutter-boundary trend is again similar for the three flow conditions. In the mid-Mach range, a strong shock is moving over the airfoil surface. Non-linear effects due to the shock motion are responsible for generating different elastic responses for each flow condition.

Chapter 10

Future work

While the present work has been successful in proving the existence of Multiple Equilibrium Points in non-linear flutter, and in assessing the importance of free-transition in transonic aeroelastic simulations, it has been limited to two-dimensional problems. The structural model used represents a mid-span section of a three-dimensional sweptback wing.

The future work will extend the results from this dissertation to three-dimensional wings, and understand if three-dimensional variations will impact the conclusions found in this document. Some preliminary results of three-dimensional aeroelastic deformations are included in appendix C, where a stable loading deforms the wing structure. Appendices A and B describe the numerical methods needed for three-dimensional structural deformation.

When computing three-dimensional free transition, crossflow instabilities must be included to obtain realistic results. A first approach can use the present e^N model for constant-span sections, along with a crossflow instability model for the third direction, and use an effective N_{crit} value combining streamwise and cross flow transition. An example of such work is detailed in [78]. A different approach is using the $Re_\theta - \gamma$ turbulence model [46], which predicts free transition in three-dimensional flow, although at higher computing cost.

Bibliography

[1] E. Albano and W. Rodden. A doublet-lattice method for calculating lift distributions on oscillating surfaces in subsonic flows. *AIAA Journal*, 7:279–285, 1969.

[2] J. Alonso and A. Jameson. Fully-implicit time-marching aeroelastic solutions. *AIAA 94-0056*, 1994.

[3] W. K. Anderson and D. L. Bonhaus. An implicit upwind algorithm for computing turbulent flows on unstructured grids. *Computers Fluids*, 23(1):1–21, 1994.

[4] K. Asai, H. Kanda, T. Kunimasu, T. Liu, and J. P. Sullivan. Boundary-layer transition detection in a cryogenic wind tunnel using luminescent paint. *Journal of Aircraft*, 34(1), 1997.

[5] K. J. Badcock, A. M. Rampurawala, and B. E. Richards. Intergrid transformation for aircraft aeroelastic simulations. *AIAA Paper 2003-3512*, 2003.

[6] B. S. Baldwin and H. J. Lomax. Thin layer approximation and algebraic model for separated turbulent flows. *AIAA Paper 78-257*, 1978.

[7] J. T. Batina. Unsteady euler airfoil solutions using unstructured dynamic meshes. *AIAA J.*, 28(8):1381 – 1388, 1990.

[8] J. T. Batina. Unsteady euler algorithm with unstructured dynamic mesh for complex-aircraft aerodynamic analysis. *AIAA J.*, 29(3):327 – 333, 1991.

[9] J. Blazek. *Computational Fluid Dynamics: Principles and Applications*. 2005.

[10] J. Bohbot and J. Garnier. Computation of the flutter boundary of and aifoil with a parallel navier-stokes solver. *39th Aerospace Sciences Meeting and Exhibit*, 2001.

[11] J. Boussinesq. Essai sur la thdorie des eaux courantes. *Mem. Pres. Acad. Sci., XXIII*, 46, 1877.

[12] J. Boussinesq. Theorie de l' dcoulement tourbillonant et tumulteur des liquides dans les lits rectiligues. *Comptes Rendus de l' Acad. des Sciences, CXXII*, page 1293, 1896.

[13] R. J. Boyle and F. F. Simon. Mach number eeffect on turbine blade transition length prediction. *43rd International Gas Turbine and Aeroengine Congress and Exhibition*, 1999.

[14] J. Cai, F. Liu, H. Tsai, and A. Wong. Static aero-elastic computation with a coupled cfd and csd method. *AIAA Paper 01-0717*, 2001.

[15] T. Cebeci. Essential ingredients of a method for low reynolds-number airfoils. *AIAA Journal*, 27(12), 1988.

[16] T. Cebeci and A. M. O. Smith. Analysis of turbulent boundary layers. *Academic Press, N. Y.*, 1974.

[17] N. G. R. Center. Rae 2822 transonic airfoil: Study 4. *NPARC Alliance Validation Archive*, http://www.grc.nasa.gov/WWW/wind/valid/raetaf/raetaf04/raetaf04.html.

[18] X. Chen, G.-C. Zha, Z. Hu, and M.-T. Yang. Flutter prediction based on fully coupled fluid-structure interactions. *9th National Turbine Engine High Cycle Fatigue Conference*, 2004.

[19] A. K. Chopra. *Dynamics of Structures*. Prentice Hall, 2000.

[20] P. H. Cook, M. A. McDonald, and M. C. P. Firmin. Aerofoil rae 2822 - pressure distributions, and boundary layer and wake measurements. *Experimental Data Base for Computer Program Assessment, AGARD Report AR 138*, 1979.

[21] R. D. Cook. *Finite Element Modeling for Stress Analysis*. John Wiley and Sons, 1995.

[22] M. Drela. Xfoil: An analysis and design system for low reynolds number airfoils. *Low Reynolds Number Aerodynamics, Springer-Verlag Lec. Notes in Eng. 54*, 1989.

[23] M. Drela and M. B. Giles. Viscous-inviscid analysis of transonic and low reynolds number airfoils. *AIAA Journal*, 25(10), 1987.

[24] J. Edwards, R. Bennett, and D. Seidel. Time marching transonic flutter solutions including angle of attack effects. *AIAA Paper 82-0685*, 1982.

[25] F. Ehlers and W. Weatherill. A harmonic analysis method for unsteady transonic flow and its application to the flutter of airfoils. *NASA Contractor Report 3537*, 1982.

[26] A. A. R. N. . Experimental Data Base for Computer Program Assessment. Nlr 7301 airfoil. *Report of the fluid dynamics panel working group 04*, 1979.

[27] C. Gao, S. Yang, S. Luo, F. Liu, and D. M. Schuster. Calculation of airfoil flutter by an euler method with approximate boundary conditions. *AIAA Journal*, 43(2), 2005.

[28] G. S. L. Goura, K. J. Badcock, M. A. Woodgate, and B. E. Richards. Transformation methods for the time marching analysis of flutter. *AIAA Paper 2001-2457*, 2001.

[29] N. Gregory and C. L. O'Reilly. Low-speed aerodynamic characteristics of naca0012 aerofoil section, including the effects of upper-surface roughness simulating hoar forst. Aeronautical research council reports and memoranda, Ministry of Defense (Procurement Executive), London, 1973.

[30] T. J. P. Hall, K. C. and E. H. Dowell. Proper orthogonal decomposition technique for transonic unsteady aerodynamic flows. *AIA Journal*, 38(10):1853–1862, 2000.

[31] A. Harten. High resolution schemes for hyperbolic conservation laws. *Journal Computational Physics*, 49:357–393, 1983.

[32] J. Held. *Large Eddy Simulations of Separated Compressible Flows Around 3-D Configurations*. PhD thesis, Lund Institute of Technology, 1998.

[33] J. L. Hess and A. M. O. Smith. Calculation of non-lifting potential flow about arbitrary three-dimensional bodies. *Douglas Aircraft Report, ES 40622*, 1962.

[34] C. Hirsch. *Numerical computation of internal and external flows*. Elseiver, 2007.

[35] T. L. Holst. Viscous transonic airfoil workshop compendium of results. *Journal of Aircraft*, 25(12), 1988.

[36] K. Isogai. On the transonic-dip mechanism of flutter of a swept back wing. *AIAA Journal*, 17(7):793–795, 1979.

[37] A. Jameson. Multigrid algorithms for compressible flow calculations. *Princeton University MAE Report 1743*, 1985.

[38] A. Jameson. Aerodynamic design via control theory. *Journal of Scientific Computing*, 3:233–260, 1988.

[39] A. Jameson. Time-dependent calculations using multigrid with applications to unsteady flows past airfoils and wings. *AIAA Paper 91-1596*, 1991.

[40] A. Jameson. Artificial diffusion, upwind biasing, limiters and their effect on accuracy and multigrid convergence in transonic and hypersonic flow. *AIAA Paper 93-3559*, 1993.

[41] A. Jameson, W. Schmidt, and E. Turkel. Numerical solution of the euler equations by finite volume methods using runge-kutta time-stepping schemes. *AIAA Paper 81-1259*, 1981.

[42] J. Johansen. Prediction of laminar/turbulent transition in airfoil flows. *Riso National Lab., Roskilde, Denmark*, 1997.

[43] J. John D. Anderson. *Computational fluid dynamics: the basics with applications*. McGraw-hill, 1995.

[44] R. A. Kilgore, M. J. Goodyer, J. B. Adcock, and E. E. Davenport. The cryogenic wind-tunnel concept for high reynolds number testing. *NASA Technical Note D-7762*, 1974.

[45] R. H. Landon. Naca 0012 oscillating and transient pitching. *Compendium of Unsteady Aerodynamic Measurements, Data Set 3. AGARD Report R-702*, 1982.

[46] R. Langtry and F. Menter. Transition modeling for general cfd applications in aeronautics. *43rd AIAA Aerospace Sciences Meeting and Exhibit*, 2005.

[47] B. E. Launder and B. Spalding. The numerical computation of turbulent flows. *Comput. Methods Appl. Mech. Eng.*, 3:269 – 289, 1974.

[48] J.-D. Lee and A. Jameson. Nlf airfoil and wing design by adjoint method and automatic transition prediction. *27th AIAA Aplied Aerodynamics Conference*, 2009.

[49] B. V. Leer. Towards the ultimate conservative difference scheme v. a second order sequel to godunov's method. *Journal Computational Physics*, 32:101–136, 1979.

[50] B. V. Leer. Flux-vector splitting for the euler equations. *Proc. 8th International Conference of Numerical Methods in Fluid Dynamics*, pages 507–512, 1982.

[51] F. Liu, J. Cai, Y. Zhu, H. M. Tsai, and A. S. F. Wong. Calculation of wing flutter by a coupled fluid-structure method. *Journal of Aircraft*, 38(2), 2001.

[52] C. M. Maksymiuk and T. H. Pulliam. Viscous transonic airfoil workshop results using arc2d. *AIAA 25th Aerospace Sciences Meeting*, 1987.

[53] F. Marti and F. Liu. Flutter study of naca 64a010 airfoil using urans and e^n transition models coupled with an integral boundary layer code. *AIAA Conference*, 2017.

[54] F. Marti and F. Liu. Multiple equilibrium points of airfoil flutter in viscous flow. *AIAA Conference*, 2017.

[55] L. Martinelli. *Calculations of Viscous Flows with a Multigrid Method*. PhD thesis, Princeton University, 1987.

[56] D. J. Mavriplis and A. Jameson. Multigrid solution of the navier-stokes equations on triangular meshes. *AIAA J.*, 28:1415 – 1425, 1990.

[57] F. Menter. Two-equation eddy-viscosity turbulence models for engineering applications. *AIAA 93-2906*, 1993.

[58] G. Moretti and M. Abbett. A time-dependent computational method for blunt body flows. *AIAA J.*, 4(12):2136–2141, December 1966.

[59] E. M. Murman and J. D. Cole. Calculation of plane steady transonic flows. *AIAA Journal*, 9:114–121, 1971.

[60] C. Nebel, R. Radespiel, and T. Wolf. Transition prediction for 3d flows using a reynolds-averaged navier-stokes code and n-factor methods. *33rd AIAA Fluid Dynamics Conference and Exhibit*, 2003.

[61] D. Patterson and J. L. Hennessy. *Computer Architecture: A Quantitative Approach*. 2012.

[62] B. Prananta, M. Hounjet, and R. Zwaan. Two-dimensional transonic aeroelastic analysis using thin-layer navier-stokes method. *Journal of Fluids and Structures*, 12:655–676, 1998.

[63] D. E. Raveh. Numerical study of an oscillating airfoil in transonic bufbuffet flows. *AIAA Journal*, 47(3), 2009.

[64] A. Relvas and A. Suleman. Aeraeroelastic of nonlinear structures using the corotational method. *Jounral of Aircraft*, 43(3):749–762, 2006.

[65] B. A. Robinson, J. T. Batina, and H. T. Y. Yang. Aeroelastic analysis of wings using the euler equations with a deforming mesh. *J. Aircraft*, 28(11):781 – 788, 1991.

[66] M. Robitaille, A. Mosahebi, and E. Laurendeau. Design of adaptive transonic laminar airfoils using the $\gamma - re_{\theta t}$ transition model. *Aerospace Science and Technology*, 46:60–71, 2015.

[67] P. Roe. Approximate riemann solvers, parameter vectors and difference schemes. *Journal of Computational Physics*, 43:357–372, 1981.

[68] M. Sadeghi. *Parallel computation of three-dimensional aeroelastic fluid-structure interaction*. PhD thesis, University of California Irvine, 2004.

[69] M. Sadeghi, F. Liu, K. L. Lai, and H. M. Tsai. Application of three-dimensional interfaces for data transfer in aeroelastic computations. *AIAA Paper 2004-5376*, 2004.

[70] D. M. Somers. Design and experimental results for a natural-laminar-flow airfoil for general aviation application. *NASA Technical Paper*, 1981.

[71] B. K. Soni. Two and three dimensional grid generation for internal flow applications of computational fluid dynamics. *AIAA Paper 85-1526*, 1985.

[72] P. Spalart. Strategies for turbulence modelling and simulations. *Int. J. Heat Fluid Flow*, 21:252 – 263, 2000.

[73] P. Spalart. Trends in turbulence treatments. *AIAA Paper 2000-2306*, 2000.

[74] P. R. Spalart and S. R. Allmaras. A one-equation turbulence model for aerodynamic flows. *30th Aerospace Sciences Meeting and Exhibit*, 1992.

[75] J. L. Steger and R. F. Warming. Flux vector splitting of the inviscid gas-dynamic equations with applications to finite difference methods. *Journal Computational Physics*, 40:263–293, 1981.

[76] H.-W. Stock. Determination of length scales in algebraic turbulence models for navier-stokes methods for airfoils. *AIAA Journal*, 27(10), 1999.

[77] H.-W. Stock and W. Haase. Feasibility study of en transition prediction in navier-stokes methods for airfoils. *AIAA Journal*, 37(10), 1999.

[78] P. Sturdza. *An Aerodynamic Design Method for Supersonic Natural Laminar Flow Aircraft*. PhD thesis, Stanford University, 2003.

[79] W. Sutherland. The viscosity of gases and molecular force. *Philosophical Magazine*, 36:507–531, 1893.

[80] R. C. Swanson and R. Radespiel. Cell centered and cell vertex multigrid schemes for the navier-stokes equations. *AIAA J.*, 29(5):697 – 703, 1991.

[81] R. C. Swanson and E. Turkel. On central difference and upwind schemes. *Journal of Computational Physics*, 101:297 – 306, 1992.

[82] H. Tsai, A. S. F. Wong, j. Cai, Y. Zhu, and F. Liu. Unsteady flow calculations with a parallel moving mesh algorithm. *AIAA J.*, 39(6):1021 – 1029, 2001.

[83] G. Wang, H. H. Mian, Z.-Y. Ye, and J.-D. Lee. Numerical study of transitional flow around nlr-7301 airfoil using correlation-based transition model. *Journal of Aircraft*, 51, 2014.

[84] D. C. Wilcox. Reassessment of the scale determining equation for advanced turbulence models. *AIAA Journal*, 26:1299 – 1310, 1988.

[85] W. L. Wood. *Practical Time-Stepping Schemes*. Oxford Applied Mathematics and Computing Science, Oxford University Press, 1990.

[86] S. Yang, Z. Zhang, F. Liu, S. Luo, H.-M. Tsai, and D. M. Schuster. Time-domain aeroelastic simulation by a coupled euler and integral boundary-layer method. *AIAA*, 2004.

Appendices

A Computational Structure Dynamics for three-dimensional applications

From classic vibration analysis theory, one can express the structural dynamics equation for a case of linear stiffness and linear damping as

$$[M]\ddot{q} + [C]\dot{q} + [K]q = F \tag{A.1}$$

where M, C and K are the mass, damping and stiffness matrices, respectively. q is the vector of displacements and F the external loading.

Normally when using Equation A.1 to perform a vibration analysis of a mechanical device, the external loading F is a function of time $F = F(t)$. For an aeroelastic computation, the loading not only depends on time but on the displacement and velocity of the geometry of study,

$$F = F(q, \dot{q}). \tag{A.2}$$

Discretizing and directly solving Equation A.1 is known as direct analysis. The direct analysis is time consuming but provides the exact solution. A different and popular approach known as modal solution is sometimes preferred. The modal analysis performs an eigenvalue and eigenvector decomposition transforming Equation A.1 into the so-called vibration equation for generalized coordinates A.7.

Since the geometry of study is represented by a discrete number of grid points, the number of degrees of freedom and therefore the number of modes (or eigenvectors) is bounded. If one would solve all the modes with the generalized equations the same solution produced by the direct analysis would be obtained.

The modal discretization also allows to study the individual contribution of each mode to the final body motion which facilitates the understanding of the physical phenomenon. The last and crucial reason for the implementation of a modal solution in ParCAE is the facility for introducing the structural inputs in our code. While the mathematics behind a modal analysis are more complicated than those of a direct solution case, the inputs required for a modal analysis are much simpler. The direct solution requires the user to input the stiffness, damping and mass matrices and the entire structural geometry. When using a modal analysis only the modes and eigenfrequencies (or eigenvalues of the free vibration problem) are required along with the surface of the body; the complete interior structure of the body is not required. Using a Finite-Element-Method software and analysing the properties of the entire structural geometry, the eigenfrequencies and eigenvectors are obtained and just the contribution from the nodes on the surface will be later used in ParCAE. The reason for only needing the points from the surface of the body is because those are the ones that receive external loading and therefore, the only ones that contribute to the structural equation in generalized coordinates (Equation A.7).

A.1 Modal Analysis

Starting by the eigenvalue and eigenvector decomposition of the free vibration problem [21], [19]

$$[M]\ddot{q} + [K]q = 0 \tag{A.3}$$

one obtains the eigenvalues

$$\lambda_i = \omega_i^2 = {\phi_i}^T[K]\phi_i \tag{A.4}$$

and the eigenvectors ω_i of the system. λ_i denotes the ith eigenvalue and ω refers to natural frequency. Such task could be done with the help of a Finite-Element-Method external software. The eigenvectors are the so-called normal modes and the eigenvalues correspond to the natural frequencies of the system. In a mechanical system where $F = F(t)$ each vibration mode ϕ_i defines the movement of the structure for a particular natural frequency ω_i. The final frequency of the structure will be a combination of the existing natural frequencies. For an aeroelastic problem, $F = F(q(t), \dot{q(t)})$. This means that the natural frequencies and the associated modes computed from Equation A.3 are not the real natural frequencies of the system and neither are the associated modes. However, a modal decomposition could be thought as a complete set of vectors that expand a vector space. As long as the set is complete the representation of a particular value will be correct no matter which specific vectors we choose to complete our set. The difference however, will lay on the lack of physical meaning when using a random set of vectors. Because the natural frequencies of the system are unknown a priori when $F = F(q(t), \dot{q(t)})$, the eigenvalues from Equation A.4 are referred as eigenfrequencies. Such eigenfrequencies do not represent physical frequencies any more. The associated eigenvectors are usually still denoted as normal modes which are associated

with the corresponding eigenfrequencies but not to any physical frequency of the problem. When analyzing the original problem where $F = F(t)$, a common approach is to use the first five or six modes to describe the entire motion of the structure. In a vector expansion, it could be thought as a truncated summation of the expansion of a solution. The first modes of the system are associated with the low natural frequencies of the system, which define the largest deformations. Therefore, using a few instead of the full set of modes provides a quite accurate description of the movement of the body and saves computational time.

For an aeroelastic problem where the eigenfrequencies do not correspond to any physical frequency of the system, the choice of the first modes to describe the vibration of the system is not so clear. Even if the natural frequencies of the aeroelatic geometry are not the eigenfrequencies whose associated modes are being used to represent the problem, the final solution is still proven to be well expanded. While in the original problem the contribution to the displacement by mode $n+1$ is below the one from mode n, in the aeroelastic problem this could not be the case. However, when the first five or six modes of the original system are used to describe the motion of the aeroelatic problem, one confirms that the contribution to the deformation by some of the higher modes is about two orders of magnitude below the contribution of the first mode. Therefore, these results validate the use of the original modes to expand the aeroelastic deformation vector.

Since the information that the modes provide is in the direction and not the magnitude of the vector, one could scale the modes to his convenience. If one defines the vector of displacements as

$$q = \eta\phi \tag{A.5}$$

where η are the so-called generalized coordinates, a convenient scaling for the modes is

$$\phi_i{}^T[M]\phi_i = 1. \tag{A.6}$$

With Equation A.5 and A.6, one can easily transform Equation A.1 into the structural dynamic equation for generalized coordinates,

$$\ddot{\eta}_i + 2\zeta_i\omega_i\dot{\eta}_i + \omega_i{}^2\eta_i = Q_i \tag{A.7}$$

where i represents each mode, ζ_i denotes the modal damping ratio and Q_i is the generalized force expressed as

$$Q_i = \phi_i{}^T F. \tag{A.8}$$

Equation A.7 is a decoupled equation for each mode. This is due to the orthogonality of the eigenvectors with both the stiffness and the mass matrices. By exploring further this equation, after using the full geometry to determine the eigenfrequencies and eigenvectors, one must use all the nodes that receive an external loading and therefore, contribute to Equation A.7. If one wants to use nodes that do not receive external loading just to study their motion, it will not affect the final solution of the generalized coordinates and it is a valid option. From this discussion, one could observe that if a body will just receive loading in force but not in moment, each eigenvector to be used can be shortened by avoiding the angular terms since they will not contribute to the generalized coordinates. This has been the approach followed in ParCAE.

A.2 Temporal discretization of the structural equations

For each mode, Equation A.7 is transformed into a system of two first-order differential equations [19], [85] by denoting

$$x_{1i} = \eta_i, \qquad \dot{x_{1i}} = x_{2i}, \qquad \dot{x_{2i}} = Q_i - 2\zeta_i\omega_i x_{2i} - {\omega_i}^2 x_{1i} \tag{A.9}$$

which expressed in matrix notation becomes

$$\dot{X}_i = [A_i]X_i + B_i \tag{A.10}$$

with

$$\dot{X}_i = \begin{bmatrix} x_{1i} \\ x_{2i} \end{bmatrix}, \qquad [A_i] = \begin{bmatrix} 0 & 1 \\ -\omega_i^2 & -2\omega_i\zeta_i \end{bmatrix}, \qquad B_i = \begin{bmatrix} 0 \\ Q_i \end{bmatrix}. \tag{A.11}$$

Using the convenient transformation $X_i = [P_i]Z_i$, where

$$[P_i] = \begin{bmatrix} -\frac{\zeta_i + \sqrt{\zeta^2 - 1}}{\omega_i} & \frac{-\zeta_i + \sqrt{\zeta^2 - 1}}{\omega_i} \\ 1 & 1 \end{bmatrix} \tag{A.12}$$

one transforms a coupled system of two first-order differential equations in X_i (Equation A.10), into a decoupled system of two first-order differential equations in Z_i (Equation A.13).

$$\dot{Z}_i = [P_i]^{-1}[A_i][P_i]Z_i + [P_i]^{-1}B_i \tag{A.13}$$

Equation A.13 in component notation is,

$$\frac{dz_{(1,2)i}}{dt} = \omega_i \left(-\zeta_i \pm \sqrt{\zeta_i^2 - 1} \right) z_{(1,2)i} + \frac{\sqrt{\zeta_i^2 - 1} \mp \zeta_i}{2\sqrt{\zeta_i^2 - 1}} Q_i \tag{A.14}$$

with $Z_i = (z_{1i}, z_{2i})^T$.

The last step is to discretize the LHS of Equation A.14. Choosing the same second-order backward temporal discretization than in the dual-time stepping scheme for the flow equations,

$$\begin{aligned} R_s^*(Z_i^{n+1}) =& \omega_i \left(-\zeta_i \pm \sqrt{\zeta_i^2 - 1} \right) z_{(1,2)i}^{n+1} + \frac{\sqrt{\zeta_i^2 - 1} \mp \zeta_i}{2\sqrt{\zeta_i^2 - 1}} Q_i^{n+1} \\ & - \frac{3z_{(1,2)i}^{n+1} - 4z_{(1,2)i}^{n} + z_{(1,2)i}^{n-1}}{2\Delta t} \end{aligned} \tag{A.15}$$

where $R_s^*(Z_i^{n+1})$ denotes the residual of iteration $n+1$. This formulation is also marched in pseudo-time like in the CFD case. When the residual tends to zero, a converged value for a particular real time step has been achieved.

Originally, Equation A.14 was marched in pseudo-time in parallel with the Navier-Stokes equations. Therefore, the same Runge-Kutta scheme for the pseudo-time marching is used. In practice, Sadeghi [68] observes that the speed at which the CSD equations converge is much higher than for the CFD case and this could lead to divergence in the results. Therefore, Sadeghi [68] chooses to march the CFD equations first, followed by some CSD iterations and repeating the whole process until convergence in the results is achieved.

B Fluid-Structure Interface for three-dimensional coupled simulations using Constant Volume Tetrahedron (CVT) method

This Section is divided in two subsections. The first part deals with the Constant Volume Tetrahedron (CVT) method used to transfer loading and deformation between the CFD and CSD wings. The second part introduces a Transfinite Finite Interpolation (TFI) method to deform the entire CFD grid contained in the flow field after the CFD wing is deformed.

The combination of CVT and TFI seems to provide accurate results with fast computational time and relative facility of implementation. On the other hand, more accurate methods provide slightly better results but imply longer computational times and significant difficulties in the implementation.

B.1 Constant Volume Tetrahedron

The CVT method introduced by Richards' group at the University of Glasgow [28] is a CFD-CSD interface that adds some relaxation to a rigid CFD-CSD connection case.

It could be a common situation where the structural model (and so the CSD grid) does not coincide with the CFD geometry. Moreover, CSD surface grids tend to be coarser than the CFD ones. For such a case, if CFD and CSD maintain a rigid connection, the transfer of loads will perform well but the transfer of deformations could lead to cells collapsing in the CFD field. Imposing invariant difference vectors may lead to unphysical deformations in the CFD geometry. The CVT formulation aims to a relatively accurate transfer of loading using a relaxed CFD-CSD attachment to prevent the grid points from collapsing.

Sadeghi [68] suggests that a fluid-structure interface must transfer smooth loading and deformations, represent exact rigid body motions, maintain physical deformations, and conserve the principle of virtual work.

If the displacements of the CFD nodes u_a are linearly dependent on the CSD nodes displacements u_s, then

$$\vec{u}_a = [G]\vec{u}_s \tag{B.16}$$

where $[G]$ is the transformation matrix the method is seeking for. The work from both grids must be equal such that

$$\vec{f}_s^T \vec{u}_s = \vec{f}_a^T \vec{u}_a = \vec{f}_a^T [G]\vec{u}_s \tag{B.17}$$

$$\vec{f_s} = [G]^T \vec{f_a} \tag{B.18}$$

where f_s is the vector of forces in the CSD geometry, and f_a the one for the CFD case. From Equation B.16 and B.18 $[G]$ must be found to compute: transfer of loading from CFD to CSD, and transfer of displacement from CSD to CFD.

Even if the above relations suggest a linear dependence to conserve the energy, the CVT formulation is in origin non-linear, and must be linearized.

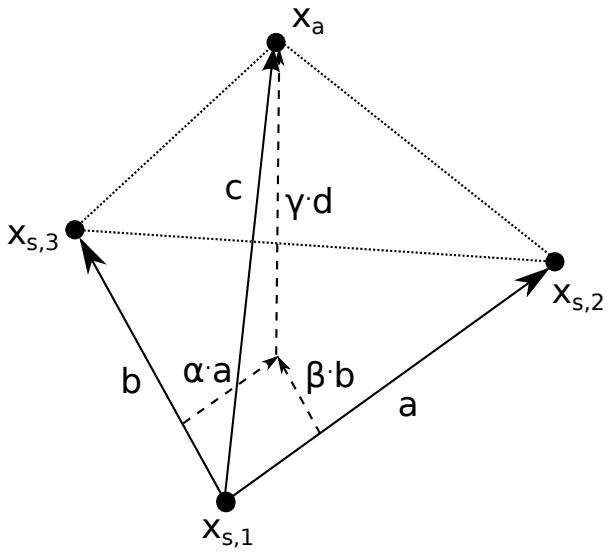

Figure B.1: CVT method: CFD-CSD grid association.

B.1.1 The non-linear formulation

Each node $\vec{x}_a$ of the CFD geometry is associated with 3 nodes from the CSD body generating a tetrahedron (Figure B.1). The restriction of constant volume in the tetrahedron will close the CVT formulation and give the name to the method: CVT. Vectors $\vec{a}$, $\vec{b}$ and $\vec{c}$ are

$$\begin{aligned} \vec{a} &= \vec{x}_{s,3} - \vec{x}_{s,1} \\ \vec{b} &= \vec{x}_{s,2} - \vec{x}_{s,1} \\ \vec{c} &= \vec{x}_a - \vec{x}_{s,1}. \end{aligned} \tag{B.19}$$

and α and β which will be constant parameters for the entire CFD-CSD computation take the form

$$\alpha = \frac{(\vec{b}\cdot\vec{b})(\vec{a}\cdot\vec{c}) - (\vec{a}\cdot\vec{b})(\vec{b}\cdot\vec{c})}{(\vec{a}\cdot\vec{a})(\vec{b}\cdot\vec{b}) - (\vec{a}\cdot\vec{b})(\vec{a}\cdot\vec{b})} \tag{B.20}$$

$$\beta = \frac{(\vec{a}\cdot\vec{a})(\vec{b}\cdot\vec{c}) - (\vec{a}\cdot\vec{b})(\vec{a}\cdot\vec{c})}{(\vec{a}\cdot\vec{a})(\vec{b}\cdot\vec{b}) - (\vec{a}\cdot\vec{b})(\vec{a}\cdot\vec{b})}. \tag{B.21}$$

Before a CSD deformation (variables defined with subindex 0), in order to perform a loading transfer from the CFD to the CSD nodes, vectors $\vec{a}$, $\vec{b}$ and $\vec{c}$ are computed. $\vec{d}$ is always defined as the cross product of $\vec{a}$ and $\vec{b}$ ($\vec{d} = \vec{a} \times \vec{b}$). The parameter γ is obtained from

$$\gamma_0 = \frac{\vec{c_0} \cdot \vec{d_0}}{\vec{d_0} \cdot \vec{d_0}} \tag{B.22}$$

After a CSD deformation, when the displacements from the CSD geometry must be transferred to the CFD one, vectors $\vec{a}$, $\vec{b}$, $\vec{c}$ and $\vec{d}$ are computed again. The new γ

$$\gamma = \frac{\vec{d_0} \cdot \vec{d_0}}{\vec{d} \cdot \vec{d}} \gamma_0 \tag{B.23}$$

is obtained by imposing a constant volume criterion in the tetrahedron.

B.1.2 Linearization

The displacement of $\vec{x}_a$ denoted as $\vec{u}_a$ can be expressed as

$$\vec{u}_a = \vec{u}_{xp} + \Delta(\gamma \vec{d}) \tag{B.24}$$

where $\vec{u}_{xp}$ is the displacement of the projection of $\vec{x}_a$ on the triangular plane formed by $< \vec{x}_{s,1} \vec{x}_{s,2} \vec{x}_{s,3} >$. Since α and β are constant parameters

$$\vec{u}_{xp} = \vec{u}_{s,1} + \alpha(\vec{u}_{s,2} - \vec{u}_{s,1}) + \beta(\vec{u}_{s,3} - \vec{u}_{s,1}) \tag{B.25}$$

and Equation B.24 can be expressed as

$$\vec{u}_a = \vec{u}_{s,1} + \alpha(\vec{u}_{s,2} - \vec{u}_{s,1}) + \beta(\vec{u}_{s,3} - \vec{u}_{s,1}) + \Delta(\gamma \vec{d}). \tag{B.26}$$

Using the definition of γ from Equation B.23, Equation B.26 becomes

$$\vec{u}_a = \vec{u}_{s,1} + \alpha(\vec{u}_{s,2} - \vec{u}_{s,1}) + \beta(\vec{u}_{s,3} - \vec{u}_{s,1}) + d_0^2\gamma_0\Delta\left(\frac{\vec{a}\times\vec{b}}{|\vec{a}\times\vec{b}|}\right). \tag{B.27}$$

This section started with a discussion about the conservation of energy between the CFD and the CSD geometry and found that a linear relation between $\vec{u}_a$ and $\vec{u}_{s,i}$ was needed in Equation B.16. Equation B.27 is linear in all terms except for the last one which requires a linearization. Badcock et al. [5] state the linearization point to be the latest time level. Sadeghi et al. [69] use a mid-deformation position for the linearization which proves to provide more accurate results. An integral method using Gauss-Legendre quadrature used by Sadeghi [69] to approximate the non-linear term of Equation B.27 reaches convergence in a minimum number of iterations.

ParCAE uses a multi-step mid-point linearization method for the evaluation of the following matrices proposed by Badcock et al. [5].

$$u_a = \sum_{i=1}^{3}[G]^{(i)}u_{s,i} \tag{B.28}$$

$$G_{ij}{}^{(1)} = \delta_{ij} - G_{ij}{}^{(2)} - G_{ij}{}^{(3)} \tag{B.29}$$

$$G_{ij}{}^{(2)} = \alpha\delta_{ij} - \gamma D_{ik}C(b)_{kj} \tag{B.30}$$

$$G_{ij}{}^{(3)} = \beta\delta_{ij} + \gamma D_{ik}C(a)_{kj} \tag{B.31}$$

where δ_{ij} is the Kronecker delta. The cross product matrix C of an arbitrary vector $\vec{z}$ is defined with the use of the permutation symbol ϵ_{ijk}

$$C(z)_{kj} = \epsilon_{ijk} z_j. \tag{B.32}$$

Matrix D_{ij} is

$$D_{ij} = \delta_{ij} - \frac{2}{d \cdot d} d_i d_j. \tag{B.33}$$

B.2 Flow Field Grid Deformation

The previous CVT method will still be used for an uncoupled aeroelastic computation for the load transfer from the CFD to the CSD geometries. The second part of the CVT method, which is in charge of transferring deformations from the CSD to the CFD geometry, would not be used. For a coupled study, once this second part of the CVT method has been used and the CFD geometry is deformed, the grid contained in the flow field must be deformed too. The present section presents the method that has been implemented in ParCAE to deform the cells from the entire flow field.

For small grid deformations, one can avoid regenerating the grid around the geometry of study. Grid regeneration is too time consuming to perform an aeroelastic study. For that reason, it is important to find an optimum method to deform an existing grid while maintaining the original grid quality. Some algebraic methods use one single processor to compute the new position of the entire grid which is not efficient. The present method uses the main processor to compute just the new position of the corners of each block. This information is then passed to the other processors which individually will obtain the new position of the grid points from their own block.

The method was introduced by Tsai et al. [82].

B.2.1 Multiblock approach

The first part of the method from Tsai et al. is originally found in the work of Batina [7]. Batina uses this method for structured [65] and unstructured [8] flow solvers. He defines a spring stiffness for each edge between two grid points. The nodes on the surface of the CFD geometry have a prescribed motion and the ones in the farfield are held fixed. The displacement of the interior points is obtained using static deformation equations for each grid point.

Tsai et al. [82] use the same technique to obtain the new position of just the corners of each block. If we enumerate the corner points of the blocks in a structured grid format, one can define the stiffness of an edge between corner points i and $i+1$ such that

$$k_{i+1/2} = \frac{1}{[(x_{i+1}-x_i)^2 + (y_{i+1}-y_i)^2 + (z_{i+1}-z_i)^2]^{p/2}}. \tag{B.34}$$

The stiffness is increased by increasing p.

The new position of the corner-block points is obtained using a two-step predictor corrector scheme. Initially, the displacement $\delta_{x,y,z}$ of a node i,j,k is estimated from a linear extrapolation of the displacements from the two previous iterations, according to

$$\begin{aligned}
\tilde{\delta}_{x_{i,j,k}} &= 2\delta^n_{x_{i,j,k}} - \delta^{n-1}_{x_{i,j,k}} \\
\tilde{\delta}_{y_{i,j,k}} &= 2\delta^n_{y_{i,j,k}} - \delta^{n-1}_{y_{i,j,k}} \\
\tilde{\delta}_{z_{i,j,k}} &= 2\delta^n_{z_{i,j,k}} - \delta^{n-1}_{z_{i,j,k}}.
\end{aligned} \tag{B.35}$$

In the corrector step, the displacements of each corner-block node are obtained from

$$\begin{aligned}
\delta^{n+1}_{x_{i,j,k}} &= \frac{k_{i+1/2,j,k}\ \tilde{\delta}_{x_{i+1,j,k}} + \ldots + k_{i,j,k-1/2}\ \tilde{\delta}_{x_{i,j,k-1}}}{k_{i+1/2,j,k} + \ldots + k_{i,j,k-1/2}} \\
\delta^{n+1}_{y_{i,j,k}} &= \frac{k_{i+1/2,j,k}\ \tilde{\delta}_{y_{i+1,j,k}} + \ldots + k_{i,j,k-1/2}\ \tilde{\delta}_{y_{i,j,k-1}}}{k_{i+1/2,j,k} + \ldots + k_{i,j,k-1/2}} \\
\delta^{n+1}_{z_{i,j,k}} &= \frac{k_{i+1/2,j,k}\ \tilde{\delta}_{z_{i+1,j,k}} + \ldots + k_{i,j,k-1/2}\ \tilde{\delta}_{z_{i,j,k-1}}}{k_{i+1/2,j,k} + \ldots + k_{i,j,k-1/2}}.
\end{aligned} \tag{B.36}$$

The summation in Equation B.36 goes from 1 to 6 in a 3D hexahedral grid where the contribution of each edge ending into the grid point i, j, k is considered. Once the new position of the corner-block points is obtained, it is passed onto each processor to calculate in parallel the new position of the interior grid points for each block.

B.2.2 Single Block Approach: Trans Finite Interpolation

A Trans Finite Interpolation (TFI) method introduced by Soni [71] is used. The displacement of the interior points of a block is obtained in three steps. First, the new position of the points along each of the 12 edges of a block is obtained using a previous parameterization of the points' position in the edge and the new position of the corner points. As an example, an edge is previously parameterized keeping two indices fixed (j^*, k^*), and marching in the third one (i). Defining F_{i,j^*,k^*} as the parameterization of the points along an edge in the i direction,

$$\begin{aligned}
s_{1,j^*,k^*} &= 0 \\
s_{i,j^*,k^*} &= s_{i-1,j^*,k^*} + \sqrt{(x_{i,j^*,k^*} - x_{i-1,j^*,k^*})^2 + (y_{i,j^*,k^*} - y_{i-1,j^*,k^*})^2 + (z_{i,j^*,k^*} - z_{i-1,j^*,k^*})^2} \\
& \quad i = 2, ..., i_{max}. \\
F_{i,j^*,k^*} &= s_{i,j^*,k^*} / s_{i_{max},j^*,k^*}
\end{aligned} \tag{B.37}$$

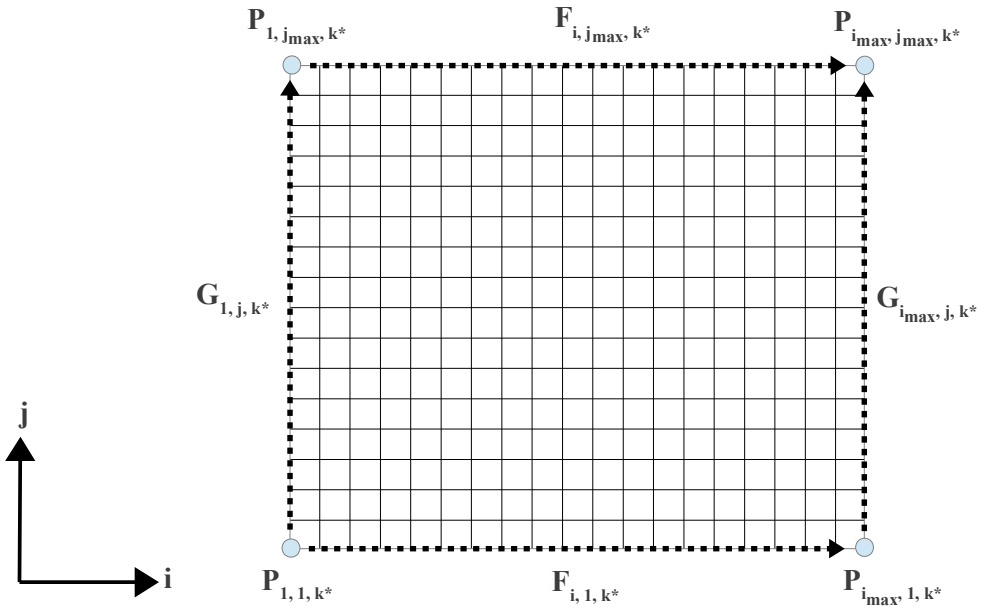

Figure B.2: k^* plane representing one of the 2 constant k faces of a block.

And the displacement of the edge points will be

$$\Delta E_{i,j^*,k^*} = (1 - F_{i,j^*,k^*})\Delta P_{1,j^*,k^*} + F_{i,j^*,k^*}\Delta P_{i_{max},j^*,k^*} \tag{B.38}$$

where $\Delta P_{1,j^*,k^*}$ and $\Delta P_{i\,max,j^*,k^*}$ are the displacement of the initial and final corner points of an $i - direction$ edge, respectively.

The second step, once the edge points of a block have been deformed, is to deform the points contained on each of the 6 surfaces of each block. Following the previous formulation, a surface defined in the i, j (Figure B.2) plane would compute its surface points displacements as

$$\begin{aligned}\Delta S_{i,j,k^*} = {} & A_{i,j,k^*}\Delta E_{1,j,k^*} + B_{i,j,k^*}\Delta E_{i_{max},j,k^*} + C_{i,j,k^*}\Delta E_{i,1,k^*} + D_{i,j,k^*}\Delta E_{i,j_{max},k^*} \\ & - A_{i,j,k^*}C_{i,j,k^*}\Delta P_{1,1,k^*} - B_{i,j,k^*}C_{i,j,k^*}\Delta P_{i_{max},1,k^*} - A_{i,j,k^*}D_{i,j,k^*}\Delta P_{1,j_{max},k^*} \\ & - B_{i,j,k^*}D_{i,j,k^*}\Delta P_{i_{max},j_{max},k^*}\end{aligned} \tag{B.39}$$

where ΔS, ΔE and ΔP denote surface, edge and corner point displacement, respectively. The remaining blending functions are

$$\begin{aligned} A_{i,j,k^*} &= 1 - \eta_{i,j,k^*} \ , \qquad B_{i,j,k^*} = \eta_{i,j,k^*} \\ C_{i,j,k^*} &= 1 - \varepsilon_{i,j,k^*} \ , \qquad D_{i,j,k^*} = \varepsilon_{i,j,k^*} \end{aligned} \tag{B.40}$$

with

$$\begin{aligned} Q_{i,j,k^*} &= 1 - (F_{i,j_{max},k^*} - F_{i,1,k^*})(G_{i_{max},j,k^*} - G_{1,j,k^*}) \\ \varepsilon_{i,j,k^*} &= [G_{1,j,k^*} + F_{i,1,k^*}(G_{i_{max},j,k^*} - G_{1,j,k^*})]/Q_{i,j,k^*} \\ \eta_{i,j,k^*} &= [F_{i,1,k^*} + G_{1,j,k^*}(F_{i,j_{max},k^*} - F_{i,1,k^*})]/Q_{i,j,k^*}. \end{aligned} \tag{B.41}$$

At this point, each block contained in each processor has already displaced the grid points from each of the 6 faces of the block. The last and third step is to displace the nodes from the interior of the blocks. Taking as a reference the previous formulation step from one-dimensional (Equation B.38) to two-dimensional (Equation B.39), and following the guidelines from Soni [71] and Tsai et al. [82] we can extend the formulation to the third dimension.

Being H the analog of F and G for the k dimension, the deformation of the interior points of the block is determined from

$$\Delta V_{i,j,k} = V_1 + V_2 + V_3 - V_{12} - V_{13} - V_{23} + V_{123} \tag{B.42}$$

with

$$
\begin{aligned}
V_1 &= (1 - F_{i,j,k})\Delta S_{1,j,k} + F_{i,j,k}\Delta S_{i_{max},j,k} \\
V_2 &= (1 - G_{i,j,k})\Delta S_{i,1,k} + G_{i,j,k}\Delta S_{i,j_{max},k} \\
V_3 &= (1 - H_{i,j,k})\Delta S_{i,j,1} + H_{i,j,k}\Delta S_{i,j,k_{max}} \\
V_{12} &= (1 - F_{i,j,k})(1 - G_{i,j,k})\Delta E_{1,1,k} + (1 - F_{i,j,k})G_{i,j,k}\Delta E_{1,j_{max},k} \\
&\quad + F_{i,j,k}(1 - G_{i,j,k})\Delta E_{i_{max},1,k} + F_{i,j,k}G_{i,j,k}\Delta E_{i_{max},j_{max},k} \\
V_{13} &= (1 - F_{i,j,k})(1 - H_{i,j,k})\Delta E_{1,j,1} + (1 - F_{i,j,k})H_{i,j,k}\Delta E_{1,j,k_{max}} \\
&\quad + F_{i,j,k}(1 - H_{i,j,k})\Delta E_{i_{max},j,1} + F_{i,j,k}H_{i,j,k}\Delta E_{i_{max},j,k_{max}} \\
V_{23} &= (1 - G_{i,j,k})(1 - H_{i,j,k})\Delta E_{i,1,1} + (1 - G_{i,j,k})H_{i,j,k}\Delta E_{i,1,k_{max}} \\
&\quad + G_{i,j,k}(1 - H_{i,j,k})\Delta E_{i,j_{max},1} + G_{i,j,k}H_{i,j,k}\Delta E_{i,j_{max},k_{max}} \\
V_{123} &= (1 - F_{i,j,k})(1 - G_{i,j,k})(1 - H_{i,j,k})\Delta P_{1,1,1} \\
&\quad + (1 - F_{i,j,k})(1 - G_{i,j,k})H_{i,j,k}\Delta P_{1,1,k_{max}} \\
&\quad + (1 - F_{i,j,k})G_{i,j,k}(1 - H_{i,j,k})\Delta P_{1,j_{max},1} \\
&\quad + (1 - F_{i,j,k})G_{i,j,k}H_{i,j,k}\Delta P_{1,j_{max},1} \\
&\quad + F_{i,j,k}(1 - G_{i,j,k})(1 - H_{i,j,k})\Delta P_{i_{max},1,1} \\
&\quad + F_{i,j,k}(1 - G_{i,j,k})H_{i,j,k}\Delta P_{i_{max},1,k_{max}} \\
&\quad + F_{i,j,k}G_{i,j,k}(1 - H_{i,j,k})\Delta P_{i_{max},j_{max},1} \\
&\quad + F_{i,j,k}G_{i,j,k}H_{i,j,k}\Delta P_{i_{max},j_{max},k_{max}}
\end{aligned}
\tag{B.43}
$$

A relaxation strategy to prevent grid discontinuities is implemented in ParCAE to treat cases of mixed block boundary conditions where a face of a block contains part of the geometry and part of the flow field. Another contribution from Tsai et al. [82] helps to maintain the original angle of the grid points in contact with a solid wall preventing the crossover of cells when large deformations occur.

C Three-dimensional preliminary results of aeroelastic computations

A steady state deformation is shown in this section. The system is tested in a coupled and uncoupled mode. For the uncoupled mode, the CFD force distribution from the rigid wing is transfered at the end of the computation generating a structural displacement. But the system is uncoupled, since the new structural position is not used in the CFD code to obtain new loading distributions.

The coupled mode produces an iterative procedure between the CFD and the CSD codes to obtain a final deformed steady state distribution where both sets of equations are satisfied. Two different grids are used for CFD and CSD computations due to the CFD grid having much higher resolution requirements. Images of both grids are shown in Figures C.3 and C.4.

C.1 Coupled and uncoupled static deformation

Cai et al. [14] present different strategies that could be used individually or combined in order to obtain a static deformation with the minimum number of iterations and avoiding large non-physical initial deformations that could lead to collapsing cells.

In their work, they suggest to eliminate the inertial term from the structure dynamics equations to suppress the oscillatory behavior of the solution and reach faster a steady state. They also recommend increasing the damping coefficient and using a blending for the displacements,

$$q^{n+1} = \alpha q^n + (1-\alpha) q^{n+1} \tag{C.44}$$

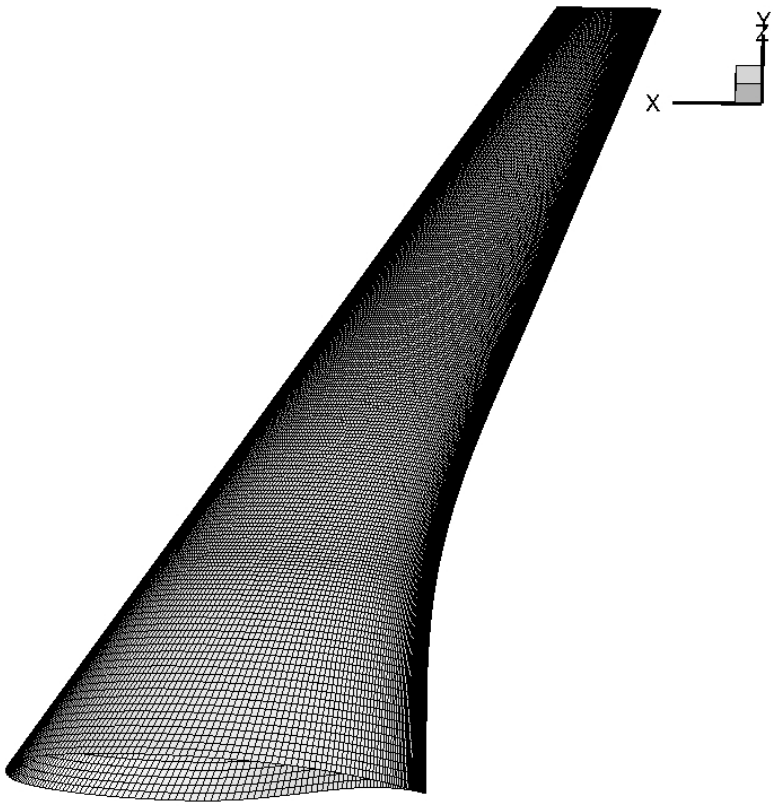

Figure C.3: 3D view of both CSD wings.

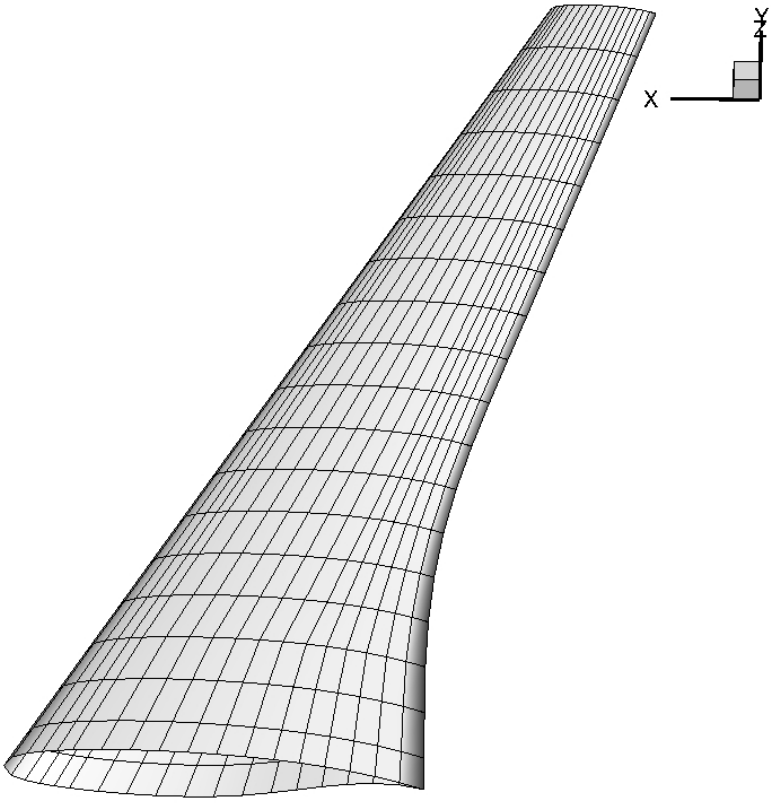

Figure C.4: Top view of both CSD wings.

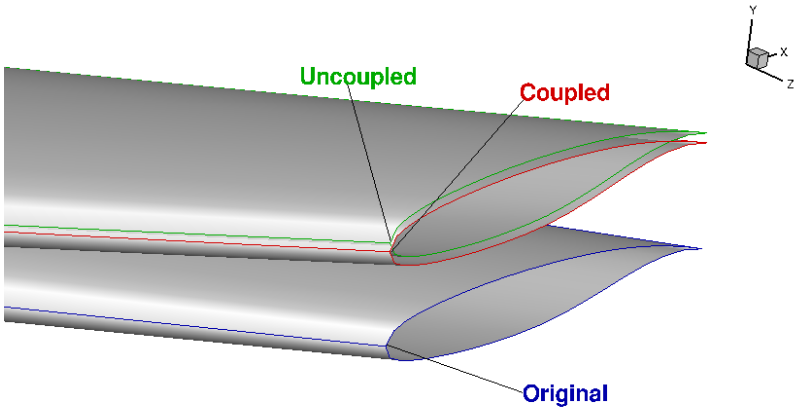

Figure C.5: Original wing position (blue), coupled (red) and uncoupled (green) aeroelastic static deformation wing positions.

where the structural displacement at each time step is blended with the displacement at the previous time step. For the present computations, α has been taken as 0.5. Blending the displacement and increasing the damping prevents the system from applying too large displacements that could lead to collapsing cells. The equations can be marched in pseudo time to steady state since accuracy in time is not required for a static deformation.

Mach number 0.8, angle of attack 0, and flight conditions at 10 km altitude are tested for the real wing size.

Figure C.5 shows the original, the coupled and the uncoupled static deformation obtained for this wing. For the uncoupled case, the flow part of the code has been marched in pseudo-time to steady state, and a single deformation step has been performed in the modal analysis type of ParCAE. The results of final loading on the wing for both coupled and uncoupled cases have been saved. We have input those into NASTRAN to compare the deformation from NASTRAN with the one we have obtained in ParCAE to validate our structural solver. The solution from NASTRAN (direct analysis) and ParCAE (modal analysis with 5 modes) have differences below 0.5% which are probably due to the use of just 5 modes in ParCAE.

Figures C.6 and C.7 show the results obtained for the coupled and uncoupled case in ParCAE.

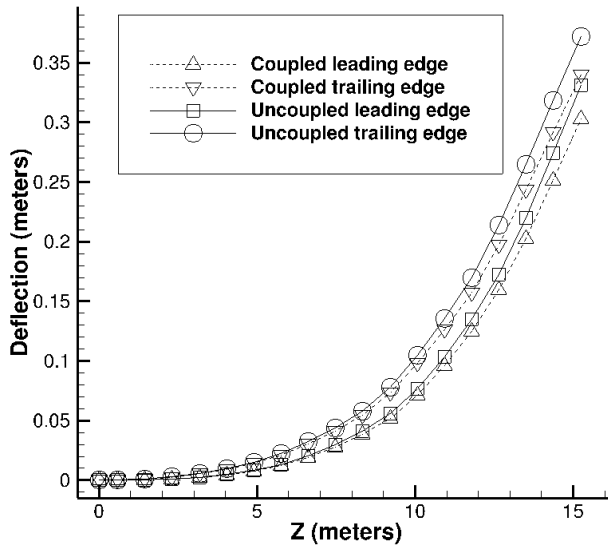

Figure C.6: Vertical deflection of leading edge and trailing edge nodes for a coupled and uncoupled aeroelastic static simulation. Z denotes the spanwise dimension, being 0 at the root of the wing.

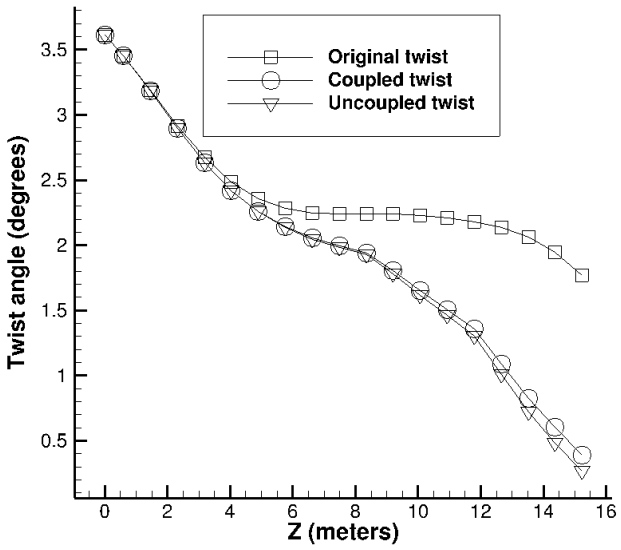

Figure C.7: Twist angle for the original wing and the deformed ones by a coupled and an uncoupled aeroelastic static simulation. Z denotes the spanwise dimension, being 0 at the root of the wing.

Figure C.6 shows the vertical deflection of the leading edge and trailing edge points, and Figure C.7 shows the original and final twist angle distribution.